NON-GAUSSIAN INTERFERENCE IN HIGH FREQUENCY, UNDERWATER ACOUSTIC, AND MOLECULAR COMMUNICATION

A Dissertation

Submitted to the Faculty

of

Purdue University

by

Hung-Yi Lo

In Partial Fulfillment of the

Requirements for the Degree

of

Doctor of Philosophy

May 2019

Purdue University

West Lafayette, Indiana

THE PURDUE UNIVERSITY GRADUATE SCHOOL
STATEMENT OF DISSERTATION APPROVAL

James S. Lehnert, Chair

School of Electrical and Computer Engineering

Mark R. Bell

School of Electrical and Computer Engineering

David J. Love

School of Electrical and Computer Engineering

Chih-Chun Wang

School of Electrical and Computer Engineering

Approved by:

Michael A. Capano

School of Electrical and Computer Engineering

Dedicated to my research advisor James S. Lehnert

ACKNOWLEDGMENTS

I would like to thank Professor James S. Lehnert for providing me a wonderful environment for research. He encouraged me to study a wide range of research topics. His countless efforts strengthened my publications. He showed me how to be more patient in research and writing. I gained a lot of research experiences because of him.

I would like to thank Professor Raymond A. DeCarlo and Professor Mike Melloch for providing me funding to continue my studies. My research could not have been completed without their help.

I would like to thank my committee members Professor Mark R. Bell, Professor David Love, and Professor Chih-Chun Wang. Their suggestions sparked new ideas and sharpened my research results.

I would like to thank Professor Young E. Kim of the Physics Department at Purdue University and Professor Chan K. Choi of Nuclear Engineering at Purdue University for their guidance regarding the modified Bi-Kappa distribution.

I would like to thank my colleagues Hang-Ting Chiang, Mu-Shen Lin, and Phuong Tran. They helped my research. I have learned to research more effectively from them. My friend Wei-Kang Hsiu and Gregory Chang helped me to become a more aggressive researcher.

TABLE OF CONTENTS

Page

LIST OF TABLES

LIST OF FIGURES

Figure Page

Figure Page

Figure Page

ABBREVIATIONS

HF	High Frequency
MUF	Maximum Usable Frequency
OWF	Optimum Working Frequency
pdf	probability density function
cdf	cumulative distribution function
MIMO	multiple-input multiple-output
EM	electromagnetic
AWGN	additive white Gaussian noise
LDPC	low density parity check
LLR	log-likelihood ratio
BER	bit error rate
BEC	binary erasure channel
BP	Bhattacharyya parameter

ABSTRACT

Lo, Hung-Yi PhD, Purdue University, May 2019. Non-Gaussian Interference in High Frequency, Underwater Acoustic, and Molecular Communication. Major Professor: James S. Lehnert.

The implications of non-Gaussian interference for various communication systems are explored. The focus is on the Kappa distribution, Generalized Gaussian distributions, and the distribution of the interference in molecular communication systems. A review of how dynamic systems that are not in equilibrium are modeled by the Kappa distribution and how this distribution models interference in HF communications systems at sunrise is provided. The channel model, bit error rate for single and multiple antennas, channel capacity, and polar code performance are shown.

Next, a review of the Generalized Gaussian distribution that has been found to model the interference resulting from surface activities is provided. This modeling is extended to find the secrecy capacity so that information cannot be obtained by the eavesdropper.

Finally, future nanomachnines are examined. The vulnerability to a receptor antagonist of a ligand-based molecule receiver is explored. These effects are considered to be interference as in other wireless systems and the damage to signal reception is quantified.

1. INTRODUCTION TO THE HIGH FREQUENCY (HF) CHANNEL

A fundamental understading of HF communication is essential for this work. In this chapter, we first look at the mechanism of HF communication. In Section 1.1, we describe the structure of the ionosphere. In Section 1.2, we study the change of the ionosphere versus time. In Section 1.3, we look at the key paramters for HF communication. In Section 1.4, we investigate the noise in the HF channel and show the model for the galactic noise in current literature.

1.1 The Ionosphere for HF Communication

Roughly speaking, HF transmission requires emitting the signal to the sky at one end, reflecting the signal from the ionosphere, and receiving the signal at the other end. Figure 1.1 [1] shows an example. The capability of the ionosphere of the Earth to reflect the electromagnetic wave makes this form of communications possible. Figure 1.2 [2] shows the location of the ionosphere of the Earth.

Figure 1.3 [2] shows the more detailed sublayers of the ionosphere. In the HF channel, when the signal enters the ionosphere, it first gets refracted into the E layer. From this point on, it has a chance to get relected at the F1 layer, and then gets refracted into the atomosphere to reach the destination. However, it also has a chance to get refracted into the F1 layer, and then get reflected at the F2 layer, and then get refracted into F1 and the atmosphere. There still exists some other cases in which more refractions and reflections have been experienced inside the ionosphere before the signal reaches back to the surface [3].

The ionosphere is not static. Rather, it fluctuates over time. It is constantly changing every moment [3], [4], [5]. Figure 1.4 [5] shows the different distributions

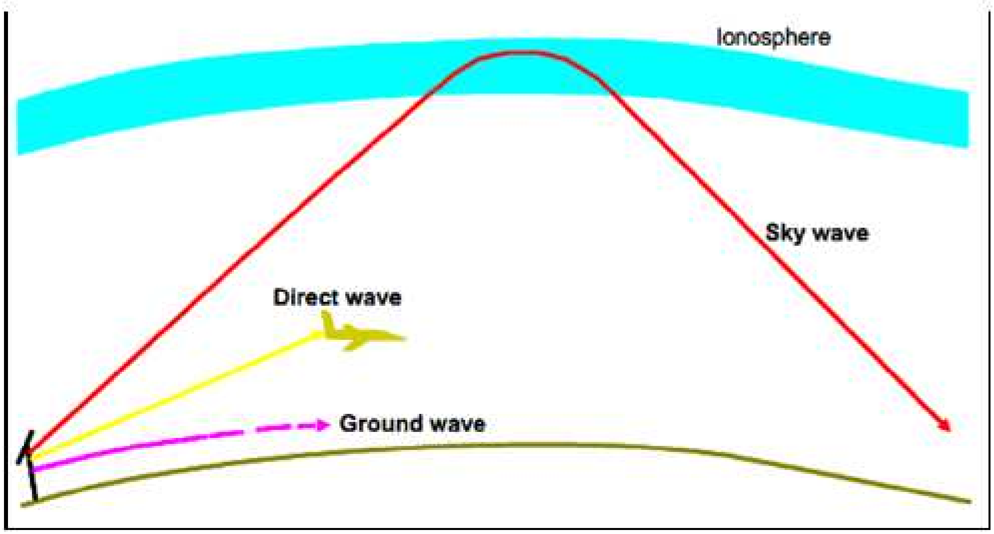

Fig. 1.1. HF communication path.

in day and night. The reason stems from the fact that it is the sun that causes the formation of the ionosphere. The Earth moves around the sun, and the Earth also spins about an axis. Hence, the ion distribution changes at least as a function of the time of a day and also as a function of the day of a year (see Figure 1.5 [4]). The sun is also known for its 11-year and 27-day sunspot cycles (see Figure 1.6 [6]). When the sunspot activity reaches maximum, the ion density in each sublayer increases. One of the induced effects is that the communication frequency increases.

One interesting thing that can be observed in Figure 1.3 and Figure 1.5 is the disappearance of certain sublayers in the ionosphere in a day. Also, the height of the sublayers changes over time. While in the daytime, D, E, F1, and F2 all exist, their behavior is different in the night. In the night, the F1 and F2 layers merge into one layer. At the same time, the D and E layer merge into one layer, and the ionization is greatly reduced. Hunt [5] points out that there are 3 important reasons that lead to the development of distinct ionospheric sublayers:

1. The solar spectrum deposits its energy at various heights, depending on the absorption characteristics of the atmosphere.

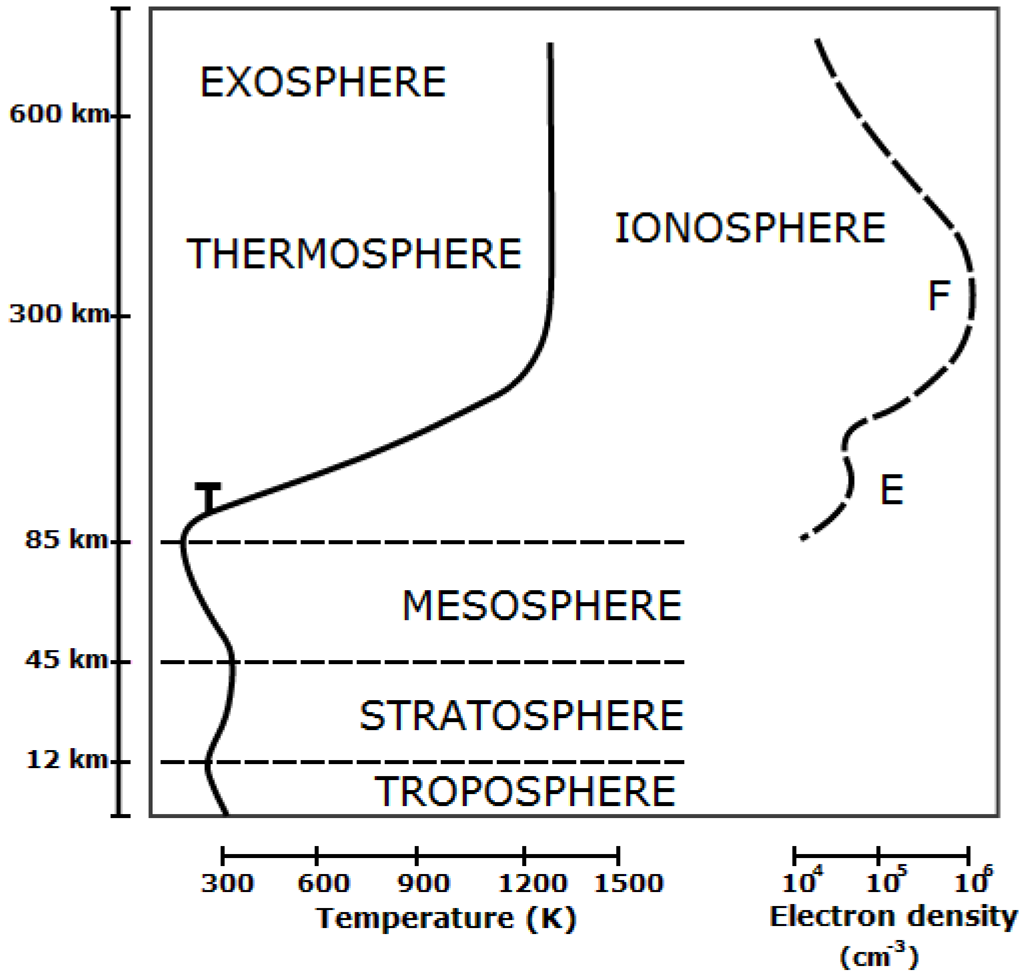

Fig. 1.2. The location of the ionosphere of the Earth.

2. The physics of recombination depends on density.
3. The composition of the atmosphere changes with height.

In addition to daily changes of the layers in the ionosphere, seasonal changes can also be observed. Figure 1.7 [7] and Figure 1.8 [8] shows results from observation. From these figures, we can see that for the F2 layer, electron density is higher in the winter than in the summer. Although it is true that ion production is faster in summer than in winter, the ion loss rate is also higher. The net result is what we observe. This phenomenon is called the winter anomaly [2] [8]. On the other hand,

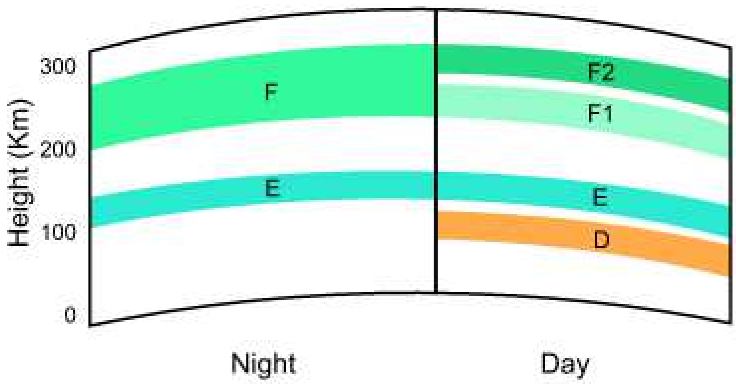

Fig. 1.3. Sublayers of the ionosphere.

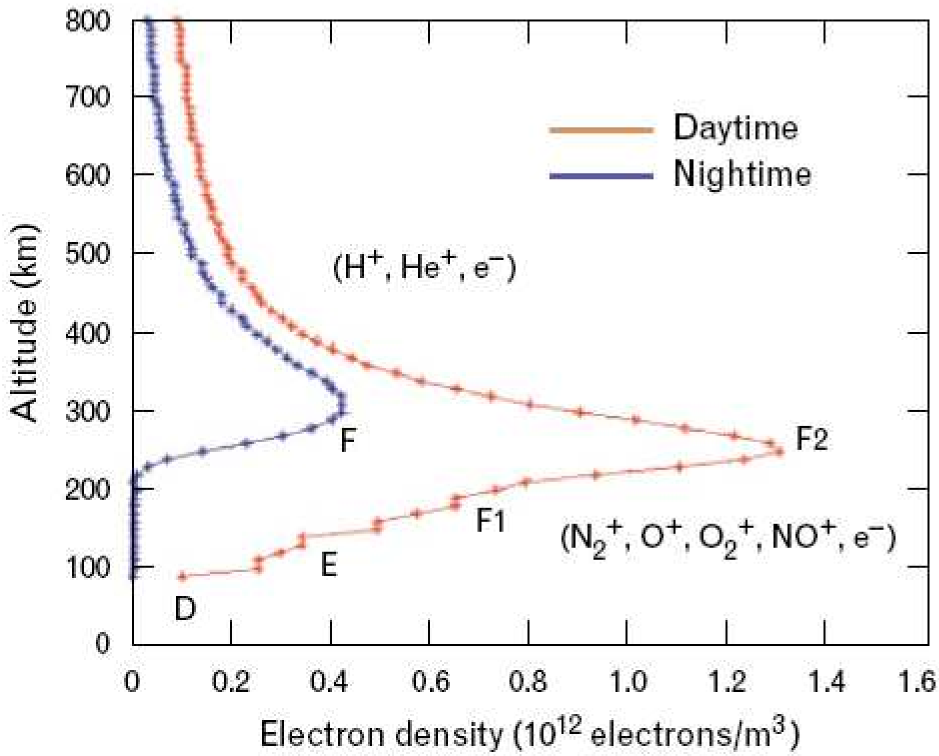

Fig. 1.4. Daily changes of the ion density in the ionosphere.

for F1, E, and D layers, the behavior is different. A closer look at Figure 1.8 reveals tht the maximum electron density of the F2 layer does not happen in winter, but rather, in equinoxes (March and September). The minimum electron density of the

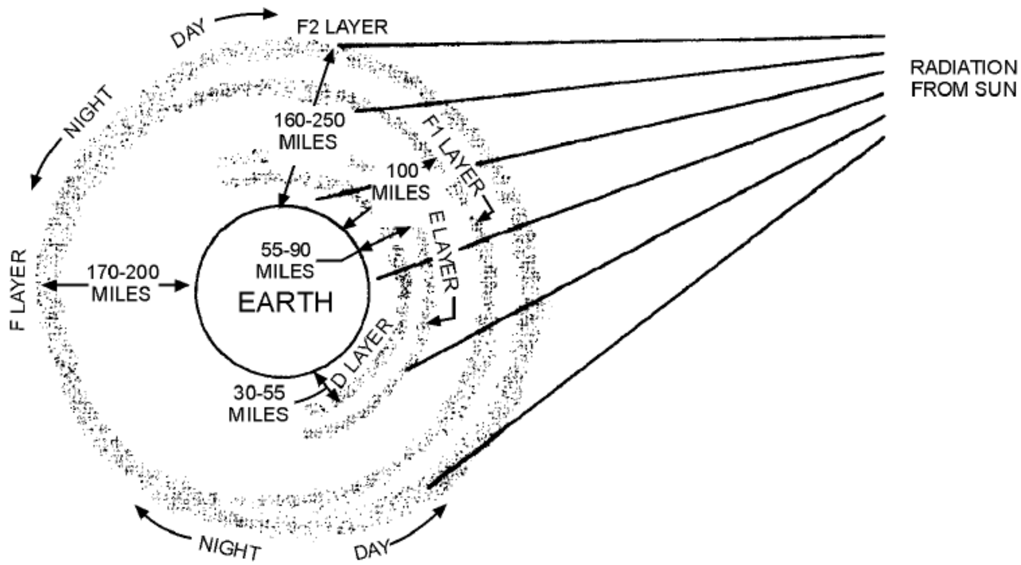

Fig. 1.5. Different ion distributions in the ionosphere and its relation with Earth rotation.

F2 layer happens in the summer. For the F1, E, and D layers, the maximum elctron density happens in the summer and the minimum happens in the winter.

It is important to point out that even though in Figure 1.8, the y-axis is not labeled as electron density (but critical frequency instead), this quantity is related to electron density through the following equation [7]:

$$f = 9\sqrt{N} \tag{1.1}$$

where f is the frequency (measured in Hz) that can be reflected by the ionospheric sublayer if the electromagnetic wave is coming in vertically. N is the ionization in units of electrons/m^3.

Figure 1.8 also shows the effect of the solar cycle on the electron density in the ionosphere. There are two types of solar cycles, one is the long term that has 11 years for a period, and another is the short term that has 27 days for a period. Figure 1.8 clearly shows the long term solar cycle effects. The F2 layer is significantly impacted. During the times of solar maximum, the electron density in the F2 layer reaches the

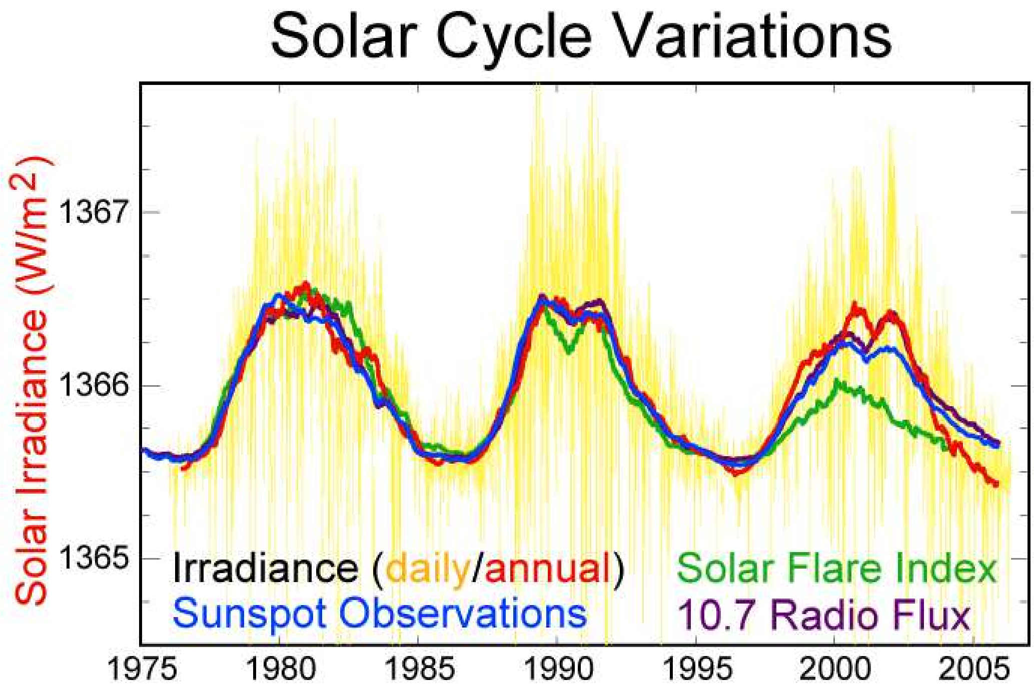

Fig. 1.6. Variation of solar radiation over the past years. From this figure we can clearly see such variation exhibits a long-term cycle (11-year) and a short term cycle (27-day).

maximum. During the times of solar minimum, the electron density in the F2 layer reaches the minimum. The same thing can be observed in the F1 layer. However, the influence is not that much compared with the F2 layer. For the E layer, such influence is even less.

Ion density changes with latitude. Figure 1.9 [8] shows how electron density changes with latitude in the daytime and night. Solar radiation on Earth is different with latitude. This leads to the general decrease in electron density from low altitude to high altidue. In daytime, the peak does not occur at the equator, but rather at 20°. The reason [2], [5], [9] is due to the Earth's magnetic lines. They are horizontal at the magnetic equator (see Figure 1.10 [10]). Solar heating and tidal oscillations in the lower ionosphere move plasma up and across the magnetic field lines. This sets up a sheet of electric current (see Figure 1.11 [2]) in the E region which, with the

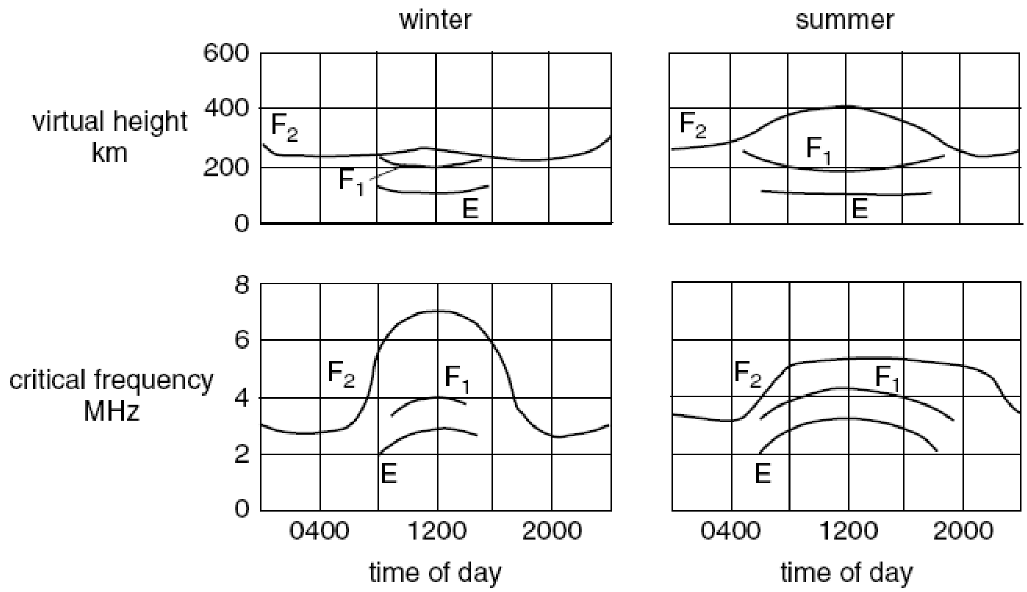

Fig. 1.7. Seasonal changes of electron density in the ionosphere.

horizontal magnetic field, forces ionization up into the F layer, concentrating at 20° from the magnetic equator. This phenomenon is called the equatorial anomaly [2] [9].

We can also observe in Figure 1.9 that during the night, there is a trough at 60°. This trough is called the mid-altitude trough. Yizengaw [11] experimentally proved that there is correlation between plasma pause and and mid-altitude trough (see Figure 1.12 [11]). They happen almost at the same altitude, except at different height. Hence, magnetosphere-ionospheric coupling (again cuased by solar radiation) is responsible for the mid-altitude trough.

Table 1.1 shows the critical frequency for each layer in the ionosphere. The frequencies are computed via Equation 1.1. The corresponding electron density data are obtained from [12]. Note that F2 plays the most important role in HF communication, because it provides the highest transmission frequency (and hence data rate) and does not disapper in the night.

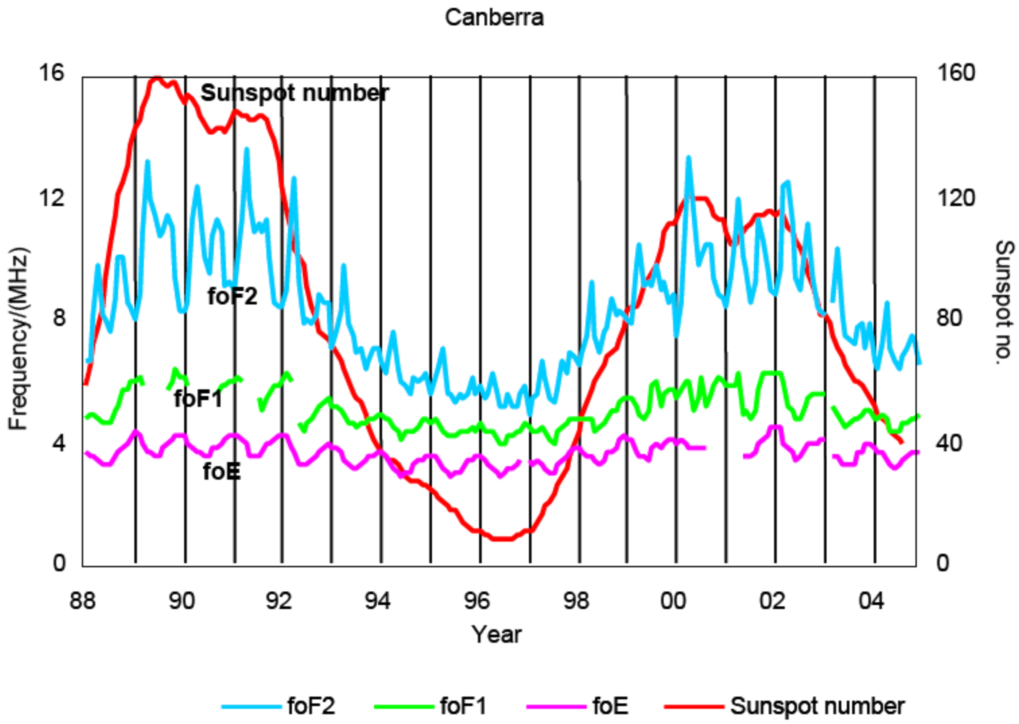

Fig. 1.8. Long term changes of electron density in the ionosphere. Notice that in this figure, the observation is made in Canberra, Australia. In other words, it is in the southern hemisphere. In the southern hemisphere, winter and summer months are opposite to that in the northern hemisphere, i.e., January is summer in Canberra, and July is winter in Canberra.

Table 1.1.
Critical frequency for each layer in the ionosphere.

Layer	**Critical Frequency f$_o$**
D	0.09MHz $\sim$ 0.9 MHz
E	$\sim$ 2.846MHz
F1	$\sim$ 4.9295MHz
F2	$\sim$ 12.728MHz

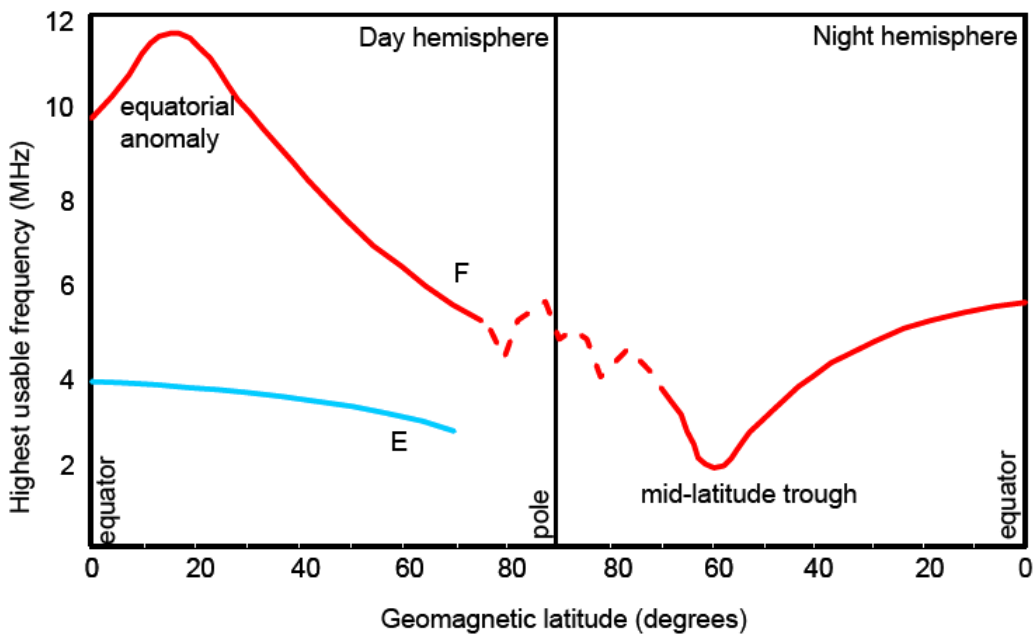

Fig. 1.9. Latitudinal changes of electron density in the ionosphere.

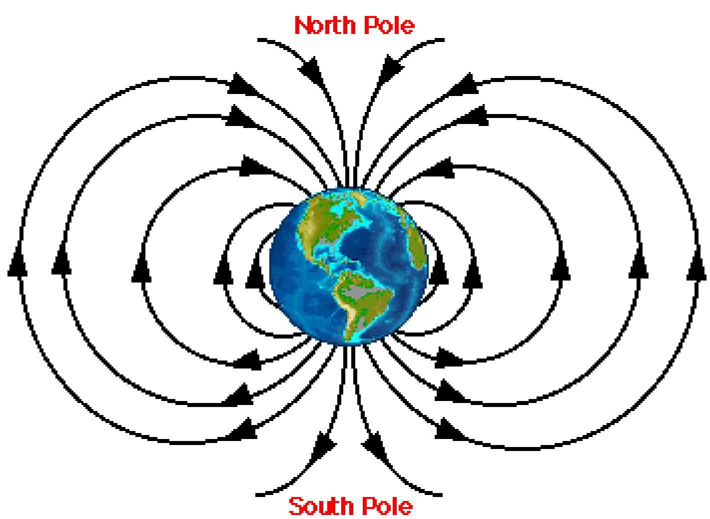

Fig. 1.10. Latitudinal changes of electron density in the ionosphere.

1.2 Irregular Variations in the Ionosphere

Section 1.1 provided information about regular variations in the ionosphere. Diurnal, seasonal, long term and short term solar cycles, and latitudinal variations all

Fig. 1.11. Latitudal changes of electron density in ionosphere.

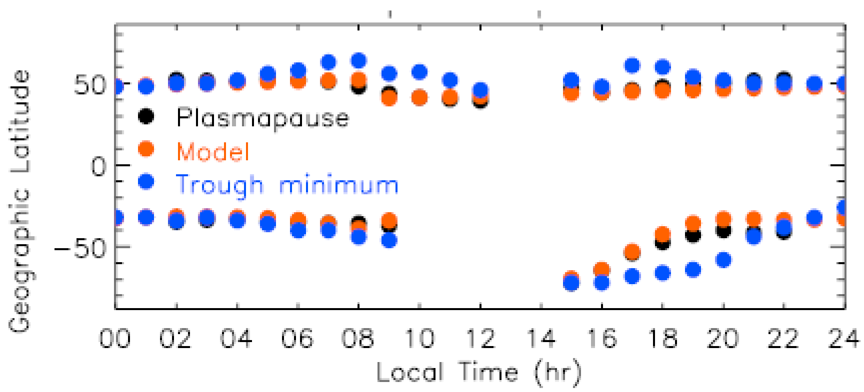

Fig. 1.12. Experimental proof of correlation between plasma pause and mid-altitude ionosphere trough.

fit into this category. However, a complete discussion of HF communication must also deal with irregular variations. As we will see, irregular variations [4], [8], [5], [9] cause a significant impact on HF communications.

Sporadic E

On some occasions, unpredictable ion clouds may be formed in some part of the E layer (see Figure 1.13 [8]). This is called sporatic E [4], [8]. The clouds may be as narrow as a few kilometers to as wide as hundreds of kilometers. The ion density in sporadic E is also unpredictable. If it is dense enough, it can act like the F2 layer so that it reflects frequencies that should be reflected by the F2 layer. Thus, it changes the communication path (see Figure 1.13). The original communication plan needs to be adjusted to accommodate this phenomenon. If the ion dentity in sporatic E is even denser, then according to Equation 1.1, the communication frequency is increased. If the ion density in sporadic E is thin, then it has less impact on HF communications. It simply passes normal HF frequency signals.

The duration of Sporatic E is also unpredictable, ranging from minutes to hours. In the low and mid-latitudes, it occurs mostly during daytime and early evening. At high latitudes, sporatic E tends to form in the night [8].

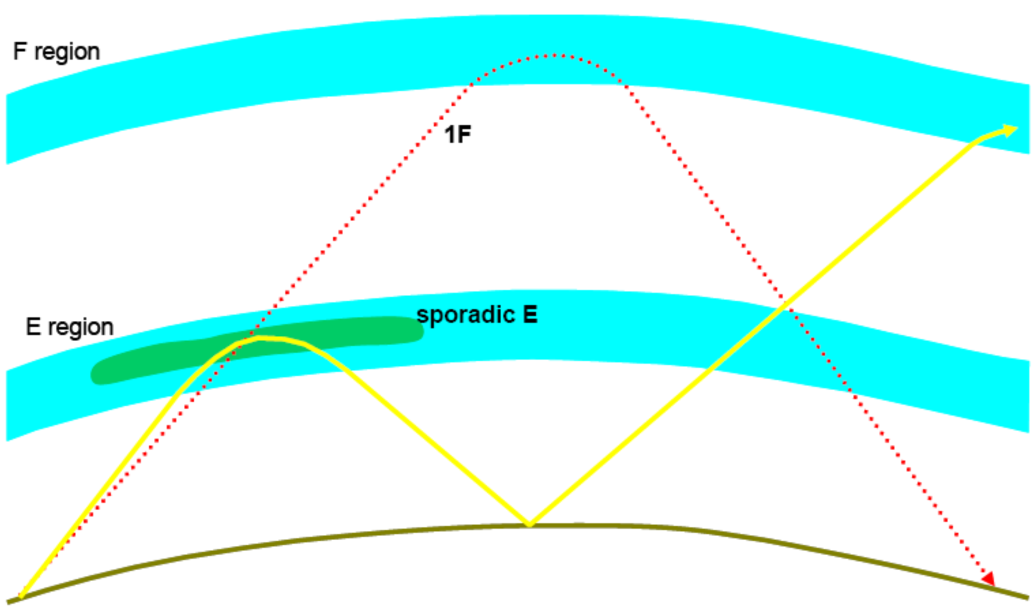

Fig. 1.13. Cause of short wave fade-out and its effect on HF communication.

Short Wave Fade-outs

The sun continuously flares. However, unexpectedly large flares may happen. This leads to the D layer (the sunward side of Earth) becoming heavily ionized. Such an abnormal D layer can absorb much of lower frequency signals in HF communication. For low frequency communication in the HF channel, the link is dead during the fade-out. Figure 1.14 [8] shows how the HF signal is affected by this fade-out. The fade-out affects lower frequencies more than higher frequencies. Figure 1.15 [8] shows these differences. From Figure 1.15, we can see that short wave fade-outs have little impact on high frequency signals for HF communications.

The duration of short wave fade-outs is also unpredictable, ranging from a few minutes to a few hours, with a fast onset and slower recovery (see Figure 1.15). The duration of fade-out is dependent on the duration of the corresponding solar flare [8]. Also, the attenuation depends on the magnitude of the flare. The larger the magnitude of the flare, the more attenuation the HF signal suffers.

Spread F

Certain sunspot activity, being unpredictable, may disturb the Earth's magnetic field. It causes observable ion density diffuse in F2 layer. This situation is described as an ionospheric storm [4]. The corresponding ion density diffuse in F2 layer is called spread F. Note that an ionospheric storm is not the only cause to form spread F [13]. Normally an ionospheic storm does not affect lower layers (F1, E and D) as much as the F2 layer. According to Equation 1.1, the operating frequency in HF communication decreases when spread F occurs. Since F2 is the most commonly used layer for HF communication due to its high frequency range, this implies an ionospheric storm normally affects the high frequencies for HF communication.

Spread F lasts several minutes to several hours [13]. At low latitudes, spread F occurs mostly during the night hours and around the equinoxes. At mid-latitudes, spread F is less likely to occur than at low and high latitudes, and is more likely to

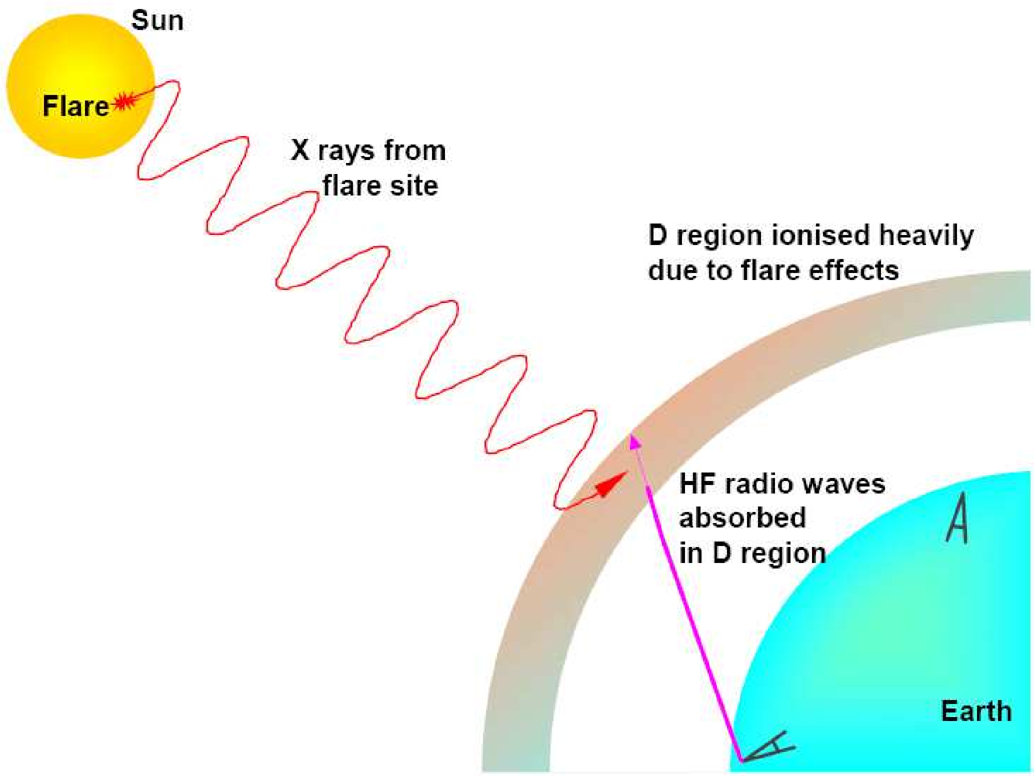

Fig. 1.14. The cause of short wave fade-out and its effect on HF communication.

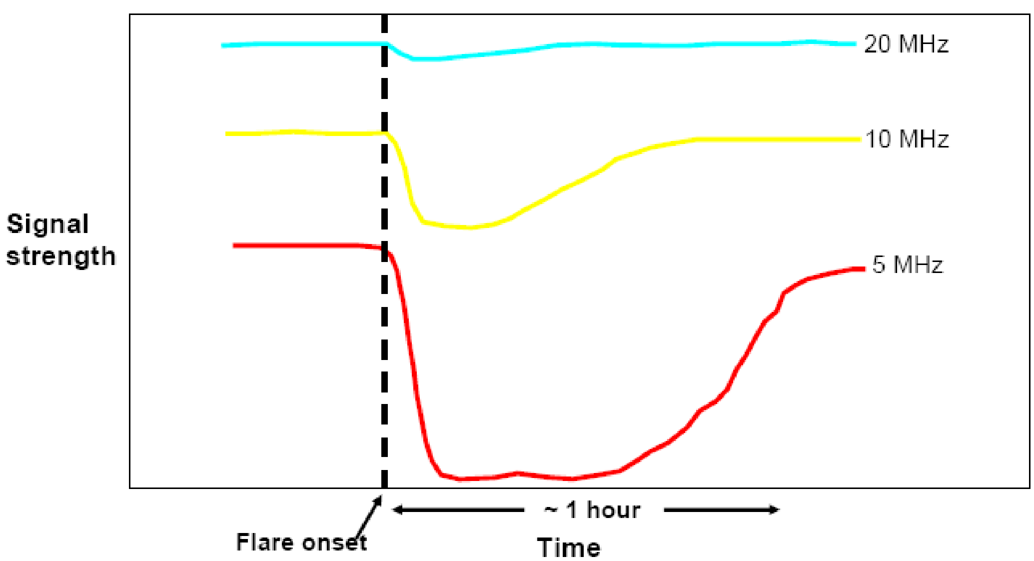

Fig. 1.15. The effect of fade-out on attenuation for various frequencies.

Table 1.2.
Effects of various irregular variations in the ionosphere. 'o' means that the indicated type of irregular variation will happen while 'x' means not.

Type	Day	Night	Effect on communication
Sporadic E	low alt : o	low alt: x	path
	mid alt: o	mid alt: x	f ↑
	high alt: x	high alt: o	
Short Wave Fade-outs	o	x	low freq: blocked
			mid freq: attenuation
			high freq: none
Spread F	low alt: x	low alt: o	f ↓
	mid alt: o (less likely)	mid alt: o	
	high alt: o	high alt: o	

occur at night and in winter. At latitudes greater than about 40°, spread F tends to be a night time phenomenon, appearing mostly around the equinoxes, while around the magnetic poles, spread F is often observed both day and night [8].

Table 1.2 summarizes this subsection by summarizing important consequences to HF communication from irregular variations in the ionosphere.

1.3 Some Important Parameters in HF Communication

Frequency

In Equation 1.1, we considered the case of vertical incidence. That is, we vertically transmit the signal to the sky, and at a certain frequency, it will be reflected back. Since the path is vertical, the return path will be the same, that is, directly back to the transmitter. When the electromagnetic wave reaches the ionosphere obliquely, the frequency that can be reflected changes with its angle relative to the horizon. This is summarized by the following equation [7]:

$$\begin{aligned} f &= k * f_o * \sec(\alpha) \\ &= k * \sec(\alpha) * f_o \\ &\equiv MUFfactor * f_o \end{aligned} \tag{1.2}$$

where f_o is the critical frequency obtained from Equation 1.1, α is the angle between the direction of the electromagnetic wave we transmit to the sky and the horizon, and k is the correction that accounts for the curvature of the Earth. The correction factor is not 1 when the the distance between the receiver and the transmitter is more than 1000km. The frequency f obtained in Equation 1.2 is called Maximum Usable Frequency (MUF).

In practice, we transmit signals at a frequency that is 85% of the MUF. This value is termed as optimum working frequency (OWF) [7]. The reason we transmit at a frequency slightly lower than the MUF is due to the vartiations in the ionosphere. Signals with frequency larger than MUF will be less likely to be reflected [7]. They penetrate into space instead. Signals with frequency slightly smaller than the MUF are still very likely to be reflected [14] [15]. The MUF is affected by ionospheric vatiations, whether it is regular or irregular. Hence, we need to keep a margin by using a frequency lower than MUF.

Range

There is a limit on the transmission range for one-hop HF communication. Figure 1.16 [7] shows the reason and the calculation. Geometrically speaking, the range of HF communication is limited by the curvature of the Earth and the finite distance between the Earth and its ionosphere. In Figure 1.16, we can see

$$\theta = \cos^{-1}\left(\frac{a}{a+h}\right) \tag{1.3}$$

Also, by investigating the sector that is involved in the calculation, we can see

$$\frac{d}{2} = a\theta \tag{1.4}$$

Hence,

$$d = 2a\cos^{-1}\left(\frac{a}{a+h}\right) \tag{1.5}$$

By substituting a = 6371 and h = 400, we get d $\sim$ 4400km. A second-hop is possible in HF communication (at the end of the first hop, the signal is reflect by the ground back to the sky) [7], thus extending the range to 8800km . For reference, the Earth's circumference is about 40000km.

1.4 The Noise in the HF Channel

The study of HF channel noise has long been of great interest. A reliable communication system is always built upon the correct knowledge of noise model. In HF channel, several types of noise have been investigated [16] [17].

1. Manmande Noise and Interference:

2. Atmospheric Noise Atmospheric noise could be generated by lightning flashes and appeared as burst noise in the HF band. The bursts comes out as a result of numerous individual lightning strokes within a single flash. The probability density function(pdf) of the burst duration can be characterized as follows (obtaines by line-fitting) [18].

$$g(x) = D_1 e^{D_2 x} + D_3 \tag{1.6}$$

where parameters D_1, D_2, and D_3 are constants.

The pdf of the interarrival time bwtween consecutive bursts is modeled as follows (obtaines by line-fitting) [18].

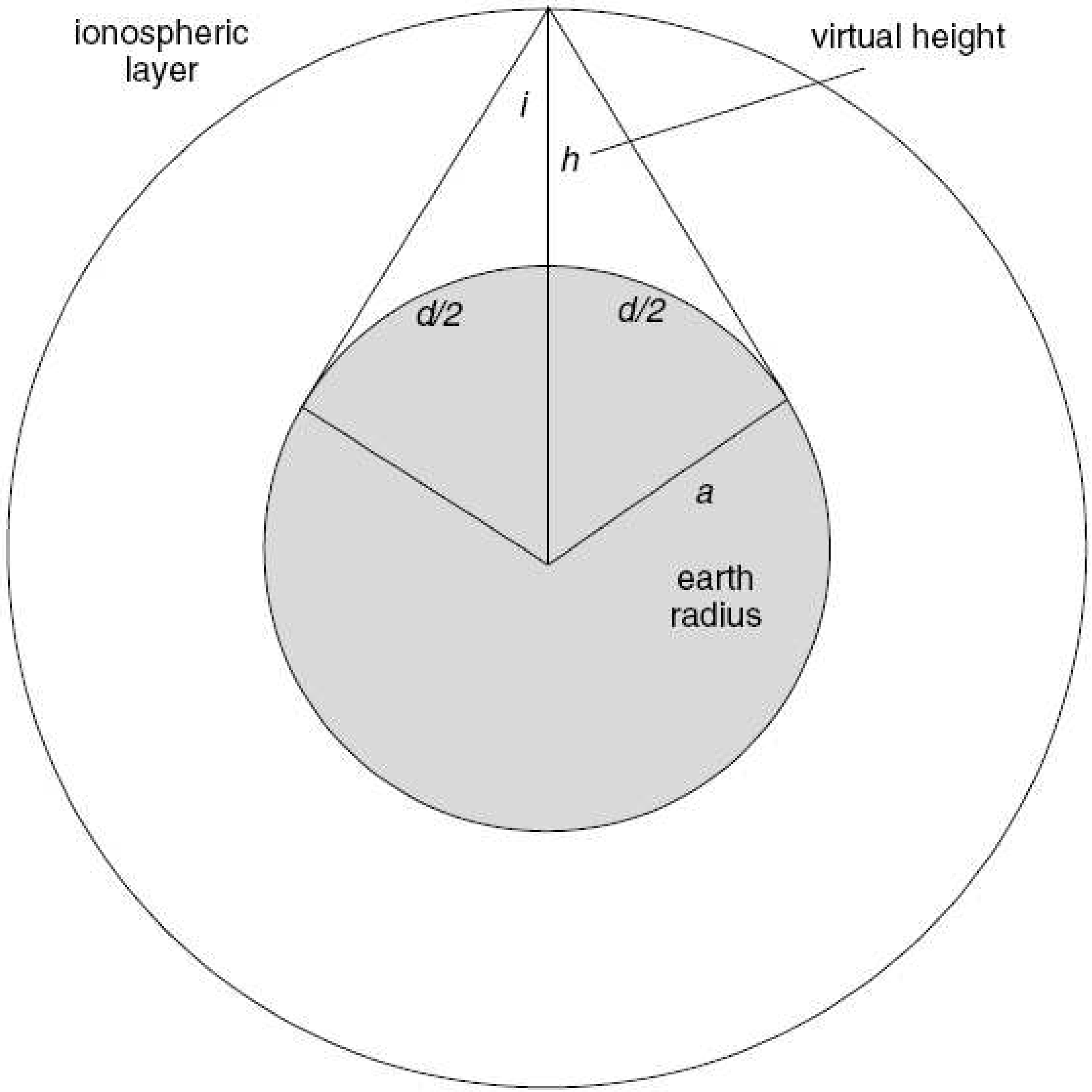

Fig. 1.16. Calculation on the maximum range for a single hop HF transmission. The radius of Earth is a. The distance between the Earth's horizon and the ionosphere is h. The maximum transmission range is d.

$$f(x) = \left(C_1 e^{-C_2 x} + C_3\right) exp\left[-\frac{C_1}{C_2}\left(1 - e^{-C_2 x}\right) - C_3 x\right] \tag{1.7}$$

where parameters C_1, C_2, and C_3 are constants.

During each burst, the phase is assumed to be uniformly distributed and the amplitude follows Hall model as shown in the following equation [19] [20].

$$p\left(A\right)=\frac{\left(\theta-1\right)\gamma^{\theta-1}A}{\left(A^{2}+\gamma^{2}\right)^{\left(\theta+1\right)/2}} \tag{1.8}$$

Here, parameters $(\gamma,\theta)=(0.2,2.0)$ and $(10^{-8},1.2)$ have been reported as examples.

On each axis, the Hall model becomes

$$p\left(x\right)=C_{4}\frac{\gamma^{\theta-1}}{\left(x^{2}+\gamma^{2}\right)^{\left(\theta-1\right)/2}} \tag{1.9}$$

where parameter C_4 is a pdf normalization constant.

However, for $2<\theta\leq 3$, the variance is infinite, and Hall model introduces an exponential decay factor to mitigate it. For example, when $\theta=3$, the Hall model becomes

$$p\left(x\right)=C_{5}\frac{\gamma^{2}}{\left(x^{2}+\gamma^{2}\right)}e^{\left(-\frac{x^{2}}{\beta^{2}\sigma^{2}\gamma^{2}}\right)} \tag{1.10}$$

where parameter C_5 is a pdf normalization constant.

Atmospheric noise changes with time. So different parameters will be obtained for different day, month, and season.

3. Galactic Noise

HF communication is established from the help of the plasma of the ionosphere. However, the plasma itself undergoes random fluctuations and hence cause the so called galactic noise. When manmade noise is not dominant, galactic noise can be measured, as shown in Giesbrecht's work [17]. Table 1.3 is extracted from one of Giesbrecht's publication [21].

Table 1.3.: Giesbrecht's [21] measurement of HF noise.

7:00	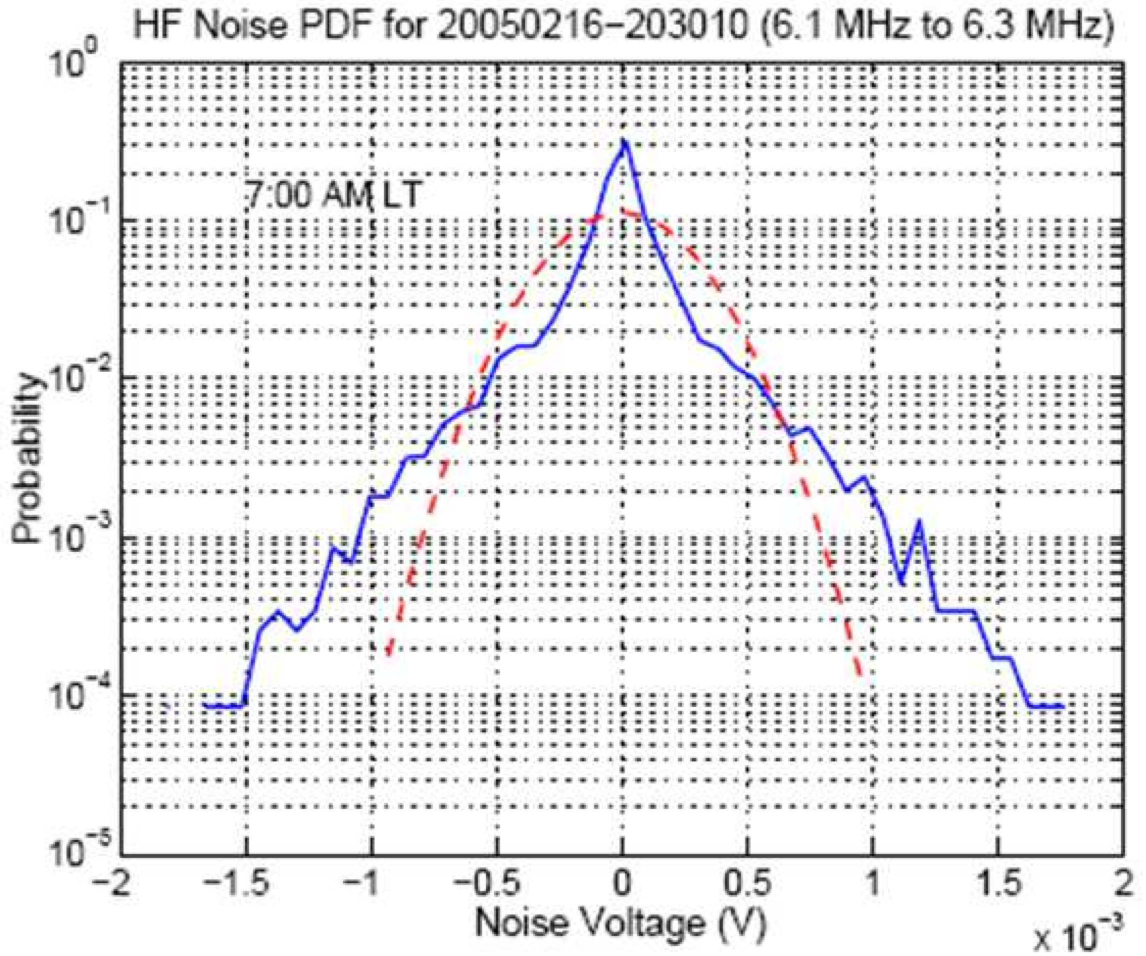

7:15	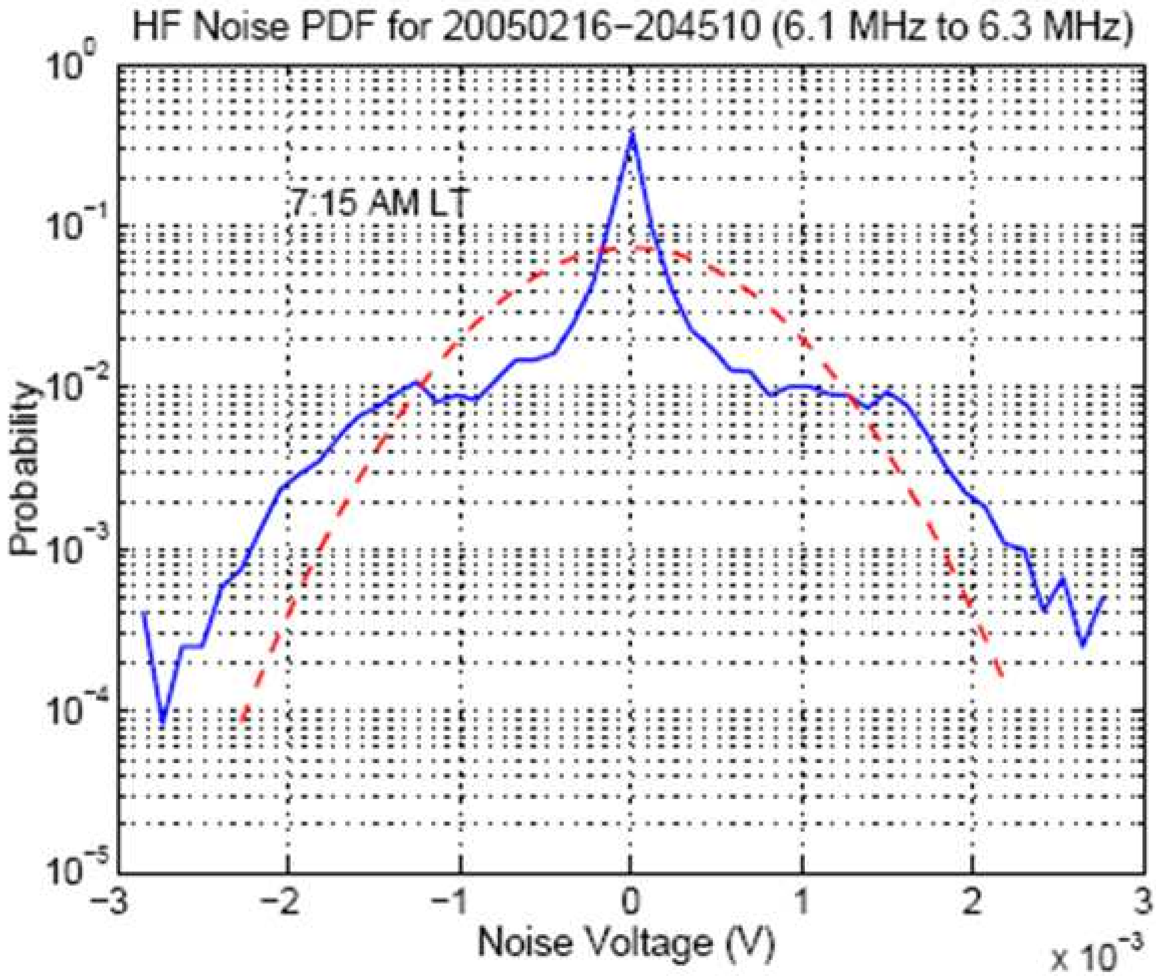HF Noise PDF for 20050216−204510 (6.1 MHz to 6.3 MHz) 7:15 AM LT Probability Noise Voltage (V) x 10^{−3}

7:30	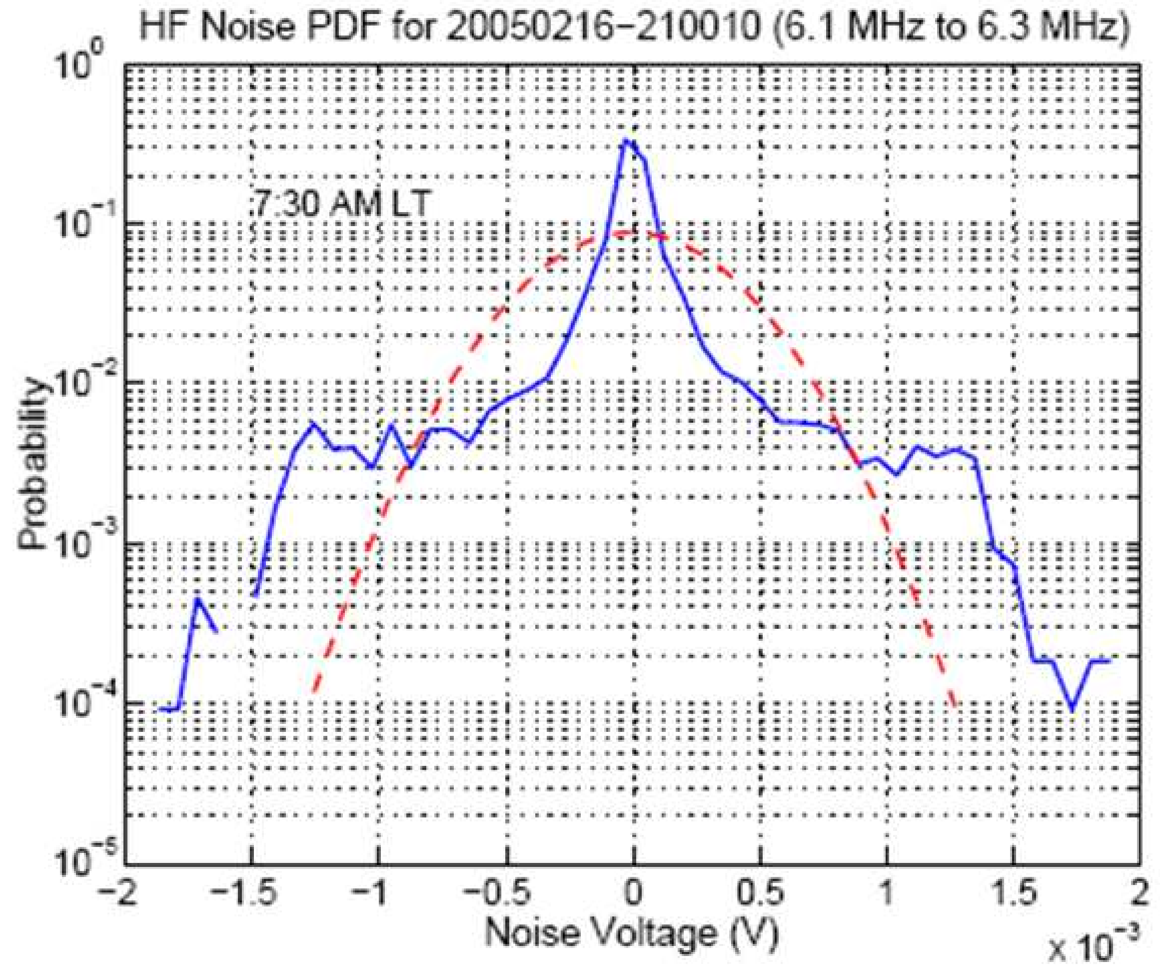HF Noise PDF for 20050216−210010 (6.1 MHz to 6.3 MHz) 7:30 AM LT Probability Noise Voltage (V) x 10^-3

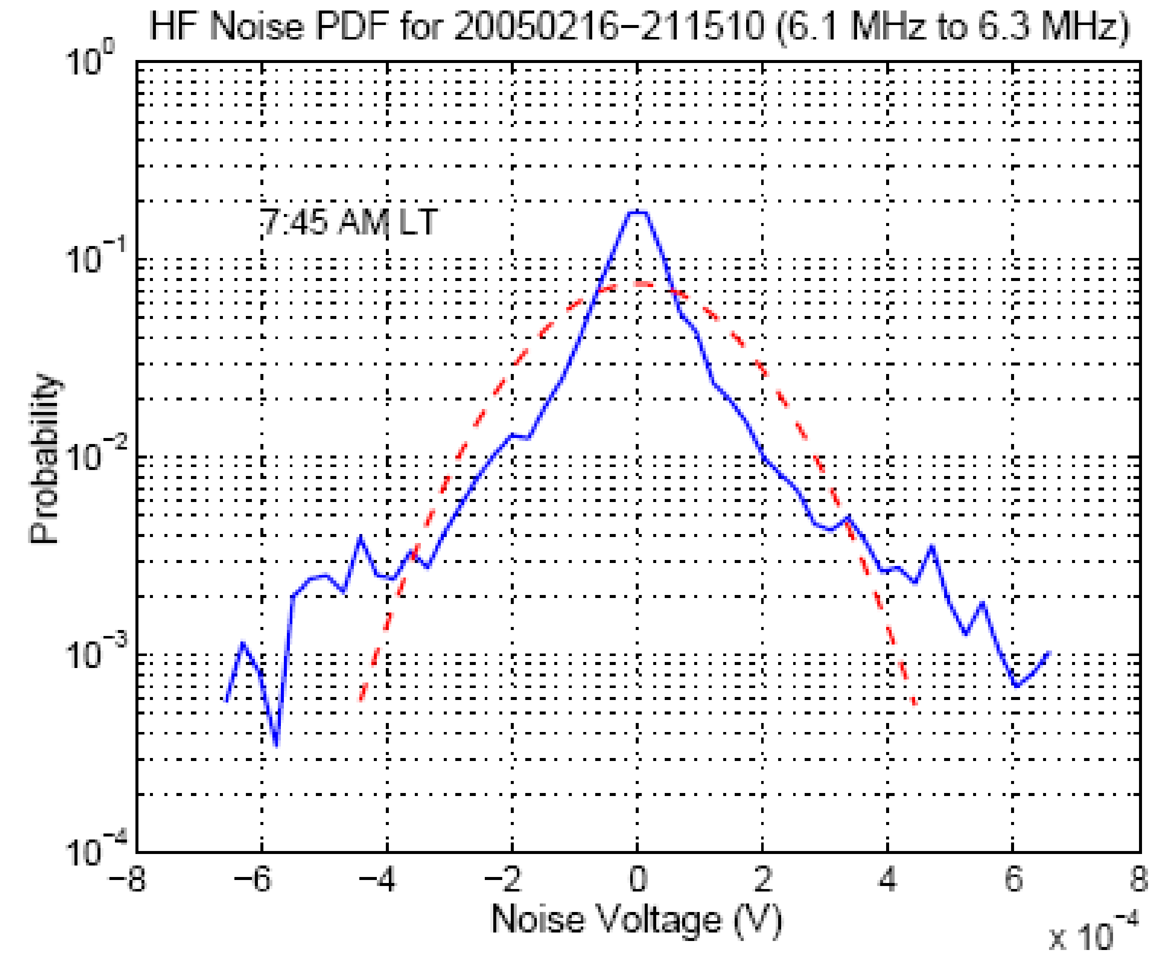
HF Noise PDF for 20050216−211510 (6.1 MHz to 6.3 MHz)
7:45 AM LT
Probability
Noise Voltage (V)
x 10^-4
10^0
10^-1
10^-2
10^-3
10^-4
−8
−6
−4
−2
0
2
4
6
8

7:45

8:00	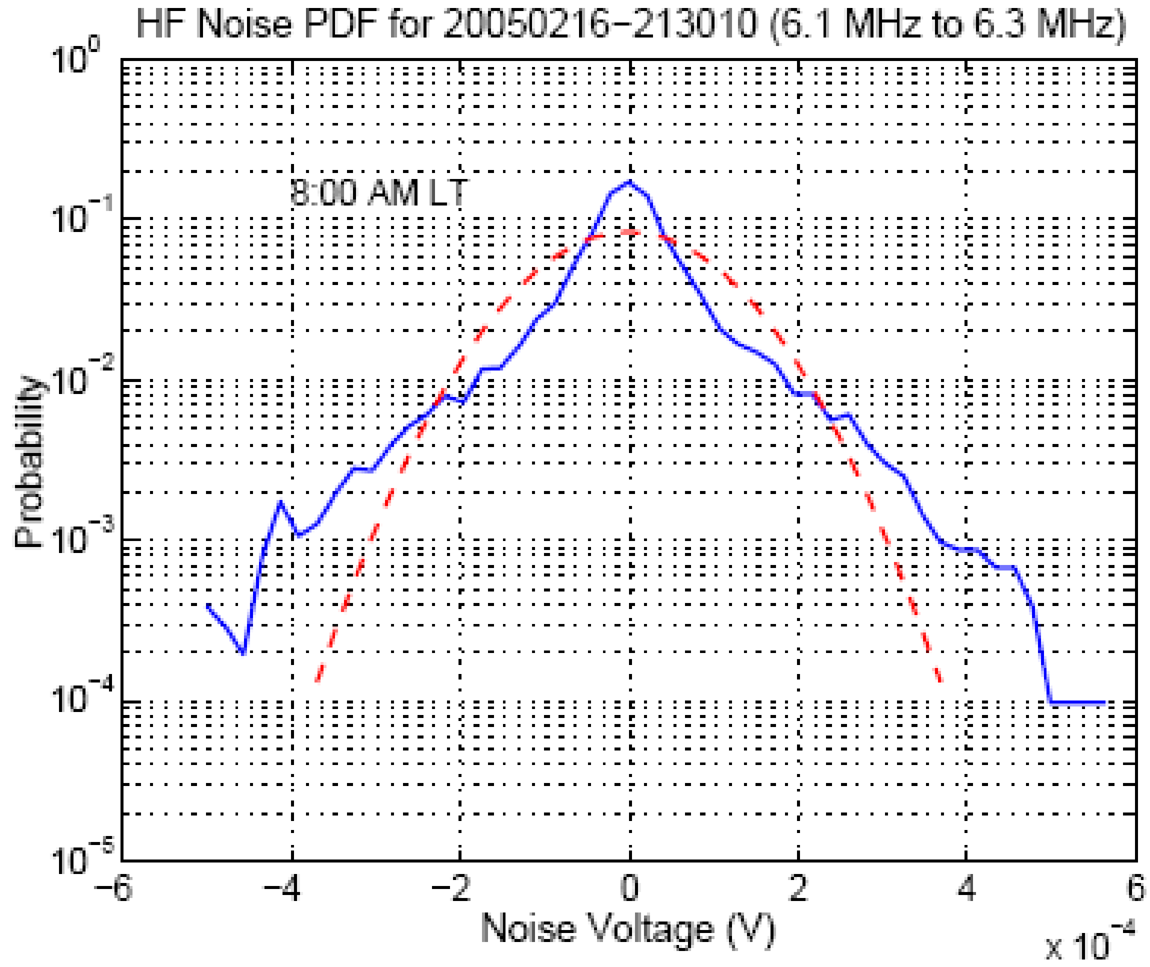HF Noise PDF for 20050216−213010 (6.1 MHz to 6.3 MHz) 8:00 AM LT Probability Noise Voltage (V) x 10^-4

8:15	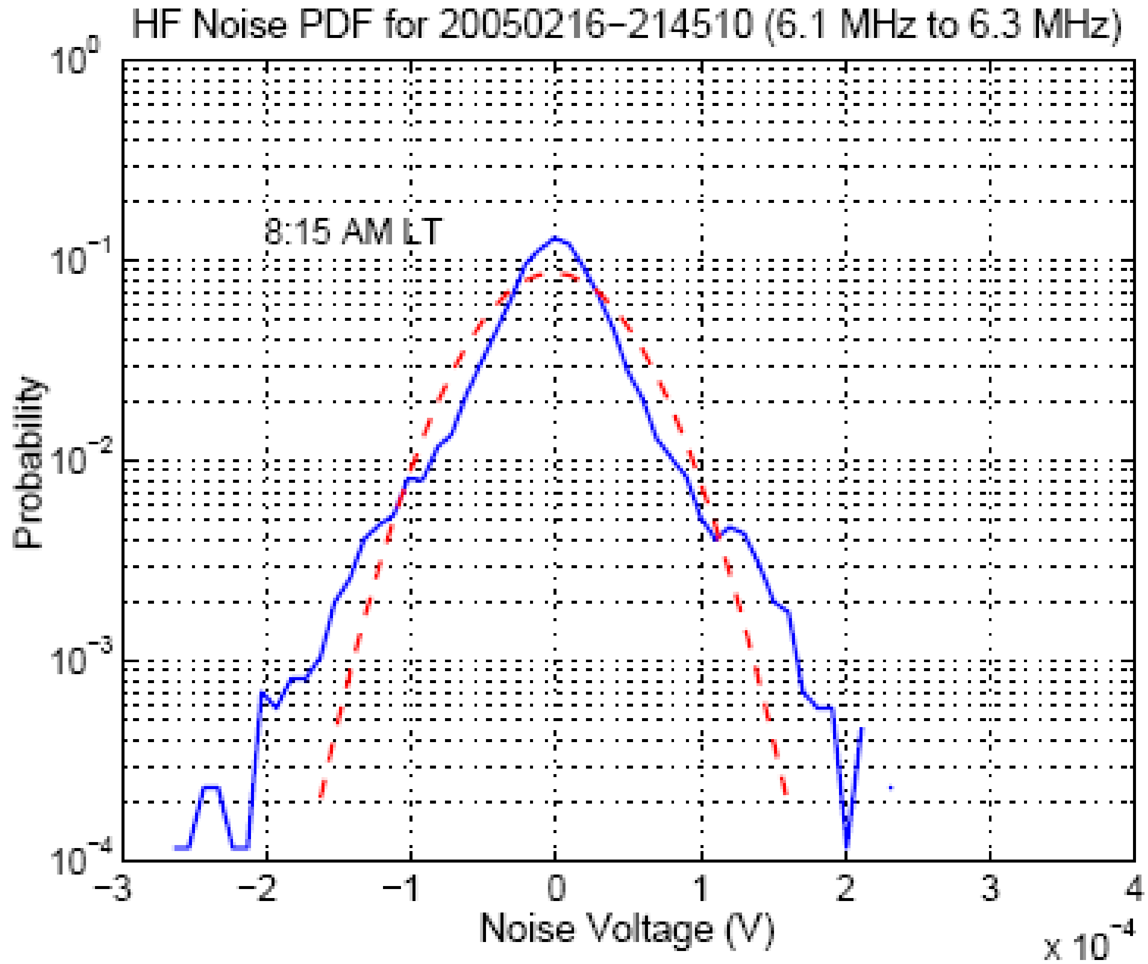 HF Noise PDF for 20050216−214510 (6.1 MHz to 6.3 MHz) 8:15 AM LT Probability Noise Voltage (V) x 10^-4 10^0 10^-1 10^-2 10^-3 10^-4 −3 −2 −1 0 1 2 3 4

8:30	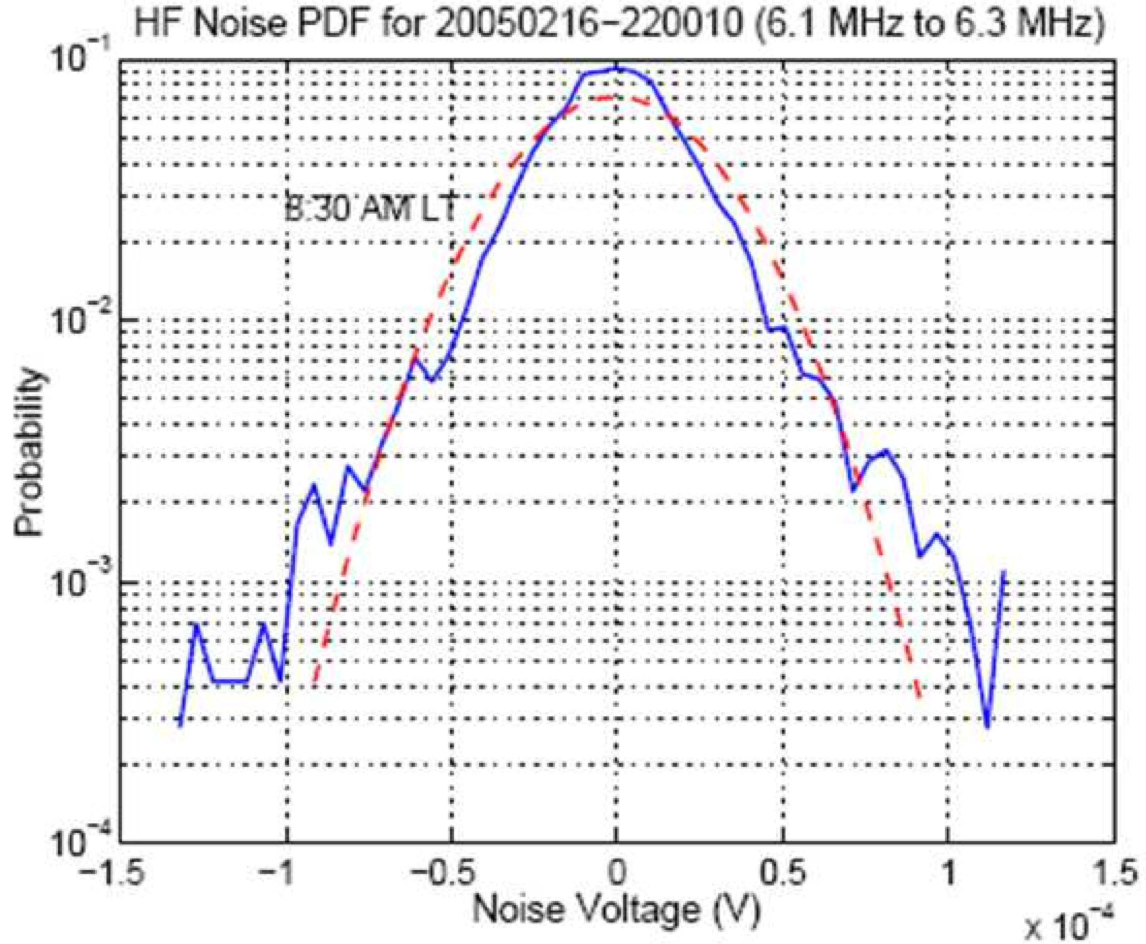HF Noise PDF for 20050216−220010 (6.1 MHz to 6.3 MHz)
8:30 AM LT
Probability
Noise Voltage (V)
x 10^-4
10^-1
10^-2
10^-3
10^-4
−1.5
−1
−0.5
0
0.5
1
1.5

8:45	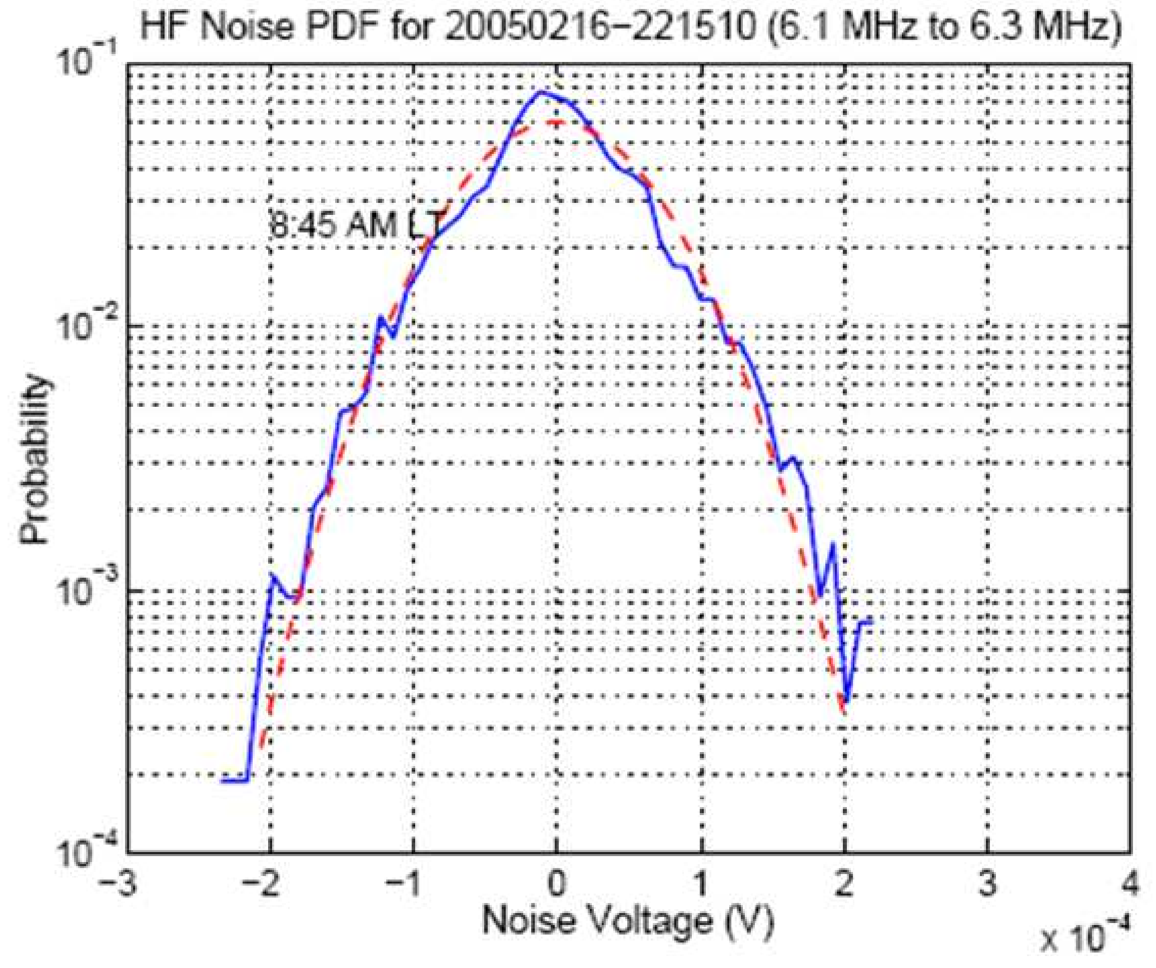HF Noise PDF for 20050216−221510 (6.1 MHz to 6.3 MHz) 8:45 AM LT Probability Noise Voltage (V) x 10^{-4}

9:00	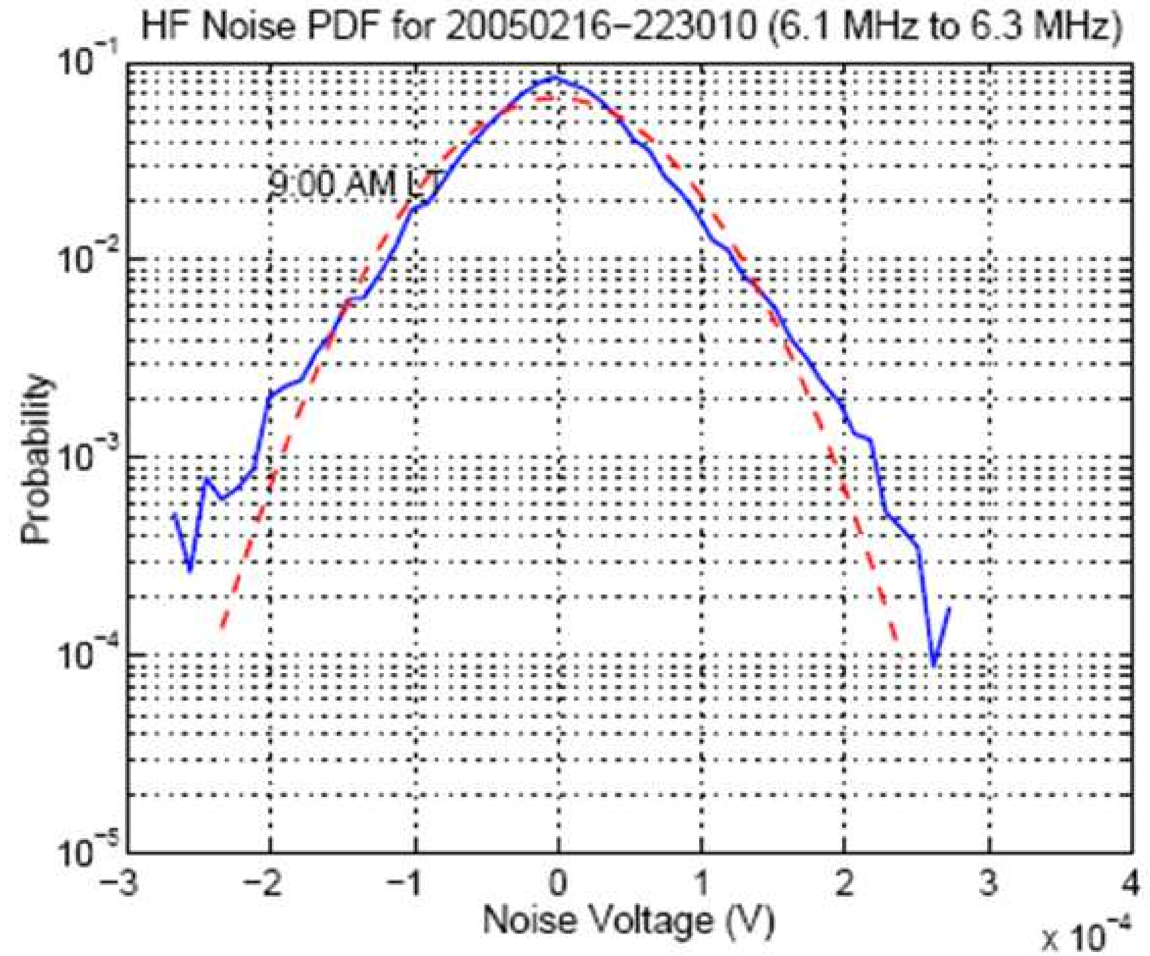

Normally, people believe that sampled noise distribution is Gaussian. However, this experimental result shows that this is not the case for the galactic noise in early morning. Giesbrecht [17] proposed his explanation to this experiment result by proposing a modified bi-Kappa distribution as shown in Equation (1.11).

$$f\left(x;K,\sigma\right)=\frac{1}{\sqrt{K}\sigma\beta\left(\frac{1}{2},K-\frac{1}{2}\right)}\left(1+\frac{x^2}{K\sigma^2}\right)^{-K}, \qquad -\infty<x<\infty, K>\frac{1}{2} \tag{1.11}$$

How well can this model describe the galactic noise? Is there a better model with more reasonalbe explanation to this? If such model exists, how does it impact wireless communication system? This thesis is developed to answer these questions.

In Chapter 2, we look at another model and explain why it could be better than existing works. In Chapter 3, we discuss the noise statistic at output of a digital filter for HF. In Chapter 4, we look at its bit error rate (BER) performance with single antenna. In Chapter 5, we extend this result to multiple input multiple output (MIMO) case. In Chapter 6, we investigate how channel coding can be used to reduce BER. In Chapter 7 we find the channel capacity. In Chapter 8 we derive the secrecy capacity for underwater acoustic communication. This result can be readily applied to the HF case. In Chapter 9, we study the effect of receptor antagonist to a molecular communication receiver. In Chapter 10, we apply our results from previous chapters to nanowire sensor for biomedical purpose.

2. A CHANNEL MODEL FOR GALACTIC NOISE IN THE HF CHANNEL AT SUNRISE

Evidence indicates that for High Frquency(HF) channel, the galactic noise distribution is not Gaussian at sunrise. Past model can be shown to be insufficient for describing this phenomenon. In this chapter, the reason that past model cannot fit the general case is explained. We then derive a new model based on new results from statistical mechanics and astrophysics. The mechanism can be thought of as the transient response of the ionosphere under solar excitation. Here, a mixture of Kappa and Gaussian distribution with correlation model is proposed. At high SNR, we can further approximate the noise distribution to be Kappa. For building up a computer simulator, we seek a genral implemetation of the new model based on Kay's method. Finally, we discuss two more possible applications based on this model: planetary wireless communication and earthquake precursor conjecture.

2.1 Introduction

HF communication involves signal transmision to the ionosphere of the Earth and then be reflected to the destination. The frequency range is between 3MHz and 30MHz. Even though the data rate is not as high as many other communication systems such as those using specifications like 3GPP and LTE-Advanced, in scenarios that civilian communication links cannot be well established(possibly due to war or great natural disaster), HF could be utilized.

Channel modeling for HF has been studied in the past. Barabashov [22] provided a ray tracing solution and Mastrangelo [16] took more parameters into consideration. Doppler shift, delay, and noise are all taken into consideration. In our work, we focus on the noise part.

Based on the work from Mastrangelo [16] and Giesbrecht [17], the noise can be classified into 4 additive components: receiver noise, interference, atmospheric noise and galactic noise. Receiver noise and interference are modeled as Gaussian distribution. The amplitude of atmospheric noise is described by Hall model. In our work, we focus on the galactic noise.

Giesbrecht [17] showed that at a quiet location where interference can be minimized, it is possible to measure the galactic noise. The measured noise distribution is not Gaussian. Giesbrecht interpreted the distribution to be modified Bi-Kappa. While this does fit the measured data, there is one problem that comes up with this solution. In [17], for one of his measurement, his parameters for the modified Bi-Kappa distribution will lead to infinite variance. In reality, any valid observation must have finite power. It could be true that the modified Bi-Kappa model does not fit under certain circumstances.

After Giesbrecht published his work, more new results in statistical mechanics showed up. With the advance of statiscal mechanics, ion behaviour in the ionosphere can be more precisely described. By utilizing the new results and Giesbrecht's data [21], we propose an explanation to this phemomenon as well as a new solution. That is, the galactic noise is a random process such that the sampled noise distribution is a mixture of Kappa and Gaussian with nonzero correlation. This solution has finite variance for all cases, and hence relieves the problems in earlier results.

A random noise generator is beneficial for assessing the performance of a communication system. In our work, we consider Kay's algorithm [23] becasue it is easier to be implemented while satisfying our requirements. In order to use this algorithm, the characteristic function of Kappa distribution must be obtained. We derive the result in this work.

The significance of this work is threefold. First, a more accurate channel model for the galactic noise is provided, giving HF communication system a higher chance of establishing quality links. Second, while HF communication utilizes the ionosphere, one can study the ionosphere by transmitting HF electromagnetic waves [24]. Further more, ionosphere does not soely exist on Earth. It can be found in other planets such as Mars, Jupitor and Saturn. Our work improves the understanding of ionosphere and can be extended to other planets. Third, this work provdes another evidence for the new statical mechanics theory in plasma particle velocity density distribution. We further propose a conjecture for the Earthquake precursor. The measured noise distribution when the ion density increases abnormally prior to a major Earthquake is a mixure of Kappa and Gaussian.

This work is organized as follows: In Section 2.2, we explain why past model doesn't work in general. In Section 2.3, we provide a new explanation to existing measurements and propose the channel model. In Section 2.4, we build up a noise generator based on our channel model. In Section 2.5, we show our experiment and simulation results. In Section 2.6, we show some applications to our noise model. Finally, in Section 2.7, we draw conclusions.

2.2 Past Model

Traditional channel model for the HF is to assume that the noise is additive white Gaussian noise(AWGN) [25]. This model has been frequently used in practice. However, non-Gaussian probability density function(pdf) of HF noise has been measured in the past. Iwama [26] and Giesbrecht [21] showed such measurement results.

One such cause is the galactic noise. The galactic noise in HF channel refers to a type of additive noise(as shown in Figure 2.1) which is caused by the ionosphere of the Earth as well as other stellar activities. To determine the behavior of this noise, Giesbrecht [21] [17] measured at a very quiet location. At sunrise and at sunset, the measured noise pdf is clearly not Gaussian while in daytime, the measured noise pdf is Gaussian.

Giesbrecht [21] proposed a modified Bi-Kappa distribution for the galactic noise based on his knowledge of statistical mechanics at that time. The pdf is shown in 2.1.

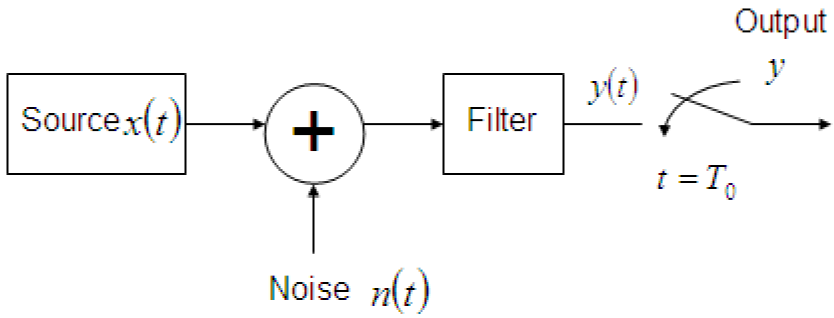

Fig. 2.1. Channel model.

$$f(x;K,\sigma) = \frac{1}{\sqrt{K}\sigma\beta\left(\frac{1}{2}, K-\frac{1}{2}\right)}\left(1+\frac{x^2}{K\sigma^2}\right)^{-K}, \quad -\infty < x < \infty, K > \frac{1}{2} \tag{2.1}$$

The function $\beta(x,y)\,, Re\{x\} \geq 0, Re\{y\} \geq 0$ is a beta function with the following equivalent definitions:

$$\beta(x,y) = \int_0^1 t^{x-1}(1-t)^{y-1}\,dt \tag{2.2}$$

$$= \frac{\Gamma(x)\Gamma(y)}{\Gamma(x+y)} \tag{2.3}$$

$$= 2\int_0^{\frac{\pi}{2}} \sin^{2x-1}\theta\cos^{2y-1}\theta d\theta \tag{2.4}$$

In [21] and [17], both documents recorded cases involving $K < \frac{3}{2}$. One such example is shown in Figure 2.2 [17].It can be seen on the figure that it closely resembles the measured pdf for the majority part. However, the theorem below shows that such cases actually lead to infinite variance.

Theorem 2.2.1 *A random variable X that has probability distribution as shown in (2.1) has finite second order moment when $K > 3/2$.*

Proof: Using the trigonometric substitution, $\tan\theta = x/\left(\sqrt{K}\sigma\right)$, we obtain

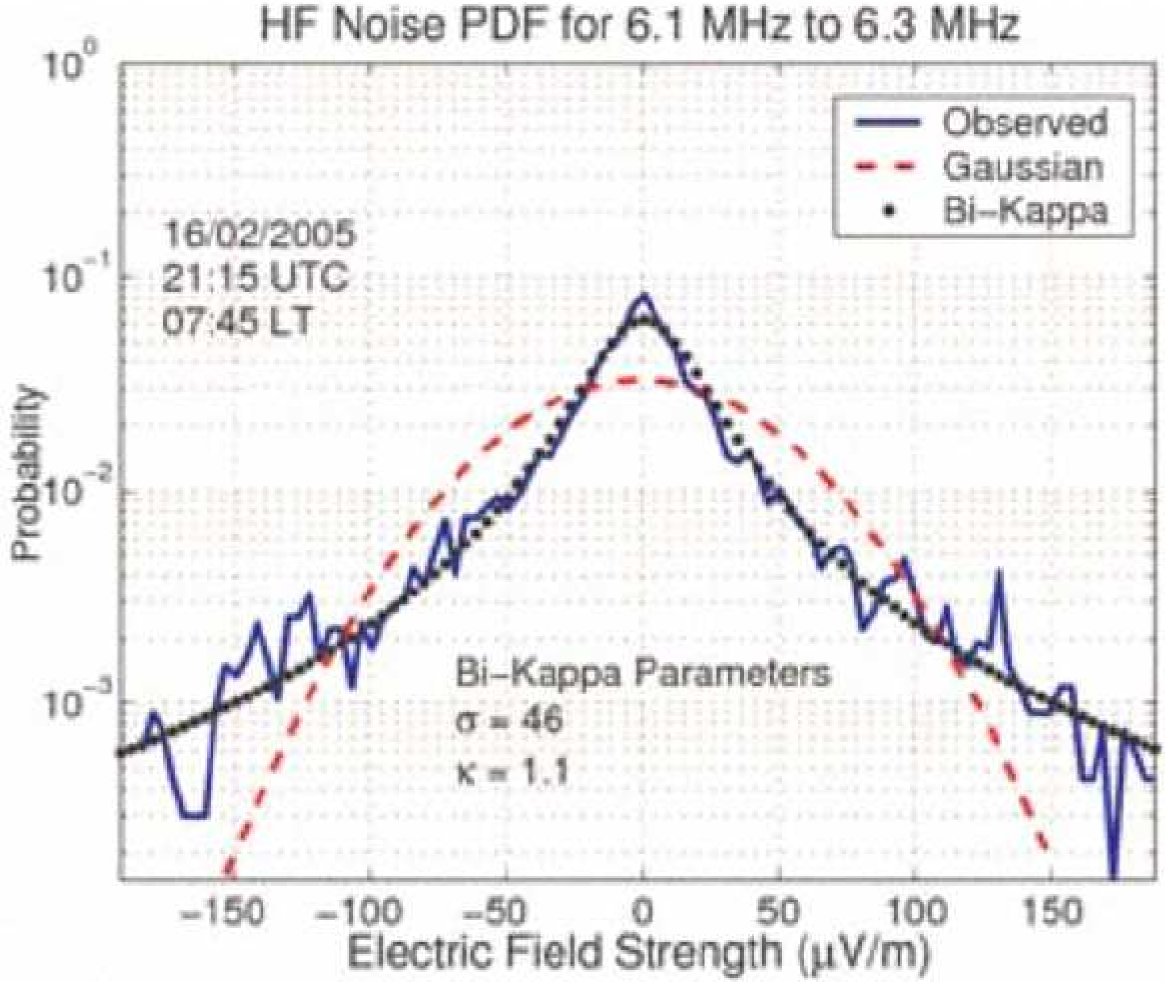

Fig. 2.2. An example of Giesbrecht's result for $K < \frac{3}{2}$. Notice that at the left and the right end, the measured pdf drops faster than the modified Bi-Kappa pdf.

$$
\begin{aligned}
E\left[\mathrm{X}^2\right] &= \int_{-\infty}^{\infty} \frac{x^2}{\sqrt{K}\sigma\beta\left(\frac{1}{2}, K-\frac{1}{2}\right)}\left(1+\frac{x^2}{K\sigma^2}\right)^{-K} dx \\
&= \int_{-\frac{\pi}{2}}^{\frac{\pi}{2}} \frac{K\sigma^2\tan^2\theta}{\sqrt{K}\sigma\beta\left(\frac{1}{2}, K-\frac{1}{2}\right)}\left(\sec^2\theta\right)^{-K}\sqrt{K}\sigma\sec^2\theta d\theta
\end{aligned}
\tag{2.5}
$$

Simplifying the above expression, we obtain

$$\begin{aligned}
&\int_{-\frac{\pi}{2}}^{\frac{\pi}{2}} \frac{K\sigma^2\left(\sec^2\theta - 1\right)}{\beta\left(\frac{1}{2}, K - \frac{1}{2}\right)} \left(\cos^{2K-2}\theta\right) d\theta \\
&= \int_{-\frac{\pi}{2}}^{\frac{\pi}{2}} \frac{K\sigma^2}{\beta\left(\frac{1}{2}, K - \frac{1}{2}\right)} \left(\cos^{2K-4}\theta\right) d\theta \\
&- \int_{-\frac{\pi}{2}}^{\frac{\pi}{2}} \frac{K\sigma^2}{\beta\left(\frac{1}{2}, K - \frac{1}{2}\right)} \left(\cos^{2K-2}\theta\right) d\theta \\
&= 2\int_{0}^{\frac{\pi}{2}} \frac{K\sigma^2}{\beta\left(\frac{1}{2}, K - \frac{1}{2}\right)} \left(\cos^{2K-4}\theta\right) d\theta \\
&-2\int_{0}^{\frac{\pi}{2}} \frac{K\sigma^2}{\beta\left(\frac{1}{2}, K - \frac{1}{2}\right)} \left(\cos^{2K-2}\theta\right) d\theta
\end{aligned} \tag{2.6}$$

Define

$$\mathrm{I} = \int_0^{\frac{\pi}{2}} \frac{1}{\cos^{K'}\theta} d\theta \tag{2.7}$$

Let $x = \cos\theta$, then $dx = -\sin\theta d\theta = -\sqrt{1-x^2}$. Hence, (2.7) becomes

$$\mathrm{I} = \int_1^0 \frac{dx}{-x^{K'}\sqrt{1-x^2}} = \int_0^1 \frac{dx}{x^{K'}\sqrt{1-x^2}} \geq \int_0^1 \frac{dx}{x^{K'}} \tag{2.8}$$

The above integral diverges for $K' \geq 1$, which implies that in (2.6), the first integral diverges when $4 - 2K \geq 1$, that is, $K \leq 3/2$. Similarly, the second integral in (2.6) diverges when $2 - 2K \geq 1$, that is, $K \leq 1/2$. Taking the union of those 2 sets, we conclude that (2.6) diverges for $K \leq 3/2$.

By using (2.4), we can see that (2.6) becomes

$$E\left[\mathrm{X}^2\right] = \frac{K\sigma^2}{\beta\left(\frac{1}{2}, K - \frac{1}{2}\right)} \left[\beta\left(\frac{1}{2}, K - \frac{3}{2}\right) - \beta\left(\frac{1}{2}, K - \frac{1}{2}\right)\right] \tag{2.9}$$

The above term is finite for $K > 3/2$. Hence, we obtain the result. Q.E.D.

This theorem indicates that if the measured results give $K < \frac{3}{2}$, then the power of the noise in infinite. In practical engineering, measurable results always have finite power. Otherwise, the measuring equipments break down. A closer examination at the left and the right end of the plot in Figure 2.2 shows that the modified Bi-Kappa distribution decays slower than the measured pdf. If the measurement could be extend further, then we expect that the measured pdf decays much faster than the modified Bi-Kappa pdf. This leads to second order moment finiteness of the measured pdf and hence gives finite power.

Figure 2.3 explains this intuition by using pictures. Wireless communication performance analysis is very interested in finding the tail probability because it represents the bir error rate (BER) or symbol error rate (SER). Such analysis usually focuses on high SNR asymptotic behavior. For the modifued Bi-Kappa distribution, the error percentage, which is contributed by the gray area, will increase as SNR increases, thus leading to inacurate results.

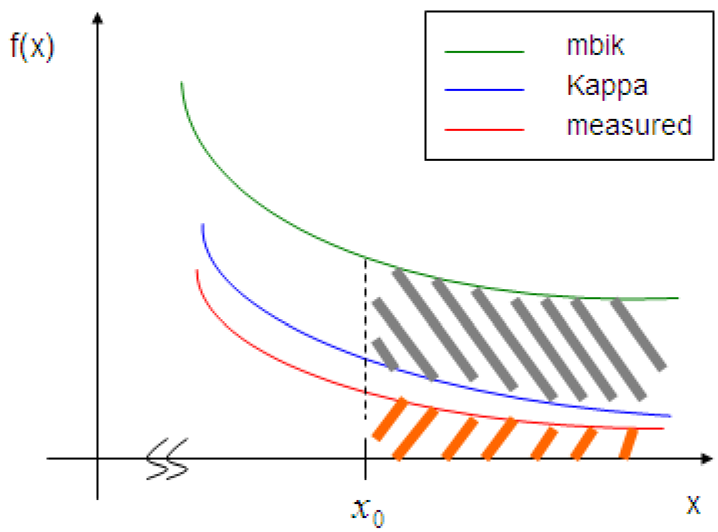

Fig. 2.3. The pdf behavior at large x for the modified Bi-Kappa and Kappa model. An example of the measured result is also shown. The orange area represents the BER/SER according to the measured data. The gray plus the orange area represents the BER/SER according to the modified Bi-Kappa model.

When working on communication systems with infinite noise variance, the knowledge of signal-to-noise ratio (SNR) can no longer be applied. The idea of geometric power [27] [28], which can be viewed as an extenstion of SNR, can be employed to find system performance such as BER and SER. However, if a more reasonable channel model is found, we can shift our attention to the new one because engineers feel more comfortable to finite noise power, which is always directly provided from measurement.

The above discussion leads to a conclusion that in certain scenarios, the modified Bi-Kappa pdf is insufficient to describe the galactic noise pdf. Nevertheless, many measured results from [21] and [17] can still be used, but should interpreted in a different way. In the next section, we give a new explanation.

2.3 Mechanism of HF Galactic Noise

The channel model for HF noise to account for the galactic noise is expressed as follows. A figure for such model is shown in Figure 2.4.

$$y = x + n_G + n \tag{2.10}$$

$$\sim x + n_G(sunrise) \tag{2.11}$$

$$\sim x + n(daytime) \tag{2.12}$$

Here, y is the received signal, x is the information signal, n_G is the sampled galactic noise, and n is the sampled Gaussian noise. n has Gaussian distribution. n represents the sum of all Gaussian noise. The galactic noise is independent of the Gaussian noise.

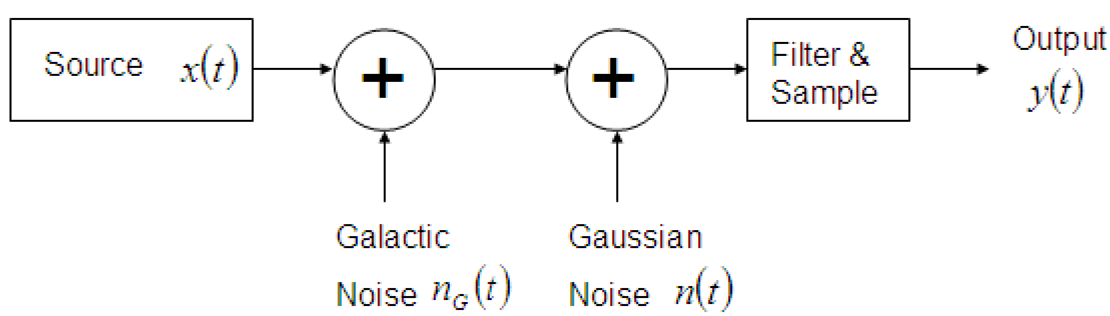

Fig. 2.4. The proposed channel model for HF noise at sunrise.

The reason for this model partially comes from measurement results by Giesbrecht [21]. In a continuous 15-minute measurement from 7:00 am to 9:00am, the pdf changes from non-Gaussian to Gaussian. Note that the sunrise time on the day of measurement (February/16/2005) is 6:50 am [29]. If we compute the variance (power) of the noise, we get a plot as shown in Figure 2.5. This figure clearly shows that the noise power decays as the time progresses at sunrise. In a quiet place for such a measurement, the Gaussian component should stay the same. So we conclude that the power of the galactic noise decreases after sunrise. Hence, at surise, we use Equation 2.11, and in daytime we use Equation 2.12.

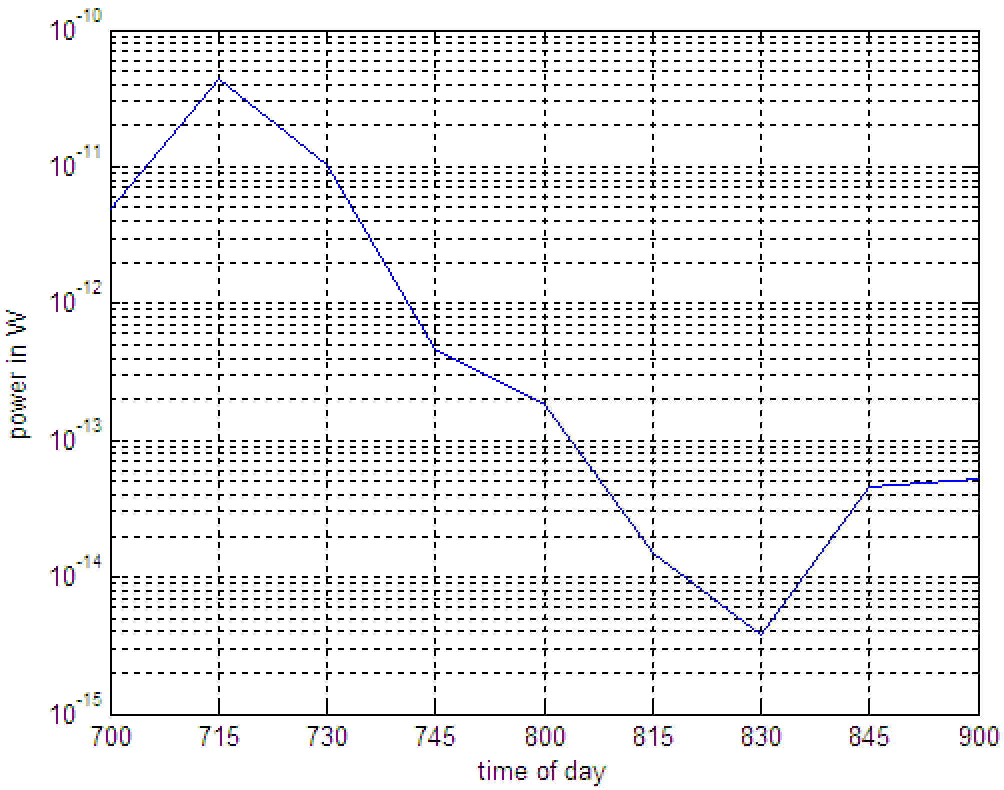

Fig. 2.5. The galactic noise power versus time of the day(plotted on log scale). Notice the galactic noise power decreases as time progresses at sunrise.

Another explanation of the channel model comes from recent physics advances [30] [31] [32]. The ionosphere can be regarded as plasma. In this environment, the fast particles rarely collide with each other. Also, such a system is described as thermal nonequilibrium but in stationary state. The fast particles can be easily acclerated such that the velocity distribution function (vdf) has its end suprathermal tails decay with power law of velocity [30]. This result is different to traditional plasma physics and statistical mechanics and is regarded as a new area called non-extensive statiscal mechanics.

It has been derived that the electron and particle tail vdf is Kappa distribution [30] [31]. Kappa distribution is shown in shown in Equation 3.1. This function is dependent on parameters K and σ. The mathematica meaning of K is that it controls the end tail decay. Smaller values of K give slower decay. The physical interpretation of K is that as K approaches 1.5, the system is shifting toward thermal nonequilibrium. As K approaches infinity, the system is shifting toward thermal equilibrium. When K approaches infinity, the Kappa function becomes Maxwellian, which is the traditional result from statistical mechanics. Thus Kappa function is the bridge between thermal nonequilibrium and thermal equilibrium.

$$\begin{aligned} f_{Kappa}\left(x;K,\sigma\right) = \frac{1}{\sqrt{K}\sigma\beta\left(\frac{1}{2},K+\frac{1}{2}\right)}\left(1+\frac{x^2}{K\sigma^2}\right)^{-K-1}&, \\ -\infty < x < \infty, K > \frac{1}{2}& \end{aligned} \tag{2.13}$$

According to [32], the core part of vdf accounts for the lesser velocity area, and hence is governed by traditional Gaussian distribution (see Equation 2.14). So the total vdf should be a mixture of Kappa (tail) and Gaussian (core). The vdf is formally written as in Equation 2.15.

$$f_{Gaussian}\left(x;\sigma\right) = \frac{1}{\sqrt{2\pi}\sigma}e^{-\frac{x^2}{2\sigma^2}}, -\infty < x < \infty \tag{2.14}$$

$$f\left(x;K,\sigma_1,\sigma_2,\epsilon\right) = \epsilon f_{Kappa}\left(x;K,\sigma_1\right) + (1-\epsilon)f_{Gaussian}\left(x;\sigma_2\right) \tag{2.15}$$

Kappa vdf has been observed in many space measurement data [30] [31]. For example, in solar wind, the terrestrial magnetosphere, the terrestiral plasmasheet, the magnetosheath, and the radiation belts. For other planets, Kappa vdf has also been found. For example, in the the plasmasheet of Jupiter, the magnetosphere of Jupiter, Saturn, Neptune, and Titan. (The readers are welcomed to read the various literatures mentioned in [30] [31] if they are interested in it.) So Kappa vdf has been found both theoretically and supported experimentally.

We now derive the received noise voltage pdf from vdf. Suppose we have a tube as shown in Figure 2.6 with infinite length and the cross section area A is fixed. Assume that the electrons are uniformly distributed in the tube with density ρ. If all of the electrons travel with velocity pointing toward one end of the tube at speed of v, then within 1 second we can see $A * v * 1 * \rho$ amount of charges passing through any cross section. When we divide this value by 1, we get the current. In other words, the current is porportional to the velocity of electrons. If the electrons have a velocity distribution with the associated random variable to be $\mathbf{v}$, it follows that the current amplitude has the same distribution $\mathbf{I_0}$ in shape.

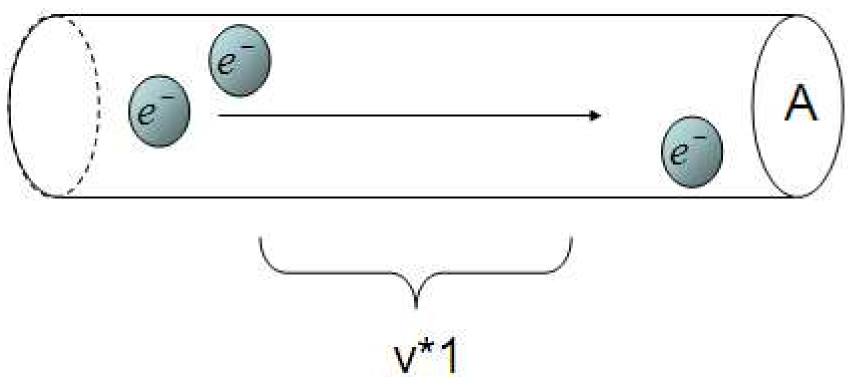

Fig. 2.6. A figure used to show that the velocity is proportional to the current amplitude.

In antenna theory, once we have determined the current amplitude, quantities such as electric field and magnetic field are proportional to current amplitude [33].

For example, for Hertzian dipole of length dl oriented along the z-axis and carrying current in Equation 2.16.

$$I = I_0 cos(\omega t) \tag{2.16}$$

the electric and magnetic fields at values of r far from the dipole are shown in Equation 2.17 and Equation 2.18.

$$\mathbf{E} = -\frac{\beta^2 I_0 dl sin(\theta)}{4\pi\varepsilon\omega r} sin(\omega t - \beta r)\mathbf{a}_\theta \tag{2.17}$$

$$\mathbf{H} = -\frac{\beta I_0 dl sin(\theta)}{4\pi r} sin(\omega t - \beta r)\mathbf{a}_\theta \tag{2.18}$$

where ε is permittivity and ω is the frequency.

The receiving antenna has pattern to be the same as the transmitting antenna by reciprocity. The voltage that is measured at the receiing antenna is approximately

$$V = \int_L \mathbf{E} \cdot \mathbf{l} \tag{2.19}$$

Hence, the voltage is proportional to the current amplitude. By combining the resuls showned in this section, we conclude that if the electron's velocity is a random variable, then the measured voltage at the receive antenna is also a random variable with pdf to have the same shape. For HF galactic noise at sunrise, the noise pdf is Kappa-Gaussian mixture.

For a more general setting, since it is shown in [34] that the galactic noise has correlation among noise samples because the measured power spectral density is not flat, we add an arbitrary autocorrelation function to our channel model.

We conclude this section with Figure 2.7. As the sun rises, the ionosphere undergoes thermal nonequilibrium, hence the electron vdf becomes Kappa-Gaussian. The galactic noise power is significantly larger than other Gaussian noise power. Hence, we get the noise pdf to be Kappa-Gaussian. For communication system operating at high SNR, the noise pdf is approximated as Kappa. As the time goes by, the ionosphere shifts towards the equilibrium state. Later, the galactic noise power decreases, to the extent that the Gaussian noise dominates in daytime. The noise pdf then becomes Gaussian.

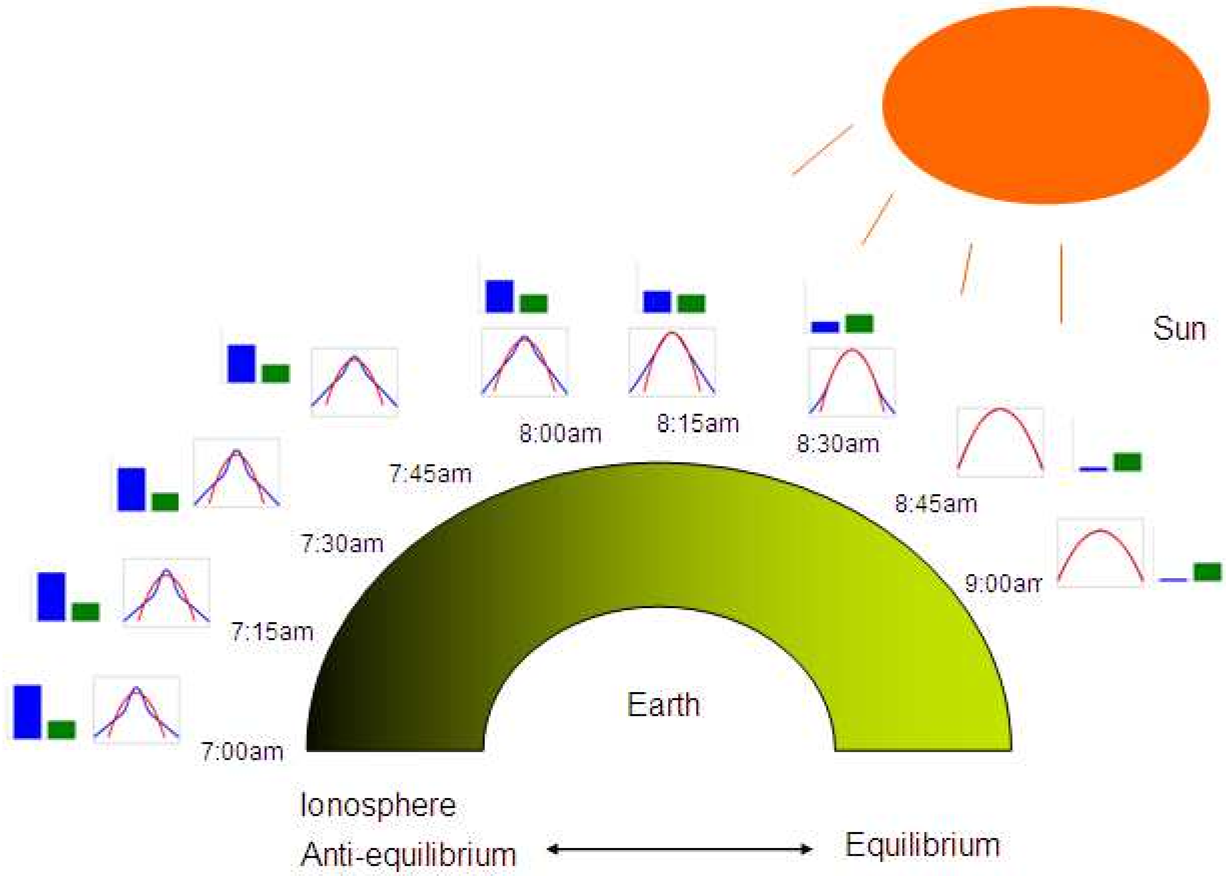

Fig. 2.7. An example shows how the thermal equilibrium state of the ionosphere changes with time at sunrise. The noise pdf and power changes with the shift of equilibrium state. The blue curve represents Kappa-Gaussian pdf, and the red curve represents closest Gaussian pdf. The pdf changes from Kappa-Gaussian distribution to Gaussian distribution gradually. The blue bar represents the galactic noise power and the green bar represents the power of Gaussian noise.

2.4 Kay's Method for Simulation

Computer simulation for HF channel is very helpful in understanding the communication system. At high SNR, the noise pdf is approximately Kappa. For the purpose of generating HF galactic noise when considering asymptotic BER analysis, we focus on the general case in which the sampled pdf is Kappa with arbitrary aurocorrelation function (or equivalently, power spectral density). There are several approaches.

In general, there are 3 approaches for generating a random process with arbitrary sampled pdf and autocorrelation function:

1. Shen's method [35]
2. Stochastic differential equation (SDE) [36]
3. Kay's method [23]

Shen's method involves a recursive calculation for the desired autocorrelation function. SDE requires finding the generating stochastic differential equation first. Such a task in general is difficult to achieve. Kay's method requires obtaining the characteristic funtion $\psi_X(x)$ of the sampled pdf. We may not get the closed form for arbitrary pdf. However, numerical apporach for this function can be easily obtained with computers. In our work, we use Kay's method. For our work, one of Kay's examples is actually the dual of what we need.

In the particular example in Kay's work [23], we can see that if

$$f_X(x) = \frac{1}{\sqrt{\pi}b\Gamma(v+1)}\left(\frac{|x|}{2b}\right)^{v+\frac{1}{2}} K_{v+\frac{1}{2}}\left(\frac{|x|}{b}\right) \tag{2.20}$$

then

$$\psi_X(x) = \int_{-\infty}^{\infty} f_X(x)\, e^{j\omega x} dx = \frac{1}{(1+b^2\omega^2)^{v+1}} \tag{2.21}$$

Notice that Kappa pdf is symmetric at y axis and so it is an even function. The following lemma shows that the characteristic function of an even pdf is even.

Lemma 2.4.1 *If a function* $f(x) \in \mathbb{R}$ *satisfies* $f(x) = f(-x)$, *then* $\psi(x) = \int_{-\infty}^{\infty} f(x) e^{j\omega x} dx$ *is even.*

Proof:

$$\psi(\omega) = \int_{-\infty}^{\infty} f(x) e^{j\omega x} dx$$

$$= \int_{\infty}^{-\infty} -f(y) e^{-j\omega y} dy \tag{2.22}$$

$$= \int_{-\infty}^{\infty} f(y) e^{-j\omega y} dy \tag{2.23}$$

$$= \psi(-\omega) \tag{2.24}$$

where (2.22) is obtained by change of variable $y = -x$, (2.23) foolows by updating the integration range, and (2.24) is obtained by the definition of characteristic funtion when ω becomes $-\omega$.

Q.E.D.

By combining Lemma 2.4.1 and the definition of Fourier transform, which is $F(\omega) \equiv \int_{-\infty}^{\infty} f(x) e^{-j\omega x} dx$, we obtain the following lemma for describing the relationship between Fourier transform and characteristic
function of its pdf.

Lemma 2.4.2 *For a random variable* X *with pdf* $f_X(x)$ *with characteristic function* $\psi_X(\omega)$,

$$\mathscr{F}\{\psi_X(\omega)\} = 2\pi f_X(x) \tag{2.25}$$

Proof: The relationship between pdf $f_X(x)$ and its corresponding characteristic function $\psi_X(\omega)$ is

$$f_X(x) = \frac{1}{2\pi} \int_{-\infty}^{\infty} \psi_X(\omega) e^{-j\omega x} dx \tag{2.26}$$

By multiplying both sides with 2π, we can see that the right hand side is $\mathscr{F}\{\psi_X(\omega)\}$ and so we get the proof.

Q.E.D.

With such a relationship, we now proceed to find the characteristic function of Kappa pdf. For $g(y) = \frac{1}{(1+b^2\omega^2)^{v+1}}$, observe that $g(y) = g(-y)$, then

$$\begin{aligned} G(\omega) &= \int_{-\infty}^{\infty} g(y)\, e^{j\omega y} dy \\ &= G(-\omega) \qquad (2.27) \\ &= \int_{-\infty}^{\infty} g(y)\, e^{-j\omega y} dy \\ &= \mathscr{F}\{g(y)\} \\ &= 2\pi f_X(x) \qquad (2.28) \end{aligned}$$

where (2.27) comes from the conclusion of Lemma 2.4.1, and (2.28) follows from (2.25). $f_X(x)$ cmes from (2.20).

Comparing our Kappa pdf from (3.1) with (2.21) shows that $v = K$ and $b = \frac{1}{\sqrt{K\sigma^2}}$. The normalization constant for (2.21) to make a valid pdf is $C = \frac{1}{\sqrt{\pi}b\Gamma(v+1)}$. Together with (2.28), the characteristic function of a Kappa pdf is

$$\begin{aligned} \psi_X(x) &= \frac{2\pi}{\sqrt{K}\sigma\beta\left(\frac{1}{2}, K+\frac{1}{2}\right)\sqrt{\pi}\frac{1}{\sqrt{K}\sigma}\Gamma\left(K+\frac{1}{2}\right)} \left(\frac{|\omega|\sqrt{K}\sigma}{2}\right)^{K+\frac{1}{2}} K_{K+\frac{1}{2}}\left(|\omega|\sqrt{K}\sigma\right) \\ &= \frac{2\sqrt{\pi}\Gamma(K+1)}{\Gamma\left(\frac{1}{2}\right)\Gamma\left(K+\frac{1}{2}\right)\Gamma(K+1)} \left(\frac{|\omega|\sqrt{K}\sigma}{2}\right)^{K+\frac{1}{2}} K_{K+\frac{1}{2}}\left(|\omega|\sqrt{K}\sigma\right) \qquad (2.29) \\ &= \frac{2}{\Gamma\left(K+\frac{1}{2}\right)} \left(\frac{|\omega|\sqrt{K}\sigma}{2}\right)^{K+\frac{1}{2}} K_{K+\frac{1}{2}}\left(|\omega|\sqrt{K}\sigma\right) \qquad (2.30) \end{aligned}$$

Here, (2.29) is obtained from (2.3), and the last equation comes from the identity $\Gamma\left(\frac{1}{2}\right) = \sqrt{\pi}$.

Now that we have obtained the characteristic functin of Kappa pdf, we carry out Kay's method in the following steps.

STEP 1: Random variable A has its pdf

$$p_A(a) = a\int_0^{\infty} \left[\psi_X\left(\sqrt{M/2}\right)\right]^{1/M} J_0(av)\, vdv \qquad (2.31)$$

STEP 2: Random variable F has its pdf

$$P_X\left(f\right) = \frac{E\left[A\right]^2}{2} p_F\left(\left|f\right|\right), -1/2 \leq f \leq 1/2 \tag{2.32}$$

Here, $p_F\left(\left|f\right|\right)$ is the input power spectral density.

STEP 3: The random process is constructed to be

$$X\left[n\right] = \frac{1}{\sqrt{M/2}} \sum_{i=1}^{M} A_i cos\left(2\pi F_i n + \Phi_i\right) \tag{2.33}$$

Here, Φ_i is a random variable with uniform distribution between $[0,2\pi)$.

2.5 Numerical Result

A. *HF noise measurement*

In this part, we use our proposed channel model to compare with the measured result by [21]. Figure 2.8 Figure 2.16 shows the result from 7:00 am to 9:00 am with 15 minutes interval. We also put the modified Bi-Kappa model proposed earlier by [21] to make comparison. Table 2.1 shows the parameters we use to obtain our model for describing the measured data. The parameters follow from Equation 2.15. Based on these results, we can say that the experiment results support our model.

B. *Kappa Noise simulation*

In this part, we use Kay's algorithm to simulate the random process for HF galactic noise at sunrise. Here, we look for an example in which $K = 1.6$ and $\sigma = 66$. This example resembles Giesbrecht's cases when his model give infinite variance. Figure 2.17 shows an example of a realization of the random process. Figure 2.18 compares the sampled noise pdf versus the desired result. Figure 2.19 compares the simulated noise autocorrelation function versus the input. As we can see, the simulation matches the input.

We would like to discuss the parameters used in this simulation. For M in (2.33), the value is 20. Judicious choice of M must be made. Even though larger M theoretically approaches the ideal; in practice, it may cause algorithm instability due to numerical issue.

Table 2.1.
The value of the parameters for measured HF noise data.

7:00	**7:15**	**7:30**
$\epsilon = 0.5$ K = 1.6 $\sigma_1 = 3.9956 * 10^{-4}$ $\sigma_2 = 1.9795 * 10^{-4}$	$\epsilon = 0.3$ K = 2 $\sigma_1 = 1.3197 * 10^{-2}$ $\sigma_2 = 7.2648 * 10^{-5}$	$\epsilon = 0.3$ K = 4 $\sigma_1 = 7.3182 * 10^{-4}$ $\sigma_2 = 6.6529 * 10^{-5}$
7:45	**8:00**	**8:15**
$\epsilon = 0.3$ K = 6 $\sigma_1 = 3.1209 * 10^{-4}$ $\sigma_2 = 7.8023 * 10^{-5}$	$\epsilon = 0.3$ K = 6.5 $\sigma_1 = 2.5509 * 10^{-4}$ $\sigma_2 = 6.3771 * 10^{-5}$	$\epsilon = 0.3$ K = 9 $\sigma_1 = 9.6731 * 10^{-5}$ $\sigma_2 = 4.8365 * 10^{-5}$
8:30	**8:45**	**9:00**
$\epsilon = 0.3$ K = 12 $\sigma_1 = 6.1156 * 10^{-5}$ $\sigma_2 = 2.5482 * 10^{-5}$	$\epsilon = 1$ K = 13 $\sigma_1 = 8.9342 * 10^{-5}$ -	$\epsilon = 1$ K = 16 $\sigma_1 = 1.055 * 10^{-4}$ -

In (2.31), the pdf of A is found numerically rather than in closed form because we are unable to find it. In practice, the upper limit in (2.31) is not infinite, and the function in the integral fluctuates too fast due to the nature of Bessel function. Figure 2.20 shows an example of (2.31) when a is large. The $g(v)$ in Figure 2.20 refers to product of the functions in the integral in (2.31), which is $\left[\psi_X\left(\sqrt{M/2}\right)\right]^{1/M} J_0(av)\,v$. So getting a very precise $p_A(a)$ is difficult. Poor choice of parameters in evaluating (2.31) will result in the pdf of A not having total integral to be 1, thus destablizing the algorithm.

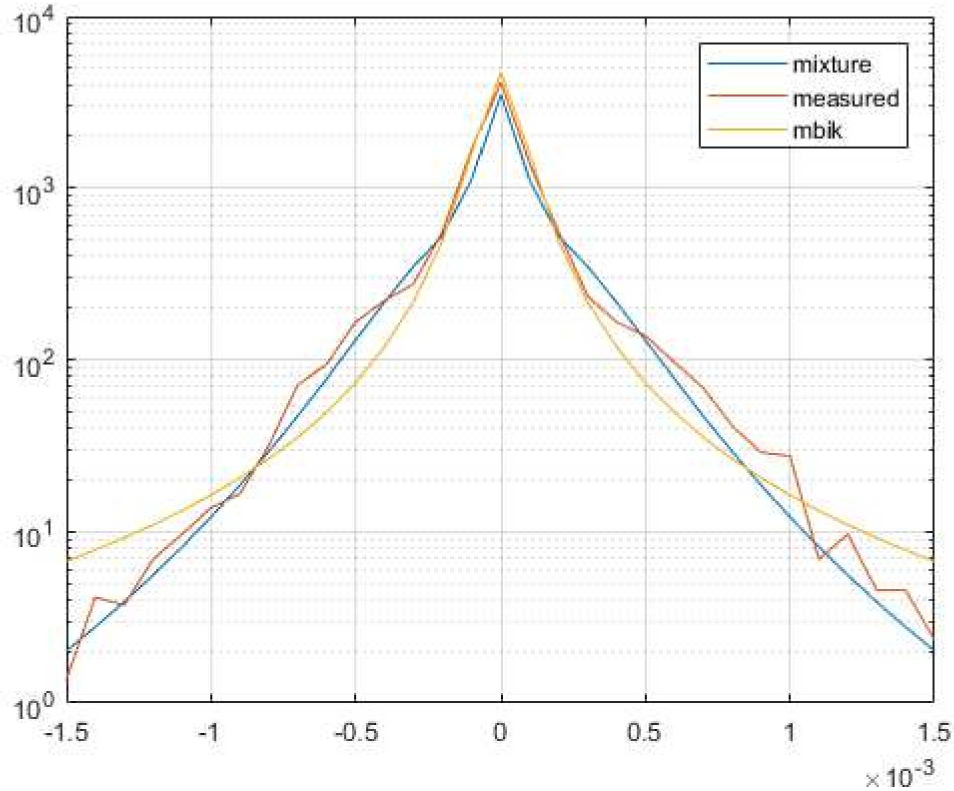

Fig. 2.8. The comparison of the measured data and our model at 7:00 am local time.

2.6 Applications

A. *Planetary communication*

Our work is not only useful to HF communication on Earth, but also on other planets. Table 2.2 lists the ion density and the corresponding critical frequency on other planets in the solar system. The density information is obtained from [7] [37] [38] [39] [40] [41] [42] and the critical frequency is calculated via [7]:

$$f = 9\sqrt{N} \tag{2.34}$$

where f is the criticaal frequency in Hz and N is ion density in $1/m^3$.

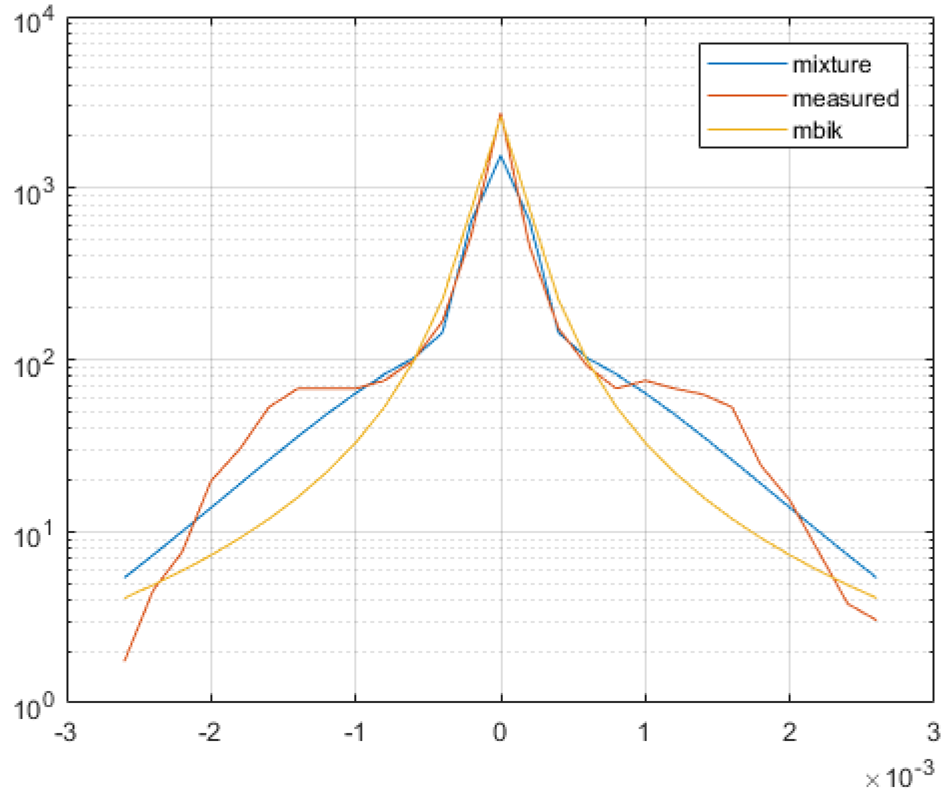

Fig. 2.9. The comparison of the measured data and our model at 7:15 am local time.

From these information we can see that the HF communcation frequencies in other planets are similar to the case in Earth. At sunrise and sunset, we expect the HF noise model to have similar results compared with Earth. When in the future, humans begin to put radio equipments on other planets. Those equipments can communicate to each other via HF. Then our results could be useful in stregthening the communication link, providing better quality of service.

B. *Earthquake precursor conjecture*

Seismologists study the patterns of earthquakes, aiming to learn more about the nature of it. One such pattern is that usually several days prior to a major earthquake, the HF communication frequency increases as a result of the increase of ion density according to Equation 2.34 [43] [44] [45]. There are several physics theory postulated

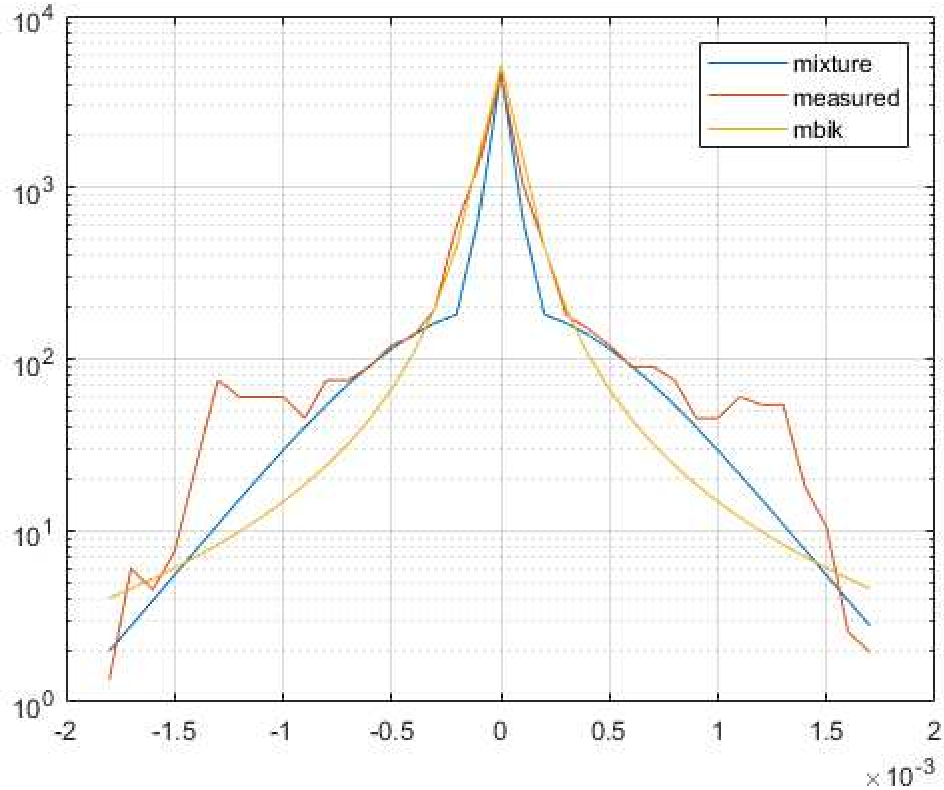

Fig. 2.10. The comparison of the measured data and our model at 7:30 am local time.

such as surface charge [46] [47] and radon emission [48] to explain this phenomenon. In our viewpoint, no matter what the cause is, the sudden increase of ion density in the ionosphere represents shifting towards thermal antiquilibrium. According to our model, such a change leads to Kappa-Gaussian mixture for the HF noise. We do not know whether this noise has sufficient power to be identified from AWGN, but we conjecture that it exists. Thus, it is beneficial to use the noise pdf to help predict possible future earthquakes.

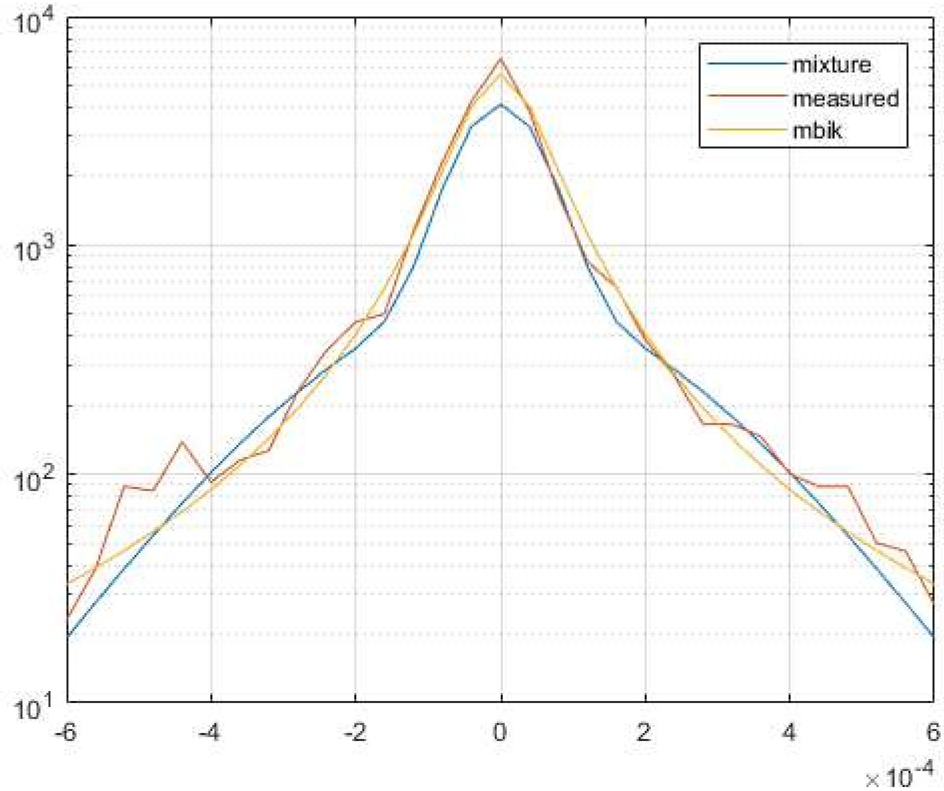

Fig. 2.11. The comparison of the measured data and our model at 7:45 am local time.

2.7 Conclusion

In this work, a new model for describing the galactic noise at sunrise has been proposed based on recent physics research. That is, the sampled pdf is Kappa-Gaussian mixture with some autocorrelation function. Single function cannot be used to describe both the core and the tail parts simultaneously. Previous work was able to describe the core part well at the cost of losing accurate tail decsription. This leads to infinite variance. The mixture model can describe the noise much better. We showed how to use Kay's method for obtaining such a noise simulator and discussed some numerical issues. This model can be used to help future space exploration and could be used to help earthquake prediction.

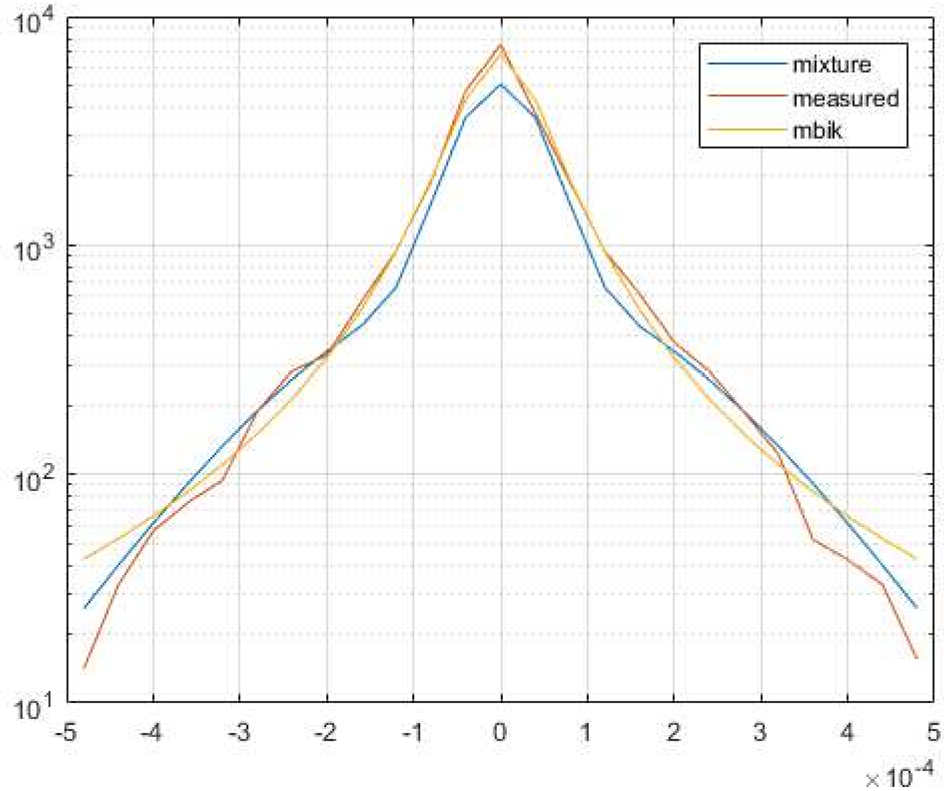

Fig. 2.12. The comparison of the measured data and our model at 8:00 am local time.

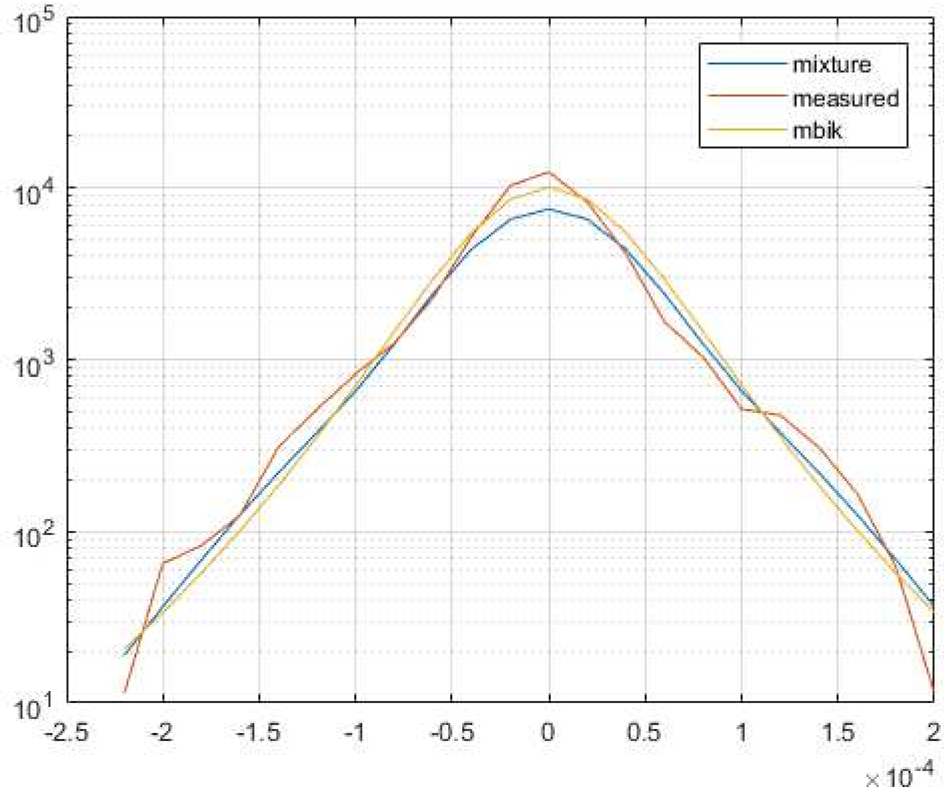

Fig. 2.13. The comparison of the measured data and our model at 8:15 am local time.

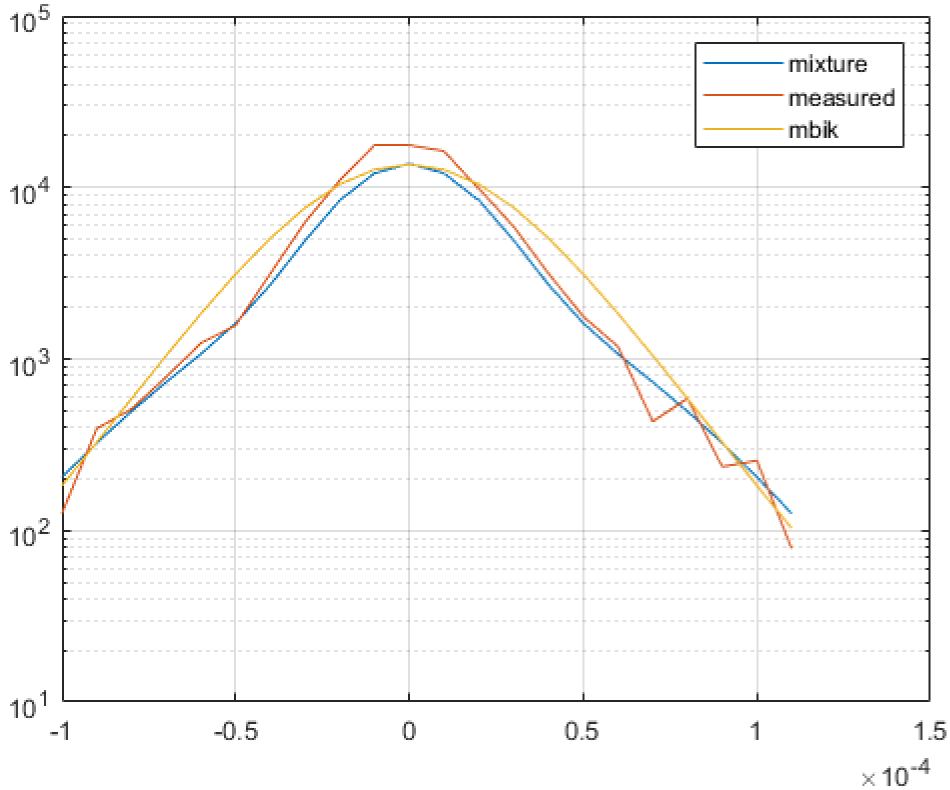

Fig. 2.14. The comparison of the measured data and our model at 8:30 am local time.

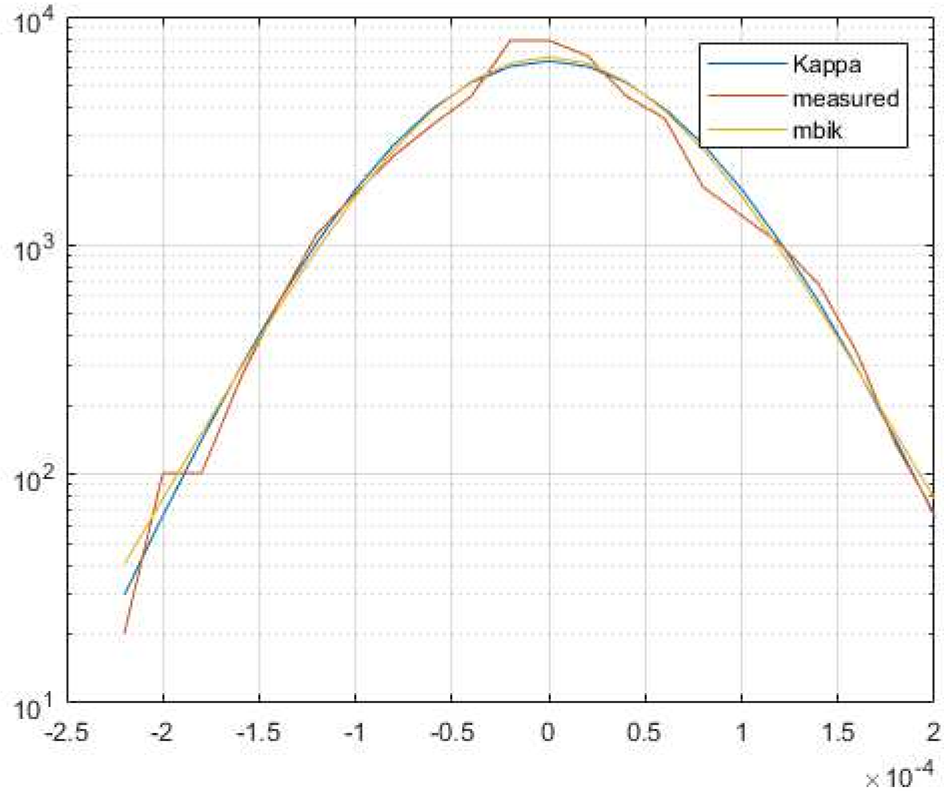

Fig. 2.15. The comparison of the measured data and our model at 8:45 am local time.

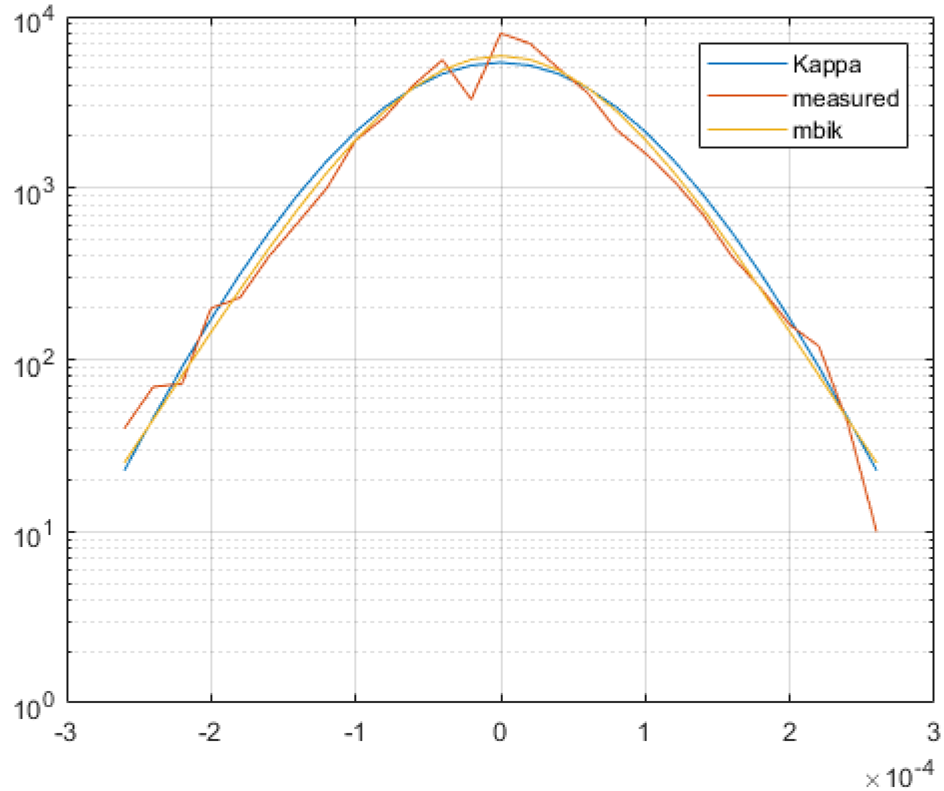

Fig. 2.16. The comparison of the measured data and our model at 9:00 am local time.

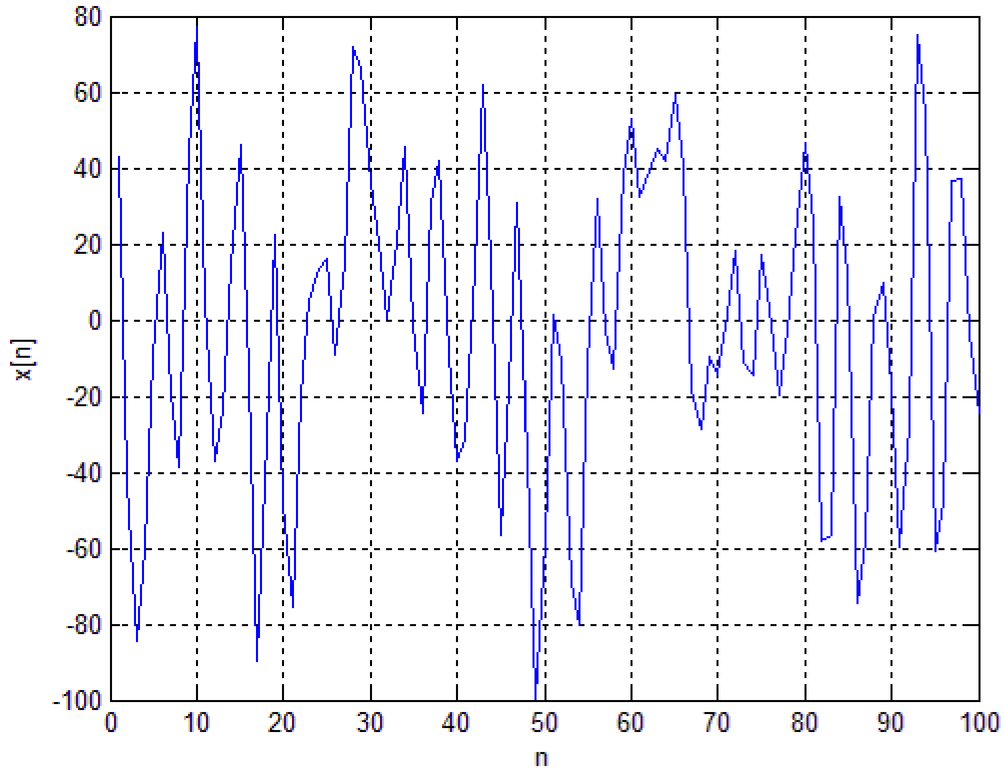

Fig. 2.17. A realization of the random process.

Table 2.2.
Critical frequency for the ionosphere in different planets in the solar system. The unit for ion density is $1/m^3$ and the unit for critical frequency is MHz.

Planet	**Ion density** N_e	**Critical Frequency** $\mathbf{f}_o$
Earth	$10^{11} - 2 * 10^{12}$	2.8 - 12
Venus	$10^{10} - 10^{12}$	0.9 - 9
Mars	$10^{10} - 10^{12}$	0.9 - 9
Jupitor	$10^{11} - 10^{12}$	0.9 - 9
Saturn	$10^{9} - 2.6 * 10^{10}$	0.28 - 1.5
Uranus	$10^{11} - 3 * 10^{12}$	2.9 - 15
Neptune	$10^{10} - 10^{11}$	0.9 - 2.8

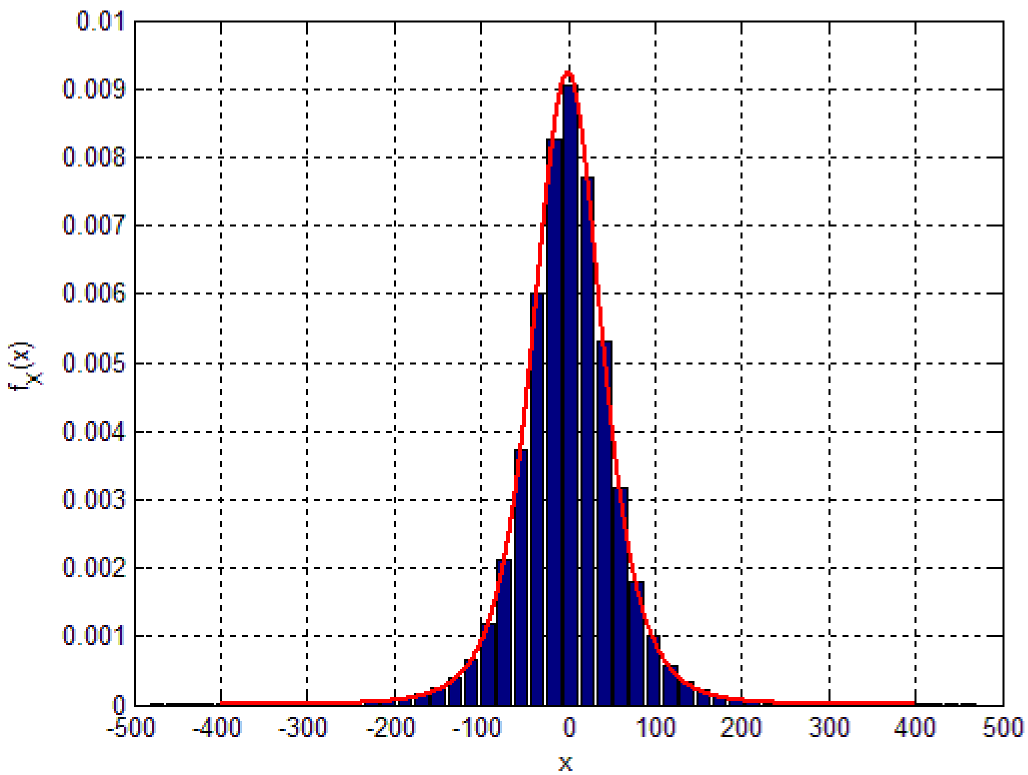

Fig. 2.18. Estimated pdf of the random process. The red line is the input Kappa pdf with $K = 1.6$ and $\sigma = 66$.

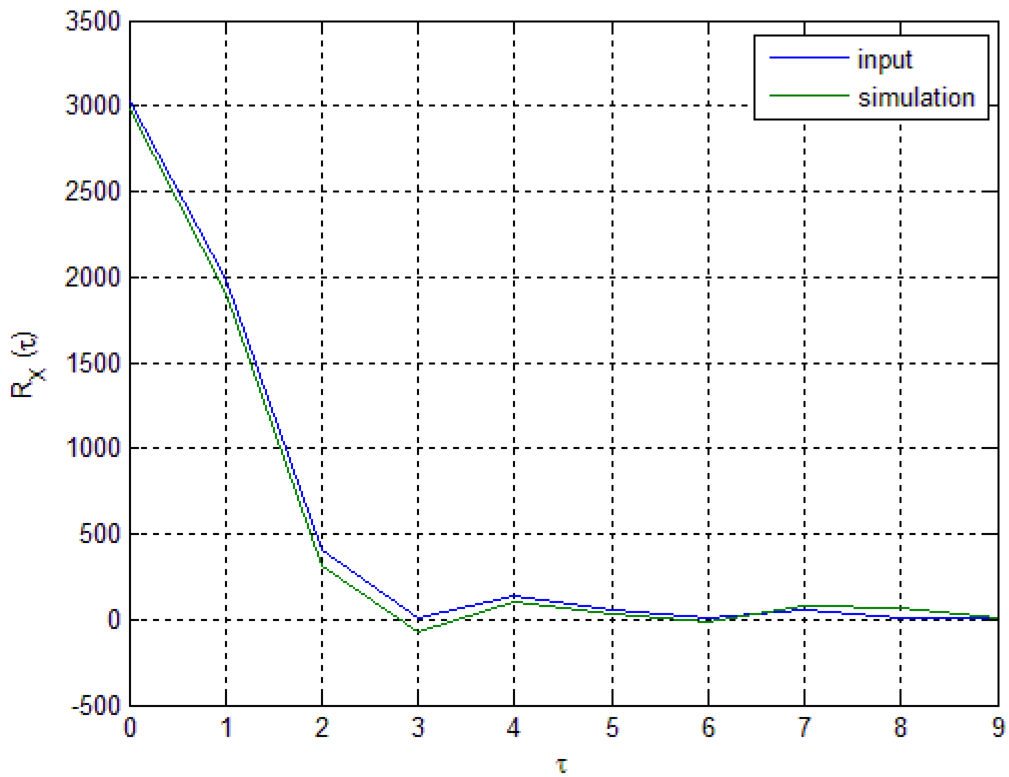

Fig. 2.19. Estimated autocorrelation function of the random process.

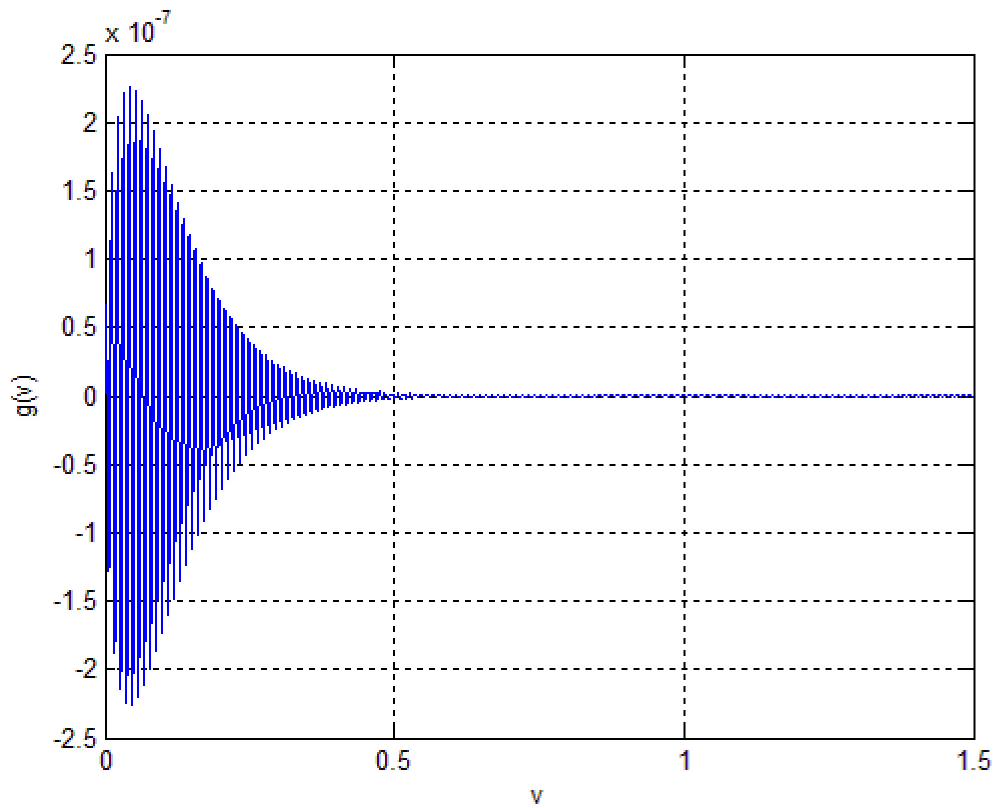

Fig. 2.20. A plot of the function used in finding $p_A(a)$ numerically. This function fluctuates very fast at large a.

3. THE TAIL DISTRIBUTION OF THE SUM OF KAPPA RANDOM VARIABLES WITH UNEQUAL WEIGHT AND CORRELATION

Applications of the Kappa distribution, which is used to describe the particle velocity distribution when a system is in thermal anti-equilibrium, to statistical mechanics and high frequency (HF) communication are considered. In particular, the tail distribution of the sum of Kappa random variables (RVs) is studied. First, an approximation for the sum of unequally weighted, uncorrelated Kappa RVs is found that provides results for the tail distribution of that sum. Correlated Kappa RVs are then examined by using the Cholesky decomposition to obtain similar results. Simulation results are shown to agree with this development.

3.1 Introduction

In HF communication, observations [21] have shown that at sunrise and at locations isolated from other disturbances, the noise is dominated by the galactic noise, and is not Gaussian. In [49], a model of the noise probability density function (pdf) that consists of a mixture of a Gaussian core and a Kappa tail is further provided.

Charged particles in the ionosphere that produce galactic noise via motion have been studied. Traditional statistical mechanics describes the particle velocity distribution to be Gaussian with the assumption that the system is at thermal equilibrium. For systems that are not at thermal equilibrium, the result is different. In astrophysics, the Kappa distribution has been observed in many areas, such as in the inner heliosheath [50], in the inner heliosphere [51], and in extreme ultraviolet flares [52]. Many theories have been proposed to explain this phenomenon [53], such as superstatistics.

The noise pdf mentioned in the previous paragraphs is only valid for the noise process at the antenna before being processed by the digital filter of the receiver. For communications, received signals need to be processed by filters before making decisions. The digital filter forms a linear combination of the sampled noise process. Hence, it is necessary to determine the noise statistics at the output of the filter in order to determine the performance of a communications receiver.

In this work, we focus on finding the tail distribution, which is necessary for evaluating the performance of a communication receiver, of the sum of Kappa RVs. The RVs can be correlated and the summing coefficients can be unequal. In this problem, the requirements of the central limit theorem are not met, and a non-Gaussian distribution is an expected result. Here, we show that the result can be approximated as a Kappa distribution.

The paper is organized as follows. In Section 3.2, we introduce the Kappa pdf and show some properties of that pdf. In Section 3.3, we find the tail distribution of a sum of independently and identically distributed (i.i.d.) Kappa RVs with unequal weighting coefficients. In Section 3.4, we consider the case when the Kappa RVs are correlated. In Section 3.5 and 3.6, we show how the model can be applied to HF communication and statistical mechanics. In Section 4.6, we provide simulation results, and in Section 3.8, we draw conclusions.

3.2 Kappa Random Variable

The pdf of a Kappa random variable $\mathbf{W}$ is given by

$$\begin{aligned} f\left(w; K, \sigma\right) = \frac{1}{\sqrt{K}\sigma\beta\left(\frac{1}{2}, K+\frac{1}{2}\right)} \left(1+\frac{w^2}{K\sigma^2}\right)^{-K-1}, \\ -\infty < w < \infty, K > \frac{1}{2}. \end{aligned} \tag{3.1}$$

where the function $\beta\left(x, y\right)$, with positive real arguments here, is the beta function. To show the parameters, the random variable is denoted as $\mathbf{W}(K, \sigma)$. Figure 3.1 shows

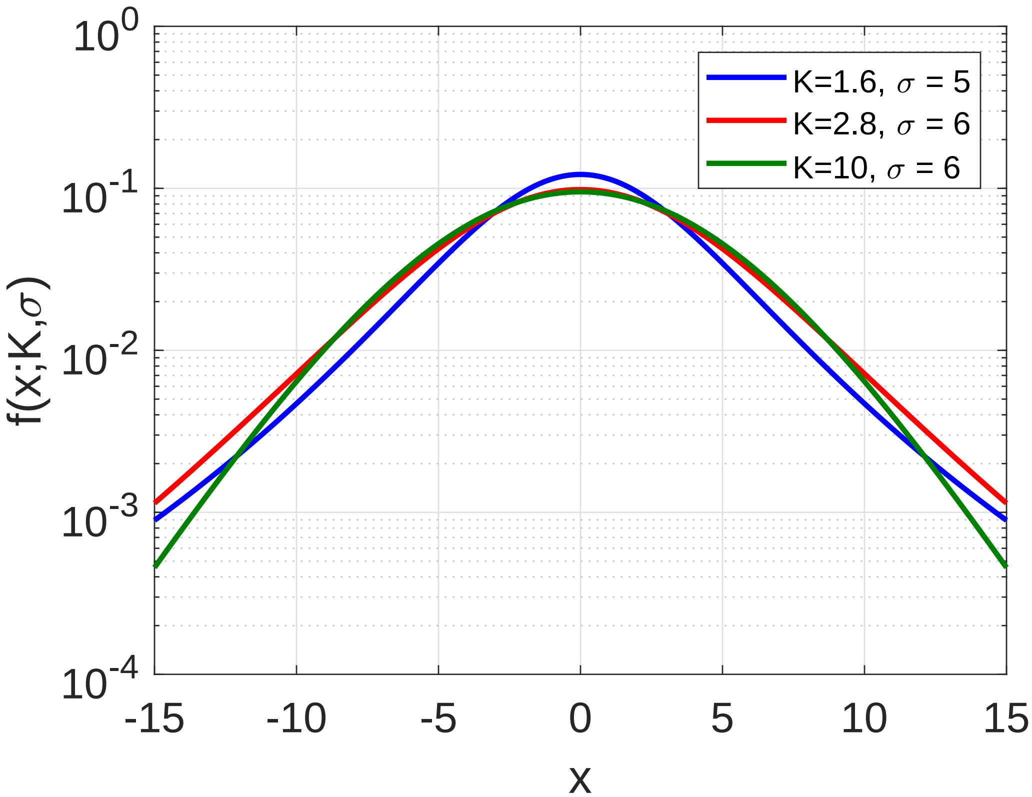

Fig. 3.1. Plots of the Kappa pdf for different parameters.

plots of the Kappa pdf for different parameters. As K increases, the pdf approaches the Gaussian distribution with variance $\frac{\sigma^2}{2}$.

The variance of the Kappa distribution is given by

$$\mathrm{Var}[\mathbf{W}] = \mathrm{E}[\mathbf{W}^2] - (\mathrm{E}[\mathbf{W}])^2 = \frac{K\sigma^2}{2K-1}. \tag{3.2}$$

If $\mathbf{Y} = a\mathbf{W}$, then $\mathrm{Var}[\mathbf{Y}] = \frac{a^2 K\sigma^2}{2K-1}$. Hence, the parameter σ is increased by a factor of $|a|$. We denote $\mathbf{Y}$ as $\mathbf{Y}(K, |a|\sigma)$.

With these preliminary results, we proceed to find the distribution of a sum of weighted Kappa RVs.

3.3 Sum of Kappa RVs with Unequal Weights

In this section, we consider the weighted sum of i.i.d. Kappa random variables with potentially unequal weighting coefficients. To find the tail distribution of the weighted sum of Kappa random variables, we first develop the following proposition.

Proposition 3.3.1 (Bimodal function decomposition.) *Let* $g(t) = C_1 C_2 \left(1 + \frac{t^2}{K a_1^2 \sigma^2}\right)^{-K-1} \left(1 + \frac{(x-t)^2}{K a_2^2 \sigma^2}\right)^{-K-1}$*, where* $C_i = \frac{1}{\sqrt{K}|a_i|\sigma\beta\left(\frac{1}{2}, K+\frac{1}{2}\right)}$*. Then for* $x \gg \sqrt{K}\sigma \max\{|a_1|, |a_2|\}$*,* $g(t) \approx g_1(t) + g_2(t)$*, where*

$$g_1(t) = C_1 C_2 \left(1 + \frac{t^2}{K a_1^2 \sigma^2}\right)^{-K-1} \left(\frac{x^2}{K a_2^2 \sigma^2}\right)^{-K-1}$$

and

$$g_2(t) = C_1 C_2 \left(\frac{x^2}{K a_1^2 \sigma^2}\right)^{-K-1} \left(1 + \frac{(x-t)^2}{K a_2^2 \sigma^2}\right)^{-K-1}.$$

Development of Approximation: First, we show that for $t \approx x$, $g_1(t) \ll g_2(t)$. Notice that this is equivalent to showing

$$\begin{aligned} &\frac{1}{\left(1 + \frac{t^2}{K a_1^2 \sigma^2}\right)^{K+1} \left(\frac{x^2}{K a_2^2 \sigma^2}\right)^{K+1}} \ll \\ &\frac{1}{\left(\frac{x^2}{K a_1^2 \sigma^2}\right)^{K+1} \left(1 + \frac{(x-t)^2}{K a_2^2 \sigma^2}\right)^{K+1}} \\ &\Leftrightarrow a_2^2 \left(1 + \frac{(x-t)^2}{K a_2^2 \sigma^2}\right) \ll a_1^2 \left(1 + \frac{t^2}{K a_1^2 \sigma^2}\right). \end{aligned} \tag{3.3}$$

Here, (3.3) is achieved when a_1 and a_2 are comparable under the assumption $x \gg \sqrt{K}\sigma \max\{|a_1|, |a_2|\}$. For this range of t, $g(t) \approx g_2(t)$ and $g(t) \approx g_1(t) + g_2(t)$.

Next, we show that for $t \approx 0$, $g_1(t) \gg g_2(t)$. This can be shown with the change of variable $u = x - t$ and proceeding in a way similar to the previous paragraph under the assumption $x \gg \sqrt{K}\sigma \max\{|a_1|, |a_2|\}$. For this range of t, $g(t) \approx g_1(t)$ and $g(t) \approx g_1(t) + g_2(t)$.

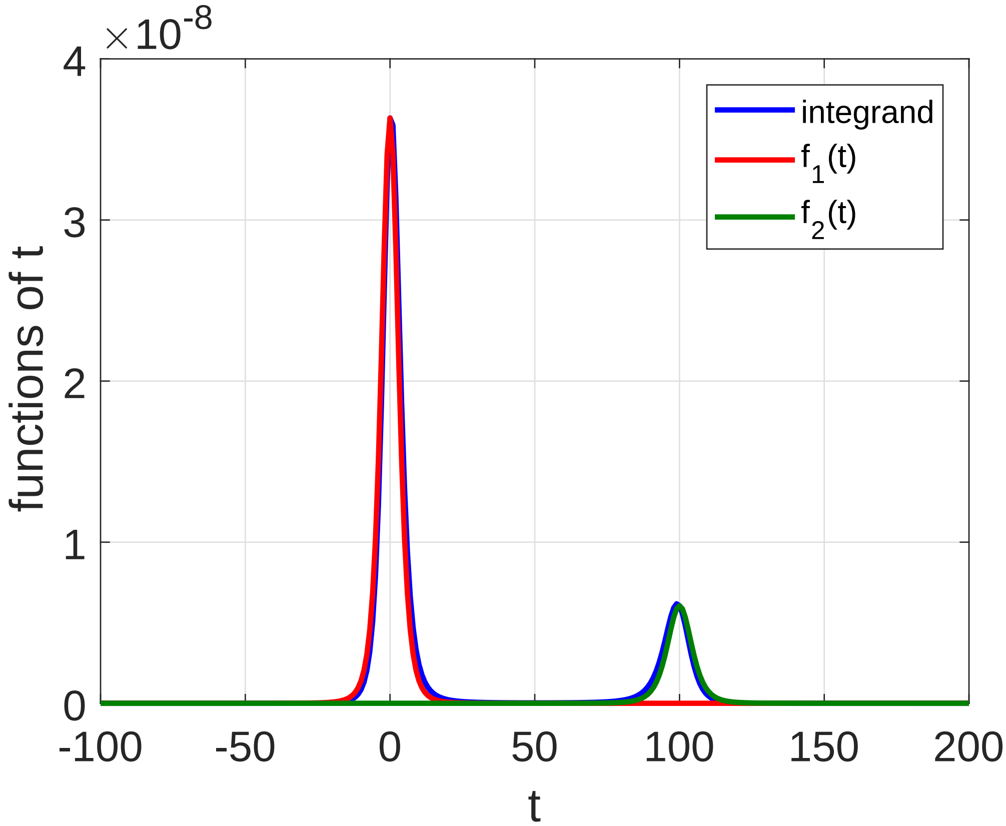

Fig. 3.2. The approximation of the integrand in (3.4a). In this example, $K = 1.6$, $\sigma = 5$, $x = 100$, $a_1 = 1$, and $a_2 = \sqrt{2}$.

For other cases of t, $g_1(t)$, $g_2(t)$, and $g(t)$ are negligible compared to the portion of $g_1(t)$ with $t \approx 0$ and the portion of $g_2(t)$ with $t \approx x$. Hence, $g(t) \approx g_1(t) + g_2(t) \approx 0$, and the entire approximation is obtained.

Figure 3.2 gives a numerical example that shows the effectiveness of the approximation method. With this decomposition result, we can find the tail pdf for the weighted sum of Kappa RVs with the following proposition.

Proposition 3.3.2 (Tail pdf for weighted-sum of Kappa RVs.) *Suppose* $\mathbf{W}_1$ *and* $\mathbf{W}_2$ *are i.i.d. Kappa random variables with parameters* K *and* σ, *and let* $\mathbf{X} = a_1\mathbf{W}_1 + a_2\mathbf{W}_2$. *Then, for* $x \gg \sqrt{K}\sigma \max\{|a_1|, |a_2|\}$ *(tail pdf),* $f_X(x) \propto x^{-2K-2}$.

Development of Approximation: Let $\mathbf{R}_i = a_i\mathbf{W}_i(K,\sigma)$ for $i = 1, 2$. Then, $\mathbf{R}_1$ and $\mathbf{R}_2$ are independent and can be denoted as $\mathbf{R}_i(K, |a_i|\sigma)$ for $i = 1, 2$. Let $C_i = \frac{1}{\sqrt{K}|a_i|\sigma\beta\left(\frac{1}{2},K+\frac{1}{2}\right)}$. The pdf of the sum of these two independent RVs can be found by evaluating the convolution integral of the two pdfs [54] to obtain

$$
\begin{aligned}
f_X(x) = \int_{-\infty}^{\infty} C_1 C_2 \left(1 + \frac{t^2}{Ka_1^2\sigma^2}\right)^{-K-1} \\
\left(1 + \frac{(x-t)^2}{Ka_2^2\sigma^2}\right)^{-K-1} dt \qquad (3.4a) \\
\approx \int_{-\infty}^{\infty} g_1(t)dt + \int_{-\infty}^{\infty} g_2(t)dt. \qquad (3.4b)
\end{aligned}
$$

Here, the integral is divided into two parts based Proposition 3.3.1.

The two components in (3.4b) can be evaluated as

$$
\int_{-\infty}^{\infty} g_1(t)dt = C_2 \left(\frac{x^2}{Ka_2^2\sigma^2}\right)^{-K-1} \propto x^{-2K-2}, \text{and}
$$

$$
\int_{-\infty}^{\infty} g_2(t)dt = C_1 \left(\frac{x^2}{Ka_1^2\sigma^2}\right)^{-K-1} \propto x^{-2K-2}.
$$

Summing up the results, the tail function is found to be proportional to x^{-2K-2}.

The result of this proposition is that the tail of the distribution of a weighted sum of i.i.d. Kappa RVs can be modeled by the tail of the pdf of a single Kappa RV. By letting $a = \sqrt{|a_1|^2 + |a_2|^2}$, the tail function can be modeled as the tail of a Kappa distribution with σ replaced with $a\sigma$ and K remaining the same. We can further generalize the result from Proposition 3.3.2 to the weighted sum of N i.i.d. Kappa RVs, and obtain a similar result.

3.4 Sum of Correlated Kappa RVs

We adopt the technique described in [55] and [56] for the case of correlated RVs and let $\mathbf{w} = [w_1, w_2, ..., w_N]$ be the vector with random variables that have tails modeled by the tails of Kappa RVs. The covariance matrix of $\mathbf{w}$ is defined as

$$\mathbf{C_w} = \mathrm{E}[(\mathbf{w} - \mathrm{E}[\mathbf{w}])(\mathbf{w} - \mathrm{E}[\mathbf{w}])^T]. \tag{3.5}$$

We assume that the covariance matrix is positive definite so that the Cholesky decomposition allows us to represent the covariance matrix as the product of a lower triangular matrix $\mathbf{L}$ and an upper triangular matrix, that is,

$$\mathbf{C} = \mathbf{L}\mathbf{L}^T. \tag{3.6}$$

If $\mathbf{x} = [x_1, x_2, ..., x_N]$ is the auxiliary vector such that the covariance $\mathbf{C_x}$ is $\mathbf{I}_N$ and

$$\mathbf{y} = \mathbf{L}\mathbf{x}, \tag{3.7}$$

then the covariance matrix of $\mathbf{y}$ is

$$\begin{aligned}
\mathbf{C_y} &= \mathrm{E}[\mathbf{L}(\mathbf{x} - \mathrm{E}[\mathbf{x}])(\mathbf{x} - \mathrm{E}[\mathbf{x}])^T\mathbf{L}^T] \\
&= \mathbf{L}\mathrm{E}[(\mathbf{x} - \mathrm{E}[\mathbf{x}])(\mathbf{x} - \mathrm{E}[\mathbf{x}])^T]\mathbf{L}^T \\
&= \mathbf{L}\mathbf{C_x}\mathbf{L}^T \\
&= \mathbf{L}\mathbf{L}^T \\
&= \mathbf{C_w}.
\end{aligned} \tag{3.8}$$

If we let $l_{i,j}$ denote the i, j entry of $\mathbf{L}$, the sum of RVs with tails modeled by the tails of Kappa RVs can be expressed as

$$\begin{aligned}
\mathbf{w} &= \sum_{i=1}^{N} \mathbf{w}_i \\
&= \sum_{i=1}^{N} \sum_{j=1}^{i} l_{i,j}\mathbf{x}_k.
\end{aligned} \tag{3.9}$$

Hence, the sum of correlated RVs that have tails modeled by the tails of Kappa RVs can be decomposed to a linear combination of uncorrelated RVs that have tails modeled by the tails of Kappa RVs. Based on Proposition 3.3.2 and an approximation

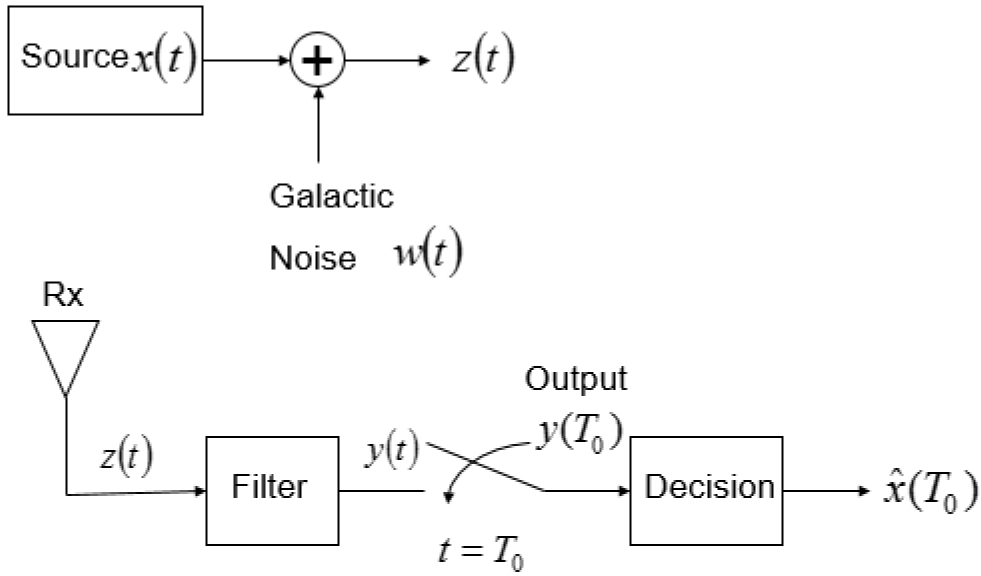

Fig. 3.3. The HF communication system with dominant galactic noise.

that these uncorrelated RVs are independent (valid for large K), we conclude that the tail distribution of **w** can still be approximated as a Kappa distribution (see simulation results).

3.5 HF Communication Application

The HF communication system with dominant galactic noise is depicted in Figure 3.3. The additive galactic noise channel model at the receive antenna is given by [49].

If the transmitting source is silenced, then $z(t)$ represents the dominant random noise, and at a particular time t, $z(t)$ is a Kappa RV. The filtering process produces a linear combination of samples of $z(t)$ given by

$$y = \sum_{i=1}^{N} a_i z(t_i), \tag{3.10}$$

where y is the noise statistic at the output of the filter, a_i represents a digital filter coefficient, t_i is the sample time, and N is the number of samples in the filtering process.

In practice, the weighting coefficients are related to the baseband waveform. If the symbol duration is T and ΔT is the sampling interval, $N = \frac{T}{\Delta T}$ samples are taken. We wish to obtain the tail distribution for y as N approaches infinity. We propose a Kappa approximation method based on Proposition 3.3.2.

Proposition 3.5.1 (Tail pdf for weighted infinite sum of Kappa RVs.) *Suppose* $\mathbf{W}_i$ *for* $i \in \{0, ..., N-1\}$ *are i.i.d. Kappa random variables with parameters* K *and* $\frac{\sigma}{\sqrt{N}}$. *let* $\mathbf{X} = \sum_{k=0}^{N-1} a_k \mathbf{W}_k$ *with* $a_k \in \mathbb{R}$. *Then, for large* x *and as* N *approaches infinity,* $f_X(x) \propto x^{-2K-2}$.

Development of Approximation: Let $\mathbf{X}_1 = \sum_{k=0}^{1} a_k \mathbf{W}_k$ and $\mathbf{X}_i = \mathbf{X}_{i-1} + a_i \mathbf{W}_i$ for $i = 2, 3, ..., N-1$. Then

$$f_{\mathbf{X}_i}(x) = \int_{-\infty}^{\infty} g_i(t; x) dt, \tag{3.11}$$

where

$$g_i(t; x) = C_{i-1} C_i \left(1 + \frac{t^2}{K \sigma'^2_{i-1}}\right)^{-K-1} \left(1 + \frac{(x-t)^2}{K a_i^2 \sigma_i^2}\right)^{-K-1}. \tag{3.12}$$

The pdf normalization constants for $\mathbf{X}_{i-1}$ and $\mathbf{W}_i$ are C_{i-1} and C_i respectively, and $\sigma'_{i-1} = \sqrt{\sum_{k=0}^{i-1} a_k^2 \frac{\sigma}{\sqrt{N}}}$. Further development can lead to a bound on the error.

In general, the noise power spectral density is not white. This means that, if the sampling interval is small enough, the noise RVs will be correlated. The tail distribution of y can be approximated as a Kappa distribution. The processing of the galactic noise by a filter is fundamental in the analysis of digital communication systems at sunrise. At sunrise, a model for the noise effects after processing with a filter is required to analyze the performances of various communication schemes. For example, [57] analyzes the bit error rate performance for different modulation schemes.

3.6 Physics Application

In the study of plasma physics, when systems are in thermal anti-equilibrium, the particle velocity distribution is given by a mixture of a Kappa tail and a Gaussian core [53]. Particles with lower energy follow traditional results from statistical mechanics, while particles with higher energy follow results involving nonextensive statistical mechanics. The velocity of the center of mass is given by

$$\vec{v}_{center} = \frac{\sum_i^N m_i \vec{v}_i}{\sum_i^N m_i}, \tag{3.13}$$

where N is the total number of particles in a system, m_i is the mass of the i-th particle, $\vec{v}_{center}$ is the velocity of the center of mass, and $\vec{v}_i$ is the velocity of the i-th particle. Only the one-dimensional case is considered in this equation.

The behaviors of the particles can be correlated. The tools developed in Section 3.3 and 3.4 can be used to describe the distribution of the velocity of the center of mass. The tail distribution can be approximated as Kappa. Knowing the distribution of the velocity of the center of mass helps us to understand the behavior of the overall system.

3.7 Simulation Results

In this section, we examine the effectiveness of the proposed approximation methods shown as red lines compared with simulations of the exact results shown with blue bars. For Section 3.3, we consider an example involving $\mathbf{X} = a_1\mathbf{W}_1 + a_2\mathbf{W}_2$, where W_1 and W_2 are independent Kappa RVs with K = 2.8 and $\sigma = 12.5$. $a_1 = 1$, and $a_2 = \sqrt{2}$. Figure 3.4 shows the simulation and approximation results.

For Section 3.4, we consider an example involving $\mathbf{X} = \mathbf{W}_1 + \mathbf{W}_2 + \mathbf{W}_3$, where the coefficients W_i are dependent Kappa RVs with K = 2.8 and $\sigma = 12.5$. The correlation matrix is given by

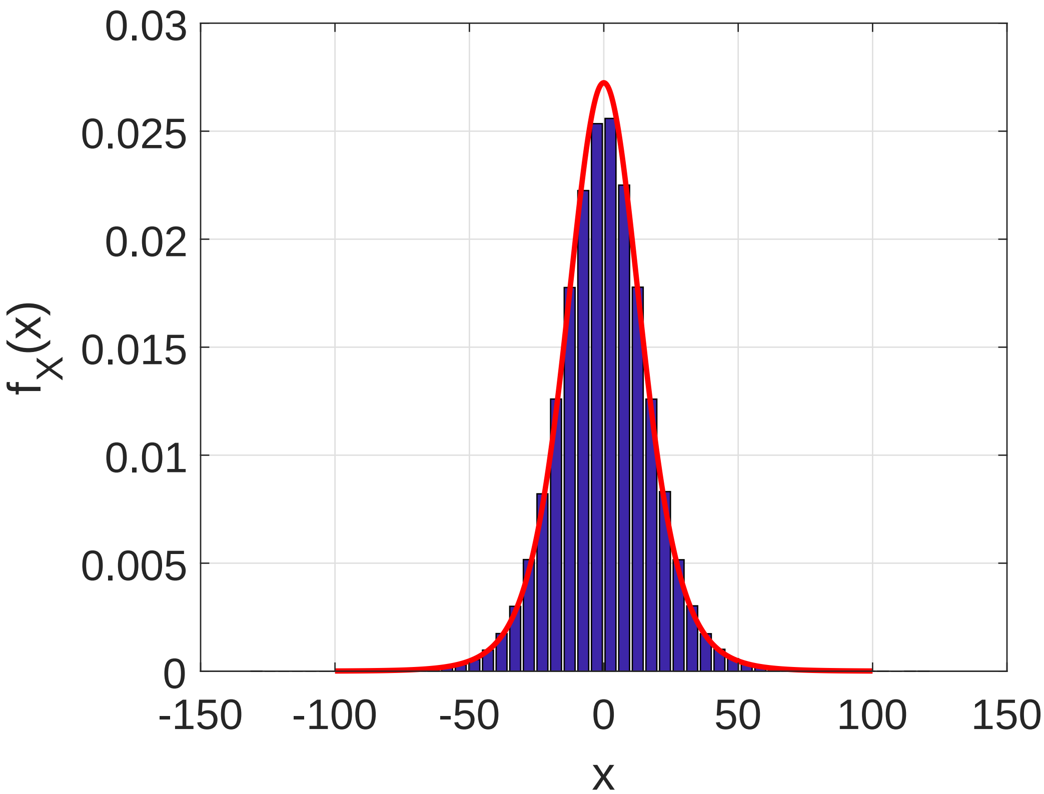

Fig. 3.4. Simulation and approximation results for the distribution of the sum of uncorrelated and unequally weighted Kappa RVs.

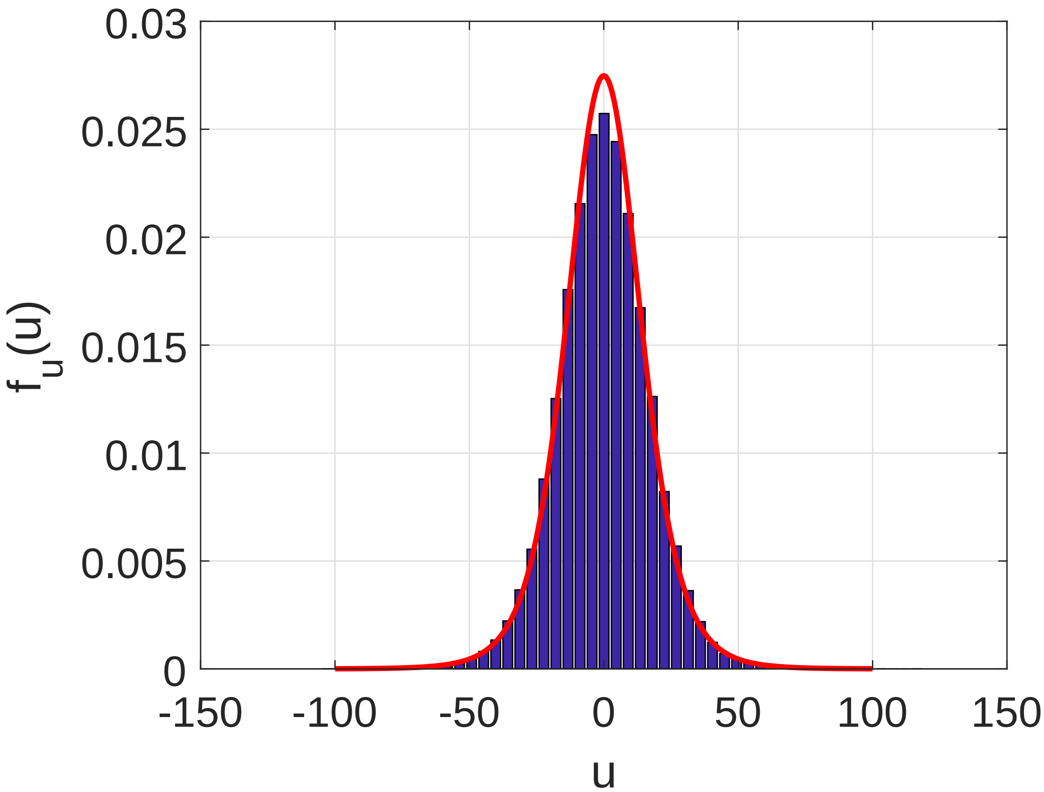

Fig. 3.5. Simulation and approximation results for the distribution of the sum of correlated Kappa RVs.

$$\mathbf{C} = \begin{bmatrix} 95.1085 & 62.4518 & 12.8718 \\ 62.4518 & 95.1085 & 62.4518 \\ 12.8718 & 62.4518 & 95.1085 \end{bmatrix}. \tag{3.14}$$

Figure 3.5 shows the simulation result. These simulation results verify that the tail distribution of the sum of Kappa RVs can be approximately modeled with the approach developed here.

Figure 3.6 shows an example that applies to HF communications. Is shows simulation and approximation results when $N = 1000$ Kappa RVs with K $= 2.8$ and $\sigma = \frac{12.5}{\sqrt{N}}$ are added together in a manner that would occur in a correlation receiver, that is, with a matched filter sampled at the optimum time for detection of a baseband

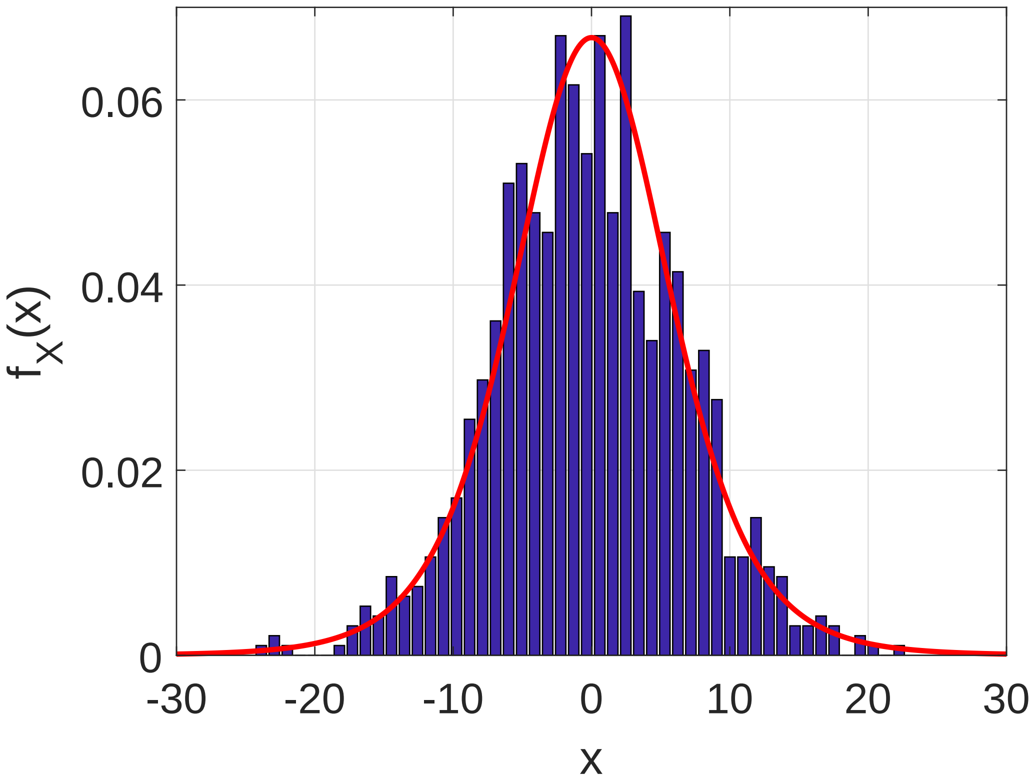

Fig. 3.6. Simulation and approximation results for the distribution of the sum of 1000 independent Kappa RVs with weighting coefficients from (3.15).

pulse. The digital receiver produces the result of (3.10) with the coefficients a_i that result from samples of the baseband pulse shape. For Figure 3.6, the samples are obtained from equally spaced samples of a half-sine pulse, that is,

$$a_i = \sin(\pi \frac{(i-1)}{N}), i = 1, 2, ..., N. \tag{3.15}$$

3.8 Conclusion

In this work, we have examined the tail distribution of the weighted sum of Kappa RVs that may involve correlation. We use the distribution of the tail of a single

Kappa RV to approximate the tail distribution of the weighted sum. The results can be used to determine the noise statistics at the output of an HF communication receiver. Furthermore, they can be used to provide information about the system velocity distribution in statistical mechanics. Simulation results have been provided to support the approximations.

3.9 Acknowledgement

The authors thank Tong Zhao of the Physics Department of Purdue University for his suggestion for Section 3.6.

4. ERROR RATE ANALYSIS FOR HF CHANNEL AROUND SUNRISE

High Frequency (HF) channel modeling has been heavily studied by antenna researchers. In this paper, we use new results to find the bit error rate (BER) for binary phase-shift keying (BPSK) under a measured special additive noise process. The decision criterion is maximum likelihood. The filtered and the sampled noise has modified Kappa distribution. The noise process may have correlation. In order to solve this case, we show that this process is a spherically invariant random process (SIRP). With this property, we use traditional decorrelation technique and a suboptimal maximum likelihood sequence detection scheme to demodulate.

4.1 Introduction

HF communication refers to the communication method that utilizes the Earth's ionosphere. The transmitter aims the signal to the sky. Then the signal gets reflected by the ionosphere and travels to the receiver. The transmission frequencies that are practical for ionospheric transmission lie in the range of $3 \sim 30$MHz. Although the available bandwidth is significantly less than the bandwidth available in modern communication systems such as Ka-Band satellite and LTE, in the case of war, satellites and civilian communication systems may not function well. Hence, HF communication can be considered as a last resort remote communication technique. The fact that HF communication utilizes the Earth's ionosphere gives scientists another technique for analyzing turbulence within the ionosphere [13]. Frequencies within the HF band are robust against tropospheric disturbances such as rain, while frequencies used for satellite communications are not.

The distribution of ions in the ionosphere plays an important role in reflecting electromagnetic waves for frequencies in the HF band. However, the distribution is known for diurnal and seasonal variations. Variations according to the sun's 27-day and 11-year solar cycle can also be observed. The distribution also changes with latitude. Certain phenomenon that occurs at certain times in the tropical region may not occur in the same way at the mid-latitude and high-latitude regions. Hence, HF channel modeling is critical for assessing the performance of communication system.

Channel modeling for HF communication systems dates back to Watterson's work [25]. The tap-delay model has many assumptions. Some of those assumptions caused significant differences between theoretical results and measured data. For example, the model is suitable for mid-latitude, but the ionosphere changes with latitude [24].

The noise and interference in the HF channel can be divided into 3 additive components [16] [17]: Gaussian components, atmospheric noise, and galactic noise. Gaussian components arise from receiver circuit noise and other various interferences. The amplitude of the atmospheric noise can be modeled by the Hall model.

The noise model described by Watterson [25] is additve white Gaussian noise (AWGN). This assumes the sum of the above 3 noises is Gaussian distributed in amplitude. However, field tests do not totally agree with this model. Iwama [26] points out that for his 24-hour test, he cannot conclude that the noise is Gaussian several times because the measured noise amplitude deviates from theoretical assumption a lot. Giesbrecht [17] conducted similar research near Adelaide, Australia, and his conclusion is that the galactic noise is not AWGN before sunrise and well after sunrise. He further approximated the measured noise to be a modified Bi-Kappa distribution. The modified Bi-Kappa distribution is very similar to the Bi-Kappa distribution, and the latter distribution has been used for studies in solar wind [58]. Solar wind plays an important role in affecting the ionosphere, and hence the HF channel.

In fact, Shinde [59] had already derived similar results by considering the ratio of a zero-mean Gaussian process and a non-Gaussian random process with strong correlation among its samples. His result is very similar to the modified Bi-Kappa distribution when K = 2.

However, Giesbrecht's result is not perfect. His model allows cases that have infinite noise power. Such cases are unrealistic in practice becasue electrical equipments will break down. Our recent work [49] shows that Giesbrecht's results can be interpreted in another way, and when combined with recent results from physics, we obtain a new channel model that always yield finite noise power. The sampled noise probability density function (pdf) is Kappa. The samples may have correlation.

In this thesis work, we wish to investigate the effect of galactic noise on communication systems, and how much the properties of actual noise deviate from the properties of AWGN theoretically. We adopt the Kappa distribution model we have previously derived.

This work is organized as follows. In Section 4.2, we show our communication system model considering additive noise that has a Kappa distribution. In Section 4.3, we derive the bit error rate for a BPSK signal by using the maximum likelihood criterion. In Section 4.4, we extend our work for the symbol error rate (SER) to the QPSK and 16-QAM case. In Section 4.5, we solve the case when the noise samples are correlated. In Section 4.6, we show our simulation results and compare with the traditional AWGN channel. We make conclusions in Section 4.7.

4.2 System Model

The galactic noise is caused by solar radiation's interaction with the ionosphere. Around sunrise, measurement results show that the power of the galactic noise is much larger than the Gaussian components. So the noise pdf is dominated by the galactic noise. In our previous work [49], we derived that the pdf of the galactic noise is Kappa distribution and may contain correlation. Here we analyze a HF communication system around sunrise.

We consider a communication system as shown in Figure 4.1. The model of the channel is very similar to the traditional AWGN channel except that in our system, each sample of the noise after filtering has a circularly-symmetric complex Kappa distribution. We assume that at output, we sample at each symbol duration T_0. Equation (4.1) shows the probability density function of the Kappa distribution according to our previous work [49].

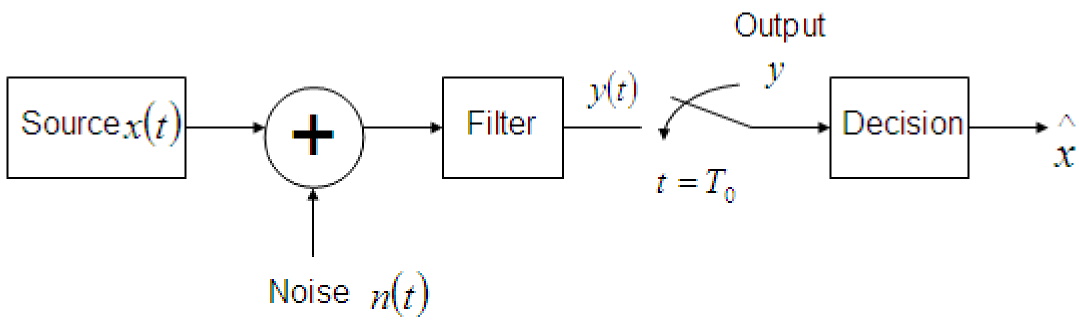

Fig. 4.1. System model.

$$f(x;K,\sigma) = \frac{1}{\sqrt{K}\sigma\beta\left(\frac{1}{2}, K+\frac{1}{2}\right)}\left(1+\frac{x^2}{K\sigma^2}\right)^{-K-1}, \quad -\infty < x < \infty, K > \frac{1}{2} \tag{4.1}$$

The function $\beta(x,y)$, $Re\{x\} \geq 0, Re\{y\} \geq 0$ is a beta function with the following equivalent definitions:

$$\beta(x,y) = \int_0^1 t^{x-1}(1-t)^{y-1}\,dt \tag{4.2}$$

$$= \frac{\Gamma(x)\Gamma(y)}{\Gamma(x+y)} \tag{4.3}$$

$$= 2\int_0^{\frac{\pi}{2}} \sin^{2x-1}\theta\cos^{2y-1}\theta d\theta \tag{4.4}$$

Suppose we transmit a BPSK symbol x with energy $\sqrt{E_b}$. Then, the relationship between the sampled output symbol y and the input symbol x can be described as

$$y = x + n, \tag{4.5}$$

where n is the sampled noise after being filtered. The random variable n has a circularly-symmetric, complex Kappa distribution. When a "+1" BPSK symbol is transmitted, x = $\sqrt{E_b}$. When a "-1" BPSK symbol is transmitted, x = $-\sqrt{E_b}$. The symbols "+1" and "-1" are sent with equal probability.

Our goal is to find the bit error rate under the maximum likelihood detection criterion. Before we analyze to obtasin the bit error rate, we look at some important properties of Kappa distribution.

Theorem 4.2.1 *A random variable X that has probability distribution as shown in (4.1) has zero mean and variance* $\frac{K\sigma^2}{2K-1}$ *for* $K > 1/2$.

Proof: Since Kappa pdf is symmetric at $x = 0$, the mean is 0. Using the trigonometric substitution, $\tan\theta = x/\left(\sqrt{K}\sigma\right)$, we obtain

$$\begin{aligned} E\left[\mathrm{X}^2\right] &= \int_{-\infty}^{\infty} \frac{x^2}{\sqrt{K}\sigma\beta\left(\frac{1}{2}, K+\frac{1}{2}\right)} \left(1 + \frac{x^2}{K\sigma^2}\right)^{-K-1} dx \\ &= \int_{-\frac{\pi}{2}}^{\frac{\pi}{2}} \frac{K\sigma^2\tan^2\theta}{\sqrt{K}\sigma\beta\left(\frac{1}{2}, K+\frac{1}{2}\right)} \left(\sec^2\theta\right)^{-K-1} \sqrt{K}\sigma\sec^2\theta d\theta \end{aligned} \tag{4.6}$$

Simplifying the above expression, we obtain

$$\int_{-\frac{\pi}{2}}^{\frac{\pi}{2}} \frac{K\sigma^2 \tan^2\theta}{\beta\left(\frac{1}{2}, K+\frac{1}{2}\right)} \left(\cos^{2K}\theta\right) d\theta$$
$$= \int_{-\frac{\pi}{2}}^{\frac{\pi}{2}} \frac{K\sigma^2}{\beta\left(\frac{1}{2}, K+\frac{1}{2}\right)} \left(\sin^2 \cos^{2K-2}\theta\right) d\theta$$
$$= 2\int_{0}^{\frac{\pi}{2}} \frac{K\sigma^2}{\beta\left(\frac{1}{2}, K+\frac{1}{2}\right)} \left(\sin^{2\left(\frac{3}{2}\right)-1} \cos^{2\left(\frac{2K-1}{2}\right)-1}\theta\right) d\theta$$
$$= K\sigma^2 \frac{\beta\left(\frac{3}{2}, K-\frac{1}{2}\right)}{\beta\left(\frac{1}{2}, K+\frac{1}{2}\right)} \tag{4.7}$$
$$= K\sigma^2 \frac{\frac{\Gamma\left(\frac{3}{2}\right)\Gamma\left(K-\frac{1}{2}\right)}{\Gamma(K+1)}}{\frac{\Gamma\left(\frac{1}{2}\right)\Gamma\left(K+\frac{1}{2}\right)}{\Gamma(K+1)}} \tag{4.8}$$
$$= K\sigma^2 \frac{\frac{1}{2}\Gamma\left(\frac{1}{2}\right)\Gamma\left(K-\frac{1}{2}\right)}{\Gamma\left(\frac{1}{2}\right)\left(K-\frac{1}{2}\right)\Gamma\left(K-\frac{1}{2}\right)} \tag{4.9}$$
$$= \frac{K\sigma^2}{2K-1}$$

where (4.7) is obtaind by (4.4), (4.8) is obtained by (4.3), and (4.9) is obtained by the property of Gamma function $\Gamma(x+1) = x\Gamma(x)$.

The final equation is obtained from (4.4). Since beta function has finite value when the inputs are both greater than 0, we conclude that $K > 1/2$. Hence, we obtain the result. Q.E.D.

For all practical measurements, $K > 1/2$. Hence, the galactic noise power is always finite. Past work in this area such as [60] and [61] used modified Bi-Kappa distributin that stems from Giesbrecht's work [17]. However, they never recognized that this pdf has infinite variance under certain case, and such case was already present in Giesbrecht's work. One can use the concept of geometric power [27] to analyze the communication system without using variance. When a more suitable noise model comes out, we should proceed the work accordingly.

With these results, we can now proceed with the uncorrelated noise BER analysis.

4.3 BER Analysis for BPSK

Suppose a "+1" symbol is transmitted. Then, the distribution of y will be the Kappa distribution in (4.1) shifted to the right by $\sqrt{E_b}$ units; that is, the following distribution will be observed:

$$\begin{aligned} & f\left(y; K, \sigma \middle| x = +\sqrt{E_b}\right) = \\ & \frac{1}{\sqrt{K}\sigma\beta\left(\frac{1}{2}, K+\frac{1}{2}\right)}\left(1+\frac{\left(y-\sqrt{E_b}\right)^2}{K\sigma^2}\right)^{-K-1}, \\ & -\infty < y < \infty, K > \frac{1}{2} \end{aligned} \tag{4.10}$$

Similarly, when a "-1" symbol is transmitted, we observe the following distribution:

$$\begin{aligned} & f\left(y; K, \sigma \middle| x = +\sqrt{E_b}\right) = \\ & \frac{1}{\sqrt{K}\sigma\beta\left(\frac{1}{2}, K+\frac{1}{2}\right)}\left(1+\frac{\left(y+\sqrt{E_b}\right)^2}{K\sigma^2}\right)^{-K-1}, \\ & -\infty < y < \infty, K > \frac{1}{2} \end{aligned} \tag{4.11}$$

For maximum likelihood detection, under the assumption of equal costs, we should decide $\hat{x} = +\sqrt{E_b}$ when

$$\frac{f\left(y; K, \sigma \middle| x = +\sqrt{E_b}\right)}{f\left(y; K, \sigma \middle| x = -\sqrt{E_b}\right)} \geq 1 \tag{4.12}$$

Simplification of (5.4) shows that we should decide $\hat{x} = +\sqrt{E_b}$ when

$$\left(y - \sqrt{E_b}\right)^2 \geq \left(y + \sqrt{E_b}\right)^2 \tag{4.13}$$

The above has a geometrical meaning, in which the decision boundary is at x = 0. Further simplification of (4.13) shows $\hat{x} = +\sqrt{E_b}$ should be decided when $y \geq 0$.

Thus, the probability of transmitting $x = +\sqrt{E_b}$ and decoding this as $\hat{x} = -\sqrt{E_b}$ is

$$P\left(\left\{x = +\sqrt{E_b}, \hat{x} = -\sqrt{E_b}\right\}\right) = \int_{-\infty}^{0} \frac{1}{\sqrt{K}\sigma\beta\left(\frac{1}{2}, K+\frac{1}{2}\right)}\left(1+\frac{\left(y-\sqrt{E_b}\right)^2}{K\sigma^2}\right)^{-K-1} dy \tag{4.14}$$

Let

$$t = \frac{y-\sqrt{E_b}}{\sqrt{Var\left[X\right]}} = \frac{\left(y-\sqrt{E_b}\right)}{\sqrt{K}\sigma}\sqrt{2\left(K-\frac{1}{2}\right)} \tag{4.15}$$

Then, (4.14) becomes

$$P\left(\left\{x = +\sqrt{E_b}, \hat{x} = -\sqrt{E_b}\right\}\right) = \int_{-\infty}^{-\sqrt{2E_b\frac{K-\frac{1}{2}}{K\sigma^2}}} \frac{1}{\sqrt{2\left(K-\frac{1}{2}\right)}\left(\beta\left(\frac{1}{2}, K+\frac{1}{2}\right)\right)}\left(1+\frac{t^2}{2\left(K-\frac{1}{2}\right)}\right)^{-K-1} dt \tag{4.16}$$

By symmetry, the probability of transmitting $x = -\sqrt{E_b}$ and decoding this as $\hat{x} = +\sqrt{E_b}$ is the same as the result above. Since each type of symbol has an equal chance of being transmitted, the result of (4.16) is actually the overall BER.

We would like to simplify (4.16) notationally by defining the following L function:

$$L\left(x;K\right) \equiv \int_{x}^{\infty} \frac{1}{\sqrt{2\left(K-\frac{1}{2}\right)}\left(\beta\left(\frac{1}{2}, K+\frac{1}{2}\right)\right)}\left(1+\frac{t^2}{2\left(K-\frac{1}{2}\right)}\right)^{-K-1} dt \tag{4.17}$$

$$-\infty < x < \infty, K > \frac{1}{2}$$

and G function

$$G\left(K,\sigma\right) \equiv \frac{K\sigma^2}{K-\frac{1}{2}} \tag{4.18}$$

$$K > \frac{1}{2}, \sigma > 0$$

Figure 4.2, 4.3, and 4.4 show some examples of the L function. Notice that for large value of K, L function approaches to Q function, which is plotted in Figure 4.5.

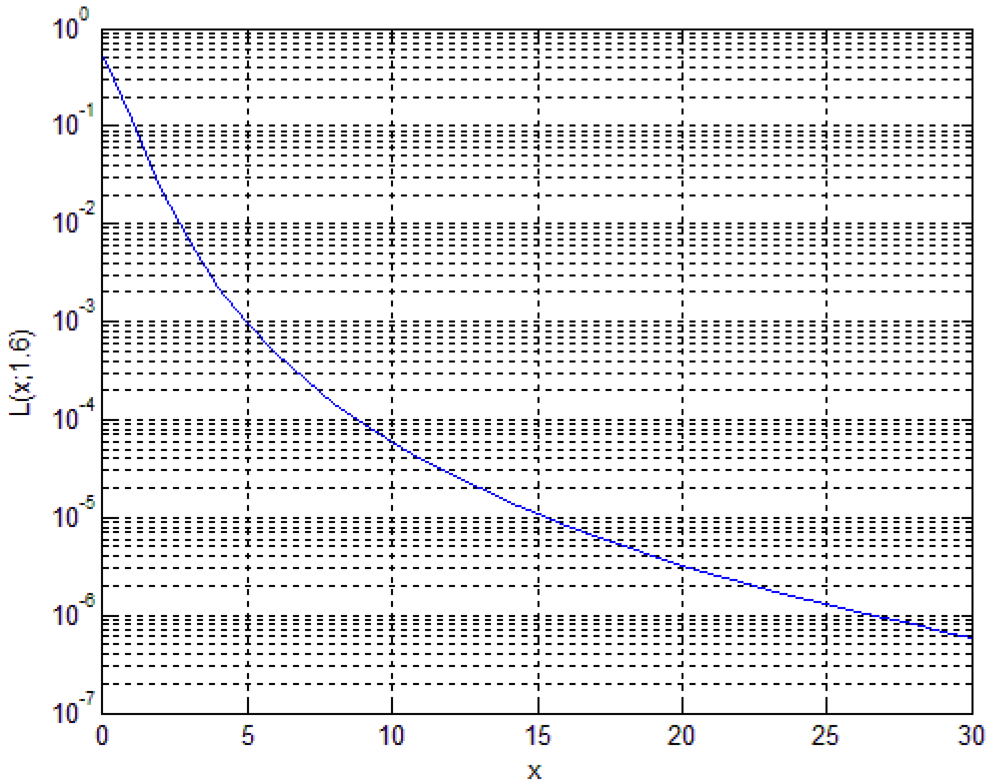

Fig. 4.2. An example L function plot with K = 1.6.

There are many similarities between the L function and the Q function that is used for AWGN. Here, 2 important properties are shown as follows:

Theorem 4.3.1 (L function properties) *The L function with definition shown in (4.17) has the following behavior:*

1. *It is monotonically decreasing.*
2. $L(\alpha; K) = 1 - L(-\alpha; K)$

Proof 1. The L function is inherently an integral of a probability density function, and a probability density function f(x) satisfies f(x)$\geq$ 0. Let f denote the the probability density function of the modified Bi-Kappa distribution, we have

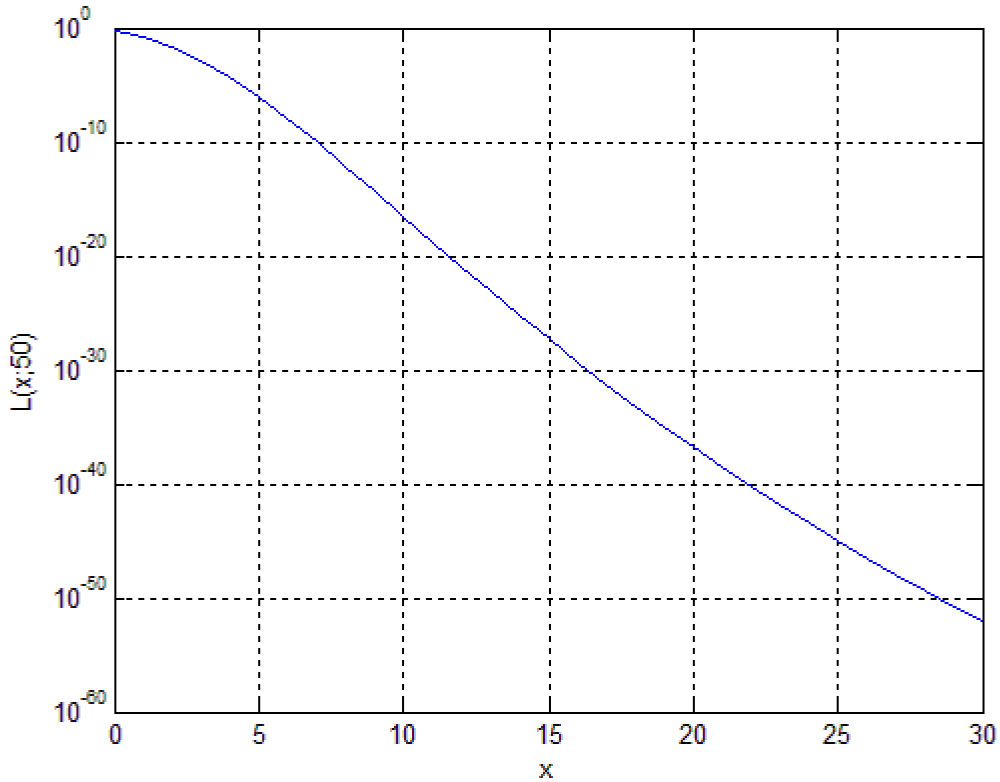

Fig. 4.3. An example L function plot with K = 50.

$$
\begin{aligned}
&\forall a < b, \\
&L(a; K,) - L(b; K,) \\
&= \int_a^\infty f(x)\,dx - \int_b^\infty f(x)\,dx \\
&= \int_a^b f(x)\,dx \\
&> 0 \,(\because f(x) \geq 0)
\end{aligned}
$$

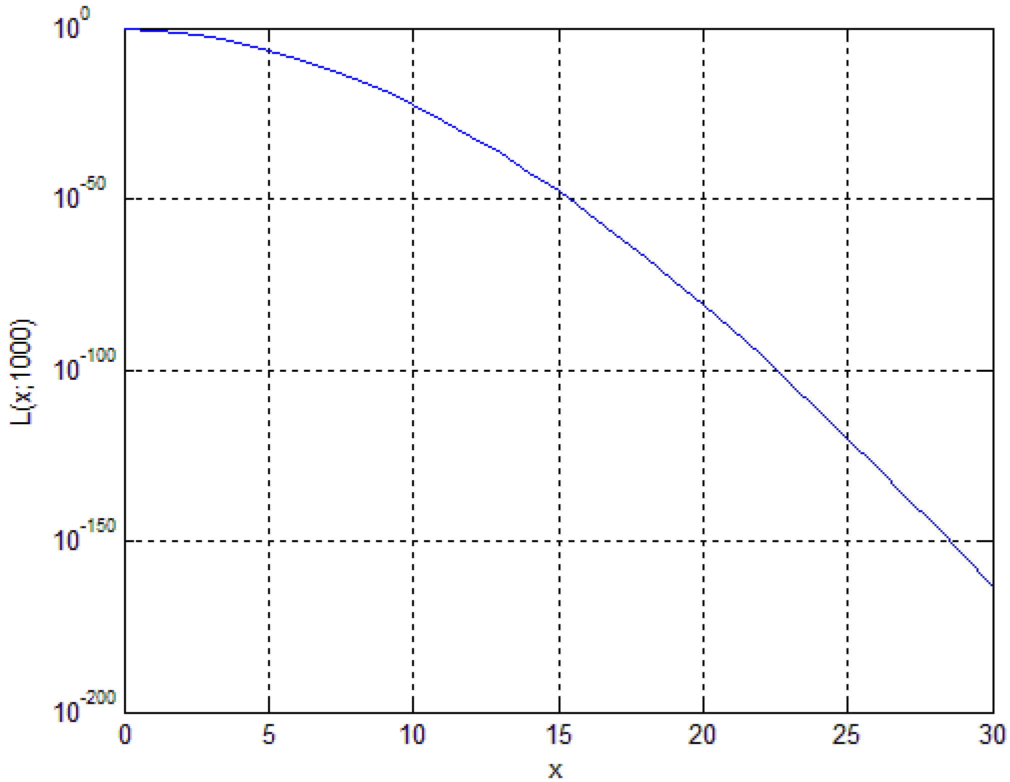

Fig. 4.4. An example L function plot with K = 1000.

2.

$$\begin{aligned}
&\forall u, f\left(u\right) = f\left(-u\right) \\
&\int_{-\infty}^{\alpha} f\left(x\right) dx \\
&= \int_{\infty}^{-\alpha} -f\left(-u\right) du \,\text{(Let u = -x, then du = -dx)} \\
&= \int_{\infty}^{-\alpha} -f\left(u\right) du \,(\because f\left(u\right) = f\left(-u\right)) \\
&= \int_{-\alpha}^{\infty} f\left(u\right) du
\end{aligned} \tag{4.19}$$

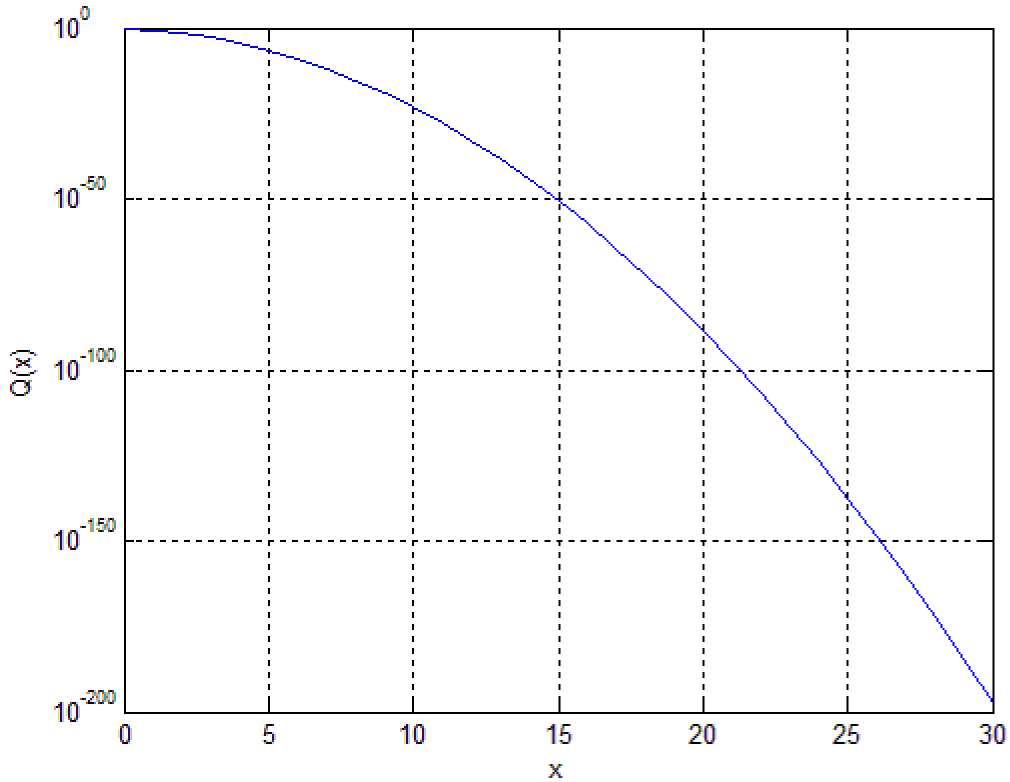

Fig. 4.5. A Q function plot.

So from

$$\begin{aligned} 1 &= \int_{-\infty}^{\infty} f(x)\,dx \\ &= \int_{-\infty}^{\alpha} f(x) + \int_{\alpha}^{\infty} f(x)\,dx \\ &= \int_{-\alpha}^{\infty} f(x) + \int_{\alpha}^{\infty} f(x)\,dx \,(\text{by}4.19) \\ &= L(-\alpha;K) + L(\alpha;K) \end{aligned}$$

we obtain the result. Q.E.D.

Hence, we can conclude that the BER, from (4.14), (4.17) and (4.18), is

$$p_{BER,BPSK} = L\left(\sqrt{2\frac{E_b}{G(K,\sigma)}};K\right) \tag{4.20}$$

4.4 SER for QPSK and 16-QAM

The derivation for the symbol error rate for QPSK and 16-QAM is similar to the derivation for the AWGN counterpart. For QPSK, we use Gray coding to minimize BER as shown in Figure 4.6. For example, transmitting "00" corresponds to transmitting s_0. We assume that each symbol is transmitted with equal probability.

The symbol error event is defined as the event in which a symbol transmitted through the channel is decoded into a symbol that is different from the transmitted one. The mathematical description is $\{s = s_i, \hat{s} \neq s_i\}$. The symbol error rate for s_0 is $P\left(\{s = s_0, \hat{s} \neq s_0\}\right)$.

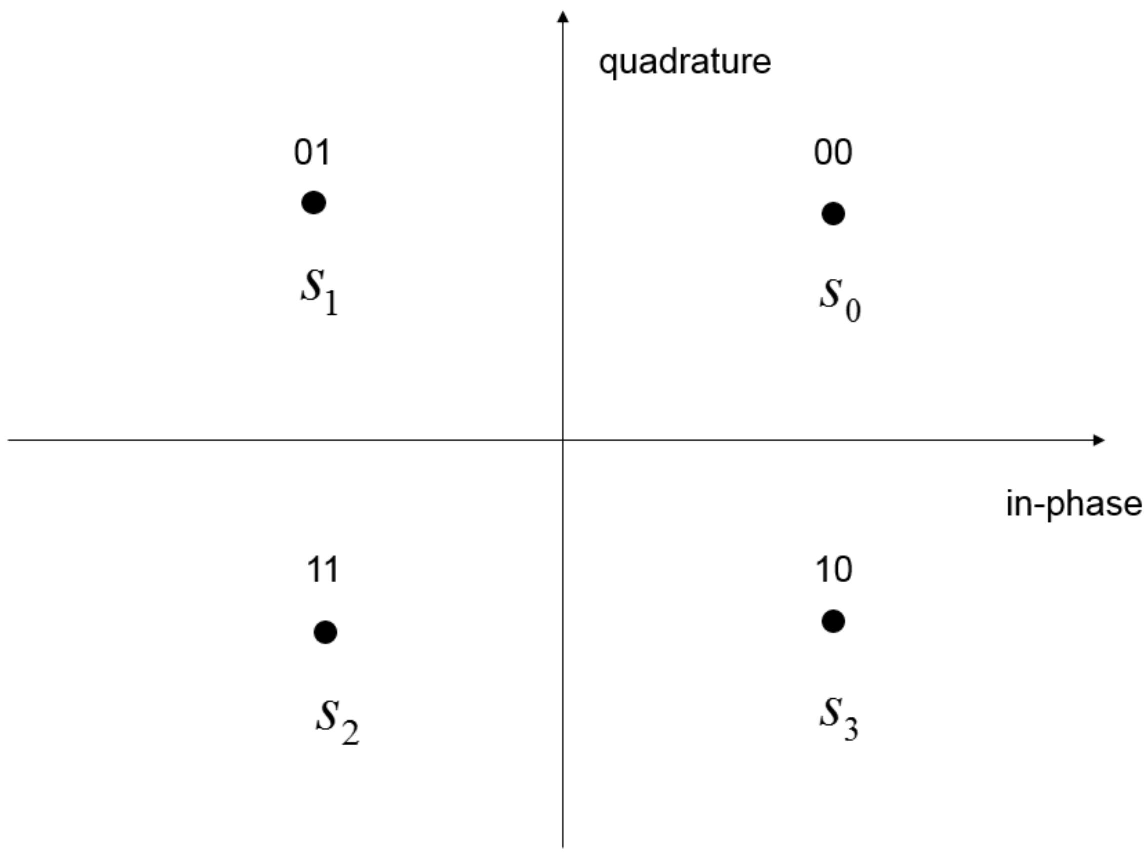

Fig. 4.6. Constellation diagram for QPSK.

For the ML decision, the decision boundaries are the axes. The ML decision regions are the corresponding quadrants of the plane. For example, for s_0, the first quadrant is its ML decision region.

Because of symmetry for all 4 symbols, the symbol error rate for each symbol is the same as the others. Hence, to find the overall SER, it suffices for us to find the symbol error rate for s_0.

We would like to define two constants that are repeatedly used throughout our analysis in this section.

$$G_1 = \frac{1}{\sqrt{K}\sigma\beta\left(\frac{1}{2}, K-\frac{1}{2}\right)} \tag{4.21}$$

$$G_2 = G_1\sqrt{\frac{G(K,\sigma)}{2}} \tag{4.22}$$

To find the SER for s_0, we first find the probability for a correct decoding event, that is, $P(\{s = s_0, \hat{s} = s_0\})$. Here, we obtain

$$\begin{aligned} p_{SER,QPSK} &= 1 - p_c \\ &= 1 - \left(\int_0^\infty G_1\left(1 + \frac{\left(x-\sqrt{E_b}\right)^2}{K\sigma^2}\right)^{-K-1} dx\right)^2 \\ &= 1 - \left(\int_{-\sqrt{\frac{2E_b}{G(K,\sigma)}}}^\infty G_2\left(1 + \frac{x^2}{2K-1}\right)^{-K-1} dx\right)^2 \\ &= 1 - \left(1 - L\left(\sqrt{\frac{2E_b}{G(K,\sigma)}}; K\right)\right)^2 \\ &= 2L\left(\sqrt{\frac{2E_b}{G(K,\sigma)}}; K\right) - L^2\left(\sqrt{\frac{2E_b}{G(K,\sigma)}}; K\right), \end{aligned} \tag{4.23}$$

Equation (4.23) is the SER for s_0, as well as the overall SER.

For 16-QAM, we now transmit a symbol containing 4 bits instead of 2. The constellation diagram is shown in Figure 4.7. We assume each symbol occurs with equal probability.

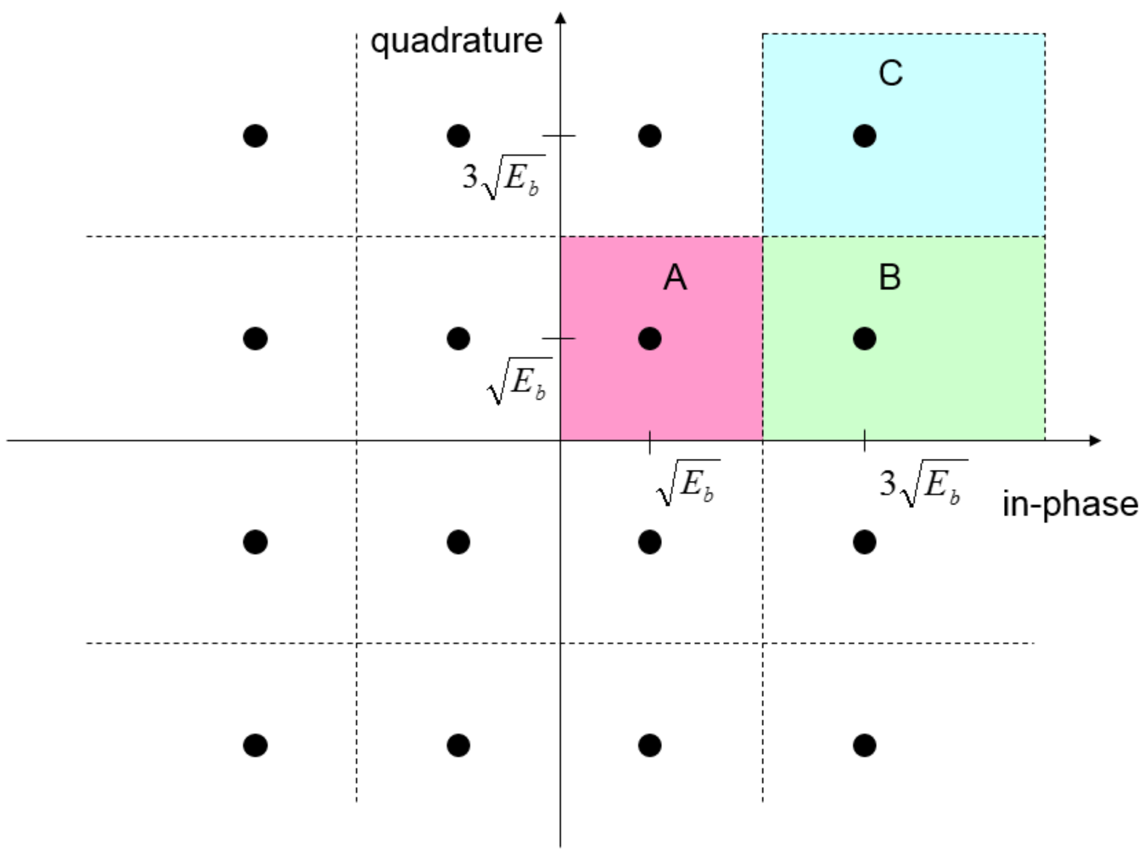

Fig. 4.7. Constellation diagram and ML decision region for 16-QAM.

Analyzing to obtain the SER in this case is similar to the above QPSK analysis except that we notice there are now 3 types of symbols if the corresponding ML decision regions are examined. We label these 3 types as A, B, and C, respectively.

For type-A symbols, consider an example symbol $\left(\sqrt{E_b}, \sqrt{E_b}\right)$ as shown in Figure 4.7. For that symbol, its ML decision is bounded by $x = 0$, $x = 2\sqrt{E_b}$, $y = 0$, $y = 2\sqrt{E_b}$. The symbol error probabilities are

$$
\begin{aligned}
p_{SER,A} &= 1 - p_c \\
&= 1 - \left(\int_0^{2\sqrt{E_b}} G_1 \left(1 + \frac{\left(x - \sqrt{E_b}\right)^2}{K\sigma^2} \right)^{-K-1} dx \right) \times \\
&\left(\int_0^{2\sqrt{E_b}} G_1 \left(1 + \frac{\left(y - \sqrt{E_b}\right)^2}{K\sigma^2} \right)^{-K-1} dy \right) \\
&= 1 - \left(\int_0^{\infty} G_1 \left(1 + \frac{\left(x - \sqrt{E_b}\right)^2}{K\sigma^2} \right)^{-K-1} dx - \right. \\
&\qquad \left. \int_{2\sqrt{E_b}}^{\infty} G_1 \left(1 + \frac{\left(x - \sqrt{E_b}\right)^2}{K\sigma^2} \right)^{-K-1} dx \right) \times \\
&\left(\int_0^{\infty} G_1 \left(1 + \frac{\left(y - \sqrt{E_b}\right)^2}{K\sigma^2} \right)^{-K-1} dy - \right. \\
&\qquad \left. \int_{2\sqrt{E_b}}^{\infty} G_1 \left(1 + \frac{\left(y - \sqrt{E_b}\right)^2}{K\sigma^2} \right)^{-K-1} dy \right) \\
&= 1 - \left(\int_{-\sqrt{\frac{2E_b}{G(K,\sigma)}}}^{\infty} G_2 \left(1 + \frac{x^2}{2K-1} \right)^{-K-1} dx - \right. \\
&\qquad \left. \int_{\sqrt{\frac{2E_b}{G(K,\sigma)}}}^{\infty} G_2 \left(1 + \frac{x^2}{2K-1} \right)^{-K-1} dx \right) \times \\
&\left(\int_{-\sqrt{\frac{2E_b}{G(K,\sigma)}}}^{\infty} G_2 \left(1 + \frac{y^2}{2K-1} \right)^{-K-1} dy - \right. \\
&\qquad \left. \int_{\sqrt{\frac{2E_b}{G(K,\sigma)}}}^{\infty} G_2 \left(1 + \frac{y^2}{2K-1} \right)^{-K-1} dy \right) \\
&= 1 - \left[1 - L\left(\sqrt{\frac{2E_b}{G(K,\sigma)}}; K \right) - L\left(\sqrt{\frac{2E_b}{G(K,\sigma)}}; K \right) \right] \times \\
&\left[1 - L\left(\sqrt{\frac{2E_b}{G(K,\sigma)}}; K \right) - L\left(\sqrt{\frac{2E_b}{G(K,\sigma)}}; K \right) \right] \\
&= 4L\left(\sqrt{\frac{2E_b}{G(K,\sigma)}}; K \right) - 4L^2\left(\sqrt{\frac{2E_b}{G(K,\sigma)}}; K \right)
\end{aligned} \tag{4.24}
$$

For type-B symbols, consider an example symbol $\left(3\sqrt{E_b}, \sqrt{E_b}\right)$ as shown in Figure 4.7. For that symbol, its ML decision is bounded by $x = 2\sqrt{E_b}$, $x = \infty$, $y = 0$, $y = 2\sqrt{E_b}$. The symbol error probabilities are

$$
\begin{aligned}
p_{SER,B} &= 1 - p_c \\
&= 1 - \left(\int_{2\sqrt{E_b}}^{\infty} G_1 \left(1 + \frac{\left(x - 3\sqrt{E_b}\right)^2}{K\sigma^2}\right)^{-K-1} dx\right) \times \\
&\left(\int_{0}^{2\sqrt{E_b}} G_1 \left(1 + \frac{\left(y - \sqrt{E_b}\right)^2}{K\sigma^2}\right)^{-K-1} dy\right) \\
&= 1 - \left(\int_{2\sqrt{E_b}}^{\infty} G_1 \left(1 + \frac{\left(x - 3\sqrt{E_b}\right)^2}{K\sigma^2}\right)^{-K-1} dx\right) \times \\
&\left(\int_{0}^{\infty} G_1 \left(1 + \frac{\left(y - \sqrt{E_b}\right)^2}{K\sigma^2}\right)^{-K-1} dy - \right. \\
&\qquad \left. \int_{2\sqrt{E_b}}^{\infty} G_1 \left(1 + \frac{\left(y - \sqrt{E_b}\right)^2}{K\sigma^2}\right)^{-K-1} dy\right) \\
&= 1 - \left(\int_{-\sqrt{\frac{2E_b}{G(K,\sigma)}}}^{\infty} G_2 \left(1 + \frac{x^2}{2K-1}\right)^{-K-1} dx\right) \times \\
&\left(\int_{-\sqrt{\frac{2E_b}{G(K,\sigma)}}}^{\infty} G_2 \left(1 + \frac{y^2}{2K-1}\right)^{-K-1} dy - \right. \\
&\qquad \left. \int_{\sqrt{\frac{2E_b}{G(K,\sigma)}}}^{\infty} G_2 \left(1 + \frac{y^2}{2K-1}\right)^{-K-1} dy\right) \\
&= 1 - \left[1 - L\left(\sqrt{\frac{2E_b}{G\left(K,\sigma\right)}}; K\right)\right] \times \\
&\left[1 - L\left(\sqrt{\frac{2E_b}{G\left(K,\sigma\right)}}; K\right) - L\left(\sqrt{\frac{2E_b}{G\left(K,\sigma\right)}}; K\right)\right] \\
&= 3L\left(\sqrt{\frac{2E_b}{G\left(K,\sigma\right)}}; K\right) - 2L^2\left(\sqrt{\frac{2E_b}{G\left(K,\sigma\right)}}; K\right)
\end{aligned} \tag{4.25}
$$

For type-C symbols, consider an example symbol $\left(3\sqrt{E_b}, 3\sqrt{E_b}\right)$ as shown in Figure 4.7. For that symbol, its ML decision is bounded by $x = 2\sqrt{E_b}$, $x = \infty$, $y = 2\sqrt{E_b}$, $y = \infty$. The corresponding symbol error probabilities are

$$\begin{aligned}
p_{SER,C} &= 1 - p_c \\
&= 1 - \left(\int_{2\sqrt{E_b}}^{\infty} G_1 \left(1 + \frac{\left(x - 3\sqrt{E_b}\right)^2}{K\sigma^2}\right)^{-K-1} dx\right) \times \\
&\left(\int_{2\sqrt{E_b}}^{\infty} G_1 \left(1 + \frac{\left(y - 3\sqrt{E_b}\right)^2}{K\sigma^2}\right)^{-K-1} dy\right) \\
&\left(\int_{-\sqrt{\frac{2E_b}{G(K,\sigma)}}}^{\infty} G_2 \left(1 + \frac{y^2 G\left(K,\sigma\right)}{2K\sigma^2}\right)^{-K-1} dy\right) \\
&= 1 - \left(\int_{-\sqrt{\frac{2E_b}{G(K,\sigma)}}}^{\infty} G_2 \left(1 + \frac{x^2}{2K-1}\right)^{-K-1} dx\right) \times \\
&\left(\int_{-\sqrt{\frac{2E_b}{G(K,\sigma)}}}^{\infty} G_2 \left(1 + \frac{y^2}{2K-1}\right)^{-K-1} dy\right) \\
&= 1 - \left[1 - L\left(\sqrt{\frac{2E_b}{G\left(K,\sigma\right)}}; K\right)\right] \times \left[1 - L\left(\sqrt{\frac{2E_b}{G\left(K,\sigma\right)}}; K\right)\right] \\
&= 2L\left(\sqrt{\frac{2E_b}{G\left(K,\sigma\right)}}; K\right) - L^2\left(\sqrt{\frac{2E_b}{G\left(K,\sigma\right)}}; K\right) \qquad (4.26)
\end{aligned}$$

Hence, the overall SER is

$$p_{SER,16QAM} = \frac{4}{16}p_{SER,A} + \frac{8}{16}p_{SER,B} + \frac{4}{16}p_{SER,C} \qquad (4.27)$$

4.5 Correlated Noise Demodulation

The general case of the galactic noise process contains non-flat power spectral density function, or in other words, non-impulse autocorrelation function. To deal with non-Gaussian correlated noise case, we look for a technique that allows us to decorrelate in a way just like Gaussian case. The tool developed by Yao [62] can be utilized to solve this case. If a random process can be categorized as a spherically-invariant random process(SIRP), then we can treat the decorrelation technique as though it were Gaussian. The only difference is that the kernal function is changed.

From [63], [64] and [65], a random real vector $\overrightarrow{\mathbf{x}} = [x_1, x_2, ..., x_n]$ with mean vector μ and covariance matrix $\mathbf{C}$ are sampled from SIRP if and only if the joint pdf has the following form:

$$f_n\left(\overrightarrow{\mathbf{x}}\right) = |\mathbf{C}|^{\frac{-1}{2}} (2\pi)^{\frac{-n}{2}} h_n\left[(\mathbf{x}-\mu)^T \mathbf{C}^{-1} (\mathbf{x}-\mu)\right] \tag{4.28}$$

h_n, which we name it to be the kernal function, satisfies the following condition:

$$h_n(q) = \int_0^\infty s^{-n} g(s)\, e^{-\frac{q}{2s^2}} ds, 0 < q < \infty \tag{4.29}$$

where $g(s)$ is some univariate pdf defined on $0 < s < \infty$, and we call it the auxillary pdf. This is called the SIRP representation theorem.

In [66], there is an equation that can be used to find the multivariate distribution from univariate characteristic function. If we can further find the auxillary pdf through (4.29), then according to the representation theorem, we can say that the random process is SIRP.

The kernal function of multivariate Kappa probability density function is shown [67] and [68] to be($b = \sqrt{K}\sigma$, $\nu = K-1$):

$$h_{n,Kappa}(q) = \frac{2^{\frac{n+3}{2}}\Gamma\left(K+\frac{n}{2}+\frac{1}{2}\right)}{\Gamma(K-1)\left(\sqrt{K}\sigma\right)^{n+3}}\left[1+\frac{q}{K\sigma^2}\right]^{-K-\frac{n}{2}-\frac{1}{2}} \tag{4.30}$$

The corresponding auxillary pdf [67] is:

$$g(s) = \frac{2\left(\sqrt{K}\sigma\right)^{2K-2}}{s^{2K-1}\Gamma(K-1)\,2^{K-1}} e^{-\frac{K\sigma^2}{s^2}}, 0 < s < \infty \tag{4.31}$$

Notice that in [67] and [68], Kappa pdf is termed as student-t distribution, which is different than the majority of literature in probability area such as [54]. Also, even though the auxillary pdf is given, there is no work as to how it is obtained. The following theorem shows that the galactic noise random process is indeed SIRP.

Theorem 4.5.1 *A random process with marginal pdf to be Kappa distribution, and with its multivariate distribution described in (4.30), belongs to spherically-invariant random process.*

Proof: By the representation theorem, it suffices for us to show that (4.31) is a valid pdf and it satisfies (4.29).

In [69], there is a formula for computing the related integral that will show up later.

$$\begin{aligned} &\int_0^\infty x^m e^{-\beta x^n} dx = \frac{\Gamma(\gamma)}{n\beta^\gamma} \\ &\gamma = \frac{m+1}{n}, \mathrm{Re}\{\beta\} > 0, \mathrm{Re}\{m\} > 0, \mathrm{Re}\{n\} > 0 \end{aligned} \tag{4.32}$$

So we get

$$\begin{aligned} &\int_0^\infty g(s)\, ds = \int_0^\infty \frac{2\left(K+\frac{1}{2}\right)^{K+\frac{1}{2}}}{s^{2K+2}} e^{-\frac{K+\frac{1}{2}}{s^2}} ds \\ &= \frac{2\left(K+\frac{1}{2}\right)^{K+\frac{1}{2}}}{\Gamma\left(K+\frac{1}{2}\right)} \int_0^\infty \frac{1}{s^{2K+2}} e^{-\frac{K+\frac{1}{2}}{s^2}} ds \\ &= \frac{2\left(K+\frac{1}{2}\right)^{K+\frac{1}{2}}}{\Gamma\left(K+\frac{1}{2}\right)} \int_0^\infty u^{2K} e^{-u^2\left(K+\frac{1}{2}\right)} du \qquad (\text{Let} \quad u = \frac{1}{s}) \\ &= \frac{2\left(K+\frac{1}{2}\right)^{K+\frac{1}{2}}}{\Gamma\left(K+\frac{1}{2}\right)} \frac{\Gamma\left(K+\frac{1}{2}\right)}{2\left(K+\frac{1}{2}\right)^{K+\frac{1}{2}}} \qquad (\text{By} \quad (4.32)) \\ &= 1 \end{aligned} \tag{4.33}$$

Now that $g(s)$ is a valid pdf, we proceed to show it satisfies (4.29).

$$
\begin{aligned}
&\int_0^\infty \frac{\frac{2\left(K+\frac{1}{2}\right)^{K+\frac{1}{2}}}{s^{2K+2}} e^{-\frac{K+\frac{1}{2}}{s^2}}}{s^n} e^{-\frac{q}{2s^2}} ds \\
&= \frac{2\left(K+\frac{1}{2}\right)^{K+\frac{1}{2}}}{\Gamma\left(K+\frac{1}{2}\right)} \int_0^\infty \frac{1}{s^{2K+2+n}} e^{-\frac{1}{s^2}\left[\frac{q}{2}+\left(K+\frac{1}{2}\right)\right]} ds \\
&= \frac{2\left(K+\frac{1}{2}\right)^{K+\frac{1}{2}}}{\Gamma\left(K+\frac{1}{2}\right)} \int_0^\infty u^{2K+n} e^{-u^2\left[\frac{q}{2}+\left(K+\frac{1}{2}\right)\right]} du \qquad (\text{Let} \quad u = \frac{1}{s}) \\
&= \frac{2\left(K+\frac{1}{2}\right)^{K+\frac{1}{2}}}{\Gamma\left(K+\frac{1}{2}\right)} \frac{\Gamma\left(K+\frac{n+1}{2}\right)}{2\left[\frac{q}{2}+\left(K+\frac{1}{2}\right)\right]^{K+\frac{n+1}{2}}} \qquad (\text{By} \quad (4.32)) \\
&= h_{n,Kappa}(q) \qquad (\text{By} \quad (4.3))
\end{aligned}
\tag{4.34}
$$

Thus we get the proof.

Q.E.D.

Theoretcially, when the channel noise samples are correlated with a fixed correlation matrix, we could perform decorrelation through correlation matrix inversion to whiten the noise. However, in practice, perfect decorrelation for the entire received bit sequence is impossible. This is because fixed size decorrelation matrix cannot deal with consecutive block of bits, and the size of the decorrelation matrix is smaller than the entire length of the received bit sequence.

We seek a suboptimal solution for this problem. The solution that is used in this work is to consider block decorrelation. We devide the received bits into contiguous blocks of bits. Within each block, we first apply decorrelation with matrix inversion and then apply maximum likelihood detection. The reason is to acknowledge the fact that the computation time of maximum likelihood detection grows exponentially as the length of each block increases linearly.

4.6 Simulation Results

In this section, we perform simulations on 2 particular data sets. The first data set has $K = 1.6$ and $\sigma = 66$, which resembles early sunrise as well as the state close to thermal anti-equilibrium. The second data set has $K = 2.8$ and $\sigma = 12.5$, which resembles sunrise as well as the state in between thermal equilibrium and thermal anti-equilibrium. Figure 4.8 and 4.9 gives the simulation and theoretical results for the first and second data set for uncorrelated noise respectively.

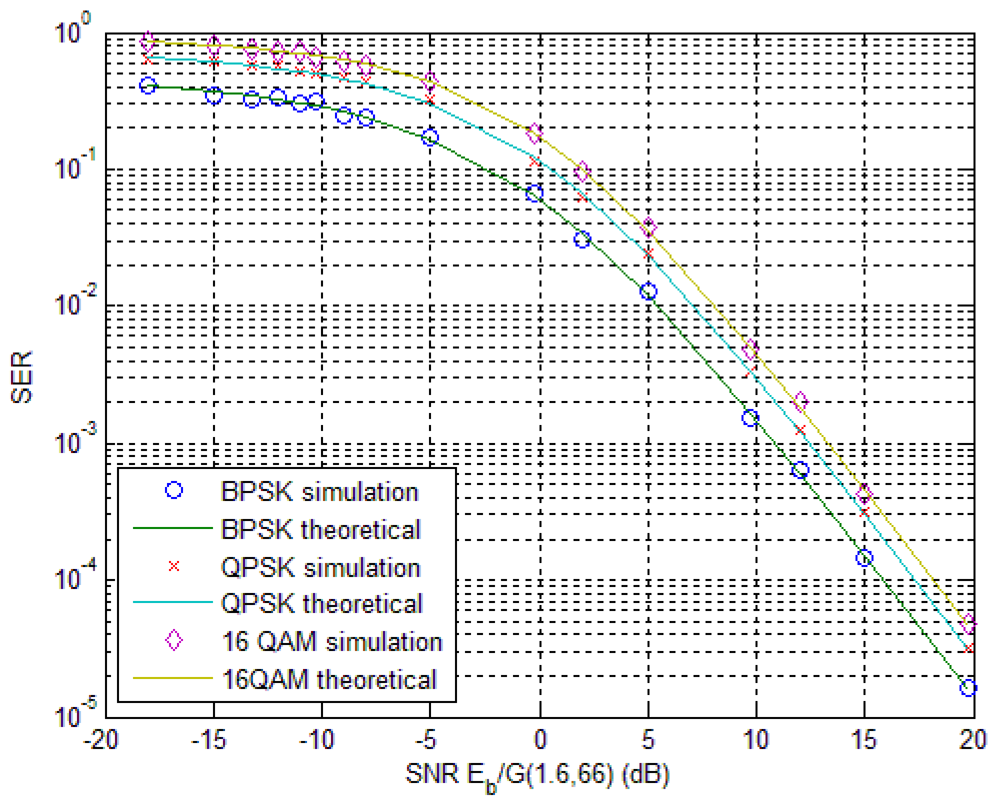

Fig. 4.8. The BER result of uncorrelated noise for the set K = 1.6, $\sigma = 66$.

To describe the correlated channel. We use the autocorrelation matrix $\mathbf{C_1}$ and $\mathbf{C_2}$ for the first and the second data set respectively. They are shown in (4.35) and (4.36). The simulation result is shown in Figure 4.10 and 4.11 for the first and second data set respectively.

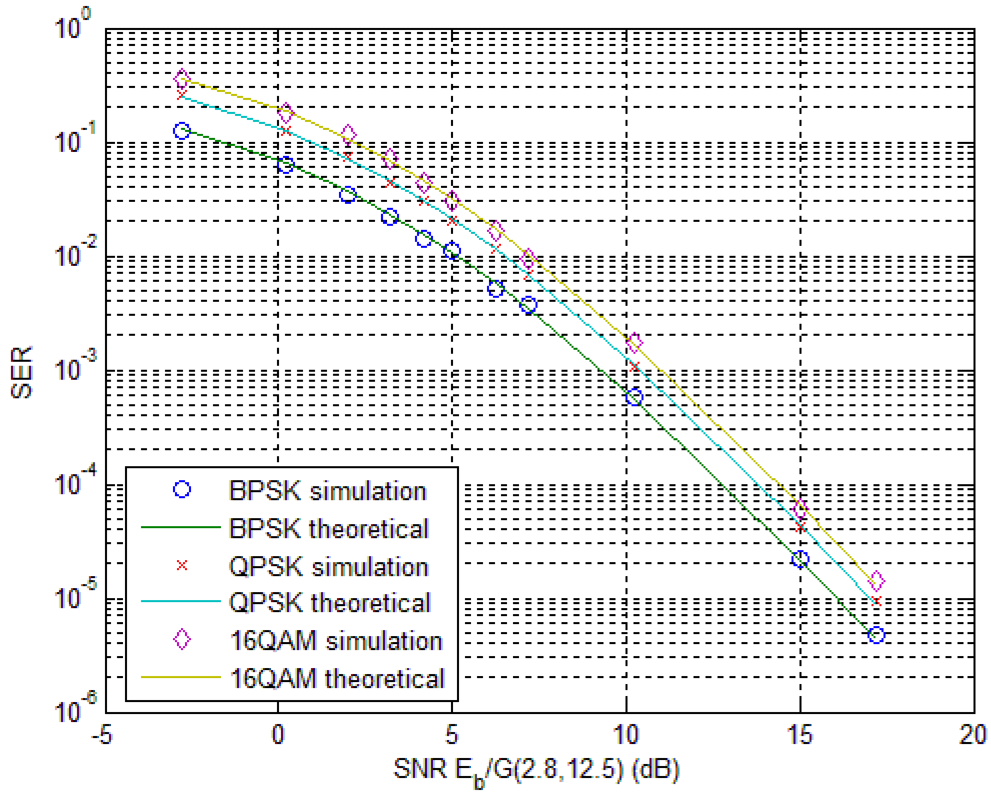

Fig. 4.9. The BER result of uncorrelated noise for the set K = 2.8, σ = 12.5.

$$\mathbf{C_1} = \begin{bmatrix} 3021 & 1984 & 408.9 & 0 & 0 \\ 1984 & 3021 & 1984 & 408.9 & 0 \\ 408.9 & 1984 & 3021 & 1984 & 408.9 \\ 0 & 408.9 & 1984 & 3021 & 1984 \\ 0 & 0 & 408.9 & 1984 & 3021 \end{bmatrix} \tag{4.35}$$

$$\mathbf{C_2} = \begin{bmatrix} 95.1085 & 62.4518 & 12.8718 & 0 & 0 \\ 62.4518 & 95.1085 & 62.4518 & 12.8718 & 0 \\ 12.8718 & 62.4518 & 95.1085 & 62.4518 & 12.8718 \\ 0 & 12.8718 & 62.4518 & 95.1085 & 62.4518 \\ 0 & 0 & 12.8718 & 62.4518 & 95.1085 \end{bmatrix} \tag{4.36}$$

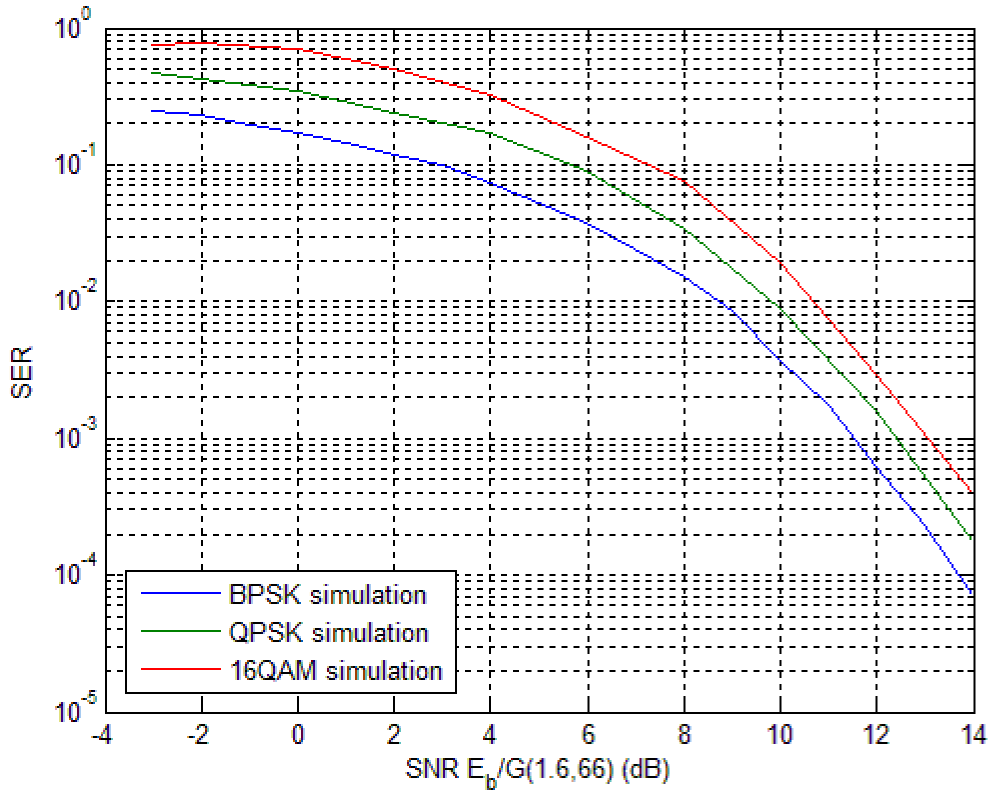

Fig. 4.10. The BER result of correlated noise for the set K = 1.6, σ = 66.

4.7 Conclusion

The ionosphere of the Earth changes daily with a certain pattern. In the past, researchers have modeled the noise as AWGN. However, before sunrise and well after sunrise, the ionosphere behaves differently than during the daytime. Hence, one would expect a different pattern of noise distribution. This was indeed observed by Geisbrecht at a quiet location. It is in this situation that we analyze in order to obtain the BER.

The modified Bi-Kappa distribution does not have finite variance for certain range of K. So Kappa distribution is used instead to gurantee finite variance for all measured data. We analyzed the system performance base on this. Not only did we study the uncorrelated case, but also the correlated case.

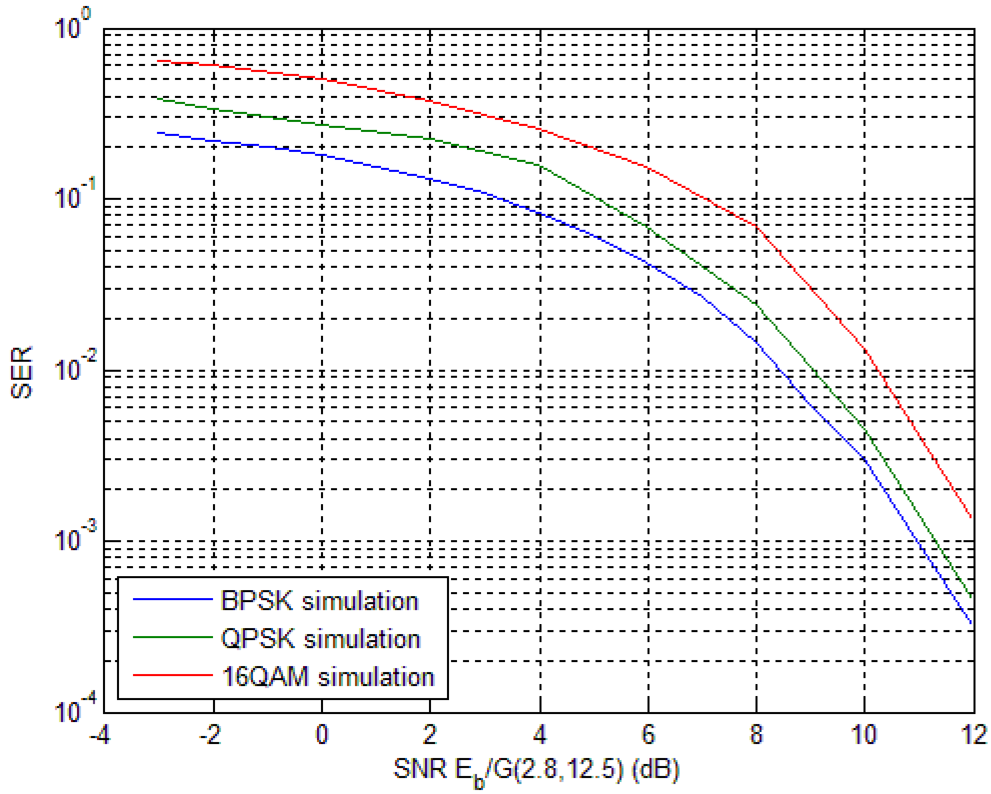

Fig. 4.11. The BER result of correlated noise for the set K = 2.8, σ = 12.5.

Our results can be readily applied to future research work for this channel. The L function will become useful just like Q function for AWGN.

We would like to see more observation results not only around sunrise, but also around midnight at quiet locations because the ionosphere distribution at that particular quiet time is different from the daytime. The location of the observation might play another important role because the ionosphere behaves differently across latitude. We propose a modified channel description for this particular scenario for radio communications.

5. PERFORMANCE ANALYSIS FOR MIMO HF COMMUNICATIONS AROUND SUNRISE

The high frequency (HF) channel provides a long distance communication link. Here, we investigate some possible techniques that enable multiple-input multiple-output (MIMO) communication at HF, namely, techniques to use multimode and polarization. We then focus on the scenario of MIMO HF communications around sunrise. At sunrise, the noise can be modeled as Kappa random process. The system performance with different cases of MIMO HF communications is discussed. We look at the uncorrelated channel case, the correlated channel case due to imperfect antennae spacing and due to polarization effects. Asymptotic bounds for packet error rate (PER) is derived and proved.

5.1 Introduction

The ionosphere of the Earth has the capability of reflecting incident electromagnetic (EM) wave at certain frequency depending on the ion density. HF communication link is established by transmitting electromagnetic wave to the ionosphere of the Earth, and then reach the destination antenna through reflection by the ionosphere.

The HF communication frequency range lies in the range of 3   30 MHz. Even though this mean slower data rate compared with civilian wireless communication systems such as LTE-a, HF communication has the advantage of covering much wider area. A single reflection from the ionosphere can reach as long as 1/5 of the Earth's circumference [7]. Furthermore, in the scenario where civilian communication link cannot be established(due to for example, natural disaster or war), HF communication becomes more important. It is always beneficial to enhance the HF communication whenever we can.

In recent years, with the advance of the MIMO technology [70], the HF communication gains the possibility of increasing data rate by using it. [71] and [72] have sucessfully established MIMO HF communication systems with data rates increased by a factor more than 2. Such research is still ongoing and we expect more results show up in the future.

All existing research consider the channel noise to be additive white Gaussian noise (AWGN). While it is true in most cases, at sunrise, this may not hold. [17] clearly showed that at sunrise, the measured noise probability density function (pdf) is not Gaussian. By using recent physics results, we concluded that the noise has Kappa distribution [49]. When the time shifts toward day time, the noise pdf shifts to Gaussian distribution. Learning the right noise pdf allows communication engineers to design a better system.

This work is organized as follows. In Section 5.2, we discuss how MIMO HF can be achieved . In Section 5.3, we show the MIMO channel model in the surise scenario. In Section 5.4, we introduce tools that are useful to analyze system performance. In Section 5.5, we derive a bound for the bit error rate (BER) for the 1x1 case and show that the bound is asymptotically tight. In Section 5.6, we find the BER for the MIMO uncorrelated channel. In Section 5.7 and Section 5.8, we find the BER for the MIMO correlated channel that is caused by imperfect antennae spacing and polarization factor respectively. In Section 5.9, we show our simulation results in the varios scenario mentioned in the previous sections. We make conclusions in Section 5.10.

5.2 MIMO for HF

There exist many modes of electromagnetic wave propagation in the HF scenario. For example, at a certain frequency f_1, an electromagnetic wave can be transmitted to the F2 layer of the ionosphere, gets reflected by the F2 layer, and then reaches the destination (this mode is termed as 1F2). At another frequency f_2, an electromagnetic wave can reach the destination via 2 reflections at the F1 layer and 1 reflection at the ground (this mode is termed as 2F1). Figure 5.1 illustrates an example of multimode transmission. Works by Gunashekar [73] have demonstrated the ability to effectively use multimode transmission at HF.

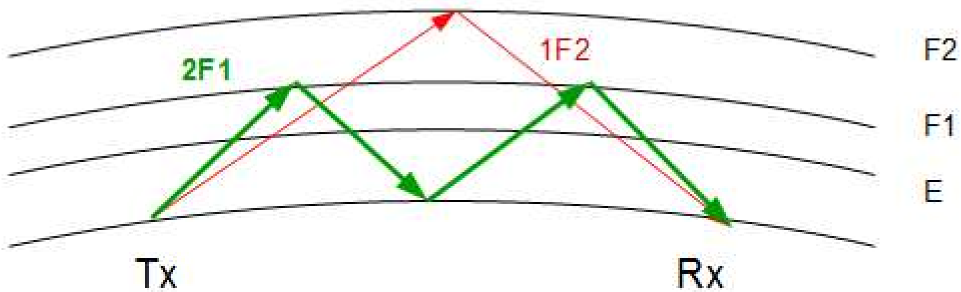

Fig. 5.1. Multimode transmission in HF.

For each mode of transmission at HF, there exist 2 additional modes associated with it. They are characterized by the polarization of the electromagnetic wave. One is called the ordinary wave (○) and another is called the extraordinary wave (X). Figure 5.2 shows an example of 1F2 transmission with the 2 polarization modes. Ndao [74] et. al. have successfully conducted such transmissions.

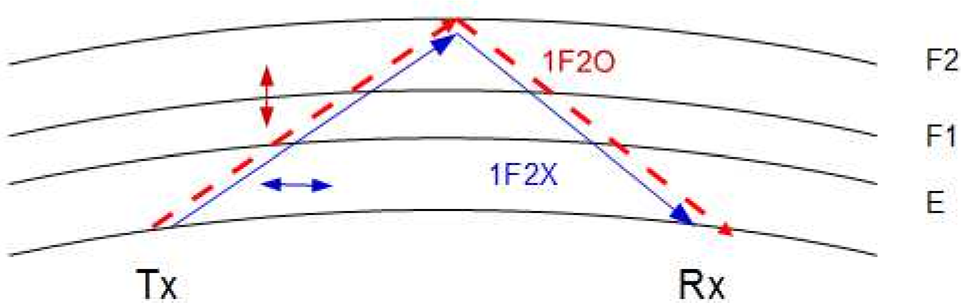

Fig. 5.2. Polarization transmission diversity in HF.

Those 2 dimensions can be combined to achieve a large dimension for communications. In fact, the previously cited two groups of researchers also have joint research [75] in this area. It is possible to achieve a higher capacity by clearly distinguishing the different modes of transmission.

5.3 System Model

By combining the results from the previous section, we formulate the system model for the MIMO HF channel around sunrise as follows:

$$\mathbf{y} = \mathbf{H}\mathbf{x} + \mathbf{n}, \tag{5.1}$$

where $\mathbf{y}$ is the received vector; $\mathbf{H}$ is the fading channel matrix, with each element h_{ij} having complex normal distribution CN(0,1), $\mathbf{x}$ is the input symbol vector, and $\mathbf{n}$ is the noise vector, with each element n_i being i.i.d. and having the complex Kappa distribution as shown below.

$$\begin{aligned} & n_i = n_{i1} + n_{i2}j \\ & n_{i1}, n_{i2} \sim f_X(x; K, \sigma) = \\ & \frac{1}{\sqrt{K}\sigma\beta\left(\frac{1}{2}, K + \frac{1}{2}\right)} \left(1 + \frac{x^2}{K\sigma^2}\right)^{-K-1}, \\ & -\infty < x < \infty, K > \frac{1}{2} \end{aligned} \tag{5.2}$$

In parallel with the signal-to-noise ratio (SNR) definition in AWGN, the SNR for Kappa noise is defined as

$$SNR \equiv \frac{E_b}{\frac{K\sigma^2}{K-\frac{1}{2}}} \tag{5.3}$$

where E_b is the energy per bit.

We are interested in using a maximum likelihood receiver to detect the transmitted symbol vector. The operation is described in Equation 5.4.

$$\hat{x} = \min_{x_i \in \{\mathbf{x}\}} \left\|\mathbf{y} - \mathbf{H}\mathbf{x}\right\|_2, \tag{5.4}$$

where $\{\mathbf{x_i}\}$ is the set of all possible symbols that can be transmitted. In this paper, we focus on the case when the symbols come from binary phase shift keying (BPSK) modulation. Each element in the symbol vector has equal probability to be $\sqrt{E_b}$ or $-\sqrt{E_b}$.

5.4 Asymptotic Behavior for High SNR

Following our previous work [57], we anticipate dealing with a term like $\mathrm{E}_{\mathrm{Y}}\left[L\left(\sqrt{\alpha SNR\left\|Y\right\|^2};K\right)\right]$, where

$$\begin{aligned}&L\left(x;K\right)\equiv\\&\int_x^{\infty}\frac{1}{\sqrt{2K-1}\beta\left(\frac{1}{2},K+\frac{1}{2}\right)}\left(1+\frac{t^2}{2K-1}\right)^{-K-1}dt,\\&-\infty<x<\infty,K>\frac{1}{2}\end{aligned}\tag{5.5}$$

is utilized in place of the Q function that is used for the AWGN channel. Y is a certain random variable that depends on the fading channel and the dimension of the input vector.

We use K(0,A) to abbreviate complex Kappa distribution having 0 mean and A as the variance. For brevity, we define

$$\eta_2\equiv\frac{1}{\sqrt{2K-1}\beta\left(\frac{1}{2},K+\frac{1}{2}\right)}\tag{5.6}$$

and

$$\eta_3\equiv\frac{1}{2K-1}.\tag{5.7}$$

Further simplification of the L function is possible, but only to some extent. We are especially interested in the case when the SNR is high. We notice that, for $x\neq 1$, $\frac{1}{1+x}<\frac{1}{x}$.Thus,

$$L(x;K) \le \int_x^\infty \frac{\eta_2}{{\eta_3}^K t^{2K+2}} dt$$
$$= \frac{\eta_2}{{\eta_3}^{K+1}} \times \frac{1}{2K+1} \times x^{-2K-1} \tag{5.8}$$

This is the high SNR approximation for the 1x1 channel (by substituting x with $\sqrt{SNR}$). Before we solve the MIMO problem, we need to solve its 1x1 version first. This is because the solution to the MIMO case requires the result from the 1x1 case.

5.5 BER for the 1x1 Fading Channel

In this part, the mathematical formulation is

$$y = hx + n \tag{5.9}$$

with every variable having the same distribution as described in Section 5.3. That is, $h \sim$ CN(0,1), and $n \sim$ K(0,$\frac{2K\sigma^2}{2K-1}$). Also, x = $\sqrt{E_b}$ or $-\sqrt{E_b}$ with equal probability. Given maximum likelihood detection, the Euclidean distance between the two possible symbol is $2\sqrt{E_b} \cdot |h|^2$. Given X = $|h|^2$, then X is a random variable with distribution as follows:

$$f_X(x) = e^{-x}, 0 \le x < \infty. \tag{5.10}$$

Hence, the bit error rate, p_e is

$$p_e = E_{\mathbf{X}}\left[L\left(\sqrt{SNR \cdot X}; K\right)\right]$$
$$= \int_0^\infty \int_{\sqrt{2SNR \cdot x}}^\infty \frac{\eta_2 e^{-x}}{(1+\eta_3 t^2)^{K+1}} dt dx \tag{5.11}$$

The last expression can be broken down to two parts from separation of the range of the integral.

$$\int_0^\infty \int_{\sqrt{2SNR\cdot x}}^\infty \frac{\eta_2 e^{-x}}{(1+\eta_3 t^2)^{K+1}} dtdx = \int_0^\gamma \int_{\sqrt{2SNR\cdot x}}^\infty \frac{\eta_2 e^{-x}}{(1+\eta_3 t^2)^{K+1}} dtdx \tag{5.12}$$

$$+ \int_\gamma^\infty \int_{\sqrt{2SNR\cdot x}}^\infty \frac{\eta_2 e^{-x}}{(1+\eta_3 t^2)^{K+1}} dtdx, \tag{5.13}$$

$$0 < \gamma < \infty.$$

Equation (5.13) can be bounded via Equation (5.8) to the expression given by:

$$\int_\gamma^\infty \int_{\sqrt{2SNR\cdot x}}^\infty \frac{\eta_2 e^{-x}}{(1+\eta_3 t^2)^{K+1}} dtdx \leq \int_\gamma^\infty \int_{\sqrt{2SNR\cdot x}}^\infty \frac{\eta_2 e^{-x}}{{\eta_3}^{K+1} t^{2K+2}} dtdx \tag{5.14}$$

Further simplification on the above expression gives

$$\int_\gamma^\infty \int_{\sqrt{2SNR\cdot x}}^\infty \frac{\eta_2 e^{-x}}{{\eta_3}^{K+1} t^{2K+2}} dtdx = \int_\gamma^\infty \frac{\eta_2 e^{-x}}{{\eta_3}^{K+1}} \cdot \frac{1}{2K+1} \cdot (2SNR)^{\frac{-2K-1}{2}} x^{\frac{-2K-1}{2}} dx \tag{5.15}$$

By changing the order of integration(see Figure 5.3), Equation (5.12) can be simplified to the expression given by:

$$\int_0^\gamma \int_{\sqrt{2SNR\cdot x}}^\infty \frac{\eta_2 e^{-x}}{(1+\eta_3 t^2)^{K+1}} dtdx = Area\ I + Area\ II$$

$$= \int_0^{\sqrt{2SNR\cdot\gamma}} \int_0^{\frac{t^2}{2SNR}} \frac{\eta_2 e^{-x}}{(1+\eta_3 t^2)^{K+1}} dxdt \tag{5.16}$$

$$+ \int_{\sqrt{2SNR\cdot\gamma}}^\infty \int_0^\gamma \frac{\eta_2 e^{-x}}{(1+\eta_3 t^2)^{K+1}} dxdt \tag{5.17}$$

Equation (5.17) can be simplified:

$$\int_{\sqrt{2SNR\cdot\gamma}}^\infty \int_0^\gamma \frac{\eta_2 e^{-x}}{(1+\eta_3 t^2)^{K+1}} dxdt = \int_{\sqrt{2SNR\cdot\gamma}}^\infty \frac{\eta_2 \left(1-e^{-\gamma}\right)}{(1+\eta_3 t^2)^{K+1}} dt \tag{5.18}$$

The above expression can be bounded via Equation (5.8) by

$$\int_{\sqrt{2SNR\cdot\gamma}}^\infty \frac{\eta_2 \left(1-e^{-\gamma}\right)}{(1+\eta_3 t^2)^{K+1}} dt \leq \int_{\sqrt{2SNR\cdot\gamma}}^\infty \frac{\eta_2 \left(1-e^{-\gamma}\right)}{{\eta_3}^{K+1} t^{2K+2}} dt \tag{5.19}$$

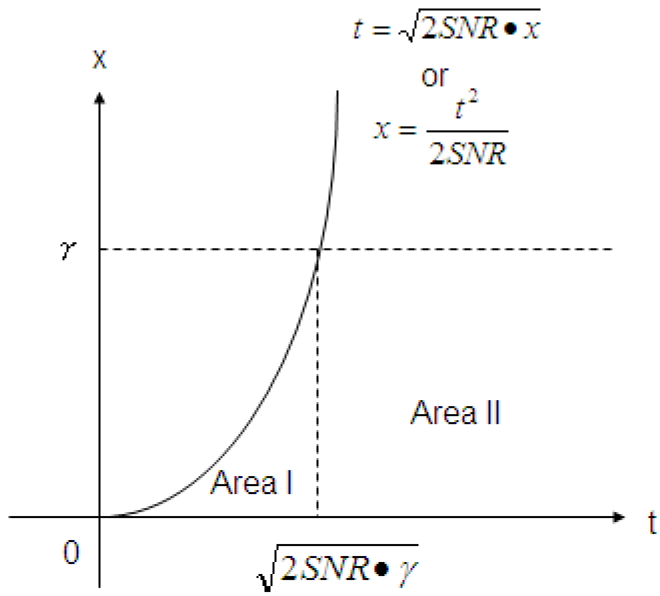

Fig. 5.3. Change of integral for Equation (5.12).

Further simplification on the above expression gives

$$\int_{\sqrt{2SNR\cdot\gamma}}^{\infty} \frac{\eta_2 \left(1 - e^{-\gamma}\right)}{{\eta_3}^{K+1} t^{2K+2}} dt = \frac{\eta_2 \left(1 - e^{-\gamma}\right)}{{\eta_3}^{K+1}} \cdot \frac{1}{2K+1} \cdot (2SNR)^{\frac{-2K-1}{2}} \gamma^{\frac{-2K-1}{2}} \tag{5.20}$$

Equation (5.16) becomes

$$\int_0^{\sqrt{2SNR\cdot\gamma}} \int_0^{\frac{t^2}{2SNR}} \frac{\eta_2 e^{-x}}{\left(1+\eta_3 t^2\right)^{K+1}} dx dt = \int_0^{\sqrt{2SNR\cdot\gamma}} \frac{\eta_2 \left(1 - e^{-\frac{t^2}{2SNR}}\right)}{\left(1+\eta_3 t^2\right)^{K+1}} dt \tag{5.21}$$

We notice that, for all x,

$$1 - e^{-x} \le x \tag{5.22}$$

Hence, Equation (5.21) can be bounded via Equation (5.22) by

$$\int_0^{\sqrt{2SNR\cdot\gamma}} \frac{\eta_2 \left(1 - e^{-\frac{t^2}{2SNR}}\right)}{\left(1+\eta_3 t^2\right)^{K+1}} dt \le \int_0^{\sqrt{2SNR\cdot\gamma}} \frac{\eta_2 t^2}{2SNR \cdot \left(1+\eta_3 t^2\right)^{K+1}} dt \tag{5.23}$$

By separating the range of the integral, we obtain the following expression

$$\int_0^{\sqrt{2SNR\cdot\gamma}} \frac{\eta_2 t^2}{2SNR\cdot(1+\eta_3 t^2)^{K+1}}dt = \int_0^{\delta} \frac{\eta_2 t^2}{2SNR\cdot(1+\eta_3 t^2)^{K+1}}dt \tag{5.24}$$

$$+\int_{\delta}^{\sqrt{2SNR\cdot\gamma}} \frac{\eta_2 t^2}{2SNR\cdot(1+\eta_3 t^2)^{K+1}}dt, \tag{5.25}$$

$$0<\delta<\sqrt{2SNR\cdot\gamma}$$

Equation (5.25) can be bounded via Equation (5.8) in a manner given by

$$\int_{\delta}^{\sqrt{2SNR\cdot\gamma}} \frac{\eta_2 t^2}{2SNR\cdot(1+\eta_3 t^2)^{K+1}}dt \le \int_{\delta}^{\sqrt{2SNR\cdot\gamma}} \frac{\eta_2 t^2}{2SNR\cdot{\eta_3}^{K+1}t^{2K+2}}dt \tag{5.26}$$

Further simplification gives the following expression

$$\int_{\delta}^{\sqrt{2SNR\cdot\gamma}} \frac{\eta_2 t^2}{2SNR\cdot{\eta_3}^{K+1}t^{2K+2}}dt = \frac{\eta_2}{{\eta_3}^{K+1}}\cdot\frac{1}{2SNR}\cdot\frac{1}{2K-1}\cdot \left[\delta^{-2K+1}-(2SNR)^{\frac{-2K+1}{2}}\gamma^{\frac{-2K+1}{2}}\right] \tag{5.27}$$

Hence, the sum of Equation (5.15), (5.20), (5.24), and (5.27) gives an upper bound of the BER. Figure 5.4 shows the effectiveness of this bound.

There are two types of bounds that are used in this work. One is mentioned above, another is very similar to the method mentioned above, the only difference is that we stop at Equation (5.21) and does no further bounding. If Equation (5.21) can be bounded, then we use the first method. If not, then we use the second method.

The two bounds constructed in this section is asymptotically tight. This is shown as follows.

Theorem 5.5.1 *The following two bounds for (5.11) are asymptotically tight:*

1. (5.11) $\le$ (5.15) + (5.20) + (5.24)+ (5.27)

2. (5.11) $\le$ (5.15) + (5.20) + (5.21)

Proof: Let A = (5.15), B = (5.20), $C_0 = \int_0^{\delta} \frac{\eta_2\left(1-e^{-\frac{t^2}{2SNR}}\right)}{(1+\eta_3 t^2)^{K+1}}dt$, C = (5.24), $D_0 = \int_{\delta}^{\sqrt{2SNR\cdot\gamma}} \frac{\eta_2\left(1-e^{-\frac{t^2}{2SNR}}\right)}{(1+\eta_3 t^2)^{K+1}}dt$, D = (5.27), E = (5.21).

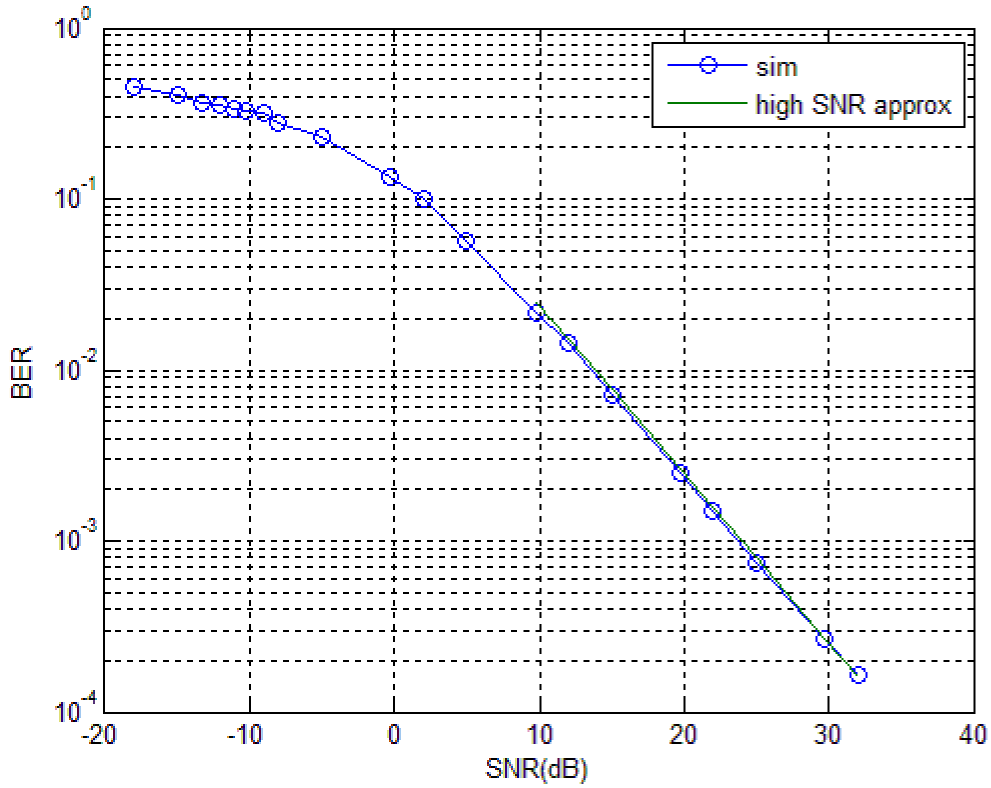

Fig. 5.4. BER for the set K = 1.6, σ = 66 and 1x1 Rayleigh fading. The approximation curve is plotted with $\gamma = 1$ and $\delta = 5$ for all SNR.

1. From $|X+Y| \leq |X| + |Y|$, we have

$$\lim_{SNR\to\infty} |(5.11) - (\mathrm{A}+\mathrm{B}+\mathrm{C}+\mathrm{D})|$$

$$= \lim_{SNR\to\infty} |[(5.13) - \mathrm{A}] + [(5.18) - \mathrm{B}] + [\mathrm{C}_0 - \mathrm{C}] + [\mathrm{D}_0 - \mathrm{D}]|$$

$$\leq \lim_{SNR\to\infty} |(5.13) - \mathrm{A}| + \tag{5.28}$$

$$\lim_{SNR\to\infty} |(5.18) - \mathrm{B}| + \tag{5.29}$$

$$\lim_{SNR\to\infty} |\mathrm{C}_0 - \mathrm{C}| + \tag{5.30}$$

$$\lim_{SNR\to\infty} |\mathrm{D}_0 - \mathrm{D}| \tag{5.31}$$

For (5.28), it suffices to show

$$\lim_{SNR\to\infty} |(5.13) - (5.14)| = 0$$

This is indeed true because

$$\begin{aligned}
&\lim_{SNR\to\infty} |(5.13) - (5.14)| \\
&= \lim_{SNR\to\infty} |\int_{\gamma}^{\infty}\int_{\sqrt{2SNR\cdot x}}^{\infty} \frac{\eta_2 e^{-x}}{(1+\eta_3 t^2)^{K+1}} dtdx - \int_{\gamma}^{\infty}\int_{\sqrt{2SNR\cdot x}}^{\infty} \frac{\eta_2 e^{-x}}{{\eta_3}^{K+1} t^{2K+2}} dtdx| \\
&= \lim_{SNR\to\infty} |\int_{\gamma}^{\infty}\int_{\sqrt{2SNR\cdot x}}^{\infty} \eta_2 e^{-x} \frac{1}{(1+\eta_3 t^2)^{K+1}} - \frac{1}{{\eta_3}^{K+1} t^{2K+2}} dtdx| \\
&\leq \lim_{SNR\to\infty} \int_{\gamma}^{\infty}\int_{\sqrt{2SNR\cdot x}}^{\infty} \eta_2 e^{-x} |\frac{1}{(1+\eta_3 t^2)^{K+1}} - \frac{1}{{\eta_3}^{K+1} t^{2K+2}}| dtdx \\
&= \lim_{SNR\to\infty} \int_{\gamma}^{\infty}\int_{\sqrt{2SNR\cdot x}}^{\infty} \eta_2 e^{-x} |\frac{{\eta_3}^{K+1} t^{2K+2} - (1+\eta_3 t^2)^{K+1}}{(1+\eta_3 t^2)^{K+1} ({\eta_3}^{K+1} t^{2K+2})}| dtdx \\
&= 0
\end{aligned} \tag{5.32}$$

For (5.29), it suffices to show

$$\lim_{SNR\to\infty} |(5.18) - (5.19)| = 0$$

The way to prove it is similar to (5.32).

For (5.30),

$$\begin{aligned}
&\lim_{SNR\to\infty} |\mathrm{C}_0 - \mathrm{C}| \\
&= \lim_{SNR\to\infty} |\int_0^{\delta} \frac{\eta_2}{(1+\eta_3 t^2)^{K+1}} \left(1 - e^{-\frac{t^2}{2SNR}} - \frac{t^2}{2SNR}\right) dt| \\
&\leq \lim_{SNR\to\infty} \int_0^{\delta} \frac{\eta_2}{(1+\eta_3 t^2)^{K+1}} |\left(1 - e^{-\frac{t^2}{2SNR}} - \frac{t^2}{2SNR}\right)| dt \\
&= \int_0^{\delta} \frac{\eta_2}{(1+\eta_3 t^2)^{K+1}} |1 - 1 - 0| dt \\
&= 0
\end{aligned} \tag{5.33}$$

For (5.31), let $\mathrm{D}_1 = (5.25)$, then

$$\begin{aligned}
&\lim_{SNR\to\infty} |\mathrm{D}_0 - \mathrm{D}| \\
&= \lim_{SNR\to\infty} |\mathrm{D}_0 - \mathrm{D}_1 + \mathrm{D}_1 - \mathrm{D}| \\
&\leq \lim_{SNR\to\infty} |\mathrm{D}_0 - \mathrm{D}_1| + \lim_{SNR\to\infty} |\mathrm{D}_1 - \mathrm{D}|
\end{aligned}$$

The proof to the first part is very similar to (5.33), and the proof to the second part is very similar to (5.32). Hence, we get the proof.

2.

$$\begin{aligned}
&\lim_{SNR\to\infty} |(5.11) - (\mathrm{A} + \mathrm{B} + \mathrm{E})| \\
&= \lim_{SNR\to\infty} |[(5.13) - \mathrm{A}] + [(5.18) - \mathrm{B}] + [(5.21) - \mathrm{E}]| \\
&\leq \lim_{SNR\to\infty} |(5.13) - \mathrm{A}| + \lim_{SNR\to\infty} |(5.18) - \mathrm{B}| + 0
\end{aligned} \tag{5.34}$$

We have already established the first two parts in 1. Hence, we get the proof. Q.E.D.

5.6 BER for the Uncorrelated Channel

In Equation (5.1), suppose that each element of $\mathbf{x}$ is a BPSK symbol. Each element takes on the value $\pm\sqrt{E_b}$ with equal probability. We consider finding the pairwise bit error probability first. Suppose a particular bit pattern $\mathbf{x_A}$ is transmitted, and a decision between $\mathbf{x_A}$ or another candidate bit pattern $\mathbf{x_B}$ is to be made. The probability of incorrectly deciding the received signal $\mathbf{y}$ to be $\mathbf{x_B}$ is denoted by P_{AB}. The pairwise bit error probability can be found as follows:

$$P_{AB} = E_{\mathbf{H}}\left[L\left(\sqrt{\frac{\left\|\mathbf{H}\left(\mathbf{x_A}-\mathbf{x_B}\right)\right\|_2^2}{4\times\frac{K\sigma^2}{2K-1}}};K\right)\right] \tag{5.35}$$

$$= E_{\mathbf{H}}\left[L\left(\sqrt{\frac{E_b\left\|\mathbf{H}\left(\mathbf{x}'_\mathbf{A}-\mathbf{x}'_\mathbf{B}\right)\right\|_2^2}{4N_T\times\frac{K\sigma^2}{2K-1}}};K\right)\right] \tag{5.36}$$

$$= E_{\mathbf{H}}\left[L\left(\sqrt{\frac{2SNR\left\|\mathbf{H}\left(\mathbf{x}'_\mathbf{A}-\mathbf{x}'_\mathbf{B}\right)\right\|_2^2}{4N_T}};K\right)\right], \tag{5.37}$$

where the vectors are given by $\mathbf{x_A} = \sqrt{\frac{E_b}{N_T}}\mathbf{x}'_\mathbf{A}$ and $\mathbf{x_B} = \sqrt{\frac{E_b}{N_T}}\mathbf{x}'_\mathbf{B}$ respectively. The vectors $\mathbf{x}'_\mathbf{A}$ and $\mathbf{x}'_\mathbf{B}$ are the normalized transmission symbol vectors, which are defined so that when $\pm\sqrt{E_b}$ is transmitted for an element, it becomes ± 1 in the normalized version.

Let $\mathbf{d} = \mathbf{x}'_\mathbf{A} - \mathbf{x}'_\mathbf{B}$. Then, each element of $\mathbf{Hd}$ is complex normal distributed, having zero mean and variance $\sum_{k=1}^{n_t} |d_k|^2$. Let $\mathbf{z} = \mathbf{Hd}$. The distribution of $\mathbf{w} \equiv \|\mathbf{z}\|_2^2$ can be found according to the dimension of $\mathbf{z}$ and the actual value of $\mathbf{z}$. Equation (5.37) can be further simplified to

$$E_{\mathbf{W}}\left[L\left(\sqrt{\frac{2SNR\cdot\mathbf{w}}{4N_T}};K\right)\right]. \tag{5.38}$$

We follow the same upper bounding procedure as described in the previous section, except that for accuracy reasons, we only use the sum of (5.15), (5.20), and (5.16) for the upper bound. Notice that due to the different dimensions involved in this case, some of the terms in (5.15), (5.20), and (5.16) need to be adjusted according to (5.38).

We then use the union bound to calculate the overall packet error rate(PER).

$$P_e = \sum_{i=1}^{2^{N_t}} \sum_{j=1, j\neq i}^{2^{N_t}-1} P\left(\mathbf{x_i}\rightarrow\mathbf{x_j}|\mathbf{x_i}\right) P\left(\{\mathbf{x_i}\text{ is sent}\}\right) = P_{i,j} \tag{5.39}$$

The BER is bounded by the following expression [76]

$$P_b \leq \frac{1}{|C|^{N_t}} \sum_{i=1}^{|C|^{N_t}} \sum_{j=1, j \neq i}^{|C|^{N_t}} w^{(i,j)} P_{i,j}, \tag{5.40}$$

where $|C|$ is the size of modulation alphabet and $w^{(i,j)} = \frac{e_b^{(i,j)}}{N_t log(|C|)}$ is the bit error rate ratio, when the transmitted symbol vector is $\mathbf{x_i}$ and is decided as $\mathbf{x_j}$. The parameter $e_b^{(i,j)}$ is the Hamming distance between $\mathbf{x_i}$ and $\mathbf{x_j}$.

5.7 BER for the Correlated Channel

In MIMO HF, the channel can be correlated because of insufficient spacing between antennae. This is especially true when the antennae are placed on vehicles. When the channel is correlated, we can use a channel model that has been used in past literature such as [76] and [77]. The new channel matrix becomes

$$\mathbf{H} = \mathbf{R_{Rx}^{1/2}} \mathbf{\bar{H}} \mathbf{R_{Tx}^{1/2}}, \tag{5.41}$$

where $\mathbf{\bar{H}}$ is a $n_t \times n_r$ matrix with each element having complex normal distribution $CN\left(0, 1\right)$. $\mathbf{R_{Rx}}$ is the receive correlation matrix, while $\mathbf{R_{Tx}}$ is the transmit correlation matrix. They are both deterministic for a given scenario. The case in which $\mathbf{R_{Tx}} = \mathbf{I}$ is called the receive correlated fading channel, and the case in which $\mathbf{R_{Rx}} = \mathbf{I}$ is called the transmit correlated fading channel. Let $\mathbf{c} = \mathbf{R_{Rx}^{1/2}} \left(\mathbf{x_i'} - \mathbf{x_j'}\right)$, and $\mathbf{c} = [c_1, c_2, \cdots, c_{n_t}]^T$. Also, let $\mathbf{R_{Tx}^{1/2}} = [\mathbf{a_1}, \mathbf{a_2}, \cdots, \mathbf{a_{n_r}}]^T$. Let $\mathbf{z} = \mathbf{R_{Tx}^{1/2}} \mathbf{\bar{H}} \mathbf{R_{Rx}^{1/2}} \left(\mathbf{x_i'} - \mathbf{x_j'}\right)$. Hence,

$$\mathbf{z} \sim \begin{bmatrix} CN\left(0, \left\|\mathbf{a_1^T}\right\|_2^2 \left\|\mathbf{c}\right\|_2^2\right) \\ CN\left(0, \left\|\mathbf{a_2^T}\right\|_2^2 \left\|\mathbf{c}\right\|_2^2\right) \\ \vdots \\ CN\left(0, \left\|\mathbf{a_{n_r}^T}\right\|_2^2 \left\|\mathbf{c}\right\|_2^2\right) \end{bmatrix} \tag{5.42}$$

Let $\mathbf{w} = \|\mathbf{z}\|_2^2$. Now, we can find the pairwise bit error probability by utilizing a procedure that is similar to the procedure described in the previous section. We obtain

$$E_{\bar{\mathbf{H}}}\left[L\left(\sqrt{\frac{2SNR\left\|\mathbf{R_{Rx}^{1/2}\bar{H}R_{Tx}^{1/2}}\left(\mathbf{x_i'}-\mathbf{x_j'}\right)\right\|_2^2}{4N_T}};K,\sigma\right)\right] \tag{5.43}$$

$$= E_{\mathbf{W}}\left[L\left(\sqrt{\frac{2SNR\cdot\mathbf{w}}{4N_T}};K,\sigma\right)\right] \tag{5.44}$$

We then use (5.39) and (5.40) to determine the BER.

5.8 The Effect of XPD

In previous sections, we identified one technique for achieving MIMO HF, through polarization. Technically, this requires the use of antennas that can distinguish between the two modes (ordinary and extraordinary). In reality, the ideal situation may not occur. According to [78], [79], and [80], we can formulate the effect of imperfect discrimination of the cross polarization on the channel by the expression

$$\mathbf{H} = \mathbf{A}\odot\left(\mathbf{R_{Rx}^{1/2}\bar{H}R_{Tx}^{1/2}}\right), \tag{5.45}$$

where $\mathbf{A}$ is the polarization influence matrix, and $\odot$ is the Hadamard product. There are many ways to describe the effect of polarization in the MIMO channel. This model has the benefit of isolating the effect of polarization and the Rx/Tx antennae's insufficient spacing. Suppose the transmitting power on an antenna is P_t and the receiving power on an antenna is P_r.The cross polarization discrimination (XPD) is defined as $\alpha = P_r/P_t$. Since we use cross polarization to enable the MIMO communication system, we have the form of $\mathbf{A}$ given by

$$\mathbf{A} = \begin{bmatrix} \sqrt{1-\alpha} & \sqrt{\alpha} & \cdots & \sqrt{\alpha} \\ \sqrt{\alpha} & \sqrt{1-\alpha} & \cdots & \sqrt{1-\alpha} \\ \vdots & \vdots & \ddots & \vdots \\ \sqrt{\alpha} & \sqrt{1-\alpha} & \cdots & \sqrt{1-\alpha} \end{bmatrix} \tag{5.46}$$

Here, $\sqrt{1-\alpha}$ and $\sqrt{\alpha}$ alternate in turn across the rows of $\mathbf{A}$.

Since $\mathbf{A}$ is deterministic for a given scenario, we use the techniques from the previous sections to analyze the BER for high SNR. Direct matrix multiplication will show that $\mathbf{z} = \left[\mathbf{A} \odot \left(\mathbf{R_{Rx}^{1/2}}\mathbf{\bar{H}}\mathbf{R_{Tx}^{1/2}}\right)\right]\left(\mathbf{x_i'} - \mathbf{x_j'}\right)$ has each entry having the distribution given by

$$\mathbf{z} \sim \begin{bmatrix} CN\left(0, \left\|\mathbf{b_1^T}\right\|_2^2 \left(\sum_{k=1}^{n_t} a_{1,k}^2 \left\|\mathbf{c_k}\right\|_2^2 |d_k|^2\right)\right) \\ CN\left(0, \left\|\mathbf{b_2^T}\right\|_2^2 \left(\sum_{k=1}^{n_t} a_{2,k}^2 \left\|\mathbf{c_k}\right\|_2^2 |d_k|^2\right)\right) \\ \vdots \\ CN\left(0, \left\|\mathbf{b_{n_r}^T}\right\|_2^2 \left(\sum_{k=1}^{n_t} a_{n_r,k}^2 \left\|\mathbf{c_k}\right\|_2^2 |d_k|^2\right)\right) \end{bmatrix}, \tag{5.47}$$

where $a_{i,k}$ is the (i,k)-entry of $\mathbf{A}$, $\mathbf{b_i^T}$ is the i-th row of $\mathbf{R_{Rx}^{1/2}}$, $\mathbf{c_i}$ is the i-th column of $\mathbf{R_{Tx}^{1/2}}$, and d_k is the k-th element of $\mathbf{x_i'} - \mathbf{x_j'}$.

Let $\mathbf{w} = \|\mathbf{z}\|_2^2$. Following a similar procedure that was shown in previous sections, we find the PER to be given by

$$E_{\mathbf{\bar{H}}}\left[L\left(\sqrt{\frac{2SNR\left\|\mathbf{A} \odot \mathbf{R_{Rx}^{1/2}}\mathbf{\bar{H}}\mathbf{R_{Tx}^{1/2}}\left(\mathbf{x_i'} - \mathbf{x_j'}\right)\right\|_2^2}{4N_T}}\right)\right] \tag{5.48}$$

$$= E_{\mathbf{W}}\left[L\left(\sqrt{\frac{2SNR \cdot \mathbf{w}}{4N_T}}\right)\right] \tag{5.49}$$

Again, we can use (5.39) and (5.40) for finding out the BER.

We notice that in finding the pdf of W, each entries of $\mathbf{z}$ may not have the same coefficients. Hence, the pdf of W will not be Chi-squared. The actual pdf of W changes from cases to cases. Herem we outline a general approach that is similar to [81] but easier to be followed.

STEP 1: Let $\mathbf{z}_{k,R}$ and $\mathbf{z}_{k,I}$ denote the real and imaginary part of $\mathbf{z}_k$. Then

$$\mathbf{w} = \sum_{k=1}^{N_T} |\mathbf{z}_k|^2 = \sum_{k=1}^{N_T} |\mathbf{z}_{k,R}|^2 + |\mathbf{z}_{k,I}|^2 \tag{5.50}$$

STEP 2: Assume $\mathbf{z}_k$ CN(0,2σ^2), then $z_{k,R}$ and $z_{k,I}$ i.i.d. N(0,σ_k^2).

$$\mathbf{w}_k \equiv |\mathbf{z}_{k,R}|^2 + |\mathbf{z}_{k,I}|^2 \tag{5.51}$$

Then $\mathbf{w}_k$ $\frac{1}{2\sigma_k^2} e^{-\frac{z}{2\sigma_k^2}} u\left(w\right)$. All $\mathbf{w}_k$'s are independent.
STEP 3: Since

$$\mathbf{w} = \sum_{k=1}^{N_T} \mathbf{w}_k \tag{5.52}$$

Then

$$f_{\mathbf{w}}\left(w\right) = f_{\mathbf{w}_1}\left(w\right) * f_{\mathbf{w}_2}\left(w\right) * \cdots * f_{\mathbf{w}_{N_T}}\left(w\right) \tag{5.53}$$

where "$*$" denotes convolution. And so we have

$$F\left(s\right) \equiv \mathscr{L}\{f_{\mathbf{w}}\left(w\right)\} = \prod_{k=1}^{N_T} \frac{1}{2^{N_T}\sigma_k^2} \frac{1}{\left(s + \frac{1}{2\sigma_k^2}\right)} \tag{5.54}$$

STEP 4: Perform partial fraction expansion, and then apply inverse Lapalce transform to get $f_{\mathbf{w}}\left(w\right)$.

5.9 Simulation Result

In this part, we simulate the scenarios mentioned above. In particular, for the correlated channel case, we assume $\mathbf{R_{RX}} = \mathbf{I}$ and consider the transmit correlated channel with the matrix given by

$$\mathbf{R_{TX}} = \begin{bmatrix} 1 & \rho & \rho^2 & \cdots & \rho^{N_t-1} \\ \rho & 1 & \rho & \cdots & \rho^{N_t-2} \\ \rho^2 & \rho & 1 & \cdots & \rho^{N_t-3} \\ \vdots & \vdots & \vdots & \ddots & \vdots \\ \rho^{N_t-1} & \rho^{N_t-2} & \rho^{N_t-3} & \cdots & 1 \end{bmatrix} \tag{5.55}$$

The relationship between ρ and antenna spacing is described [77] by

$$\rho = J_0\left(2\pi\frac{d}{\lambda_c}\right), \tag{5.56}$$

where J_0 is the 0th order Bessel function, λ_c is the carrier wavelength, and d is antenna spacing.

Figure 5.5 and Figure 5.6 shows the simulation and high 2SNR approximation for the 2x2 uncorrelated channel. For the first data set, Figure 5.7, 5.8, and 5.9 shows the simulation and high SNR approximation for the 2x2 correlated channel with ρ equal to 0.9, 0.5, and 0.2, respectively. For the second data set, Figure 5.10, 5.11, and 5.12 shows the simulation and high SNR approximation for the 2x2 correlated channel with ρ equal to 0.9, 0.5, and 0.2, respectively. Currently, only the packet error rate(PER) is shown. These results show that the bound derived in this paper is capable of accurately assessing performance.

We also perform simulation for MIMO HF when XPD effect is considered. To stress such effect, we assume $\mathbf{R_{TX}} = \mathbf{I}$ and $\mathbf{R_{RX}} = \mathbf{I}$. For the first data set, Figure 5.13, 5.14, and 5.15 shows the simulation and high SNR approximation for the 2x2 correlated channel due to antenna XPD with α equal to 0.8, 0.6, and 0.3, respectively. For the second data set, Figure 5.16, 5.17, and 5.18 shows the simulation and high SNR approximation for the 2x2 correlated channel due to antenna XPD with ρ equal to 0.8, 0.6, and 0.3, respectively.

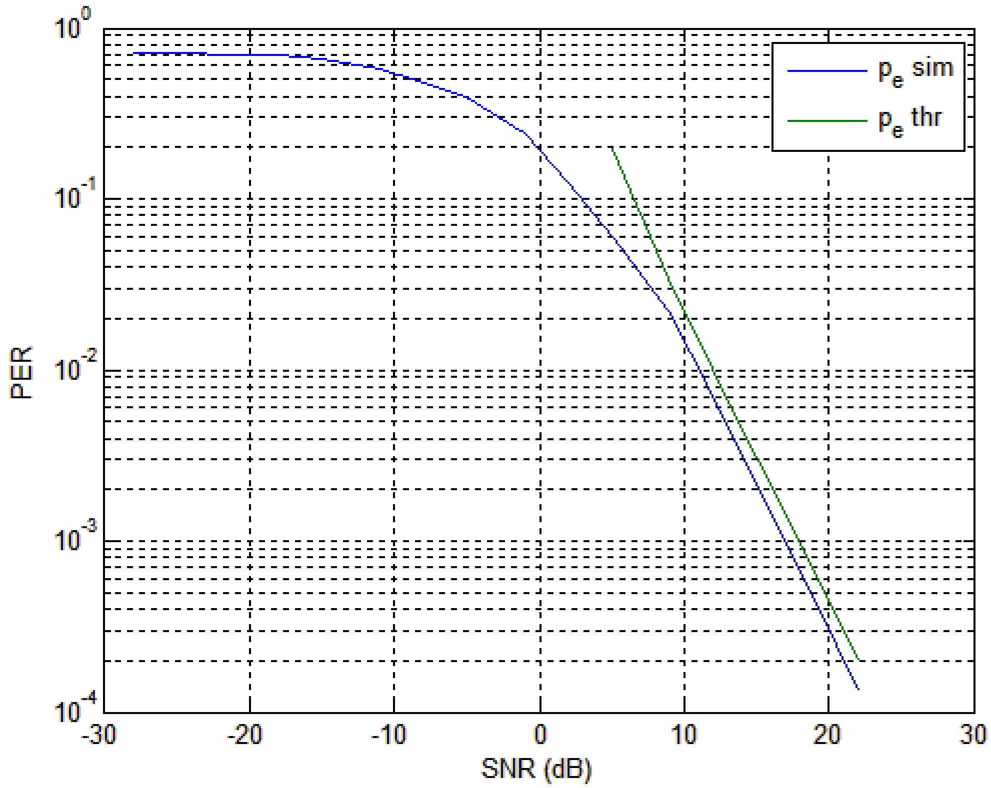

Fig. 5.5. PER for the set K = 1.6, σ = 66 in 2x2 uncorrelated scenario.

5.10 Conclusion

In recent years, MIMO HF experiments have been actively carried out, but few have focused on the special scenario when the measured time is around sunrise. The measurements indicate the need for research on bit error rate prediction. The situation becomes complicated when the measurements imply additive non-Gaussian noise, especially a new type of noise with infinite variance. The mathematical tool developed in this work provides a guideline for evaluating such system performance, and can be readily applied to problems that arise in the future.

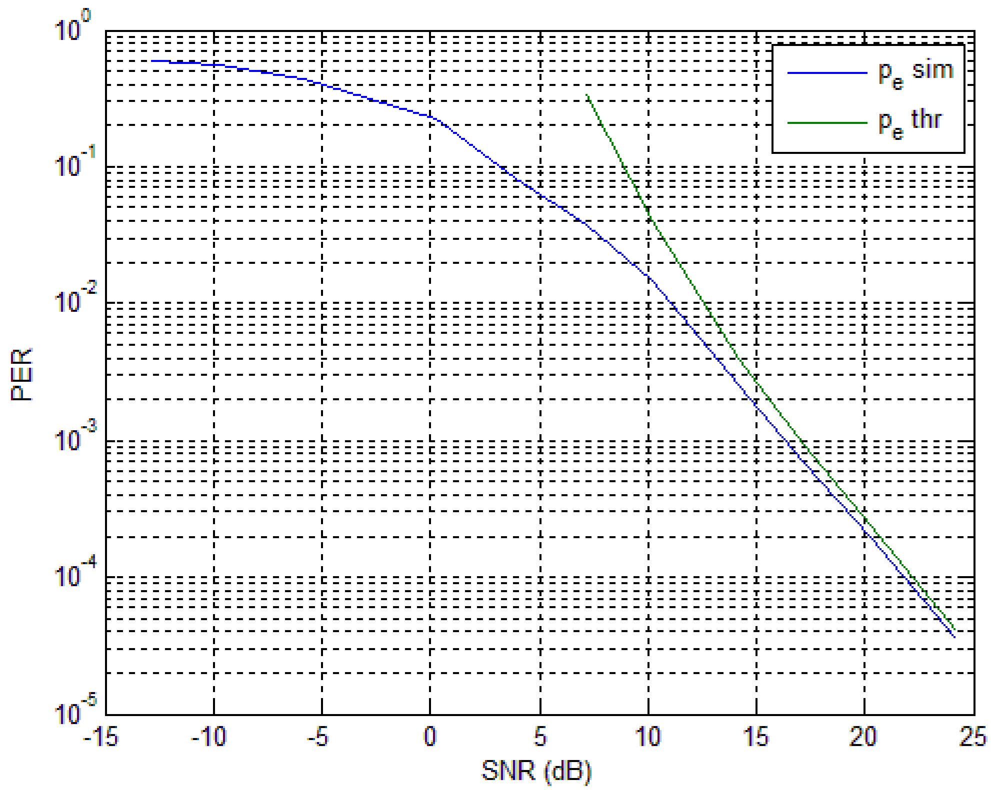

Fig. 5.6. PER for the set K = 2.8, σ = 12.5 in 2x2 uncorrelated scenario.

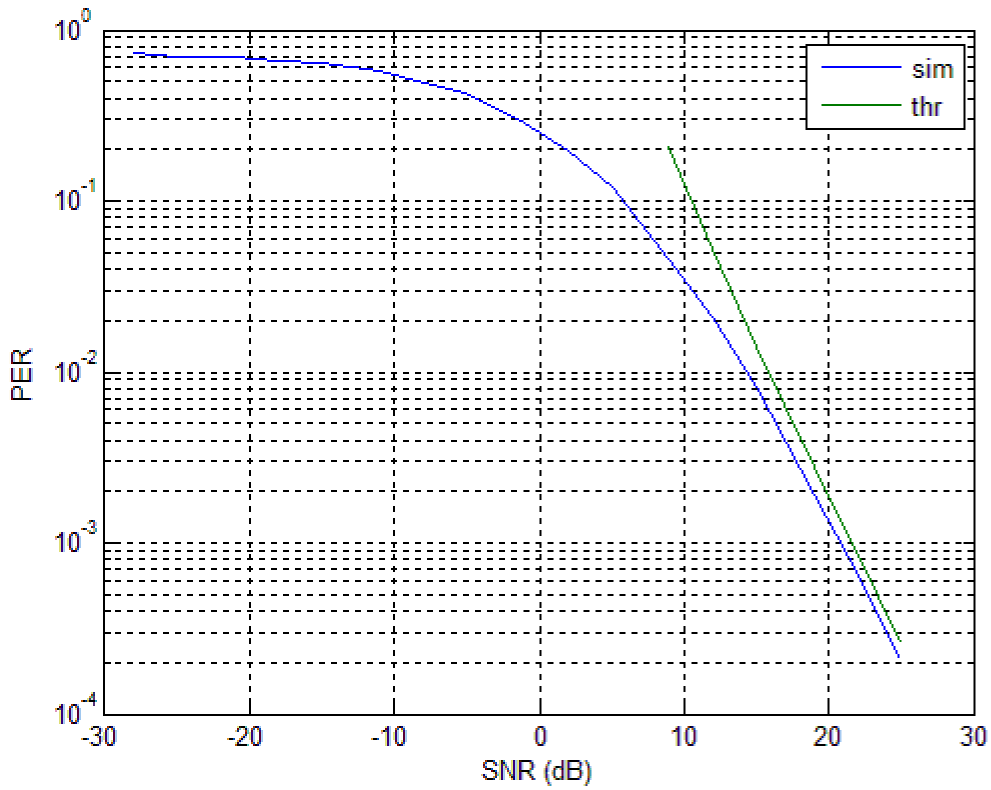

Fig. 5.7. PER for the set K = 1.6, σ = 66 in 2x2 correlated scenario with $\rho = 0.9$.

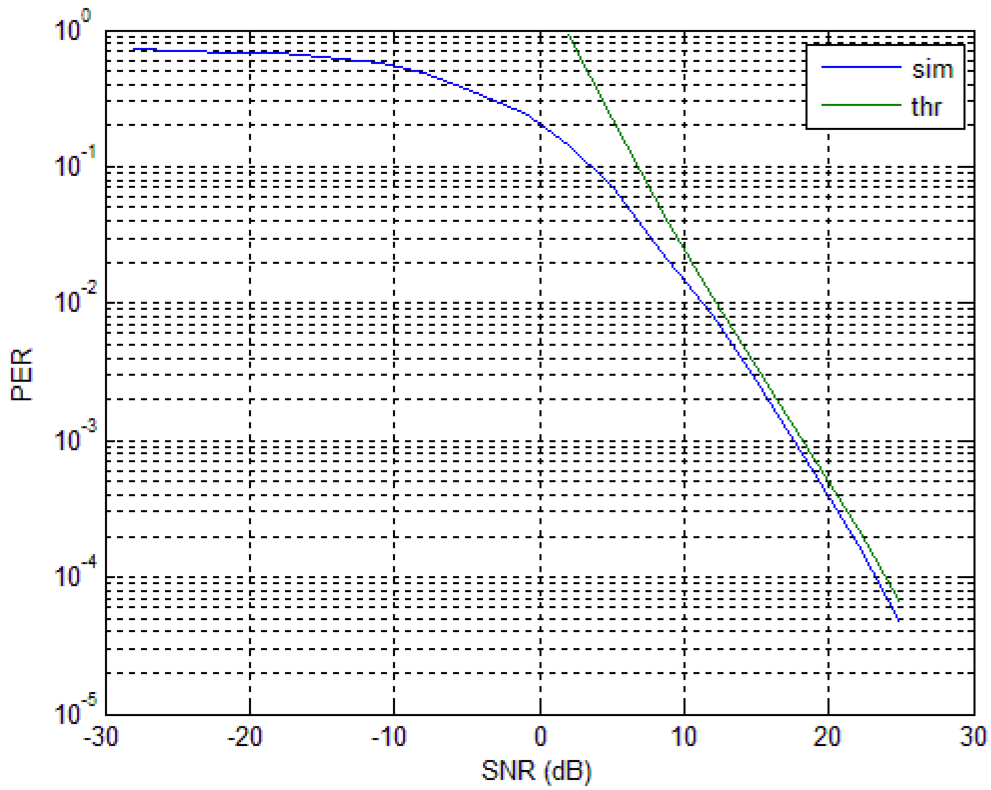

Fig. 5.8. PER for the set K = 1.6, σ = 66 in 2x2 correlated scenario with ρ = 0.5.

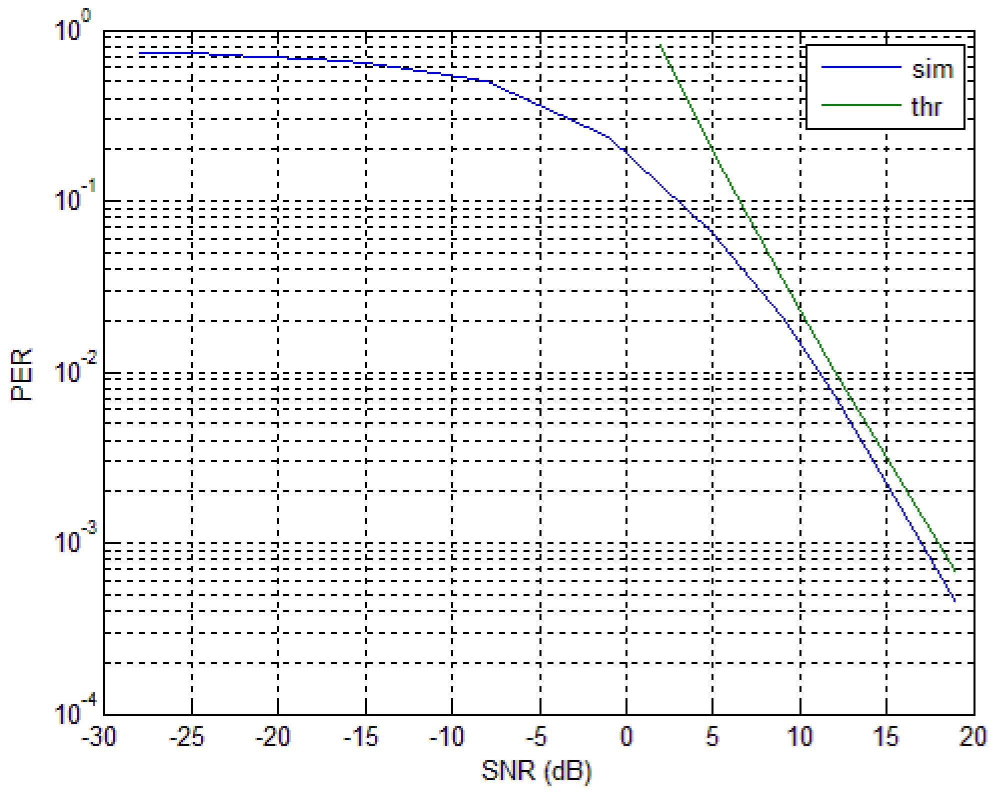

Fig. 5.9. PER for the set K = 1.6, σ = 66 in 2x2 correlated scenario with $\rho = 0.2$.

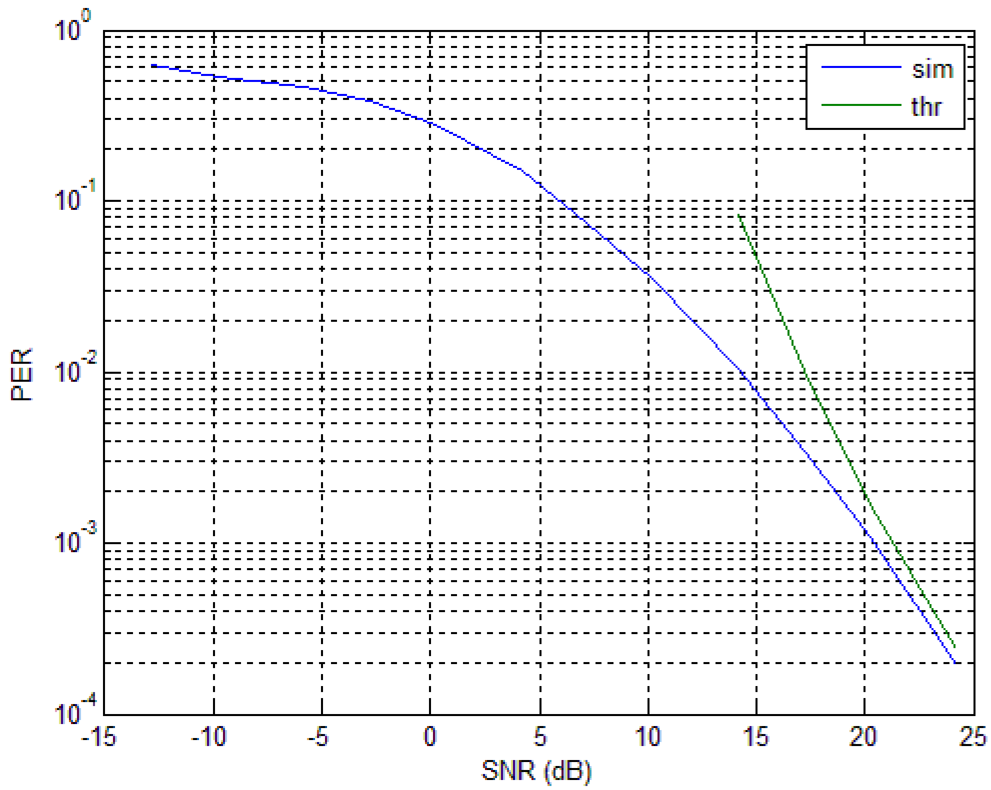

Fig. 5.10. PER for the set K = 2.8, $\sigma = 12.5$ in 2x2 correlated scenario with $\rho = 0.9$.

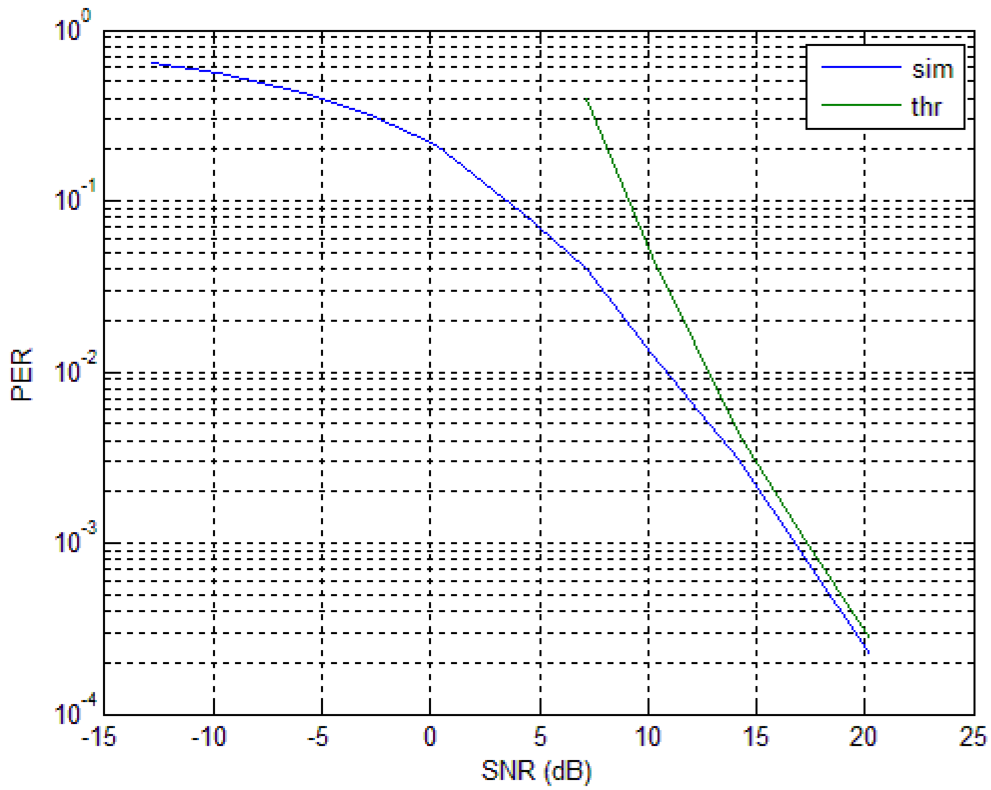

Fig. 5.11. PER for the set K = 2.8, $\sigma = 12.5$ in 2x2 correlated scenario with $\rho = 0.5$.

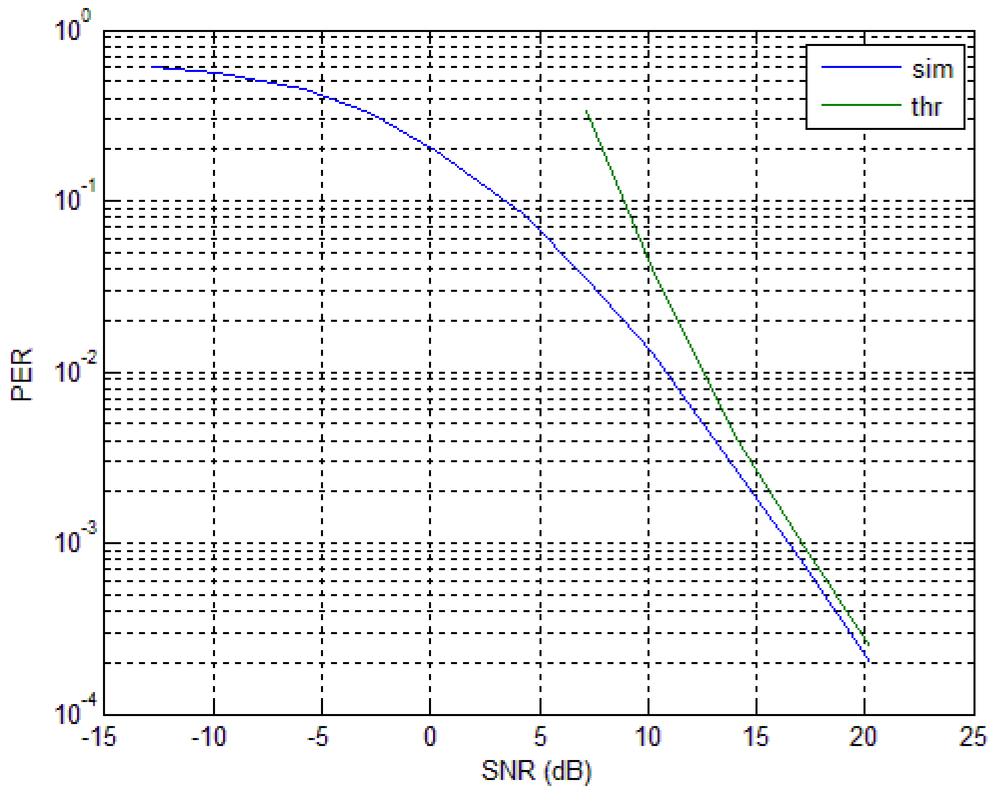

Fig. 5.12. PER for the set K = 2.8, $\sigma = 12.5$ in 2x2 correlated scenario with $\rho = 0.2$.

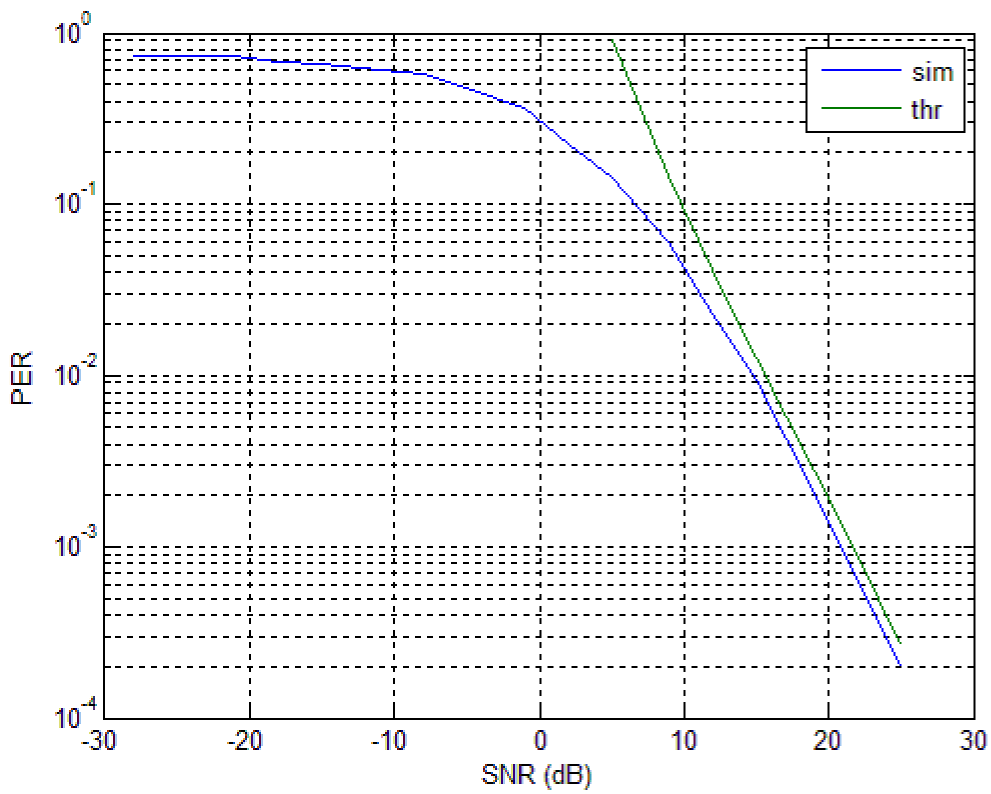

Fig. 5.13. PER for the set K = 1.6, σ = 66 in 2x2 correlated scenario due to antenna XPD with α = 0.8.

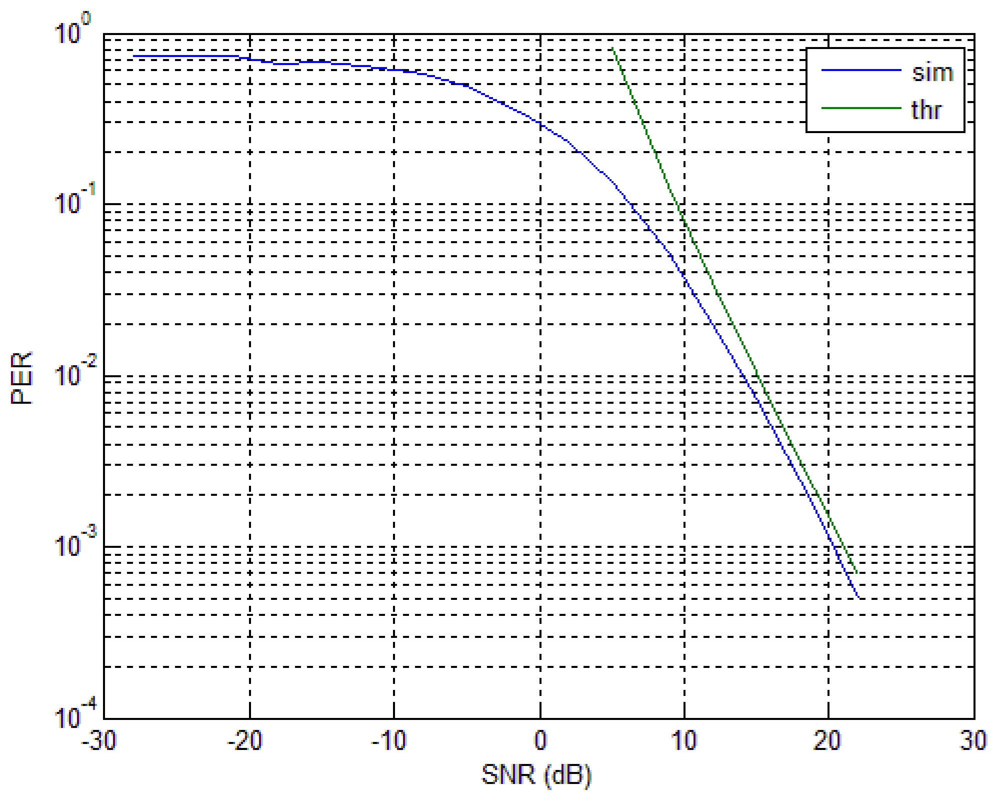

Fig. 5.14. PER for the set K = 1.6, σ = 66 in 2x2 correlated scenario due to antenna XPD with α = 0.6.

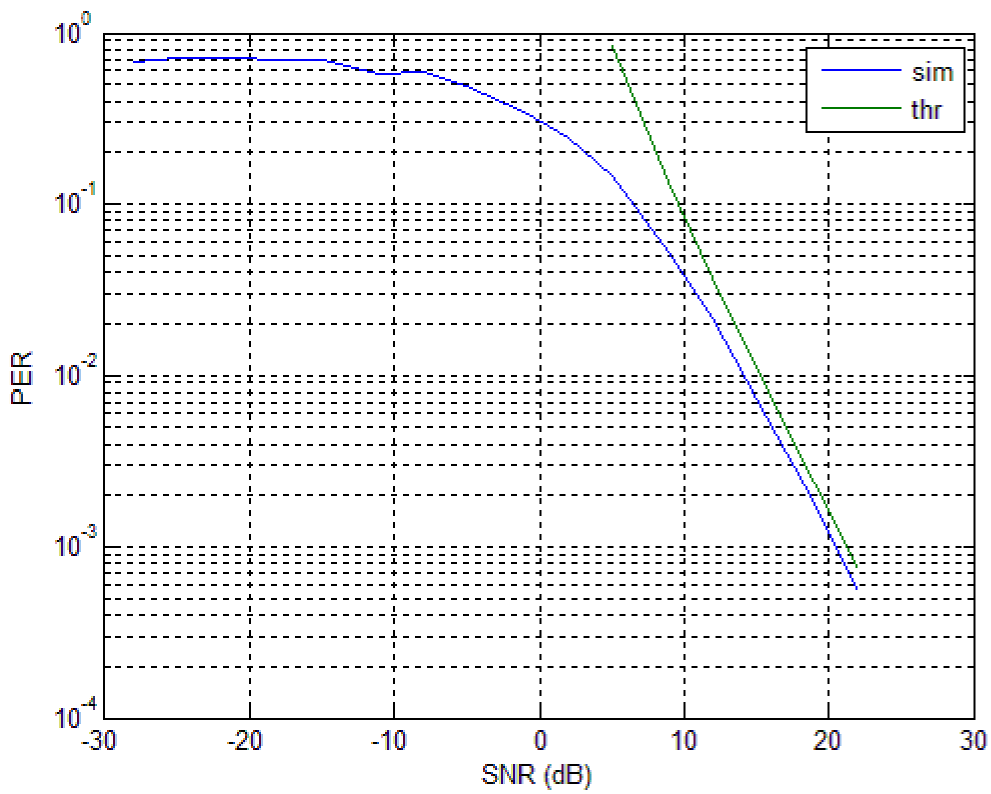

Fig. 5.15. PER for the set K = 1.6, σ = 66 in 2x2 correlated scenario due to antenna XPD with α = 0.3.

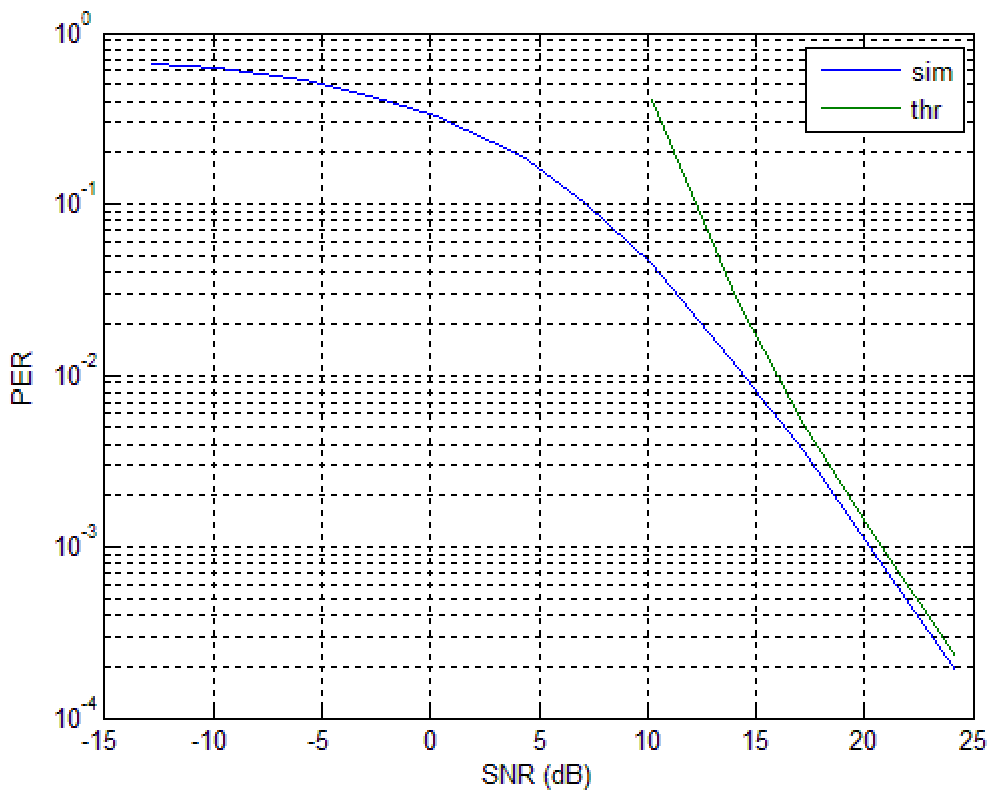

Fig. 5.16. PER for the set K = 2.8, σ = 12.5 in 2x2 correlated scenario due to antenna XPD with α = 0.8.

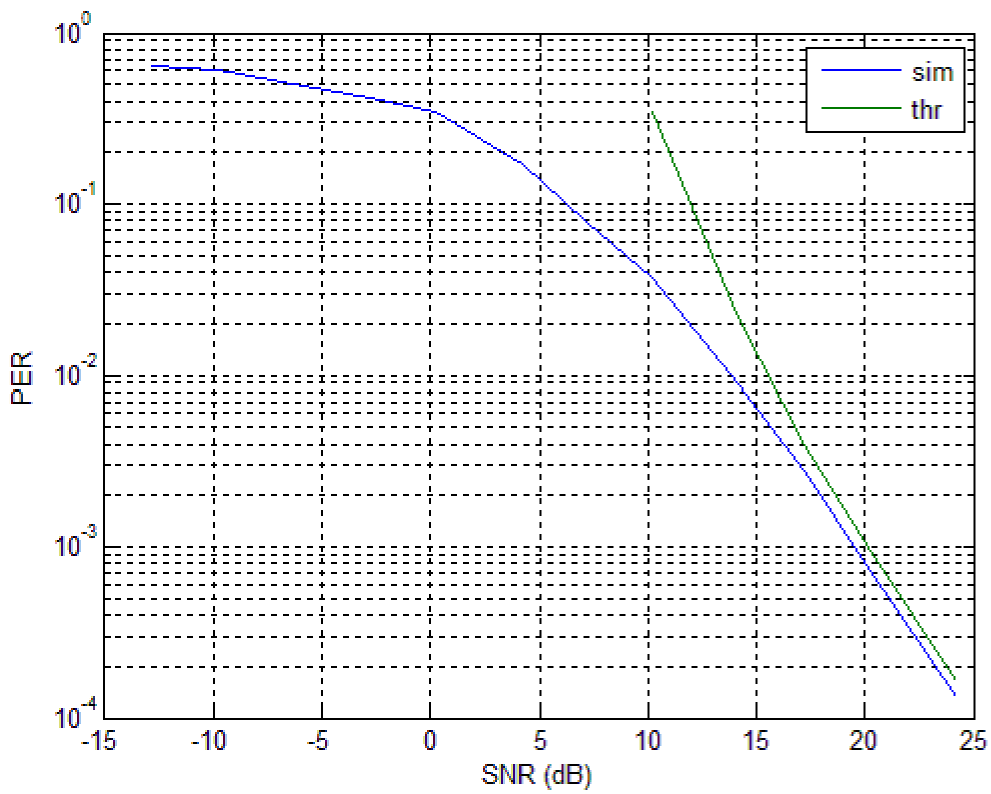

Fig. 5.17. PER for the set K = 2.8, $\sigma = 12.5$ in 2x2 correlated scenario due to antenna XPD with $\alpha = 0.6$.

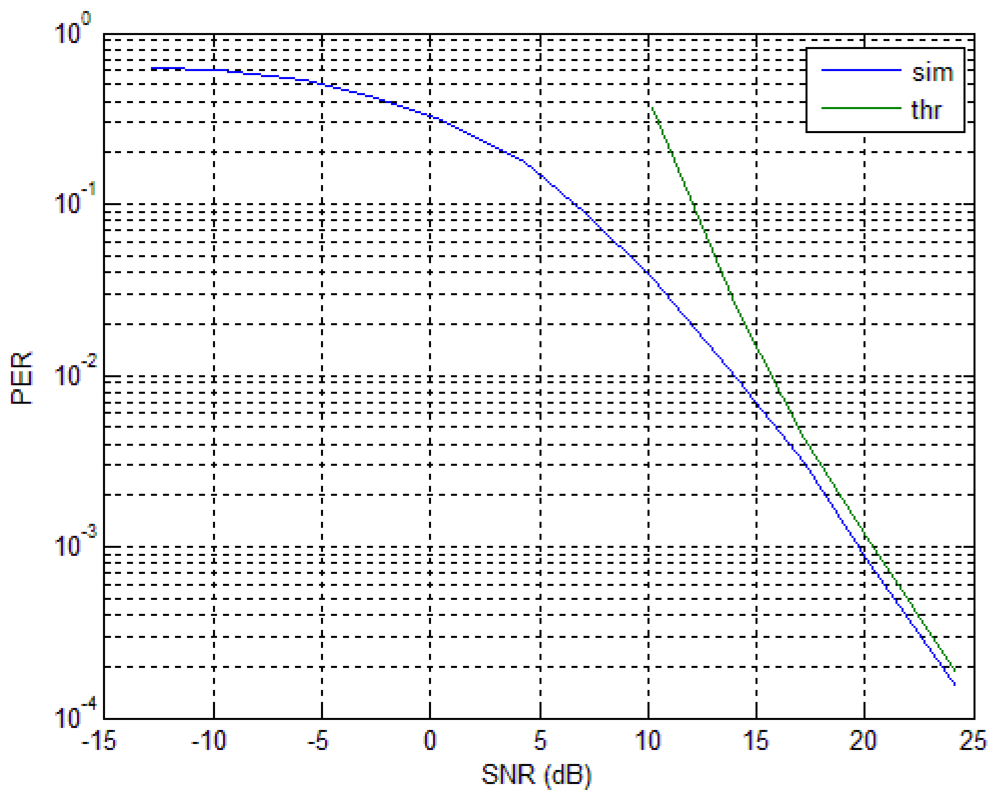

Fig. 5.18. PER for the set K = 2.8, $\sigma = 12.5$ in 2x2 correlated scenario due to antenna XPD with $\alpha = 0.3$.

6. POLAR CODE FOR HF AROUND SUNRISE

Communication link can be more reliable if appropriate channel coding is used. For High Frequency (HF) communication around sunrise, the noise can be approximated as having Kappa distribution. For this particualr type of noise, we apply a particular type of channel coding to reduce the bit error rate (BER). The one that we use is polar code, which is discovered recently. In this work, we look for a good polar code among various factors that can change the performance. Those factors include rate, block length, encoding signal-to-noise ratio (SNR), encoding algorithm, and encoding initial value. We exploit each factor to heuristically determine a suboptimal solution.

6.1 Introduction

HF communication is established by transmitting the electromagnetic (EM) wave via the ionosphere of the Earth. With certain operating frequency, the EM wave will be reflected to the desitnation. The operating frequency is dependent on the ion density of the ionosphere. This value is between 3 to 30 MHz.

Even though the frequency range implies lower data rate compared with existing civilian communication system such as LTE-a and the upcoming 5G, HF communicatin has the advantage of covering wider transmission range. In scenarios like natural disasters and wars, where civilian communication systems may not be functioning, HF is still usable. Hence, any research for improving HF communication is still needed.

The noise model mentioned by [25] states that the sampled noise has Gaussian distribution. Many subsequent research use this result. However, at sunrise, measurement result by [21] shows that it is not. Our research [49] shows that the noise should be modeled as Kappa distribution. The intuition is that at sunrise, the galactic noise is dominant, hence, the Gaussian components are negligible. For the galactic noise, it is related to electron velocity distribution, which has been proven to be Kappa [30] [31].

Channel coding is crucial in a communication system in that with a slight decrease in the data transmission rate, one can achieve much lower bit error rate (BER) than the uncoded case. Algebraic coding schemes such as Hamming code and Reed-Solomon code, and probabilistic coding schemes such as turbo code and low density parity check (LDPC) code have been proven to be sucessful in the past. The latter group are especially good in the sense that the results are close to the Shannon limit. In recent years, another coding schemes called polar code showed up [82]. It has similar performance compared with turbo code and LDPC code. In addition to that, unlike the prvious two coding schemes, polar code does not have error floor.

Polar code is already included in the standard for 5G system. However, it has not been studied in the particular HF Kappa noise. In , the performance of polar code over Middleton-A noise has been investigated. It is well known [83] [84] [85] that the encoding prodedure for polar code changes with channel and the initial SNR. The encoding process could use differnt algorithms. The block length has significant effect under a certain range. Therefore, finding the best polar code for Kappa case can be exhaustive. Lots of factors should be considered at the same time. In our work, we investigate the effect of each factor, and then heuristically choose a good polar code.

The work is organized as follows. In Section 6.2, we define the system model and describe part of the polar code process that is essential for our work. In Section 6.3, we look at the effect of different rate and block size. In Section 6.5, we investigate the effect of input SNR. In Section 6.4, we look for several possibilities for the initial value. In Section 6.6, we study the impact of different encoding algorithms. In Section 6.7, we provide simulation resuls and show our solution to finding a suboptimal polar code for this channel. In Section 6.8, we draw conclusion.

6.2 System model

For HF communication at sunrise, the discrete baseband channel model can be written as Equation 6.1.

$$y = x + n_G \tag{6.1}$$

where x is the transmitted symbol, y is the received symbol and n_G is the additive white noise with Kappa distribution shown in Equation 6.2. This noise comes from the galactic component of the HF noise. Around sunrise, this component is dominant [49]. Hence, additive white Gaussian noise (AWGN) is neglected. We assume that binary phase shift keying (BPSK) is used for the modulation part. That is, we assume that when the bit "0" is transmitted, $x = \sqrt{E_b}$, and when the bit "1" is transmitted, $x = -\sqrt{E_b}$.

$$\begin{aligned} f\left(x; K, \sigma\right) = \frac{1}{\sqrt{K}\sigma\beta\left(\frac{1}{2}, K+\frac{1}{2}\right)}\left(1+\frac{x^2}{K\sigma^2}\right)^{-K-1}&, \\ -\infty < x < \infty, K > \frac{1}{2}& \end{aligned} \tag{6.2}$$

For this channel, the SNR and $G\left(K, \sigma\right)$ are defined as [57]

$$SNR \equiv \frac{E_b}{G\left(K, \sigma\right)} = \frac{E_b}{\frac{K\sigma^2}{K-\frac{1}{2}}} \tag{6.3}$$

The uncoded BER for BPSK is found by Equation (6.4) [57]

$$p_{BER,BPSK} = L\left(\sqrt{2\frac{E_b}{G\left(K, \sigma\right)}}; K\right) = L\left(\sqrt{2SNR}; K\right) \tag{6.4}$$

The definition of the L function is given by Equation (6.5) [57]. The purpose of the L function is simliar to the Q function used in AWGN.

$$L\left(x;K\right)\equiv$$
$$\int_{x}^{\infty}\frac{1}{\sqrt{2K-1}\beta\left(\frac{1}{2},K+\frac{1}{2}\right)}\left(1+\frac{t^{2}}{2K-1}\right)^{-K-1}dt, \tag{6.5}$$
$$-\infty<x<\infty, K>\frac{1}{2}$$

The block diagram for employing polar code to the HF channel is shown in Figure 6.1. Here, we provide the nomenclature for the polar code used in our work. Let N denote the block size used for each transmission, and k/N be the coding rate. The generating matrix is denoted as $\mathbf{G}$. ψ represents the set of indicies ranging from 1 to N. F represent the set of indicies of frozen bits, and F^C represents the set of indicies of information bits. $\mathbf{x}$ denotes the transmitted bit vector and $\mathbf{y}$ denotes the received bit vector. $\mathbf{u}$ represents the information bits and $\widehat{\mathbf{u}}$ represents the decoded bits.

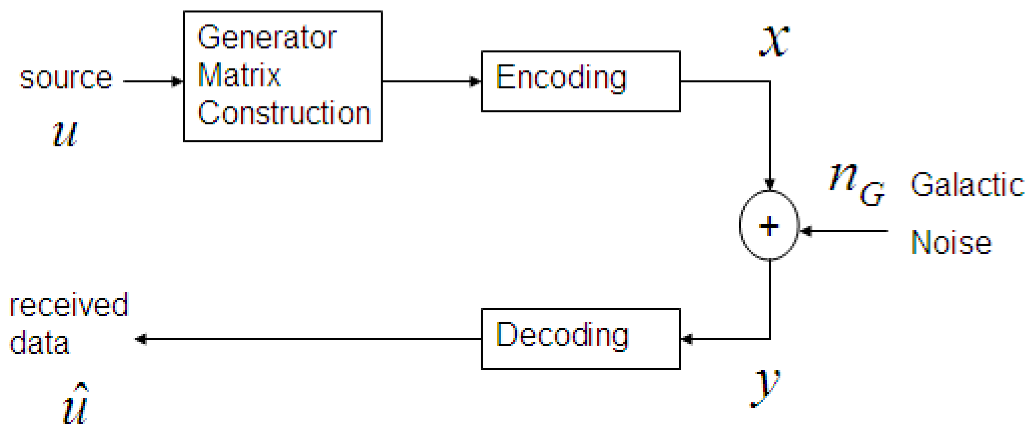

Fig. 6.1. System model.

As shown in Figure 6.2, the first step of the encoding part of polar code is to obtain the generating matrix $\mathbf{G}$ by using $\mathbf{G}=\mathbf{A}^{\bigotimes n}$. $n=\lceil \log_2 N\rceil$ Here, "$\bigotimes$" represents the kronecker product and

$$\mathbf{A}=\begin{bmatrix}1 & 1\\ 0 & 1\end{bmatrix} \tag{6.6}$$

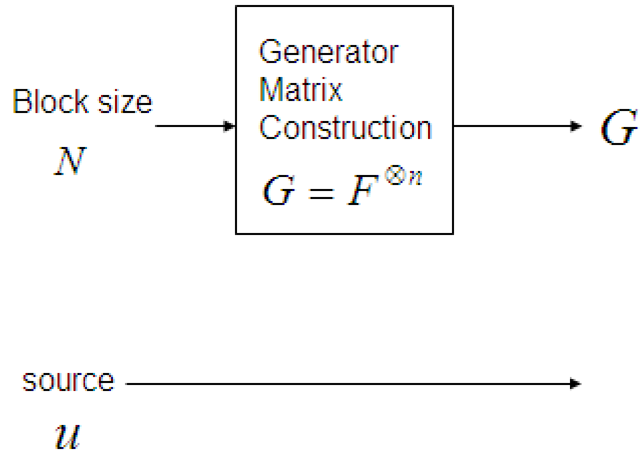

Fig. 6.2. The structure of constructing generation matrix block.

The second step is to obtain the initial value z_0 for channel polarization. Then, we recursively generate N channels by using the algorithm $z \to \{2z - z^2, z^2\}$. The output is N real numbers that indicates the "wellness" of the channels. We select the best k out of N channels and assign the indicies to F^C while the remaining indicies are assigned to F. This is shown in Figure 6.3.

After obtaining F and F^C, we assign "0" to the frozen bit slots and the information bits to the information bit slots. We thus obtain the vector $\mathbf{v}$. Finally, by multiplying the generating matrix G and $\mathbf{v}$, we get $\mathbf{x}$, the bit vector to be transmitted to the channel. This is shown in Figure 6.4.

The decoding part is achieved by using sucessive cancelation decoding. The calculation is based on the log-likelihood domain. The initial log-likelihood ratio is given by

$$\lambda(y) \equiv \frac{f_Y(y|0)}{f_Y(y|1)} = (-K-1)\log\frac{\left[1+\frac{\left(y+\sqrt{E_b}\right)^2}{K\sigma^2}\right]}{\left[1+\frac{\left(y-\sqrt{E_b}\right)^2}{K\sigma^2}\right]} \tag{6.7}$$

As we can see in this section, there are many factors used for polar code construction. In the following sections, we discuss the effect of each factor.

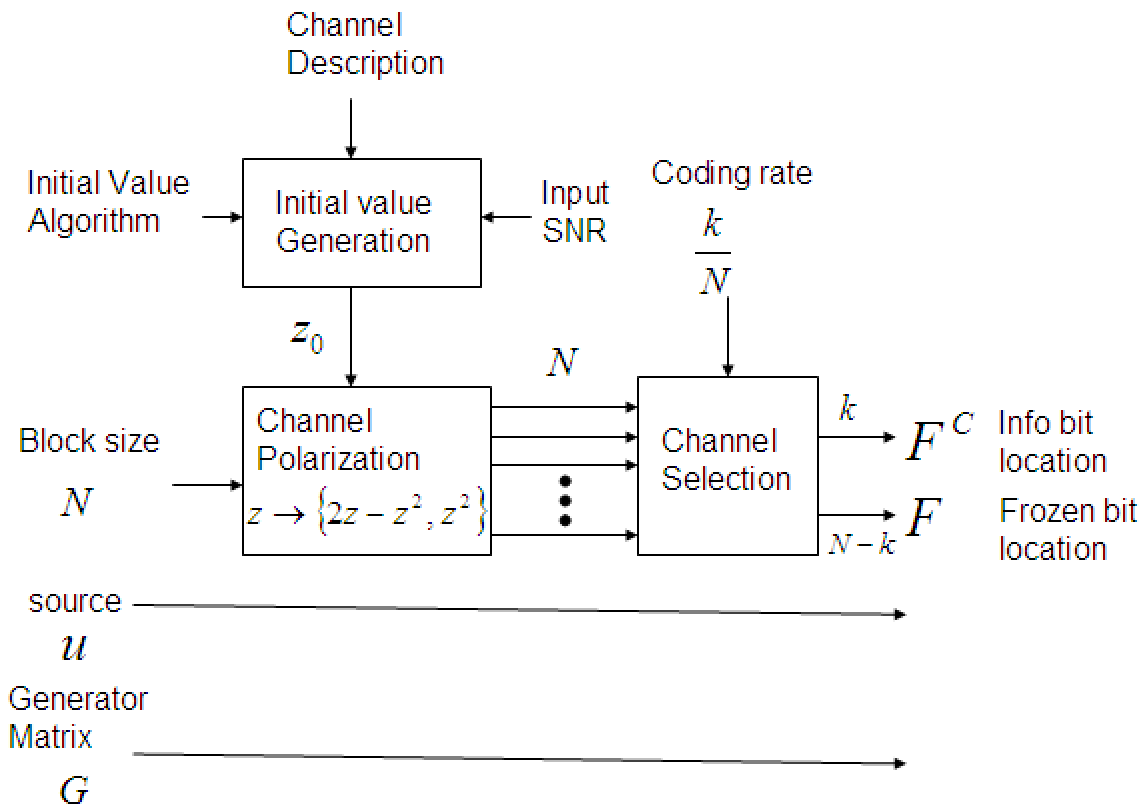

Fig. 6.3. Polar code encoding, part 1.

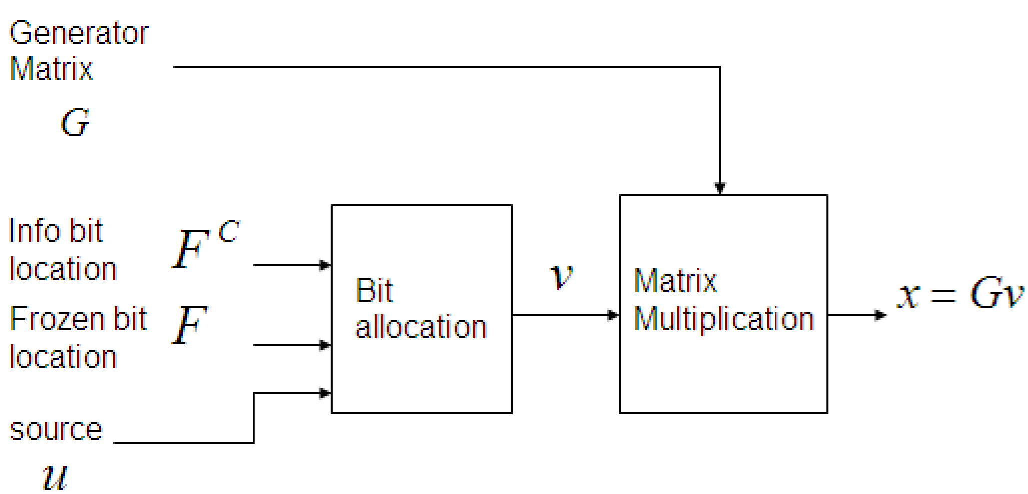

Fig. 6.4. Polar code encoding, part 2.

6.3 Rate and Block Size

[86] and [87] showed results of BER when polar code is used under various rate and block size with AWGN. As the coding rate decreases, one expects the BER performance to be better. The same thing holds for increasing block size. However, it is unclear as to for what threshold value of the coding rate, dereasing coding rate does not affect the BER curve as much as it did before the threshold. Similarly, we want to find such threshold for increasing block size. Even though we know [82] polar code is a capacity-achieving error control code when the block size approaches infinity, we still don't know how exactly the block size changes the BER. So when the noise distribution changes, the results could change.

6.4 Initial Value

In [88], for binary erasure channel (BEC), the author proposed a fixed initial value $z_0 = 0.5$. For other channels, the author proposed a heuristic value to be $z_0 = 1 - C$. Where C is the channel capacity for the equivalent BEC channel. For additive noise with continuous pdf, we consider in our work to use the capacity of the channel. However, since the channel capacity for the HF Kappa channel is unknown now, we use the Gaussian channel with the same SNR for approximation.

In [89], the authors proposed the use of the Bhattacharyya parameter (BP) to be the initial value for AWGN. That is,

$$z_0 = \int_{-\infty}^{\infty} \sqrt{p\left(y|0\right) p\left(y|1\right)} dy \tag{6.8}$$

For the HF Kappa channel, this value will be evaluated with the following integral:

$$z_0 = \int_{-\infty}^{\infty} \frac{1}{\sqrt{K}\sigma\beta\left(\frac{1}{2}, K + \frac{1}{2}\right)} \left\{ \left[1 + \frac{\left(y - \sqrt{E_b}\right)^2}{K\sigma^2}\right] \left[1 + \frac{\left(y + \sqrt{E_b}\right)^2}{K\sigma^2}\right] \right\}^{\frac{-K-1}{2}} dy \tag{6.9}$$

The strenghth of polar code is that it uses the information of the channel to contruct the code. The code is said to be channel-dependent. However, since it is unknown as to what is the best choice of z_0, we need to try out.

6.5 Input SNR

As shown in Section 6.2 and Figure 6.3, there is a parameter used for polar encoding, that is, the initial SNR. Depending on the algorithm used in Section 6.4, it could be used or not. Suppose that we select the algorithm that requires it (one such example is Equation (6.8)), then exactly what value we should choose remains unknown.

Each time we transmit the signal, we could observe the SNR of the channel first, and then choose the optimal initial SNR for polar code construction in terms of BER. Note that the initial SNR may not be the same as the observed SNR. There is no literature up to this date that deals this problem. So we can only experiment on it. We conjecture that there exists such a relationship. for the HF Kappa channel. Also, for practical purpose, it is beneficial if we can find one or a few initial SNRs that can be used for all transmissions.

As we oberve in Equation (6.9), we cannot find a way to express the BP in terms of SNR for the HF Kappa channel. So the input SNR tuning is achieved by adjusting E_b in BP calculation.

Since the value of K changes as the time goes on, the variance of the noise changes with repect to time. Such a change is faster than other AWGN channel used in daytime HF communication or civilian communication channel such as the ones used in LTE-a and 5G. In [90], the authors experimented this value for AWGN. It is unknown for the Kappa case, and we will investigate it.

6.6 Encoding Algorithm

[91] proposed systematic encoding technique in which the message bits are directly mapped to the codeword $\mathbf{x}$. To be more specific, based on the notation used in Section 6.2, at $\mathbf{x}$, the indicies that belong to F^C belong to the information bits $\mathbf{u}$, while at $\mathbf{y}$ the indicies that beong to F belong to the frozen bits.

The complexity for systematic polar encoding is higher than the non-systematic counterpart. [83] established an efficient algorithm for reducing the complexity of systematic polar code. In [91], the result shows that for AWGN, systematic encoding achieves better BER while for frame error rate (FER), there is no improvement. In [92], the authors used computer to obtain the distance spectrum and use this to indicate that the observation result in [91] is correct. For the HF Kappa channel, we envsion that in terms of BER, the systematic encoding is better, but we do not know how much better is that. If the result is very close, then it makes sense to adopt the non-systematic method for practical purpose. In our work, we aim to solve this issue.

6.7 Simulation Result

For simulation, we consider the set of HF Kappa channel paremeters that represents the case when the ionosphere is close to thermal antiequilibrium state. That is, $K = 1.6$, $\sigma = 66$. For this case, the noise pdf exhibits significant difference as compared with the Gaussian pdf.

In order to find a good polar code, we first look for the block size. Figure 6.5 shows the simulation result when we use systematic encoding with various block size. While larger block size provides better BER, it also increases computation time. We believe that N = 1024 is good enough and subsequent simulation are all based on this block size.

Next, we investigate the difference between systematic encoding and non-systematic encoding. Figure 6.6 shows such simulation result. As we can see, in HF Kappa chan-

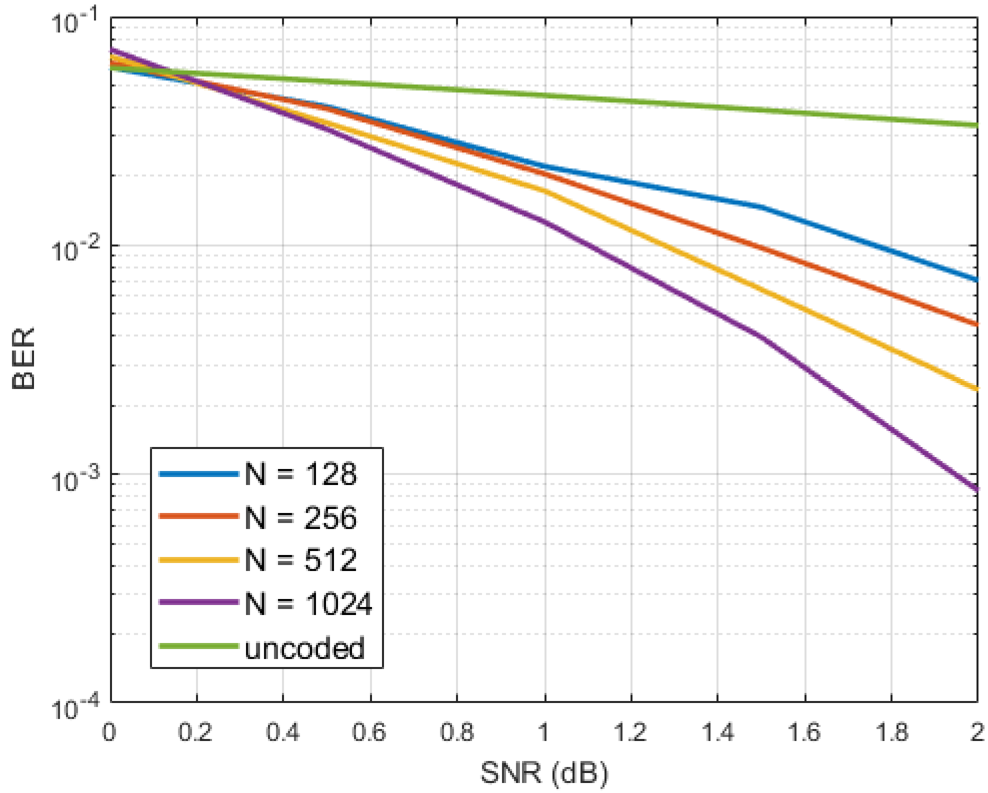

Fig. 6.5. Polar code with variation of block size N.

nel, the difference is large enough for us to choose systematic encoding. From now on, we always adopt systematic encoding method.

Next, we look at the performance of polar code with different rates under this channel. Figure 6.7 shows the result. While it is true that the lower the rate, the better the BER performance, we also care about the loss of such data rate. We believe that the rate $= 1/2$ is a good choice.

For the proper choice of the initial value and the associated SNR, Figure 6.8 and 6.9 shows the simulation results by using the three algorithms explained in Section 6.4 along with various initial SNRs. As we cam see, BP performs slightly better than the other two algorithms. One could argue that because we used AWGN to approximate

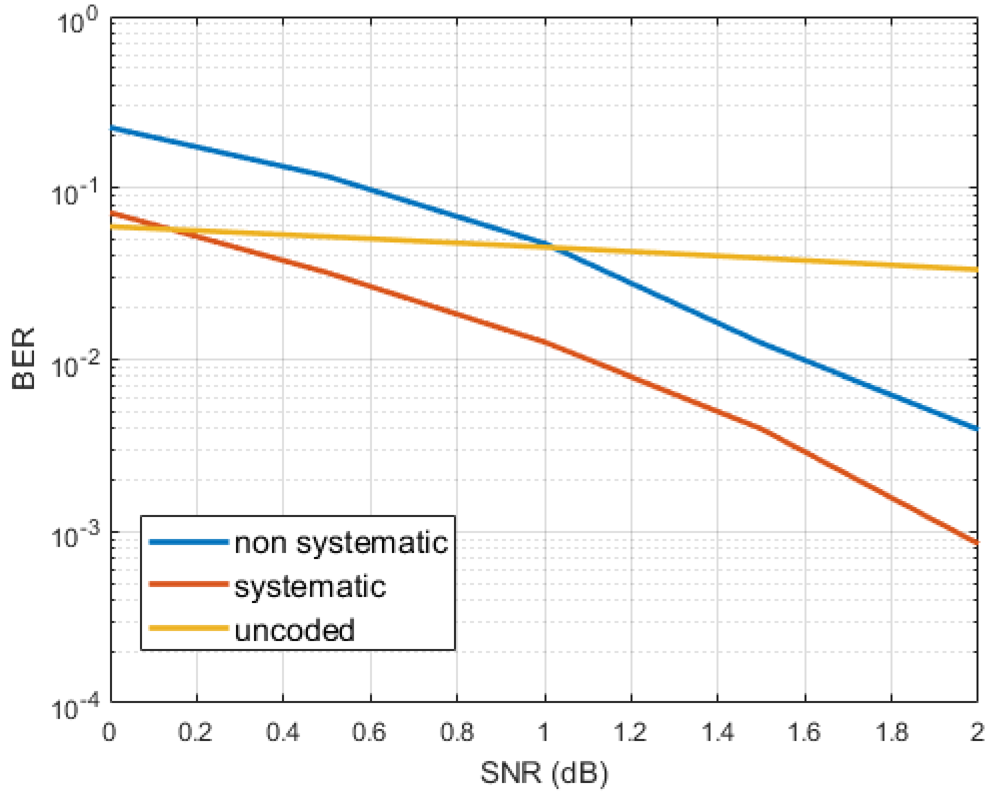

Fig. 6.6. Polar code encoding methods comparison.

the HF Kappa channel capacity, the result is inferior. We can only estimate that BP achieves similar performance to capacity method.

For the initial SNR, we oberve that in the case of BP, for lower SNR, lower initial SNR provides better performance while for higher SNR, higher initial SNR provides better performance result. In the case of capacity method, for lower SNR, higher initial SNR provides better performance while for higher SNR, only slightly lower initial SNR provides better performance. If only one initial SNR is used for all SNRs, then is is reasonable to choose 0dB. However, if some intial SNR values can be chosen to tune up for better performance, then we can see the direction of paramter tuning.

We note the for Figure 6.5, 6.6, and 6.7, the simulation is based on the use of BP with initial SNR = 0dB.

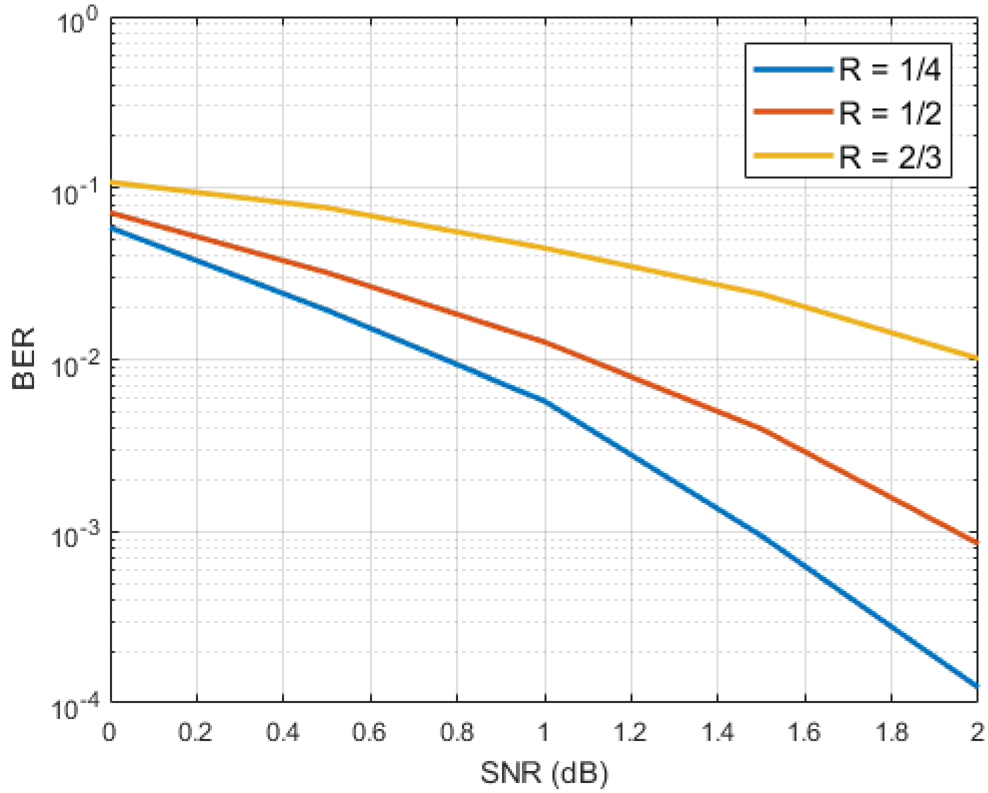

Fig. 6.7. Polar code rate comparison.

6.8 Conclusion

In this work, we have discussed how to construct polar code for the HF communication link around sunrise. Simulation results shows that by properly design the polar code, one can achieve significantly lower BER compared with the uncoded case. Poler code can make this communication link more reliable.

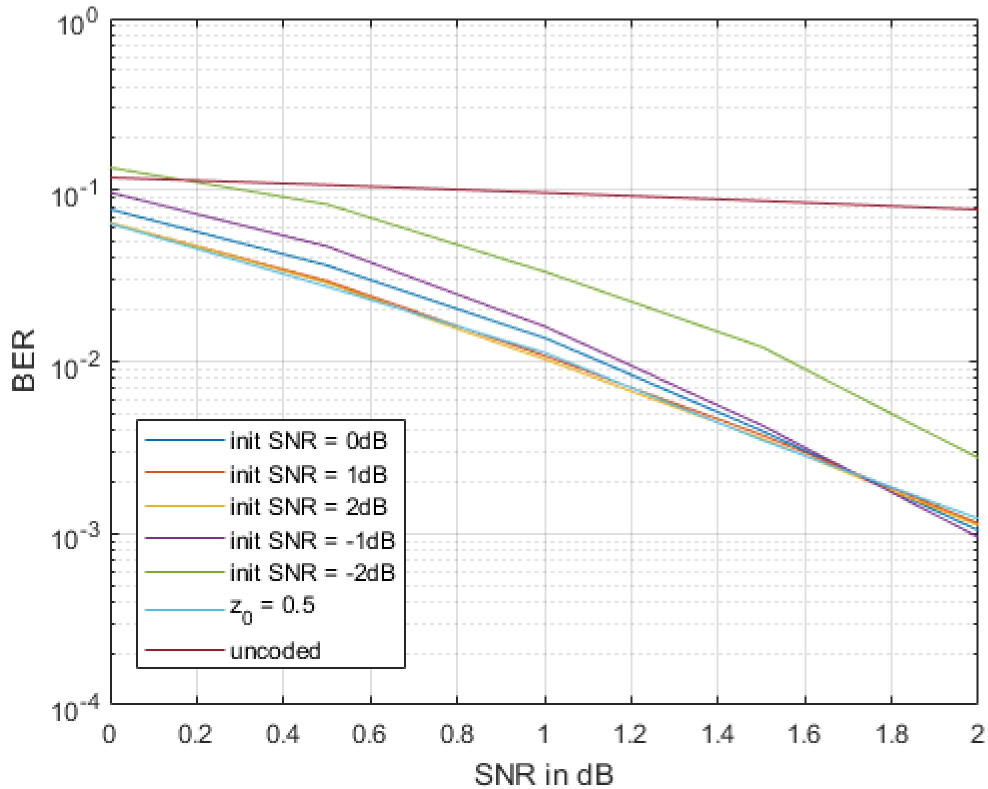

Fig. 6.8. Polar code initial value selection comparison with $z_0 = 0.5$ and $z_0 = 1 - C$.

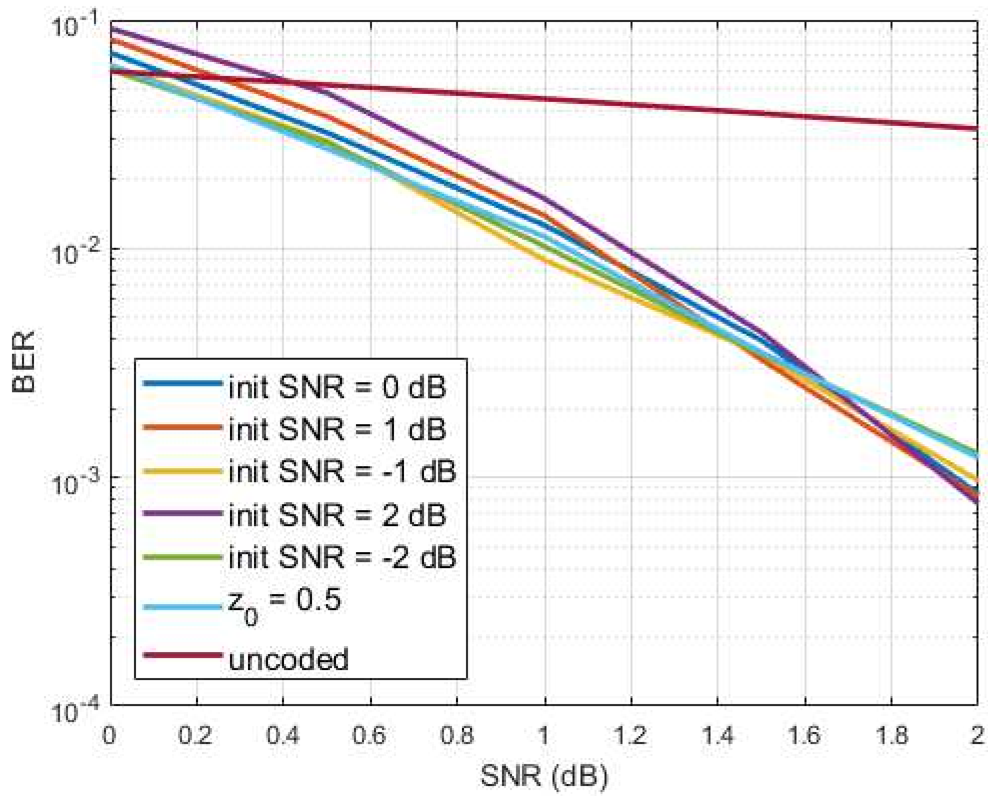

Fig. 6.9. Polar code initial value selection comparison with $z_0 = BP$.

7. THE CHANNEL CAPACITY FOR HF AROUND SUNRISE

In this work, we look at the high frequency (HF) channel model for the sunrise scenario. The noise is considered to be dominated by additive Kappa noise process. We find the channel capacity in this case. We then find out the fading channel capacity with Rayleigh and Rician fading as well as the outage probability. The results indicate that, when the sun just rises, the ionosphere is near thermal antiequilibrium state, the capacity is higher than normal.

7.1 Introduction

HF communication represents the communication link via the usage of the ionosphere of the Earth. The transmitter sends the signal to the ionosphere and the reach the destination by reflection. The frequency range is between 3 to 30 MHz. Although this means smaller data rates compared with the civilian communication systems such as 3GPP and LTE-a, in cases that civilian communication are not available such as disaster, war, and space planetary communication, HF becomes much more important.

It has been shown in [26] that for HF, the sampled noise distribution cannot be concluded as Gaussian. In [17], the author concluded that the noise at sunrise obtained in a quiet place has modified Bi-Kappa distribution. We analyzed the measured data in [17], [21], and [34] and concluded that the noise should be better modeled as Kappa-Gaussian mixture distribution [49]. At high signal-to-noise ratio (SNR), it can be approximated as Kappa. The reason stems recent physics result [32]. The electron density distribution should be considered as Kappa-Gaussian mixture. The Gaussian part accounts for the slower electrons while the Kappa portion accounts for the faster electrons. Electrons with higher energy deviates from standard statistical mechanics result and have been proven to behave in Kappa distribution [30] [31]. It can be shown [49] that electron velocity distribution can be mapped to the sampled noise probability density function (pdf). Thus, we arrive the claimed channel model.

Once the channel model has been established, a natural question rises up as to what the channel capacity is in this case. Also, past literature [93] [94] [95] reported that fading problems exist in HF communication, ranging from Rayleigh to Rician. The channel capacity will be degraded by this behavior. How much performance is lost is studied in this work.

Our work can be easily applied to any channel with capacity of similar form. In underwater acoustic (UWA) communication, under certain circumstances [96], the dominated noise component can be described by the Generalized Gaussian distribution. The capacity for such channel has been derived in [97] [98], the capacity result bears same form as the Kappa case. So the capacity for the fading case can be found according to our work.

We present our work as shown in the following order. In Section 7.2, we provide the basic channel model. In Section 7.3, we derive the channel capacity. In Section 7.4, we derive the capacity due to Rician and Rayleigh fading. In Section 7.5, we find out the corresponding outage probability. In Section 7.6, we show how our analysis can be applied to other communication channel with same form in capacity. In Section 7.7, we provide numerical result. In Section 7.8, we draw conclusions.

7.2 System Model

The HF communication system at sunrise is shown in Equation (7.1) and Figure 7.1. Here, y is the output, x is the input, and z is the noise.

$$y = x + z \tag{7.1}$$

The noise behaves Kappa distribution with pdf given in Equation (7.2).

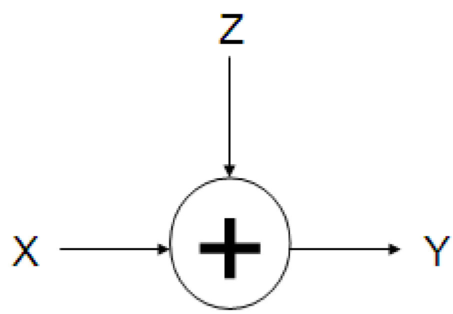

Fig. 7.1. Additive channel model.

$$f\left(z;K,\sigma\right)=\frac{1}{\sqrt{K}\sigma\beta\left(\frac{1}{2},K+\frac{1}{2}\right)}\left(1+\frac{z^2}{K\sigma^2}\right)^{-K-1}, \quad -\infty<z<\infty, K>\frac{1}{2} \tag{7.2}$$

The K value in the Kappa distribution represents the state of thermal equilibrium. When K is small, it indicates thermal antiequilibrium. The electrons moves much faster and thus form the polynomial tail distribution. When K is large, the pdf becomes Gaussian. In statistical mechanics, this represents thermal equilibrium.

The input is subjected to power constraint as shown in Equation (7.4).

$$C=\max I\left(X;Y\right) \tag{7.3}$$

$$\text{subject to } E\left[X^2\right]\leq P \tag{7.4}$$

The signal-to-noise ratio (SNR) is defined as shown in Equation (7.5) [57].

$$SNR=\frac{P}{\frac{K\sigma^2}{2K-1}} \tag{7.5}$$

7.3 Channel Capacity

The differential entropy of z is derived as follows.

$$h(Z)=-\int_{-\infty}^{\infty}f(z)\log_2 f(z)\ dz$$

$$=\frac{K+1}{\sqrt{K}\sigma\beta\left(\frac{1}{2},K+\frac{1}{2}\right)\ln 2}\int_{\infty}^{\infty}\left(1+\frac{z^2}{K\sigma^2}\right)^{-K-1}\ln\left(1+\frac{z^2}{K\sigma^2}\right)^{-K-1}dz \tag{7.6}$$

$$+\frac{1}{\ln 2}\ln\left[\sqrt{K}\sigma\beta\left(\frac{1}{2},K+\frac{1}{2}\right)\right]\int_{-\infty}^{\infty}f(z)\ dz \tag{7.7}$$

$$=\frac{1}{2}\log_2 e^{2g(K)} \tag{7.8}$$

$$+\frac{1}{2}\log_2 K\sigma^2\beta^2\left(\frac{1}{2},K+\frac{1}{2}\right) \tag{7.9}$$

$$=\frac{1}{2}\log_2 e^{2g(K)}K\sigma^2\beta^2\left(\frac{1}{2},K+\frac{1}{2}\right) \tag{7.10}$$

Here, Equation (7.7) evaluates to Equation (7.9) because the integral of a pdf is 1. $g(K)$ is defined in Equation (7.11).

$$g(K) \equiv (K+1)\left[\Psi\left(K+1\right)-\Psi\left(K+\frac{1}{2}\right)\right] \tag{7.11}$$

where $\Psi(x)$ is the Euler function.

We now prove that Equation (7.6) leads to Equation (7.8).

$$\begin{aligned}
(7.6) &= \frac{(K+1)}{\beta\left(\frac{1}{2},K+\frac{1}{2}\right)\ln 2}\int_1^{\infty} u^{-K-1}\left(u-1\right)^{-\frac{1}{2}}\ln u\ du && (7.12)\\
&= \frac{-(K+1)}{\beta\left(\frac{1}{2},K+\frac{1}{2}\right)\ln 2}\int_0^{1} v^{K-\frac{1}{2}}\left(1-v\right)^{-\frac{1}{2}}\ln v\ dv && (7.13)\\
&= \frac{-(K+1)}{\beta\left(\frac{1}{2},K+\frac{1}{2}\right)\ln 2}\beta\left(\frac{1}{2},K+\frac{1}{2}\right)\left[\Psi\left(K+1\right)-\Psi\left(K+\frac{1}{2}\right)\right] && (7.14)\\
&= (7.8)
\end{aligned}$$

Equation (7.12) is obtained by change of variable $u=1+\frac{x^2}{K\sigma^2}$. Equation (7.13) is obtained by change of variable $v=\frac{1}{u}$. Equation (7.14) is obtained by Equation 4.253-1 in P540 of [69] with $\mu=K+\frac{1}{2}$, $r=1$, and $v=\frac{1}{2}$.

We now find the channel capacity according to [99].

$$
\begin{aligned}
C &= \max_{f_X(x):\mathrm{E}[X^2]\leq P} I\left(X;Y\right) \\
&= \max_{f_X(x):\mathrm{E}[X^2]\leq P} h\left(Y\right) - h\left(Y|X\right) \\
&= \max_{f_X(x):\mathrm{E}[X^2]\leq P} h\left(Y\right) - h\left(X+Z|X\right) \\
&= \max_{f_X(x):\mathrm{E}[X^2]\leq P} h\left(Y\right) - h\left(Z|X\right) \\
&= \max_{f_X(x):\mathrm{E}[X^2]\leq P} h\left(Y\right) - h\left(Z\right) \\
&= \frac{1}{2}\log_2 2\pi e\left(P + \frac{K\sigma^2}{2K-1}\right) \\
&- \frac{1}{2}\log_2 e^{2g(K)} K\sigma^2\beta^2\left(\frac{1}{2}, K+\frac{1}{2}\right) \qquad (7.15) \\
&= \frac{1}{2}\log_2 \alpha(K)(1+SNR) \qquad (7.16)
\end{aligned}
$$

Here, Equation (7.15) is obtained by Equation (7.10), Equation (7.5), and the fact that Gaussian distribution maximized the differential entropy for $h(Y)$. The definition of $\alpha(K)$ is shown in Equation (7.17). A plot of $\alpha(K)$. Notice that for large K, it approaches to 1, the channel becomes Gaussian. This function shows the gap between Gaussian and Kappa. The gap decreases for increasing K.

$$
\alpha\left(K\right) \equiv \frac{2\pi}{e^{2g(K)-1}\left(2K-1\right)\beta^2\left(\frac{1}{2}, K+\frac{1}{2}\right)} \qquad (7.17)
$$

7.4 Capacity for Fading Case

For fading case, the system model is updated into Equation (7.18).

$$
y = hx + z \qquad (7.18)
$$

According to Equation (7.16), the capacity for this case is described in Equation (7.19).

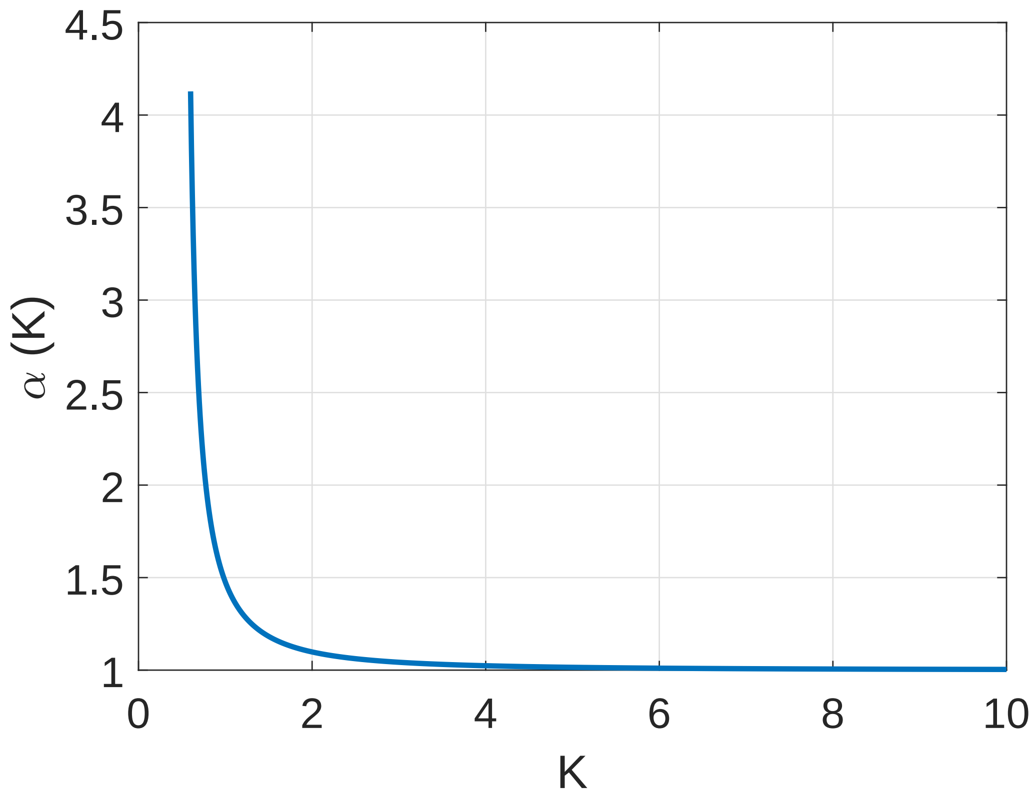

Fig. 7.2. The plot of $\alpha(K)$.

$$C_{fading} = \mathrm{E}_h \left[\log_2 \alpha(K) \left(1 + SNR|h|^2\right)\right] = \mathrm{E}_\gamma \left[\log_2 \alpha(K) \left(1 + \gamma\right)\right] \tag{7.19}$$

We assume the fading process has Rician distribution. We also assume that the formation of this Rician distribution is by $\sqrt{U^2 + V^2}$, where U and V have variance equal to $\frac{1}{2}$. The distribution for γ is given by Equation (7.20) [100] [101].

$$f_\gamma(\gamma) = \frac{e^{-K_a^2}}{SNR} e^{-\frac{\gamma}{SNR}} I_0 \left(\frac{2K_a\sqrt{\gamma}}{\sqrt{SNR}}\right) \tag{7.20}$$

where K_a is the Rician factor, and $I_0(x)$ is the modified Bessel function of the first kind of order zero. Its series representation is shown in Equation (7.21) [69].

$$I_0(z) = \sum_{k=0}^{\infty} \frac{\left(\frac{1}{4}z^2\right)^k}{(k!)^2} \tag{7.21}$$

Rician distribution is a general distribution used for describing fading statistics. When $K_a = 0$, it reduces to Rayleigh distribution. The average channel capacity is derived as follows.

$$(7.19) = \int_0^\infty \log_2 \alpha(K) f_\gamma(\gamma) d\gamma \tag{7.22}$$

$$+ \int_0^\infty \log_2 (1 + \gamma) f_\gamma(\gamma) d\gamma \tag{7.23}$$

We evaluate Equation (7.23) as follows.

$$(7.23) = \frac{e^{-K_a^2}}{SNR\ln 2}\int_0^\infty e^{-\frac{\gamma}{SNR}} I_0\left(\frac{2K_a\sqrt{\gamma}}{\sqrt{SNR}}\right)\ln(1+\gamma)d\gamma$$

$$= \frac{e^{-K_a^2}e^{\frac{1}{SNR}}}{SNR\ln 2}\int_1^\infty e^{-\frac{u}{SNR}}\ln u \sum_{k=0}^{\infty}\frac{\left(\frac{K_a^2}{SNR}\right)^k (u-1)^k}{(k!)^2}du \tag{7.24}$$

$$= \frac{e^{-K_a^2}e^{\frac{1}{SNR}}}{SNR\ln 2}\sum_{k=0}^{\infty}\frac{\left(\frac{K_a^2}{SNR}\right)^k}{(k!)^2}\sum_{j=0}^{k}\binom{k}{j}(-1)^j\times$$

$$\int_1^\infty e^{-\frac{u}{SNR}}u^j\ln u du \tag{7.25}$$

$$= \frac{e^{-K_a^2}e^{\frac{1}{SNR}}}{SNR\ln 2}\sum_{k=0}^{\infty}\frac{\left(\frac{K_a^2}{SNR}\right)^k}{(k!)^2}\sum_{j=0}^{k}\binom{k}{j}(-1)^j\times$$

$$\left[\int_0^\infty e^{-\frac{u}{SNR}}u^j\ln u du - \int_0^1 e^{-\frac{u}{SNR}}u^j\ln u du\right]$$

$$= \frac{e^{-K_a^2}e^{\frac{1}{SNR}}}{SNR\ln 2}\sum_{k=0}^{\infty}\frac{\left(\frac{K_a^2}{SNR}\right)^k}{(k!)^2}\sum_{j=0}^{k}\binom{k}{j}(-1)^j\times$$

$$\left((SNR)^{j+1}\Gamma(j+1)\left[\Psi(j+1)+\ln SNR\right] - \delta(SNR,j)\right) \tag{7.26}$$

where Equation (7.24) is obtained by change of variable $u = 1+\gamma$, Equation (7.25) is obtained by using Equation (7.21). Equation (7.26) is obtained by [69](P.573 4.352-1) and by setting $\delta(SNR,j) \equiv \int_0^1 e^{-\frac{u}{SNR}}u^j\ln u du$.

By using Equation (7.22), (7.23), (7.26) the capacity is shown in Equation (7.27)

$$(7.19) = \log_2\alpha(K) + (7.26) \tag{7.27}$$

Special Case: Rayleigh fading

Rayleigh fading refers to the case when the envelope distribution is Rayleigh, this corresponds to

$$f_\gamma(\gamma) = \frac{1}{\overline{\gamma}}e^{-\frac{\gamma}{\overline{\gamma}}}u(\gamma) \tag{7.28}$$

Here, we have incorporated SNR into γ. So γ represents average SNR. In Equation (7.20), when $K_a = 0$, the pdf reduces to Rayleigh fading. However, there exists an easier representation for capacity analysis. Let $E_1(x) = \int_x^{\infty} \frac{e^{-t}}{t}\, dt$. This is the exponential integral defined in [102]. By using change of variables with $r = e^{-t}$ and $ds = \frac{1}{t}dt$, we get $\int_x^{\infty} e^{-t}\ln t\; dt = E_1\left(x\right) + e^{-x}\ln x$. So the Rayleigh fading capacity can be found as shown in Equation (7.29).

$$\begin{aligned} C_{fading,Rayleigh} &= \int_0^{\infty} \left[\log_2 \alpha(K) + \frac{\ln(1+\gamma)}{\ln 2}\right] \frac{1}{\bar{\gamma}} e^{-\frac{\gamma}{\bar{\gamma}}} d\gamma \\ &= \log_2 \alpha(K) + \frac{e^{\frac{1}{\bar{\gamma}}}}{\ln 2} E_1\left(\frac{1}{\bar{\gamma}}\right) \end{aligned} \tag{7.29}$$

7.5 Outage Probability

The outage probability is defined as the probability that the average channel capacity falls below a given rate R. For Rician fading we obtain the result in Equation (7.30) with the help from [101].

$$\begin{aligned} P_{outage}\left(\{C_{fading} < R\}\right) &= P_{outage}\left(\left\{\gamma < \frac{2^R}{\alpha(K)} - 1\right\}\right) \\ &= \int_0^{\frac{2^R}{\alpha(K)}-1} f_\gamma(\gamma) \\ &= 1 - Q_1\left(\sqrt{2K_a}, \frac{\sqrt{\frac{2^R}{\alpha(K)} - 1}}{\sqrt{2SNR}}\right) \end{aligned} \tag{7.30}$$

where $Q_1(x, y)$ is the first-order Marcum Q function. The above result is only valid for the case when $R > \log_2 \alpha(K)$. For the case when $R \leq \log_2 \alpha(K)$, we get 0 because $f_\gamma(\gamma)$ is 0 for $\gamma < 0$.

For Rayleigh fading, we obtain an easier representation as shown in Equation (7.31).

$$
\begin{aligned}
&P_{outage}\left(\{C_{fading} < R\}\right) = P_{outage}\left(\left\{\gamma < \frac{2^R}{\alpha(K)} - 1\right\}\right) \\
&= \int_0^{\frac{2^R}{\alpha(K)}-1} \frac{1}{\bar{\gamma}} e^{-\frac{\gamma}{\bar{\gamma}}} \\
&= 1 - e^{-\frac{\frac{2^R}{\alpha(K)}-1}{\bar{\gamma}}}
\end{aligned}
\tag{7.31}
$$

7.6 Application

The channel capacity for UWA with Generalized Gaussian noise has been found as shown in Equation (7.33) [97] [98]. The pdf is provided in Equation (7.32).

$$
f_{\mathbf{X}}(x) = \frac{\beta}{2\alpha\Gamma(\frac{1}{\beta})} e^{-\frac{|x|^\beta}{\alpha^\beta}}, -\infty < x < \infty \tag{7.32}
$$

$$
C_{AWGGN}\left(SNR;\beta\right) = \frac{1}{2}\log_2\left[G\left(\beta\right)\left(1 + SNR\right)\right] \tag{7.33}
$$

where

$$
G\left(\beta\right) = \frac{\pi\beta^2\Gamma\left(\frac{3}{\beta}\right)}{2\Gamma^3\left(\frac{1}{\beta}\right)e^{\frac{2}{\beta}-1}}
$$

is a constant for any fixed channel upon transmission that only depends on β. Notice that the channel capacity for this case has the same form as in the HF Kappa case in that both expressions can be written as $\log_2 A\left(1 + SNR\right)$. The constant A provides a constant change in the capacity and a nonlinear change in the outage probability. Thus, by substituting the $\alpha(K)$ with $G\left(\beta\right)$, we get the fading capacity and outage probability for the UWA case. In the future, people could find other channels with capacity expressions to share the same form as the one we presented. Our results can be readily utilized to solve for the fading capacity.

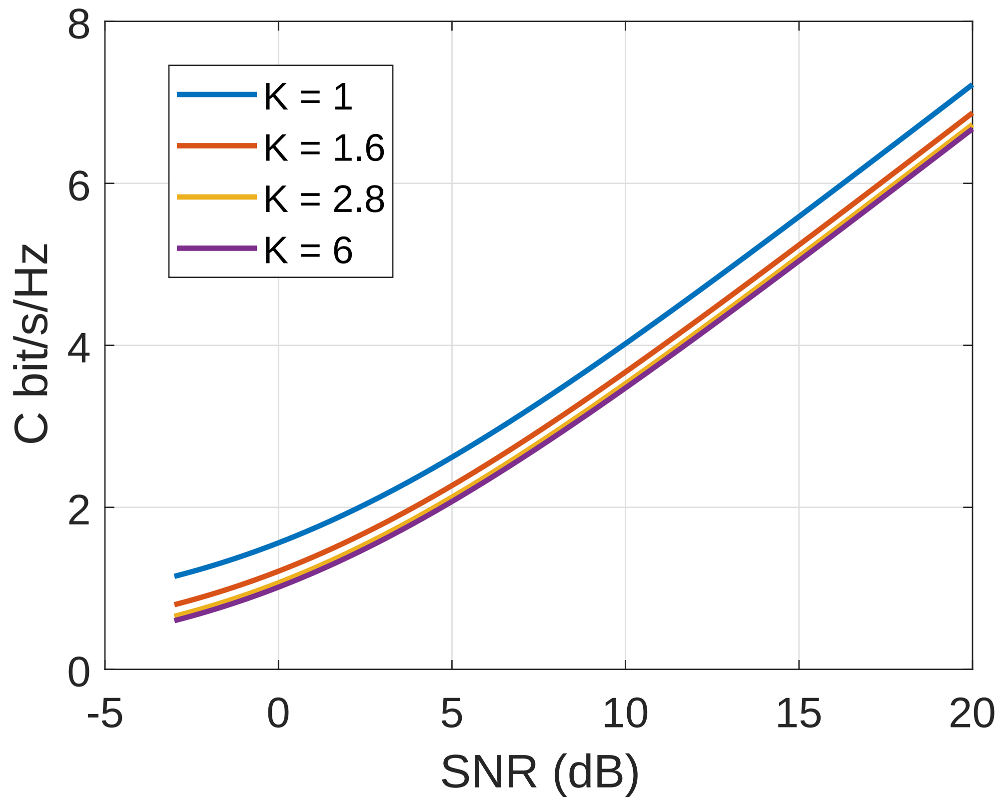

Fig. 7.3. The channel capacity for HF communication dominated by Kappa noise.

7.7 Numerical Result

In this section, we provide numerical result for the various capacity scenarios we have discussed up to now. The capacity of HF is shown in Figure 7.3. As K increases, the result becomes the standard capacity of Gaussian noise. Notice that higher K represents earlier time, so this result shows that at sunrise (or when the ionosphere is closer to thermal instability), we actually have higher capacity.

Figure 7.4 and 7.6 show the HF capacity with Rayleigh and Rician fading ($K_a = 2$) respectively. Line of sight component strengthens the capacity and its relative power increases. The relationship of those capacities with K is the same as in the previous paragraph.

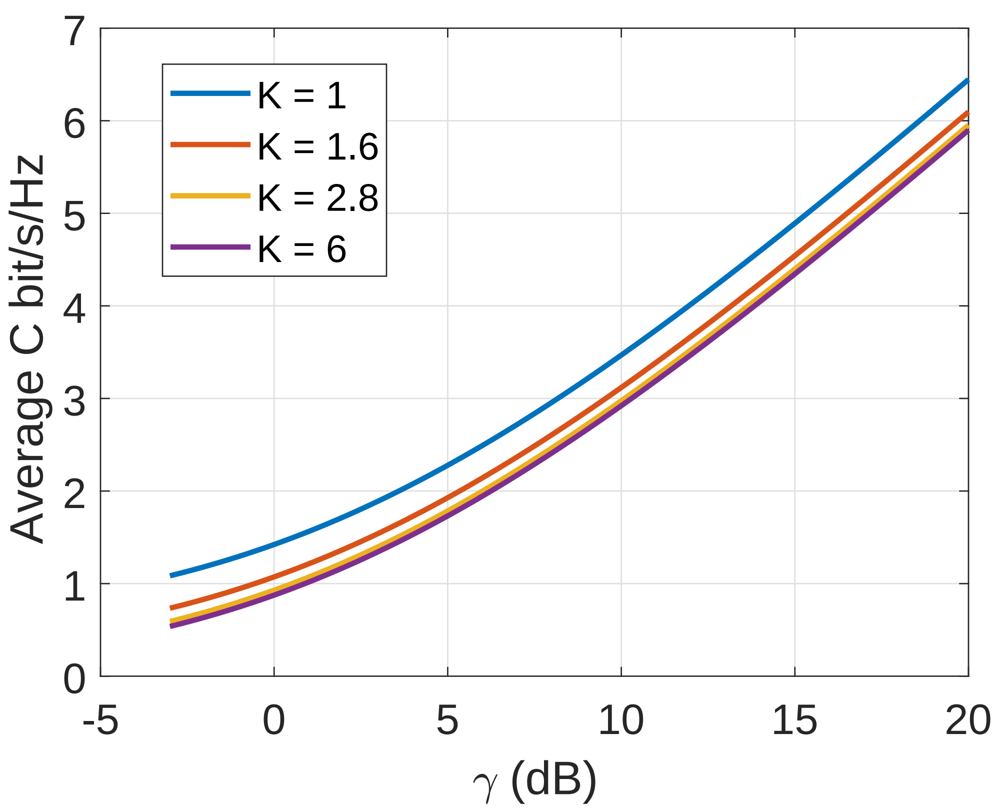

Fig. 7.4. The channel capacity for HF communication dominated by Kappa noise with Rayleigh fading.

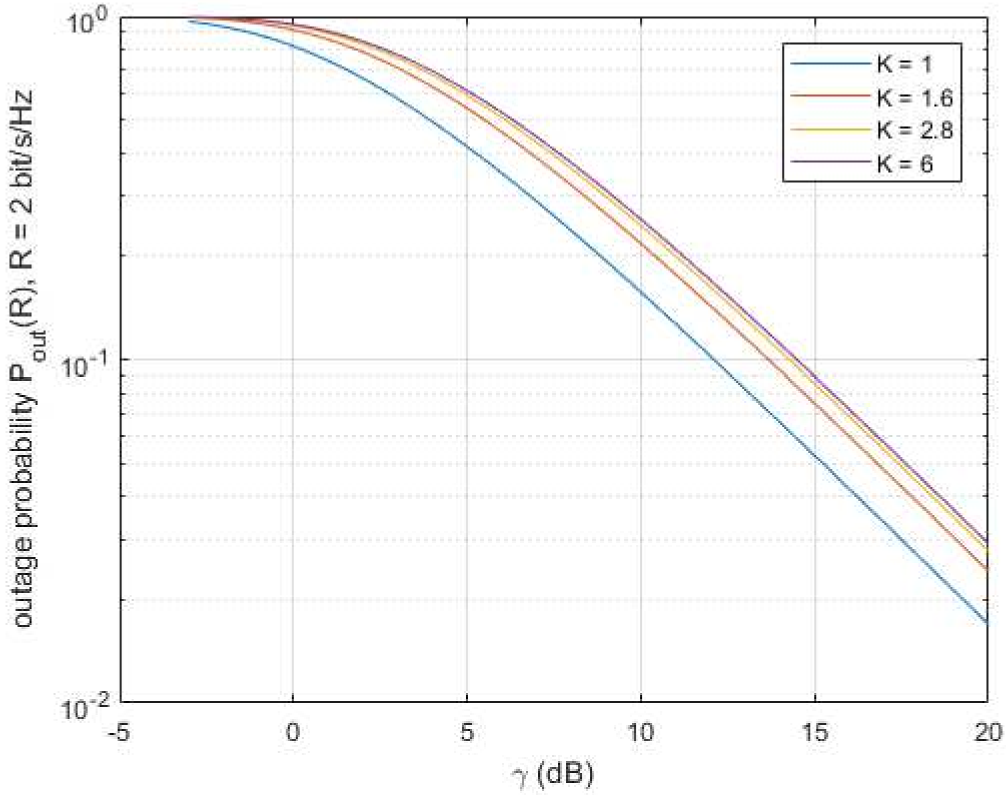

Fig. 7.5. The outage probability for HF communication dominated by Kappa noise with Rayleigh fading. R = 2.

Figure 7.5 and 7.7 show the HF outage probability with Rayleigh and Rician fading ($K_a = 2$) respectively. Here, we use the fixed rate R = 2. The outage probability is higher in Rayleigh fading than in Rician fading. As SNR increases, the outage probability decreases.

7.8 Conclusion

In this work, we introduced the HF galactic Kappa noise model. We derived the channel capacity and then found the capacity for the fading scenario. The fading can be Rayleigh or Rician. We also derived the outage probability. We have proven that our analysis can be applied to every channel capacity with the same form as in

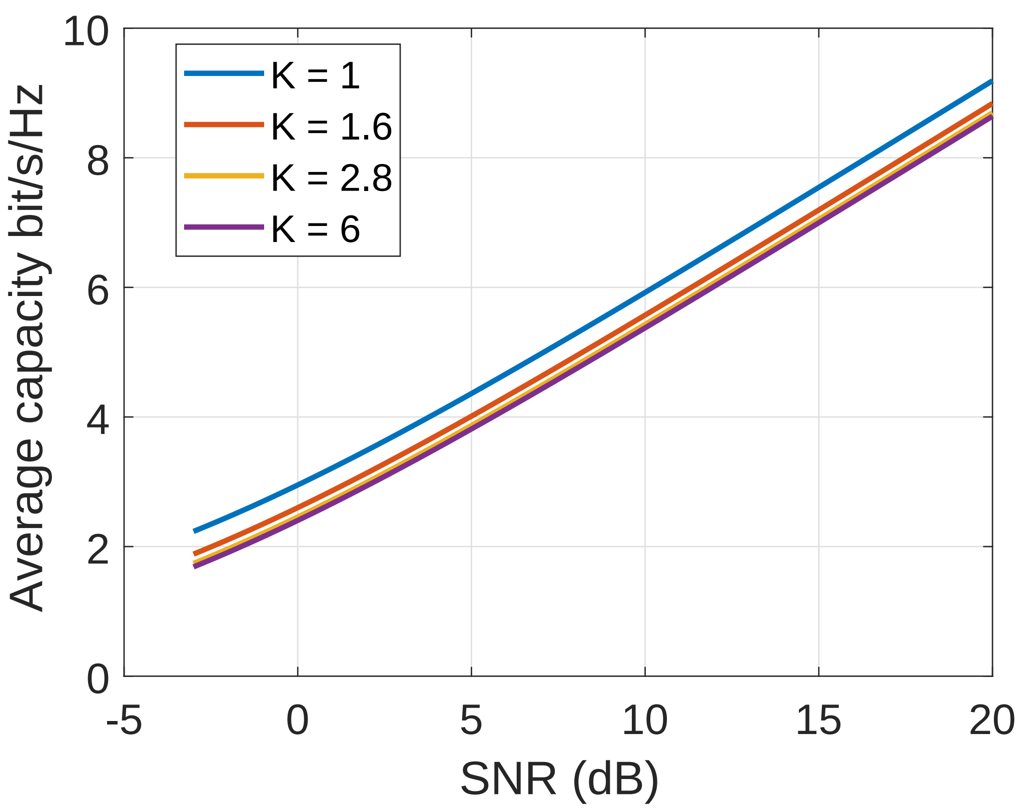

Fig. 7.6. The channel capacity for HF communication dominated by Kappa noise with Rician fading. $K_a = 2$.

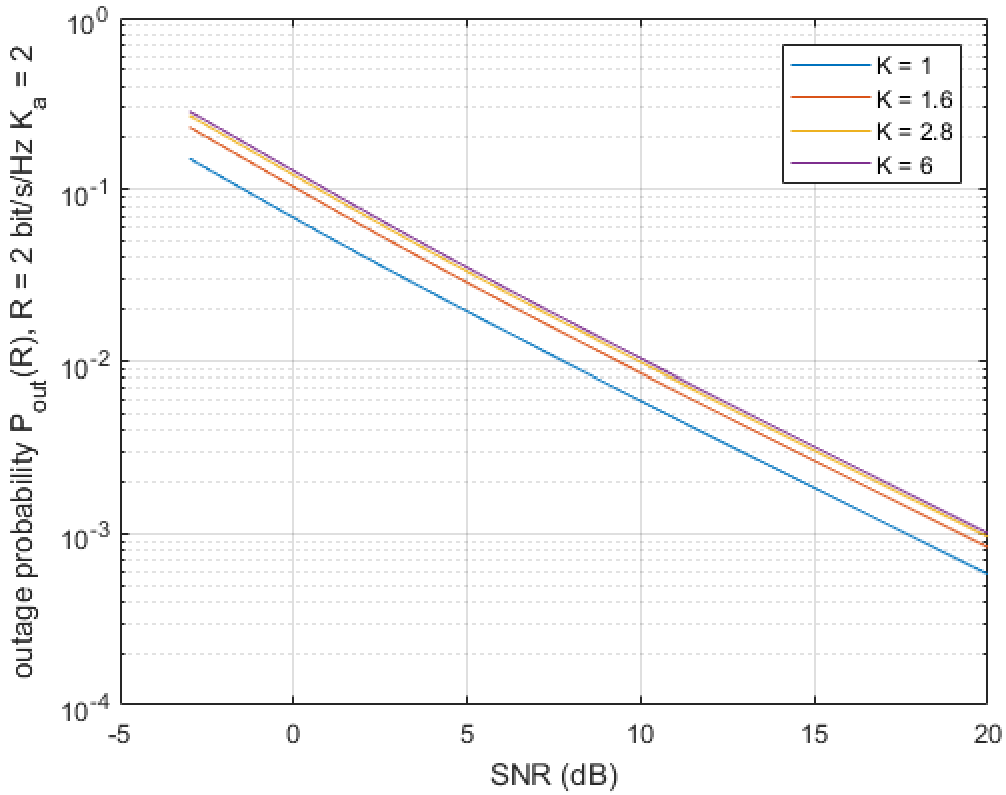

Fig. 7.7. The outage probability for HF communication dominated by Kappa noise with Rician fading. R = 2, $K_a = 2$.

our work. The numerical results shows that at lower values of K (shifting towards thermal antiequilibrium), we have higher capacity.

8. THE SECRECY CAPACITY FOR UNDERWATER ACOUSTIC CHANNEL WITH DOMINANT NOISE SOURCE

In this work, we explore the underwater acoustic (UWA) channel. When there exist some dominant noise sources in the shallow water region, the sampled noise probability density function (pdf) may not be Gaussian. Specifically the noise model is additive generalized Gaussian (AWGGN). We derive the average secrecy capacity and the outage probability of secrecy capacity in this case. We then look at one particular underwater communication scenario for numerical example. Our results shows that even if the eavesdropper has better channel condition, there still exists nonzero average secrecy capacity. This enables the communication link to develop coding schemes to protect the information.

8.1 Introduction

The UWA communication [103] [104] [105] environment poses significant difference to the wireless communication system based on electromagnetic waves. The issue arises from the fact that acoustic wave travels with much less speed (1500 m/s) compared with electromagnetic waves ($3 * 10^8$ m/s). Various physical effects and noise make this channel challenging. From the commercial and scientific point of view, understanding this channel improves communication quality such as oil-drilling and biology observation. From the military point of view, understanding this channel provides the submarines more robust communication link and thus can operate better.

Channel modeling for this communication link has been extensively investigated. The Gaussian noise model is widely used. However, there are cases in which the sampled noise may not be Gaussian. As depicted in [103], site-specific noise are often non-Gaussian. Furthermore, such non-Gaussian noise could dominate the noise pdf. In [96], the authors chose the additive Generalized Gaussian distribution to capture the algebraic tail in the shallow water region. The UWA communication contains multipath fading as well. Fading degrades the received signal-to-noise ratio (SNR), making detection less accurate. In [106] [107] [108], Rayleigh distribution for fading statistics are proposed. Our work is based on the additive Generalized Gaussian noise with Rayleigh fading.

Several research in the past deal with the Generalized Gaussian noise. In [96], the authors derived bit error rate (BER) for various modulation schemes. In [109], the authors built up a simulator for this type of noise. In [97] and [98], channel capacity is investigated. Specifically in [97], the authors mentioned secrecy capacity without considering fading because their system model did not include such case. Therefore, much more work can be developed when fading is utilized.

The idea of secrecy capacity stems from the scenario in which the legitimate users (Alice and Bob) wish to communicate without letting the eavesdropper (Eve) know their information. At the application layer, the scheme for secure transmission is termed as cryptography [110]. Recently, at physical layer, [111] devised secure transmission based on fading. Presumably, one would expect that if Eve has higher average SNR than Bob, then there is no chance Alice can secure the communication link. However, the fading process provides some chance in which the instantaneous SNR for Alice to Bob is higher than Alice to Eve. The secrecy capacity is not 0 in this case. Hence, coding schemes on the physical layer can secure transmission.

In our work, we wish to find the average secrecy capacity for the case of additive Generalized Gaussian noise with Rayleigh fading. Outage probability for the secrecy capacity analysis will be performed as well. A realistic communication scenario is provided to show the opportunities for secure transmission.

The channel capacity for the generalized Gaussian case is the product of a constant and the term for the Gaussian case. The value of the constant affects the analysis for secrecy capacity and outage probability. We develop a novel way to analyze these quantities by separating cases. Our method can be applied to other channels with capacity bearing the same form as the generalized Gaussian case.

Generalized Gaussian distribution is not only found in UWA. It has been reported [112] that in multiple-input multiple-output (MIMO) diffusion-based molecular communication, the noise statistics at the output of receive antenna with zero forcing algorithm follows Generalized Gaussian distribution. Thus, our analysis is not only beneficial to UWA communication, but to other communication systems as well.

The remaining sections proceed as follows. In Section 8.2, we state the system model. In Section 8.3, we derive some math formula to facilitate later analysis. In Section 8.4, we derive the secrecy capacity. In Section 8.5, we derive the outage probability. In Section 8.6, we provide numerical result. Finally, in Section 8.7, we draw conclusions.

8.2 System Model

Figure 8.1 shows the UWA communication scenario involving an eavesdropper.

$$\mathrm{y}_i = \mathrm{h}_i \mathrm{x} + \mathrm{n}_i \tag{8.1}$$

where i = B or E. B represents Bob the receiver and E represents Eve the eavesdropper. h_i is assumed to be Reyleigh fading with complex normal distribution CN(0,σ^2). Hence, $\gamma = |h|^2$ has exponential distribution as shown in Equation (8.2).

$$f_\gamma\left(\gamma\right) = \frac{1}{\overline{\gamma}} e^{-\frac{\gamma}{\overline{\gamma}}} u\left(\gamma\right), \overline{\gamma} = \sigma^2 \tag{8.2}$$

From [96], the noise pdf is shown in Equation 8.3.

$$f_{\mathbf{X}}(x) = \frac{\beta}{2\alpha\Gamma(\frac{1}{\beta})} e^{-\frac{|x|^\beta}{\alpha^\beta}}, -\infty < x < \infty \tag{8.3}$$

We assume in this work that all communication links are slow fading. Alice and Bob have perfect knowledge on the noise and fading statistics for their link. They

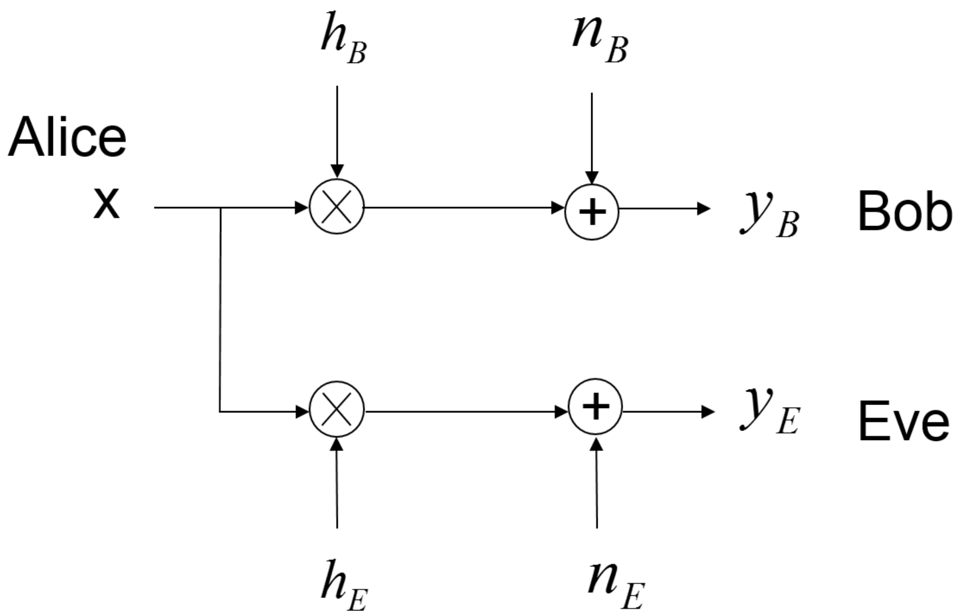

Fig. 8.1. The UWA secrecy transmission system. Bob represents the intended receiver. Eve represents the eavesdropper.

also have partial knowledge on Eve's fading statistics. Eve has perfect knowledge on noise and fading statistics for her link. We also assume that the channel input, the noise and the fading statistics are all independent.

The channel capacity for the non-fading case has been found as shown in Equation (8.4) [97].

$$C_{AWGGN}\left(SNR;\beta\right) = \frac{1}{2}\log_2\left[G\left(\beta\right)\left(1+SNR\right)\right] \tag{8.4}$$

where

$$G\left(\beta\right) = \frac{\pi\beta^2\Gamma\left(\frac{3}{\beta}\right)}{2\Gamma^3\left(\frac{1}{\beta}\right)e^{\frac{2}{\beta}-1}}$$

is a constant for any fixed channel upon transmission that only depends on β.

For fading case, the average channel capacity is shown in Equation (8.5).

$$C_{AWGGN}\left(SNR;\beta\right) = E_{\mathbf{h}}\left[\log_2\left(G\left(\beta\right)\left(1+|h|^2 SNR\right)\right)\right] \tag{8.5}$$

Notice that the factor $\frac{1}{2}$ has been replaced by 1. The reason is to account for the real and imaginary parts. From now on, we replace $|h|^2 SNR$ with random variable γ.

The channel capacity for the receiver is shown in Equation (8.6) while for the eavesdropper is shown in Equation (8.7).

$$C_B\left(\gamma_E;\beta_E\right) = \frac{1}{2}\log_2\left[G\left(\beta_B\right)\left(1+\gamma_B\right)\right] \tag{8.6}$$

$$C_E\left(\gamma_E;\beta_E\right) = \frac{1}{2}\log_2\left[G\left(\beta_E\right)\left(1+\gamma_E\right)\right] \tag{8.7}$$

8.3 Math Tools

Before we derive the average secrecy capacity. It is beneficial to construct some lemma that will useful in later stages.

Definition 8.3.1 *The exponential integral is defined as [102]*

$$E_1(x) = \int_x^\infty \frac{e^{-t}}{t}\,dt \tag{8.8}$$

Following the definition of exponential integral, we develop some tools that can help us evaluate certain integral in the future.

Lemma 8.3.1

$$1.\ \int_x^\infty e^{-t}\ln t\,dt = E_1\left(x\right) + e^{-x}\ln x \tag{8.9}$$

$$2.\ \int_{u_0}^\infty e^{-\alpha u}\ln u\,du = \frac{1}{\alpha}\left[E_1\left(\alpha u_0\right) + e^{-\alpha u_0}\ln\left(u_0\right)\right] \tag{8.10}$$

$$3.\ \int_0^\infty e^{-\alpha u}\ln\left(1+u\right)\ du = \frac{e^\alpha}{\alpha}E_1\left(\alpha\right) \tag{8.11}$$

Proof: 1. Change of variables on the left hand side by using $r = e^{-t}$ and $ds = \frac{1}{t}dt$. 2. Let $x = \alpha u_0$, then the left hand side of Equation (8.10) becomes

$\int_{\alpha u_0}^{\infty} e^{-x}\left(\ln x - \ln\alpha\right)\frac{1}{\alpha}\,dx$. By using Equation (8.9), we get the proof. 3. Let $x = u+1$, the left hand side of Equation (8.11) becomes $e^{\alpha}\int_1^{\infty} e^{-\alpha x}\ln x\,dx$. By using Equation (8.10), we get the proof.

Q.E.D.

8.4 Average Secrecy Capacity

We reformulate the secrecy capacity for one realization (γ_B, γ_E) that was introduced in [111]. This is shown in Equation 8.12.

$$C_s\left(\gamma_B, \gamma_E\right) = \begin{cases} C_B - C_E & \text{if } C_B > C_E \\ 0 & \text{if } C_B \le C_E \end{cases} \tag{8.12}$$

If we assume perfect channel side information (CSI) of the eavesdropper's channel is available to Alice the transmitter, then the average secrecy capacity can be found as

$$\overline{C}_s = \int_0^{\infty}\int_0^{\infty} C_s\left(\gamma_B, \gamma_E\right) f_B\left(\gamma_B\right) f_E\left(\gamma_E\right) d\gamma_B d\gamma_E \tag{8.13}$$

From Equation (8.12), the condition can be further simplified to the following:

$$\begin{aligned} C_B > C_E &\Leftrightarrow G\left(\beta_B\right)\left(1+\gamma_B\right) > G\left(\beta_E\right)\left(1+\gamma_E\right) \\ &\Leftrightarrow \gamma_B > \frac{G\left(\beta_E\right)}{G\left(\beta_B\right)}\gamma_E + \frac{G\left(\beta_E\right)}{G\left(\beta_B\right)} - 1 \end{aligned} \tag{8.14}$$

Define $a = \frac{G(\beta_E)}{G(\beta_B)}$ and $b = \frac{G(\beta_E)}{G(\beta_B)} - 1$. Notice that $G(\beta) > 0$ so $a > 0$, $b \ge -1$. To proceed the analysis, we must discuss the range of b.

Case 1: b ≥ 0

This case corresponds to $G\left(\beta_E\right) \ge G\left(\beta_B\right)$. For this case, we can decompose Equation (8.13) into 3 terms.

$$\overline{C}_s = \int_{\gamma_E=0}^{\gamma_E=\infty} \int_{\gamma_B=a\gamma_E+b}^{\gamma_B=\infty} \log_2 \frac{G(\beta_B)}{G(\beta_E)} f_{\gamma_B}(\gamma_B) f_{\gamma_E}(\gamma_E) d\gamma_B d\gamma_E \tag{8.15}$$

$$+ \int_{\gamma_E=0}^{\gamma_E=\infty} \int_{\gamma_B=a\gamma_E+b}^{\gamma_B=\infty} \log_2(1+\gamma_B) f_{\gamma_B}(\gamma_B) f_{\gamma_E}(\gamma_E) d\gamma_B d\gamma_E \tag{8.16}$$

$$- \int_{\gamma_E=0}^{\gamma_E=\infty} \int_{\gamma_B=a\gamma_E+b}^{\gamma_B=\infty} \log_2(1+\gamma_E) f_{\gamma_B}(\gamma_B) f_{\gamma_E}(\gamma_E) d\gamma_B d\gamma_E \tag{8.17}$$

Equation (8.15) can be evaluated down to Equation (8.18).

$$(8.15) = -[\log_2 a] e^{-\frac{b}{\overline{\gamma}_B}} \frac{\overline{\gamma}_B}{a\overline{\gamma}_E + \overline{\gamma}_B} \tag{8.18}$$

For Equation (8.16), we first change the order of integration and then evaluate as

$$\begin{aligned}(8.16) &= \int_{\gamma_B=b}^{\gamma_B=\infty} \int_{\gamma_E=0}^{\gamma_E=\frac{1}{a}\gamma_B-\frac{b}{a}} \log_2(1+\gamma_B) f_{\gamma_B}(\gamma_B) f_{\gamma_E}(\gamma_E) d\gamma_E d\gamma_B \\ &= \int_{\gamma_B=b}^{\gamma_B=\infty} \left(1 - e^{\frac{b}{a\overline{\gamma}_E}} e^{-\frac{\gamma_B}{a\overline{\gamma}_E}}\right) \log_2(1+\gamma_B) f_{\gamma_B}(\gamma_B) d\gamma_B \end{aligned} \tag{8.19}$$

Let $u = 1 + \gamma_B$, we can simplify Equation (8.19) as

$$\begin{aligned}(8.19) &= e^{\frac{1}{\overline{\gamma}_B}} \frac{1}{\overline{\gamma}_B \ln 2} \int_{b+1}^{\infty} e^{-\frac{u}{\overline{\gamma}_B}} \ln u \, du - e^{\frac{b+1}{a\overline{\gamma}_E}} \frac{1}{\overline{\gamma}_B \ln 2} e^{\frac{1}{\overline{\gamma}_B}} \int_{b+1}^{\infty} e^{-u\left(\frac{1}{a\overline{\gamma}_E}+\frac{1}{\overline{\gamma}_B}\right)} \ln u \, du \\ &= \frac{e^{\frac{1}{\overline{\gamma}_B}}}{\ln 2} \left[E_1\left(\frac{b+1}{\overline{\gamma}_B}\right) + e^{-\frac{b+1}{\overline{\gamma}_B}} \ln(b+1)\right] \\ &- \frac{e^{\frac{b+1}{a\overline{\gamma}_E}+\frac{1}{\overline{\gamma}_B}} (a\overline{\gamma}_E\overline{\gamma}_B)}{\overline{\gamma}_B(a\overline{\gamma}_E+\overline{\gamma}_B)\ln 2} \left[E_1\left(\frac{b+1}{a\overline{\gamma}_E} + \frac{b+1}{\overline{\gamma}_B}\right) + e^{-\left(\frac{b+1}{a\overline{\gamma}_E}+\frac{b+1}{\overline{\gamma}_B}\right)} \ln(b+1)\right] \end{aligned} \tag{8.20}$$

Note that the last equality is achieved by using Equation (8.10). For Equation (8.17), by direct integration with the help of Equation (8.10) gives the result as shown in Equation (8.21).

$$(8.17) = -\frac{e^{-\frac{b}{\overline{\gamma}_B}} \overline{\gamma}_B}{(\overline{\gamma}_B + a\overline{\gamma}_E)\ln 2} e^{\frac{1}{\overline{\gamma}_E}+\frac{a}{\overline{\gamma}_B}} E_1\left(\frac{1}{\overline{\gamma}_E} + \frac{a}{\overline{\gamma}_B}\right) \tag{8.21}$$

Thus, the sum of Equation (8.18), (8.20), and (8.21) is the average secrecy capacity for this case.

Case 2: b < 0

This case corresponds to $G(\beta_E) < G(\beta_B)$. For this case, when combined with $f_{\gamma_B}(\gamma_B)$ and $f_{\gamma_E}(\gamma_E)$, we obtain the integration area as shown in Figure 8.2. We can divide the integral into 2 parts, Area I and Area II.

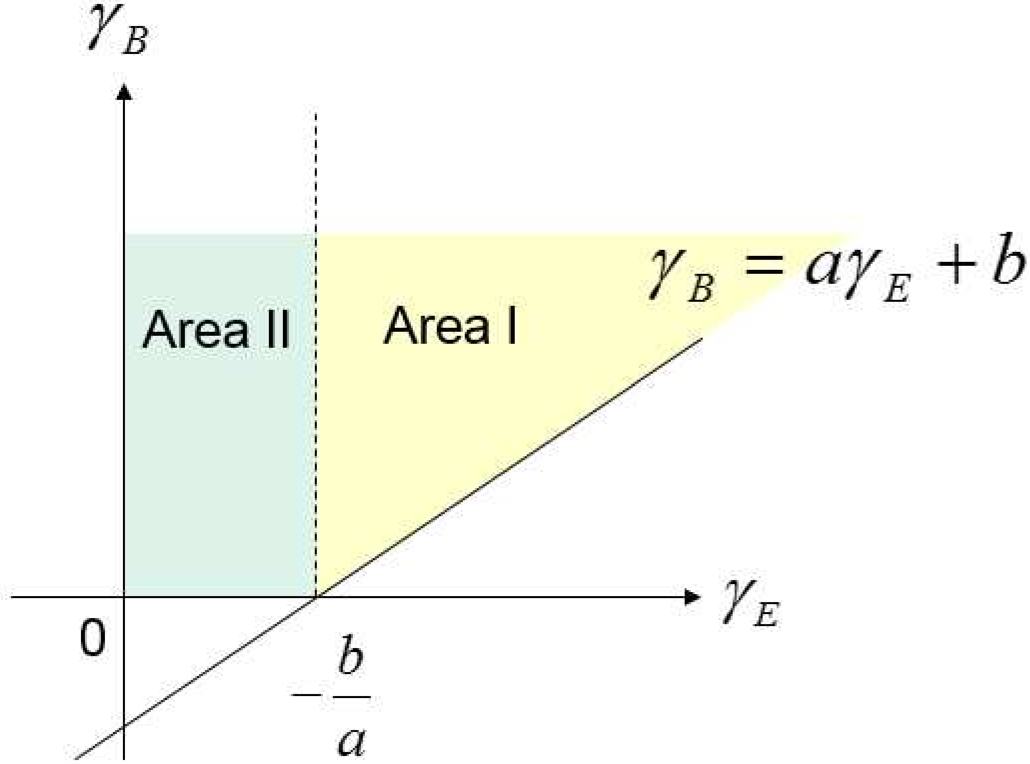

Fig. 8.2. The integration area for Case 2. It can be decomposed of 2 disjoint areas.

Area I can be divided into 3 terms which is similar to Equation (8.15), (8.16), and (8.17).

$$\overline{C}_{s,AreaI} = \int_{\gamma_E=-\frac{b}{a}}^{\gamma_E=\infty} \int_{\gamma_B=a\gamma_E+b}^{\gamma_B=\infty} \log_2 \frac{G(\beta_B)}{G(\beta_E)} f_{\gamma_B}(\gamma_B) f_{\gamma_E}(\gamma_E)\, d\gamma_B d\gamma_E \tag{8.22}$$

$$+ \int_{\gamma_E=-\frac{b}{a}}^{\gamma_E=\infty} \int_{\gamma_B=a\gamma_E+b}^{\gamma_B=\infty} \log_2(1+\gamma_B) f_{\gamma_B}(\gamma_B) f_{\gamma_E}(\gamma_E)\, d\gamma_B d\gamma_E \tag{8.23}$$

$$- \int_{\gamma_E=-\frac{b}{a}}^{\gamma_E=\infty} \int_{\gamma_B=a\gamma_E+b}^{\gamma_B=\infty} \log_2(1+\gamma_E) f_{\gamma_B}(\gamma_B) f_{\gamma_E}(\gamma_E)\, d\gamma_B d\gamma_E \tag{8.24}$$

Equation (8.22) is evaluated to Equation (8.25).

$$(8.22) = -[\log_2 a] e^{-\frac{b}{\overline{\gamma}_B}} \frac{\overline{\gamma}_B}{A\overline{\gamma}_E + \overline{\gamma}_B} e^{b\left(\frac{1}{\overline{\gamma}_B} + \frac{1}{a\overline{\gamma}_E}\right)} \tag{8.25}$$

Following the techniques for deriving Equation (8.20) and Equation (8.11), Equation (8.23) is evaluated to Equation (8.26).

$$(8.23) = \frac{e^{\frac{b}{a\overline{\gamma}_E} + \frac{1}{\overline{\gamma}_B}}}{\ln 2} E_1\left(\frac{1}{\overline{\gamma}_B}\right) - \frac{a\overline{\gamma}_E e^{\frac{b+1}{a\overline{\gamma}_E} + \frac{1}{\overline{\gamma}_B}}}{(a\overline{\gamma}_E + \overline{\gamma}_B)\ln 2} E_1\left(\frac{1}{a\overline{\gamma}_E} + \frac{1}{\overline{\gamma}_B}\right) \tag{8.26}$$

Using the same technique for deriving Equation (8.21) and Equation (8.11), Equation (8.24) is evalueated to Equation (8.27).

$$(8.24) = -\frac{\overline{\gamma}_B e^{\frac{a-b}{a\overline{\gamma}_B} + \frac{1}{\overline{\gamma}_E}}}{(a\overline{\gamma}_E + \overline{\gamma}_B)\ln 2} E_1\left(\frac{1}{\overline{\gamma}_E} + \frac{a}{\overline{\gamma}_B}\right) \tag{8.27}$$

Area II can be divided into 3 terms which is similar to Equation (8.15), (8.16), and (8.17).

$$\overline{C}_{s,AreaII} = \int_{\gamma_E=0}^{\gamma_E=-\frac{b}{a}} \int_{\gamma_B=0}^{\gamma_B=\infty} \log_2 \frac{G(\beta_B)}{G(\beta_E)} f_{\gamma_B}(\gamma_B) f_{\gamma_E}(\gamma_E) d\gamma_B d\gamma_E \tag{8.28}$$

$$+ \int_{\gamma_E=0}^{\gamma_E=-\frac{b}{a}} \int_{\gamma_B=0}^{\gamma_B=\infty} \log_2(1+\gamma_B) f_{\gamma_B}(\gamma_B) f_{\gamma_E}(\gamma_E) d\gamma_B d\gamma_E \tag{8.29}$$

$$- \int_{\gamma_E=0}^{\gamma_E=-\frac{b}{a}} \int_{\gamma_B=0}^{\gamma_B=\infty} \log_2(1+\gamma_E) f_{\gamma_B}(\gamma_B) f_{\gamma_E}(\gamma_E) d\gamma_B d\gamma_E \tag{8.30}$$

Equation (8.28) is evaluated to Equation (8.31).

$$(8.28) = -[\log_2 a]\left(1 - e^{\frac{b}{a\overline{\gamma}_E}}\right) \tag{8.31}$$

Following the techniques for deriving Equation (8.20) and Equation (8.11), Equation (8.29) is evaluated to Equation (8.32).

$$(8.29) = \frac{\left(1 - e^{\frac{b}{aa\overline{\gamma}_E}}\right) e^{\frac{1}{\overline{\gamma}_B}}}{\ln 2} E_1\left(\frac{1}{\overline{\gamma}_B}\right) \tag{8.32}$$

Using the same technique for deriving Equation (8.21) and Equation (8.11), Equation (8.30) is evaluated to Equation (8.33).

$$(8.30) = -\frac{e^{\frac{1}{\overline{\gamma}_E}}}{\ln 2}\left[E_1\left(\frac{1}{\overline{\gamma}_E}\right) - E_1\left(\frac{1}{a\overline{\gamma}_E}\right) + e^{\frac{1}{a\overline{\gamma}_E}}\ln a\right] \tag{8.33}$$

Hence, the average capacity for this case is the sum of Equation (8.25), (8.26), (8.27), (8.31), (8.32), and (8.33).

8.5 Outage Probability of Secrecy Capacity

We follow the technique mentioned in [113] to find the outage probability.

$$\begin{aligned} P_{out}\left(R_s\right) &= P\left(\{C_s \leq R_s | \gamma_B > a\gamma_E + b\}\right) * P\left(\{\gamma_B > a\gamma_E + b\}\right) + P\left(\{\gamma_B \leq a\gamma_E + b\}\right) \\ &= P\left(\{C_s \leq R_s | \gamma_B > a\gamma_E + b\}\right) * P\left(\{\gamma_B > a\gamma_E + b\}\right) + \left(1 - P\left(\{\gamma_B > a\gamma_E + b\}\right)\right) \end{aligned} \tag{8.34}$$

Similar to Section 8.4, we discuss 3 cases on the range of b and R_s. Notice that the condition $\{C_s \leq R_s\}$ is equivalent to $\left\{\gamma_B \leq a2^{R_s}\left(1+\gamma_E\right) - 1\right\}$. The reason we have 3 cases is because we do not know whether $a2^{R_s} - 1$ is positive or negative. This changes the range of the integrals.

Case 1: b ≥ 0

For this case, we evaluate $P\left(\{C_s \leq R_s | \gamma_B > a\gamma_E + b\}\right)$ as shown in Equation (8.35).

$$\begin{aligned} P\left(\{C_s \leq R_s | \gamma_B > a\gamma_E + b\}\right) &= \int_{\gamma_E=0}^{\gamma_E=\infty}\int_{\gamma_B=a\gamma_E+b}^{a2^{R_s}(1+\gamma_E)-1} f_{\gamma_B}\left(\gamma_B\right) f_{\gamma_E}\left(\gamma_E\right) d\gamma_B d\gamma_E \\ &= \int_0^{\infty}\left(e^{-\left(\frac{a\gamma_E+b}{\overline{\gamma}_B}\right)} - e^{-\frac{a2^{R_s}(1+\gamma_E)-1}{\overline{\gamma}_B}}\right)\frac{1}{\overline{\gamma}_E}e^{-\frac{\gamma_E}{\overline{\gamma}_E}}\, d\gamma_E \\ &= \frac{\overline{\gamma}_B e^{-\frac{b}{\overline{\gamma}_B}}}{\overline{\gamma}_B + a\overline{\gamma}_E} - \frac{\overline{\gamma}_B e^{-\frac{a2^{R_s}-1}{\overline{\gamma}_B}}}{\overline{\gamma}_B + \overline{\gamma}_E a2^{R_s}} \end{aligned} \tag{8.35}$$

$P(\{\gamma_B > a\gamma_E + b\})$ can be evaluated by letting the R_s in Equation (8.35) approach ∞. Thus, we obtain the result as shown in Equation (8.36).

$$P(\{\gamma_B > a\gamma_E + b\}) = \frac{\overline{\gamma}_B e^{-\frac{b}{\overline{\gamma}_B}}}{\overline{\gamma}_B + a\overline{\gamma}_E} \tag{8.36}$$

Case 2: b < 0, $R_s \geq -\log_2 a$

Figure 8.3 shows the integration range. For this case, we can divide the integral into 2 parts (Area I and Area II) as shown in Figure 8.3. For the computation of $P(\{C_s < R_s|\gamma_B > a\gamma_E + b\})$, Area I can be evaluated as shown in Equation (8.37).

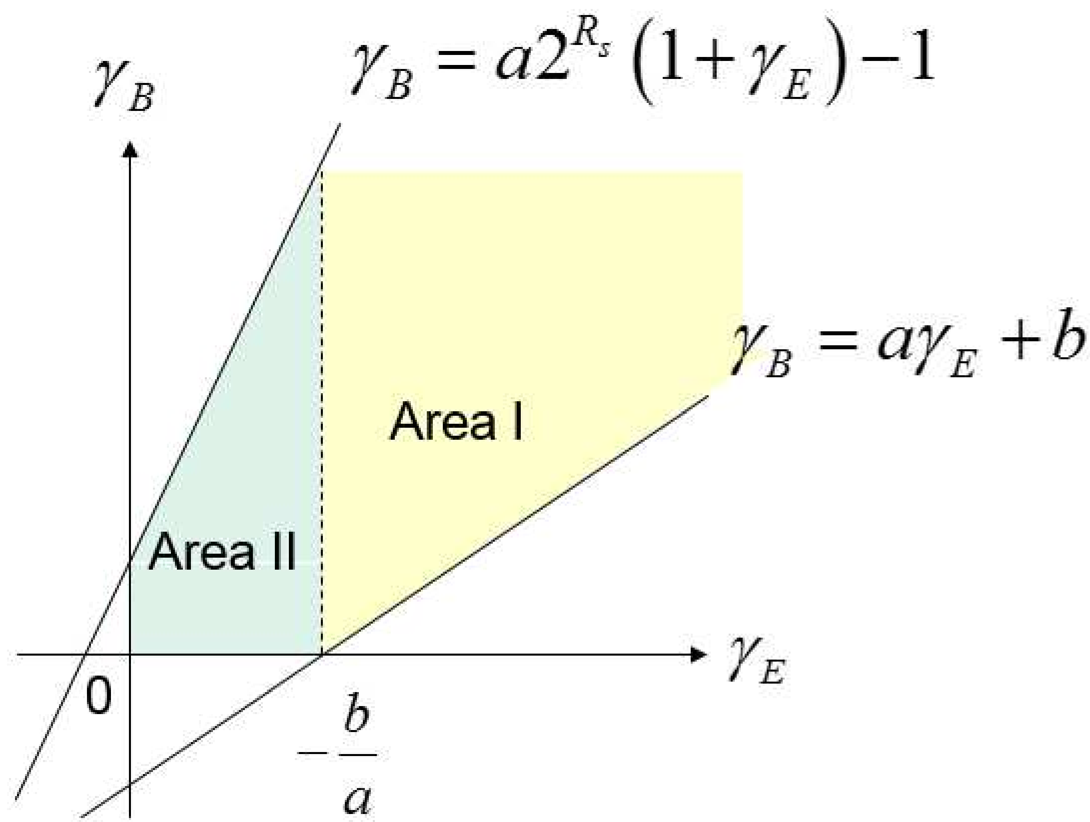

Fig. 8.3. The integration area for Case 2 of outage probability analysis. It can be decomposed of 2 disjoint areas.

$$P\left(\{C_s \le R_s|\gamma_B > a\gamma_E + b\}\right)_{AreaI} = \int_{\gamma_E=-\frac{b}{a}}^{\gamma_E=\infty} \int_{\gamma_B=a\gamma_E+b}^{\gamma_B=a2^{R_s}(1+\gamma_E)-1} f_{\gamma_B}(\gamma_B) f_{\gamma_E}(\gamma_E)\, d\gamma_B d\gamma_E$$

$$= \frac{\overline{\gamma}_B e^{-\frac{b}{\overline{\gamma}_B}}}{a\overline{\gamma}_E + \overline{\gamma}_B} e^{b\left(\frac{1}{\overline{\gamma}_B}+\frac{1}{a\overline{\gamma}_E}\right)} - \frac{\overline{\gamma}_B e^{-\frac{a2^{R_s}-1}{\overline{\gamma}_B}}}{a2^{R_s}\overline{\gamma}_E + \overline{\gamma}_B} e^{b\left(\frac{2^{R_s}}{\overline{\gamma}_B}+\frac{1}{a\overline{\gamma}_E}\right)} \tag{8.37}$$

For the computation of $P\left(\{C_s \le R_s|\gamma_B > a\gamma_E + b\}\right)$, Area II can be evaluated as shown in Equation (8.38).

$$P\left(\{C_s \le R_s|\gamma_B > a\gamma_E + b\}\right)_{AreaII} = \int_{\gamma_E=0}^{\gamma_E=-\frac{b}{a}} \int_{\gamma_B=0}^{\gamma_B=a2^{R_s}(1+\gamma_E)-1} f_{\gamma_B}(\gamma_B) f_{\gamma_E}(\gamma_E)\, d\gamma_B d\gamma_E$$

$$= \left(1 - e^{\frac{b}{a\overline{\gamma}_E}}\right) - \frac{\overline{\gamma}_B e^{-\frac{a2^{R_s}-1}{\overline{\gamma}_B}}}{a2^{R_s}\overline{\gamma}_E + \overline{\gamma}_B} \left(1 - e^{b\left(\frac{2^{R_s}}{\overline{\gamma}_B}+\frac{1}{a\overline{\gamma}_E}\right)}\right) \tag{8.38}$$

Hence, $P\left(\{C_s \le R_s|\gamma_B > a\gamma_E + b\}\right)$ is the sum of Equation (8.37) and (8.38). For the computation of $P\left(\{\gamma_B > a\gamma_E + b\}\right)$, Area I and Area II can be found be letting R_s in Equation (8.37) and (8.38) approach ∞ respectively. Thus, we obtain the result as shown in Equation (8.39).

$$P\left(\{\gamma_B > a\gamma_E + b\}\right) = \frac{\overline{\gamma}_B e^{-\frac{b}{\overline{\gamma}_B}}}{a\overline{\gamma}_E + \overline{\gamma}_B} e^{b\left(\frac{1}{\overline{\gamma}_B}+\frac{1}{a\overline{\gamma}_E}\right)} + \left(1 - e^{\frac{b}{a\overline{\gamma}_E}}\right) \tag{8.39}$$

Case 3: b < 0, $R_s < -\log_2 a$

Figure 8.4 shows the integration range. For this case, we can devide the integral into 2 parts (Area I and Area II) as shown in Figure 8.3. For the computation of $P\left(\{C_s \le R_s|\gamma_B > a\gamma_E + b\}\right)$, Area I is the same as the one shown in Case 2. So $P\left(\{C_s \le R_s|\gamma_B > a\gamma_E + b\}\right)_{AreaI} =$ Equation (8.37).

For the computation of $P\left(\{C_s \le R_s|\gamma_B > a\gamma_E + b\}\right)$, Area II can be evaluated as shown in Equation (8.40).

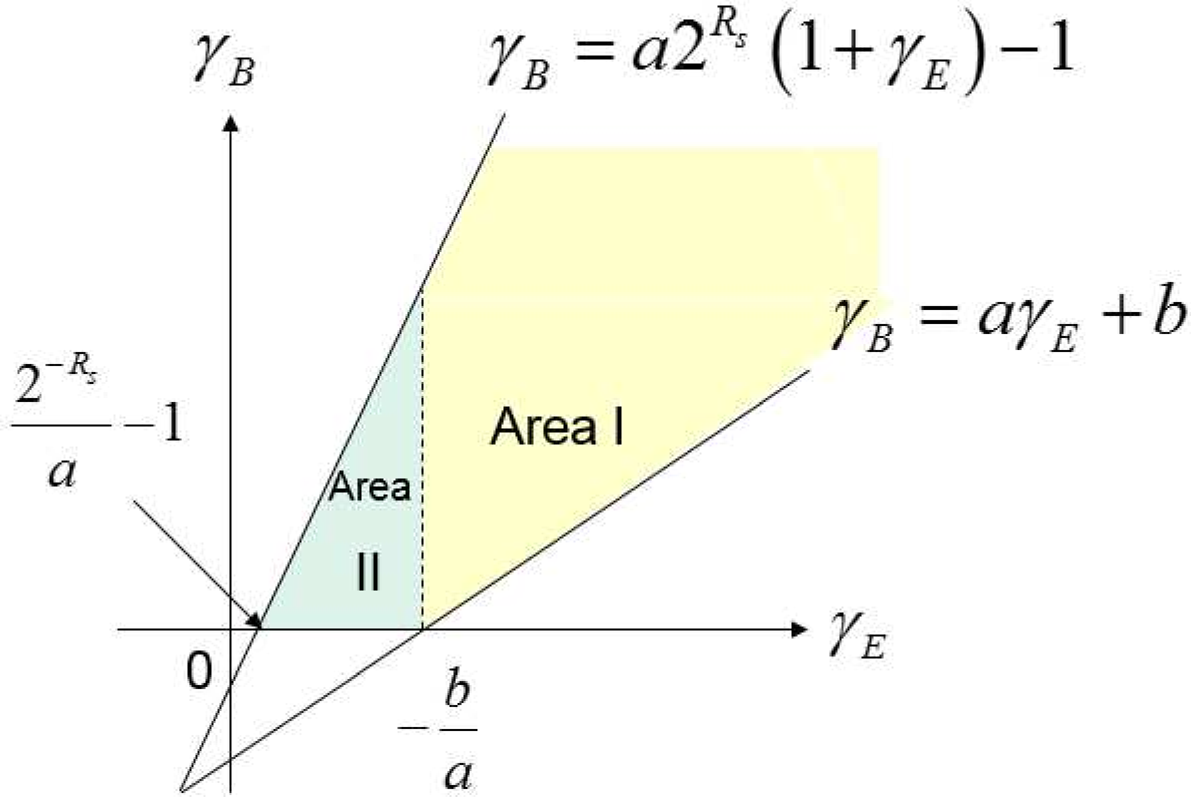

Fig. 8.4. The integration area for Case 3 of outage probability analysis. It can be decomposed of 2 disjoint areas.

$$P\left(\{C_s \le R_s|\gamma_B > a\gamma_E + b\}\right)_{AreaII} =$$
$$\int_{\gamma_E=\frac{2^{R_s}}{a}-1}^{\gamma_E=-\frac{b}{a}} \int_{\gamma_B=0}^{\gamma_B=a2^{R_s}(1+\gamma_E)-1} f_{\gamma_B}\left(\gamma_B\right) f_{\gamma_E}\left(\gamma_E\right) d\gamma_B d\gamma_E$$
$$= \left(e^{-\frac{2^{R_s}-a}{a\overline{\gamma}_E}} - e^{\frac{b}{a\overline{\gamma}_E}}\right) - \frac{\overline{\gamma}_B e^{-\frac{a2^{R_s}-1}{\overline{\gamma}_B}}}{a2^{R_s}\overline{\gamma}_E + \overline{\gamma}_B}\left(e^{\left(\frac{2^{-R_s}}{a}-1\right)\left(\frac{2^{R_s}}{\overline{\gamma}_B}+\frac{1}{a\overline{\gamma}_E}\right)} - e^{b\left(\frac{2^{R_s}}{\overline{\gamma}_B}+\frac{1}{a\overline{\gamma}_E}\right)}\right) \quad (8.40)$$

Hence, $P\left(\{C_s \le R_s|\gamma_B > a\gamma_E + b\}\right)$ is the sum of Equation (8.37) and (8.40). For the computation of $P\left(\{\gamma_B > a\gamma_E + b\}\right)$, Area I can be found be letting R_s in Equation (8.37) approach ∞ respectively. For Area II, the integration range is the Area II shown in Figure 8.2. So we obtain the result as shown in Equation (8.41).

$$P\left(\{\gamma_B > a\gamma_E + b\}\right)_{AreaII} = \int_{\gamma_E=0}^{\gamma_E=-\frac{b}{a}} \int_{\gamma_B=0}^{\gamma_B=\infty} f_{\gamma_B}\left(\gamma_B\right) f_{\gamma_E}\left(\gamma_E\right) d\gamma_B d\gamma_E$$
$$= 1 - e^{\frac{b}{a\overline{\gamma}_E}} \tag{8.41}$$

The final result for $P\left(\{\gamma_B > a\gamma_E + b\}\right)$ is shown in Equation (8.42).

$$P\left(\{\gamma_B > a\gamma_E + b\}\right) = \frac{\overline{\gamma}_B e^{-\frac{b}{\overline{\gamma}_B}}}{a\overline{\gamma}_E + \overline{\gamma}_B} e^{b\left(\frac{1}{\overline{\gamma}_B} + \frac{1}{a\overline{\gamma}_E}\right)} + \left(1 - e^{\frac{b}{a\overline{\gamma}_E}}\right) \tag{8.42}$$

8.6 Numerical Result

In this section we look at an UWA communication example. Consider a scenario as depicted in Figure 8.5. Bob is close to the sea surface while Eva tries to listen from beneath. According to Table II of [96], $\beta_B = 2.7787$ and $\beta_E = 1.62844$. We use the results in Section 8.4 and 8.5 to find out the average secrecy, outage probability versus average main channel SNR γ_B, and outage probability versus specified rate R_s. The results are shown in Figure 8.6, 8.7, and 8.8 respectively.

Figure 8.6 and 8.7 show that Alice and Bob have less average secrecy capacity and higher outage probability for better communication link on Eve. However, since the secrecy capacity is not 0, one can use better coding schemes for secure transmission. Such schemes are, for example, the low density parity check code mentioned in [111] and the polar code mentioned in [114].

In Figure 8.8, when R_s approaches ∞, the outage probability approaches $P^2 + 1 - P$, where $P = P\left(\{\gamma_B > a\gamma_E + b\}\right)$.

8.7 Conclusion

In this work, the average secrecy capacity of UWA with dominant Generalized Gaussian noise and Rayleigh fading is investigated. The outage probability of secrecy capacity is also derived. Our analysis result shows that, even if the eavesdropper has better channel condition in terms of SNR, the average secrecy capacity is still

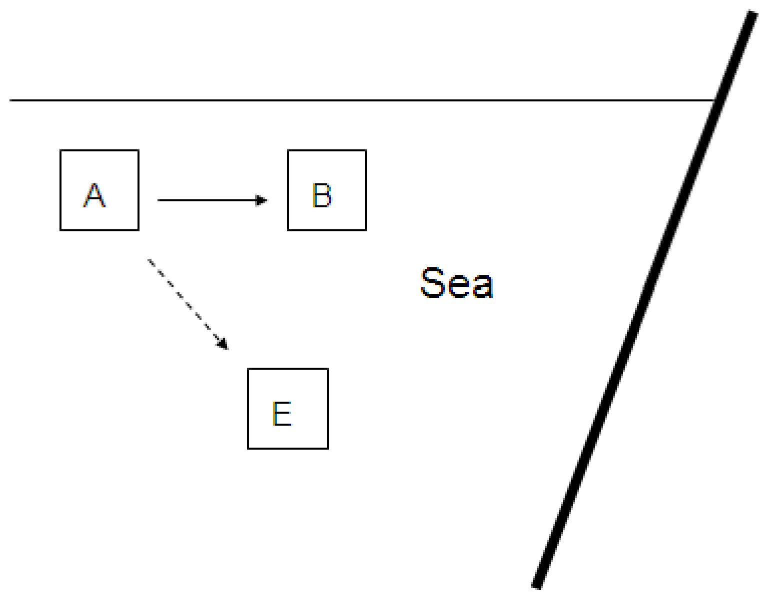

Fig. 8.5. A scenario for UWA communication. Bob is close to the sea surface while Eva lies beneath the communication link.

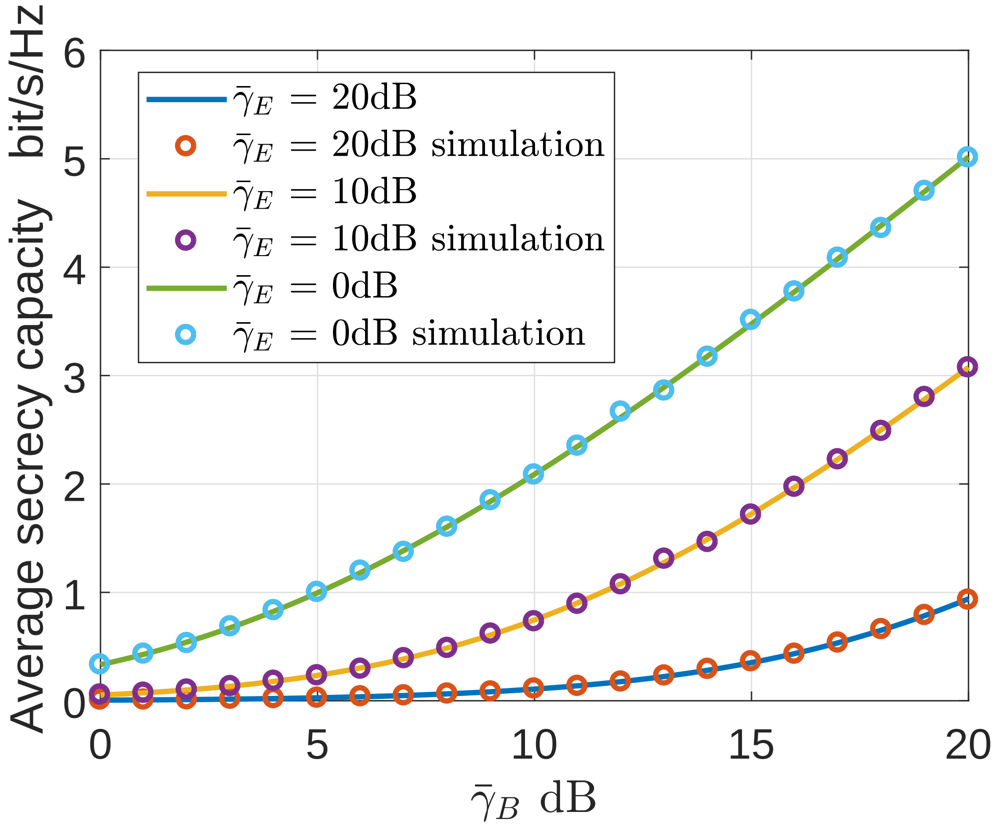

Fig. 8.6. The secrecy capacity with $\gamma_E = 1$, 10, 20 dB.

not 0 due to the presence of fading. This provides an opportunity for legitimate users to devise communication strategy to secure the information. Our work can also be applied to problems involving Generalized Gaussian noise such as molecular communication.

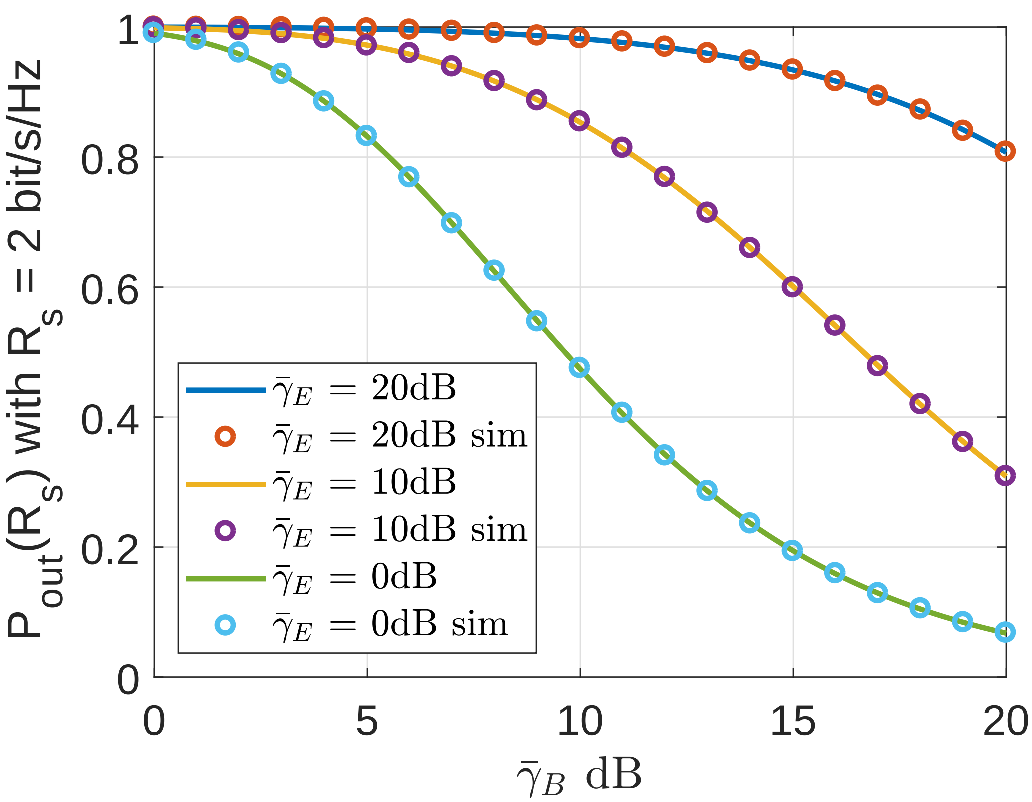

Fig. 8.7. The outage probability of secrecy capacity versus γ_B with $\gamma_E = 1$, 10, 20 dB and $R_s = 2$ bit/s/Hz.

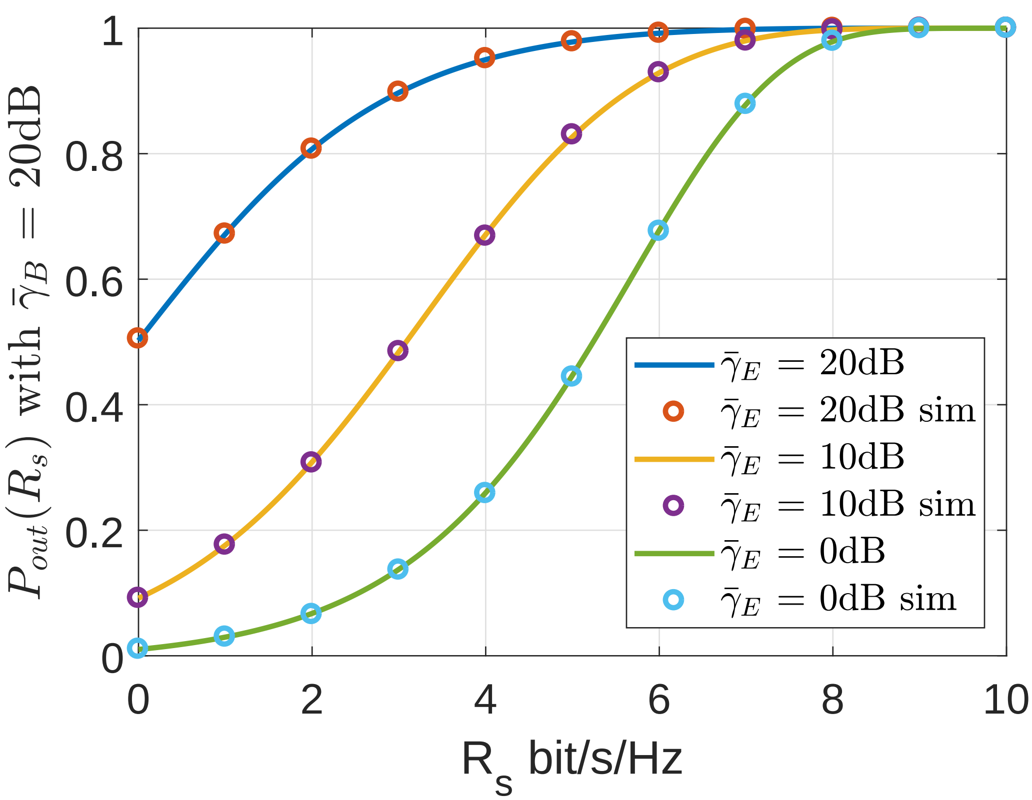

Fig. 8.8. The outage probability of secrecy capacity versus R_s with $\gamma_E = 1$, 10, 20 dB.

9. RECEPTOR ANTAGONIST AND ITS EFFECT IN DIFFUSION BASED MOLECULAR COMMUNICATION

Molecular communication relies on the usage of particular molecules such that specific receptor proteins can receive it. However, there exist other molecules that can bind that receptor and cause negative effects. Such molecules are called receptor antagonists. In our work, we wish to study how receptor antagonists affect molecular communication system. Based on the assumption that the antagonists can be removed from its effect for a finite duration, we derive the jamming relationship that has been used in wireless communication system. The inter-symbol interference (ISI) issue is also brought in. The error probability is derived based on this model with various scenarios. We also look for a practical solution in which we increase the number of transmission molecules. The amount of such increase is calculated with simulation results.

9.1 Introduction

In recent years, the research of molecular communication has gained lots of attraction. On one hand, it provides a mathematical model for describing cell behavior. On the other hand, it gives analysis results such that future scientists and engineers can utilize for developing nanomachines. Those nannomachines will dwell in organisms. Nanomachines could use various ways to communicate. One promising method which is inspired by biological systems, is to communicate through molecules. Inside an organism, molecules communicate through diffusion process just like the heat transfer studied in mechanical engineering.

Past research in this area has established the additive white Gaussian noise (AWGN) channel model with time-varying mean and variance [115]. [116] proposed and analyzed methods to communicate such as concentration shift keying, pulse position modulation, and molecule shift keying. All these methods require the receiver being able to bind particular molecules. In cell biology, this is achieved by receptor proteins. The receptors are thought to be able bind only a specific kind of molecule. When such binding is successful, the receiver cell will begin a series of subsequent reactions. Later, the molecule will be disintegrated and the receptor will be available for the next communication.

In molecular biology, there exist other types of molecules that can bind to a certain receptor. Unlike the original molecule, those molecules produce opposite result when they bind the receptors. The subsequent reactions stop, some such molecules stay at the receptor for a much longer period of the time that inhibit original molecules from binding in the future. The worst case is that such binding becomes permanent, making the receptor useless for future communication. Those molecules are called receptor antagonist. From communication perspective, since the existence of receptor antagonists inhibit the transmission of the legitimate user, the role of receptor antagonists can be regarded as jammer. They reduce the quality of the link by degrading signal-to-interference-plus-noise ratio (SINR). The lower this value, the higher chance the communication system is vulnerable to transmission error.

To assess the effect of receptor antagonist in molecular communication, we look at the time that the molecules stay at target receptor and discuss different cases accordingly. Even without the presence of receptor antagonist, the original molecule could stay at the receptor protein for a longer period of time that makes the next transmission unavailable. From communication perspective, this is ISI. Diffusion process is used to describe how molecules diffuse to the destination with time. The molecules could be released at once like impulse function or continuously like step function. Hence, the different cases are combinations of the way the molecules are released and the amount of time they occupy the receptor.

The remaining sections are organized as follows. In Section 9.2, we explain receptor antagonist from biology and biochemistry perspective. In Section 9.3, we show the diffusion process results from literature that are needed for this work. In Section 9.4, we find the concentration of molecules and the ratio. We investigate three scenarios according to the behavior of the molecules in Section 9.5, 9.7, and 9.7. In Section 9.8, we show the simulation and theoretical result. Finally, in Section 9.9, we draw conclusion.

9.2 Biology of Receptor Antagonists

The nervous system of animals transmit information to and from the body. This is achieved with the help of neural cells. The neural cells typically align themselves in a line. Neural cells communicate through molecules called neural transmitters. Examples of neural transmitters are acetylcholine (ACh), glutamate, glycine, and histamine [117]. We use ACh as an example for explaining signal transmission. There are two types of ACh receptors: nicotinic and muscarinic. For our example, we only look at the nicotinic receptors.

When a nerve cell intends to communicate with the next cell, it synthesizes ACh (Figure 9.1, A). Then, it releases ACh, which diffuses to the receptor of the next cell (Figure 9.1, B). The nicotinic ACh receptors of the next cell will bind to ACh. Such binding will allow the nicotinic ACh receptors to open their gates and allow ions flow through it (Figure 9.1, C). The flow of ions indicates a change in electrical potential of the nerve cell and hence signal is transmitted. Shortly afterwards, the acetylcholinesterase (AChE) will hydrolyze ACh into acetate and choline (Figure 9.1, D). The choline that is produced in this process will eventually be transported back to the previous cell [117].

Several other molecules can bind the nicotinic ACh receptor. This is how poisonous plants and venomous animals work. One example is the many-banded krait (*Bungarus multicinctus*), which can be found in Southeast Asia, injects α-bungarotoxin into its prey upon biting. Research [118] shows that these molecules bind ACh recep-

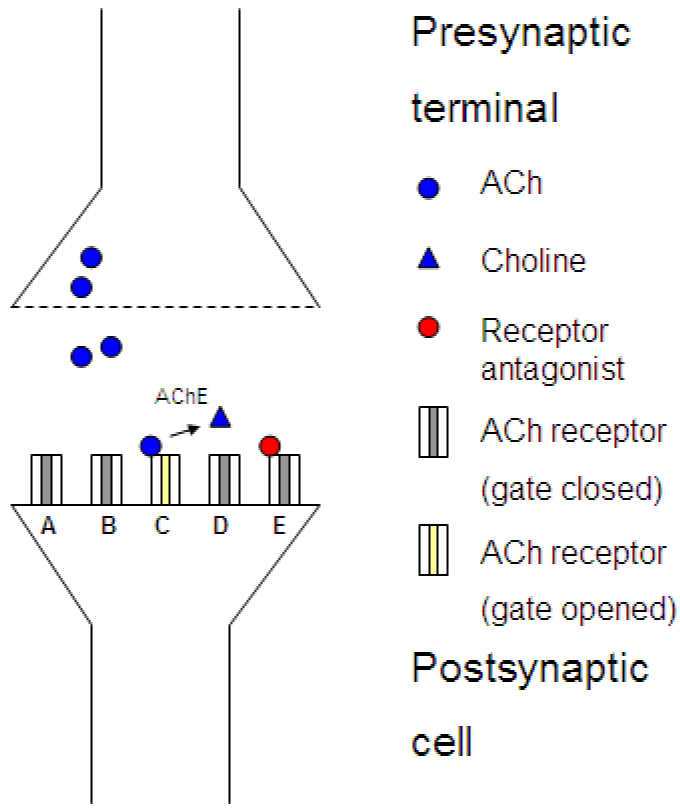

Fig. 9.1. The way neural cells communicate through neural transmitter molecules.

tors irreversibly and upon binding, it causes the gates to close. This stops future ion flow and hence disables future nerve cell communication.

Receptor antagonists do not always mean bad thing. Some drugs are designed to be receptor antagonists to meet specific requirements. For example, atracurium besilate is also a nicotinic ACh receptor antagonist. It is used to relax muscle in anesthesia [119].

9.3 Diffusion Process

We summarize the diffusion process results mentioned in [115] [120] for the purpose of our subsequent work. We first find the mean molecular concentration in molecule/m^3 which is denoted as $\bar{U}(\mathbf{X}, t)$. Here, $\mathbf{X}(t)$ is the molecule position at time

t. Also, let D be the diffusion coefficient in m^2/s. The concentration can be found by using Fick's second law of diffusion as shown in Equation (9.1) [121].

$$\frac{\partial \bar{U}(\mathbf{X},t)}{\partial t} = D\nabla^2 \bar{U}(\mathbf{X},t) \tag{9.1}$$

The solution to Equation (9.1) depends on the initial condition. There are two main cases we are interested in. The first one is the case when the nanomachine uses impulse function for releasing the messenger molecules. With Q messenger molecules at the time of release, the mean concentration can be found as shown in Equation (9.2). Here, $\mathbf{X}_{TX}$ is the location of the transmitting nanomachine.

$$\bar{U}(\mathbf{X},t)_{impulse} = \frac{Q}{(4\pi Dt)^{\frac{3}{2}}} \exp\left(-\frac{|\mathbf{X}-\mathbf{X}_{TX}|^2}{4Dt}\right) \tag{9.2}$$

The 2D mean concentration of messenger molecules can be found as shown in Equation (9.3).

$$\bar{U}_{2d}(x,y,t) = \int_{-\infty}^{\infty} \bar{U}(\mathbf{X},t)dz \tag{9.3}$$

The amplitude of the received signal is proportional to the received molecules. The mean of the signal is given by Equation (9.4). Here, A_{RX} is the receiver sensing area.

$$s(t) = \int\int_{A_{RX}} \bar{U}_{2d}(x,y,t)dxdy \tag{9.4}$$

The second case is when the nanomachine uses step function for releasing the messenger molecules. With Q messenger molecules as the height of the step function, the mean concentration can be found as shown in Equation (9.5) [120].

$$\bar{U}(\mathbf{X},t)_{step} = \frac{Q}{2D\pi|\mathbf{X}-\mathbf{X}_{TX}|} \mathrm{erfc}\left(\frac{|\mathbf{X}-\mathbf{X}_{TX}|}{\sqrt{4Dt}}\right) \tag{9.5}$$

where erfc is the complementary error function given by $\mathrm{erfc}(x) = \frac{2}{\sqrt{\pi}}\int_x^{\infty} e^{-t^2}dt$. To find the 2D mean concentration and the amplitude of the received signal, we employ Equation (9.3) and (9.4) except that we now substitute the mean concentration from Equation (9.5).

9.4 Concentration of the Molecules at the Receptor

Molecules diffuse to the receptor. The mean concentration is shown in Equation (9.3), and the number of molecules that will be received by the receptor is shown in Equation (9.4). When the receptor antagonist is present, the ratio of the number of messenger molecules to the number of the antagonist molecules becomes significant.

To display the effect in a much easier understandable way, we assume that in Equation (9.4), the integrand in the double integral does not vary much in the integration process. Hence, we can approximate Equation (9.4) as shown in Equation 9.6.

$$s(t) \approx \bar{U}_{2d}(x_{RX}, y_{RX}, t) A_{RX} \tag{9.6}$$

The ratio we are interested in is termed as molecule ratio (R), which can be found as shown in Equation (9.7). This quantity is similar to the singal-to-interference ratio (SIR) in wireless communication.

$$R = \frac{s(t)_{user}}{s(t)_{antagonist}} = \frac{\bar{U}_{2d,user}(x_{RX}, y_{RX}, t)}{\bar{U}_{2d,antagonist}(x_{RX}, y_{RX}, t)} \tag{9.7}$$

Depending on the function used for transmission by the user and the antagonist, there are 4 cases. They are expressed as follows (User/Antagonist): impulse/impulse, impulse/step, step/impulse, and step/step. The molecular ratio for each case is plotted in Figure 9.2, 9.3, 9.4, and 9.5 respectively.

We observe that the molecular ratio changes over time. For the impulse/impulse, step/impulse, and step/step cases, one needs to wait for sufficient amount of time to obtain the desired molecular ratio. For the impulse/step case, there exists an optimal amount of time to reach the highest molecular ratio. Hence, designing fast algorithms to classify which case is encountered in the communication link is critical. Also, fast

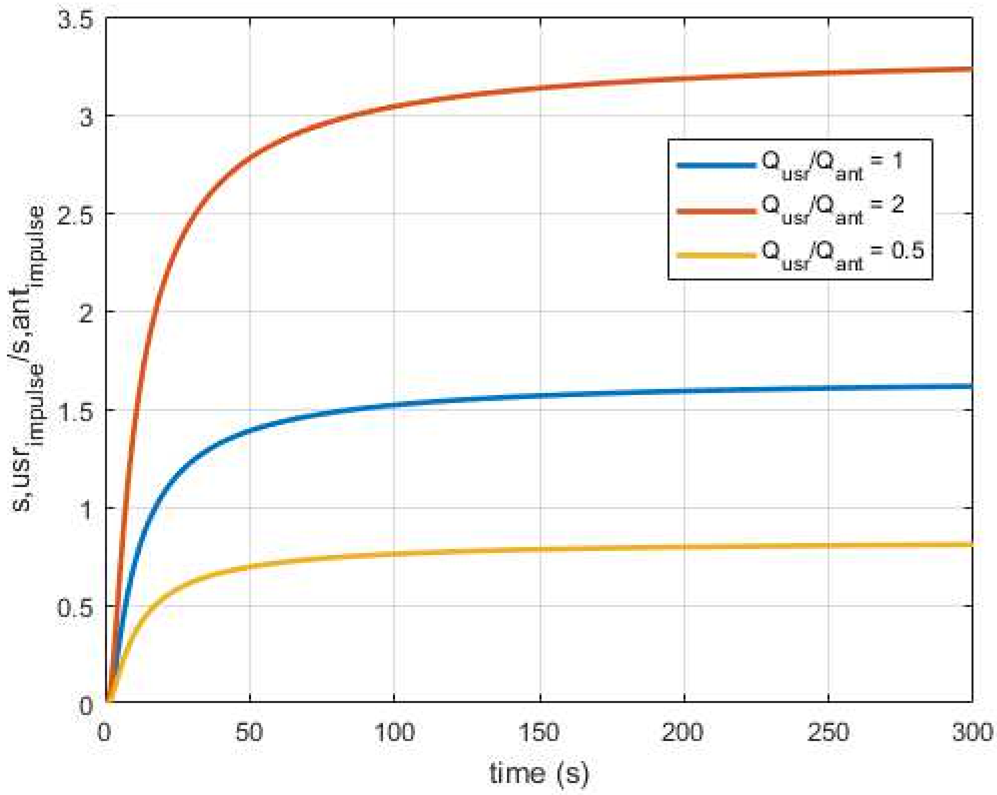

Fig. 9.2. The molecule ratio with user and antagonist both using impulse function to transmit. The distance between the user and the receptor is 15 μm. The distance between the user and the receptor is 25 μm.

communication processing algorithm is required in the impulse/step case because we have to utilized the maximum molecular ratio to achieve the best communication quality.

9.5 Instant Hydrolysis for Both Links

In this section, we investigate the simplest case when both the user and the antagonist have their molecules hydrolyzed instantly. This also represents the case when the transmission rate is smaller than the maximum hydrolysis period.

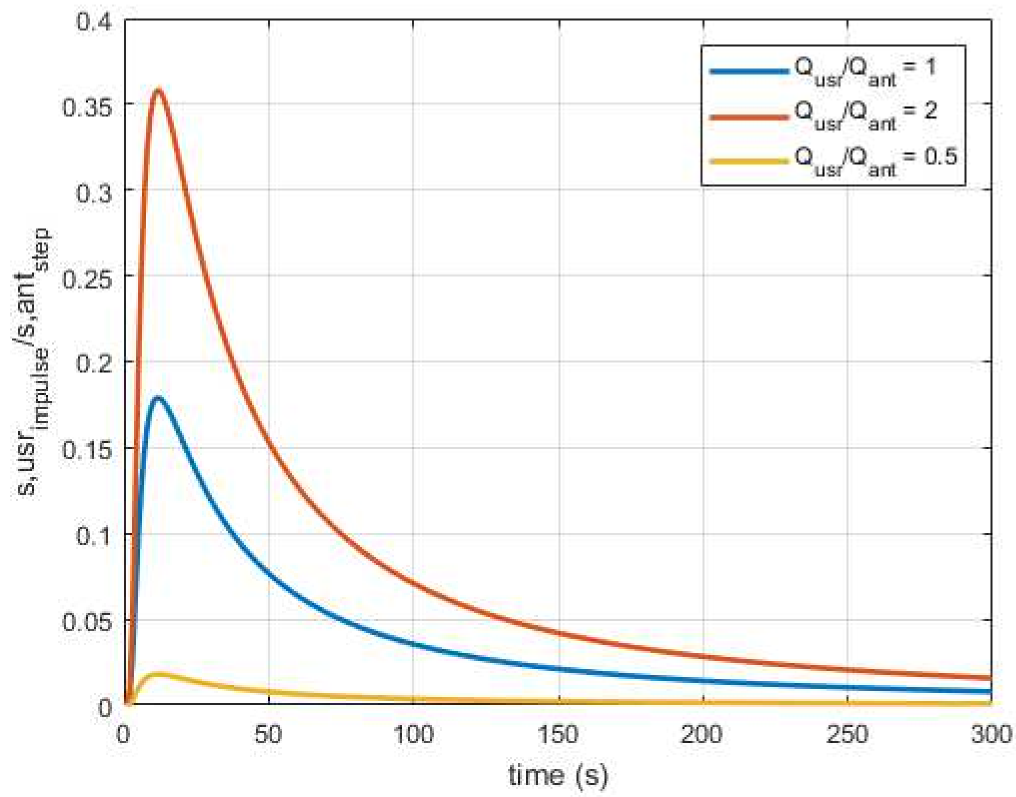

Fig. 9.3. The molecule ratio with user using impulse and antagonist using step function to transmit. The distance between the user and the receptor is 15 μm. The distance between the user and the receptor is 4243 μm.

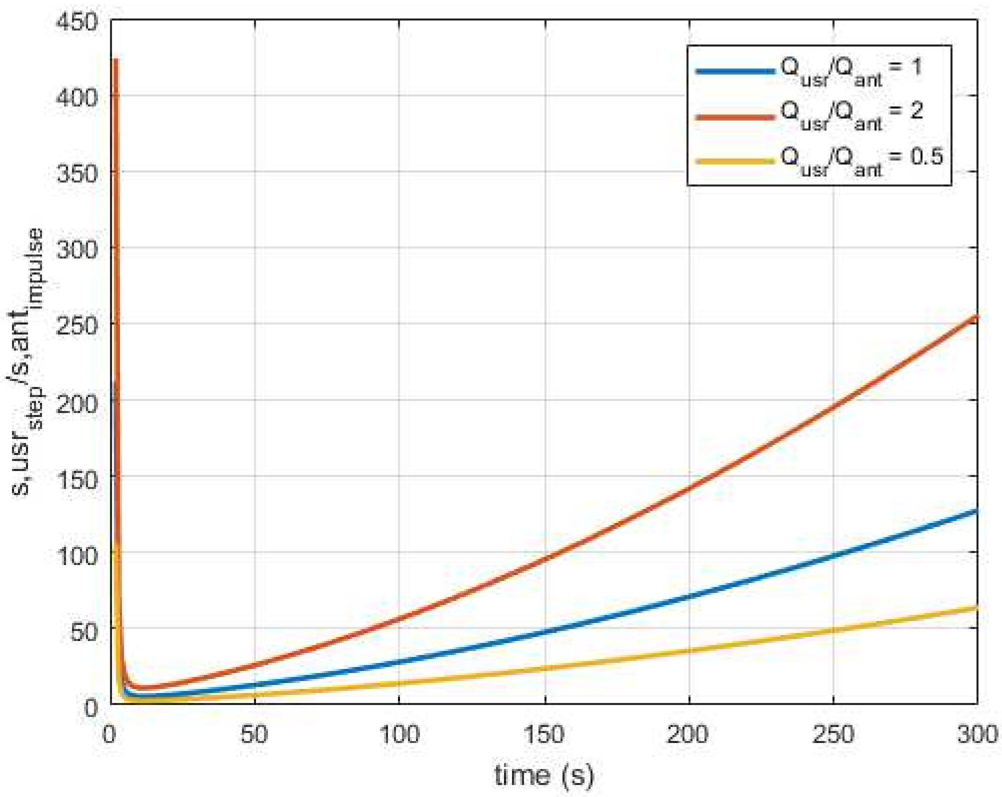

Fig. 9.4. The molecule ratio with user using step and antagonist using impulse function to transmit. The distance between the user and the receptor is 4243 μm. The distance between the user and the receptor is 15 μm.

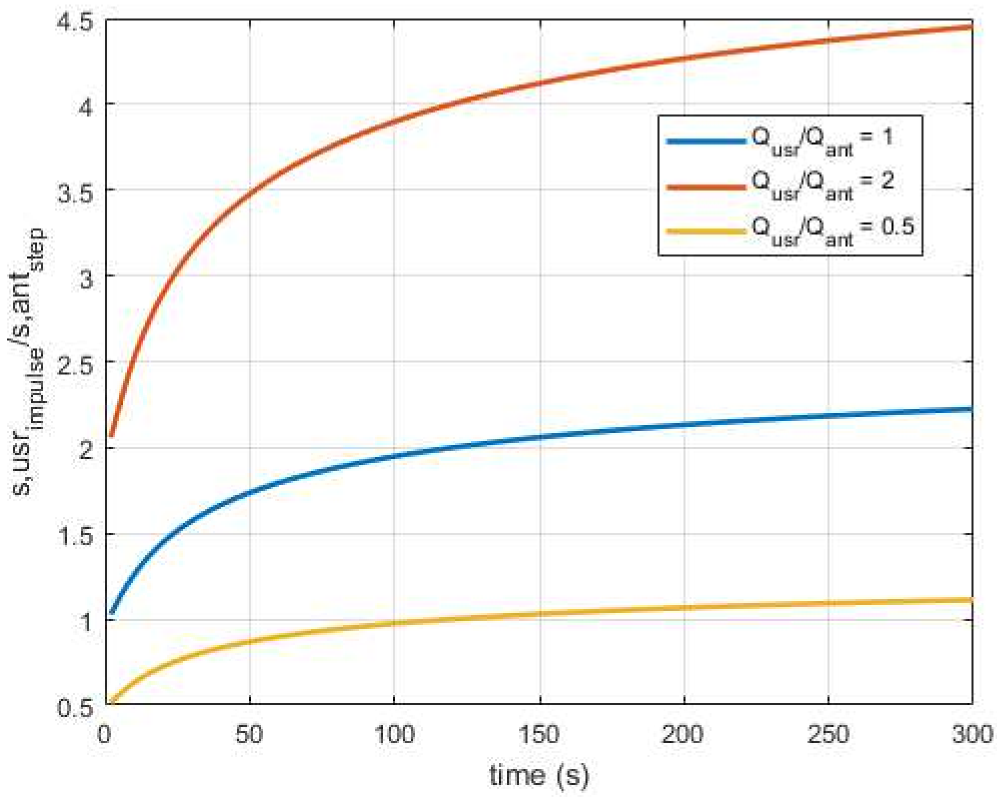

Fig. 9.5. The molecule ratio with user and antagonist both using step function to transmit. The distance between the user and the receptor is 2357 μm. The distance between the user and the receptor is 4243 μm.

We describe the scenario as follows. Suppose there are Q_1 user molecules and Q_2 antagonist molecules near the receptors. Let N be the number of receptors of a cell responsible for receiving these molecules as shown in Figure 9.6. A receptor has a probability of p_1 and p_2 to receive the user molecule or the antagonist molecule. The receptor can only receive at most one such molecule at any time instant. We assume that if a receptor receives both types of molecules at any time instant, it always favors the user molecule. We also assume that $Q_1 \gg N$ and $Q_2 \gg N$.

To analyze this communication link, we first derive the probability distribution of all possible cases when $N = 1$. There are only 3 possible cases: one with antagonist molecule, one with nothing, and one with user molecule. Equation (9.10), (9.11), and (9.12) shows the corresponding probability respectively.

For the general case, consider Figure 9.7 in which we have N receptors with i receptors filled with user molecules, j receptors filled with antagonist molecules, and $N - i - j$ receptors filled with nothing. The corresponding probability, denoted as $P(i, j)$ can be found in the right hand side of Equation (9.13).

We are interested in the communication scheme in which successful transmission is defined to be the case when the receptors receive user molecules greater than the threshold τ. In biology, this value varies between cases. Such a communication scheme is inspired by neural cells. The error probability is shown in Equation (9.8).

$$P_e\left(\frac{Q1}{Q2};\tau\right) = \sum_{i=0}^{\tau-1}\sum_{j=0}^{j=N-i} P(i,j) \tag{9.8}$$

9.6 Antagonists Occupy the Receptor

In this section, we investigate a more realistic case when the antagonist molecules never leaves the receptors upon binding.

To analyze this communication link, we first derive the probability distribution of all possible cases when $N = 1$. Given there are N available receptors, let $\mathbf{B}_{N+1}$ be the matrix containing those probabilities as shown in Equation (9.9). Each element

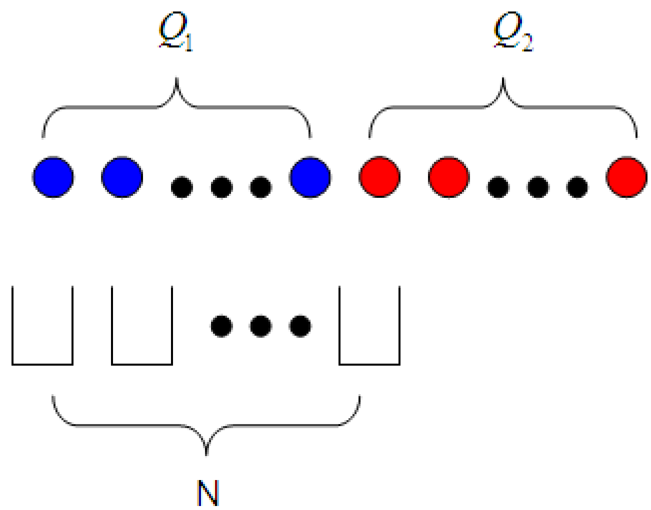

Fig. 9.6. The balls-in-a-box representation of the problem for finding the number of messenger molecules received by the receptor. The blue dots represent the messenger molecules. The red dots represent the antagonists. The boxes represent the receptors.

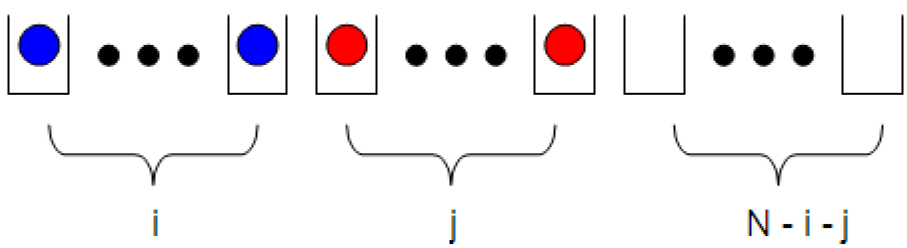

Fig. 9.7. The general case of the problem. Some of the receptors receive the messenger molecules, some of them receive the antagonists, while the rest receive nothing. The meaning of the symbols follows from Figure 9.6.

is labeled as $P_{N+1}(i,j)$. It represents the probability that the N available receptors receive i user molecules and j molecules. Those values are found through Equation (9.10), (9.11), and (9.12). Note that for $\mathbf{B}_1$, there is only one value and it is 1.

$$\mathbf{B}_2 = \begin{array}{c c} & \begin{array}{cc} 1 & 0 \end{array} \\ \begin{array}{c} 0 \\ 1 \end{array} & \begin{pmatrix} P_2(0,1) & P_2(0,0) \\ 0 & P_2(1,0) \end{pmatrix} \end{array} \tag{9.9}$$

$$P_2(0,1) = [1-(1-p_2)^{Q_2}](1-p_1)^{Q_1} \tag{9.10}$$

$$P_2(0,0) = (1-p_1)^{Q_1}(1-p_2)^{Q_2} \tag{9.11}$$

$$P_2(1,0) = (1-p_1)^{Q_1} \tag{9.12}$$

We then derive the probability distribution for $N > 1$ cases. Let $\mathbf{B}_{N+1}$ be the matrix responsible for the case with N available receptors. Each entry $B_{N+1}(i,j)$ can be found as shown in Equation (9.13).

$$B_{N+1}(i,j) = \begin{cases} P_2(1,0)^i * P_2(0,1)^j * P_2(1,0)^k * \frac{N!}{i!j!(N-i-j)!} & ,i+j \le N \\ 0 & ,i+j > N \end{cases} \tag{9.13}$$

We propose a Markov chain solution to this problem. Define the states S_i to be the scenario when there are $i+1$ available receptors. Let $\mathbf{A}$ be the transition matrix with each entry $A(i,j)$ shown in Equation (9.14).

$$A(i,j) = \begin{cases} P\left(\{S_j \to S_i\}\right) = B_{j+1}(0,j) & ,i \le j \\ 0 & ,i > j \end{cases} \tag{9.14}$$

The initial condition vector $\mathbf{x}_0$ (with dimension N+1 by 1) has 1 in the last element and 0 in the rest of the entries. The distribution of the states $\mathbf{x}_k$ ($k \ge 1$) is found by $\mathbf{x}_k = \mathbf{A}\mathbf{x}_{k-1}$. Note that $\mathbf{A}$ is an upper triangular matrix.

Once we have found the distribution of the states, we can then find the probability of every case in each time slot k. The probability that at time slot k, the number of available receptor is N' while receiving i user molecule and j antagonist molecule is $\mathbf{x}_k(N'+1) * B_{N'+1}(i,j)$. From this point on, various quantities of interest can be derived.

A. Expected number of time the receptors are depleted

Understanding the behavior of the channel over time is beneficial to learn its limit. Since $\mathbf{x}_k(1)$ represent the probability that all of the receptors are occupied by the antagonist molecules at time k, the expected number of such time $T_{deplete}$ can be found by Equation (9.15).

$$T_{deplete} = \sum_{k=1}^{\infty} \mathbf{x}_k(1) * k \tag{9.15}$$

B. Error probability

The idea is the same as the one proposed in Section 9.5. The error event includes every scenario in which the receptors receive user molecules less than the threshold τ. Hence, the error probability $P_e\left(\frac{Q1}{Q2};\tau\right)$ is derived in Equation (9.16).

$$P_e\left(\frac{Q1}{Q2};\tau\right) = \sum_{m=1}^{N+1} \mathbf{x}_k(m) * \left(\sum_{i=0}^{i=\tau-1}\sum_{j=0}^{j=m-1} B_m(i,j)\right) \tag{9.16}$$

9.7 Antagonists Occupy the Receptor with Channel Memory

This is the most realistic scenario for molecular communication. The user molecule occupies the receptor for a period of time before it is hydrolyzed. If we wish to communicate during this interval, then these past messenger molecules block the future messenger molecules. This is called self-interference. The communication link now has memory. Suppose the messenger molecules only occupy the receptor for w transmission time slots, then we can say we have a w-tap delay system. The faster we wish to communicate, the more serious this problem poses.

The idea mentioned in Section 9.7 can be used to solve this case with slight modifications. The transition matrix $\mathbf{A}$ shown in Equation (9.14) will be augmented with more states. These additional states accounts for the channel memory. Each addi-

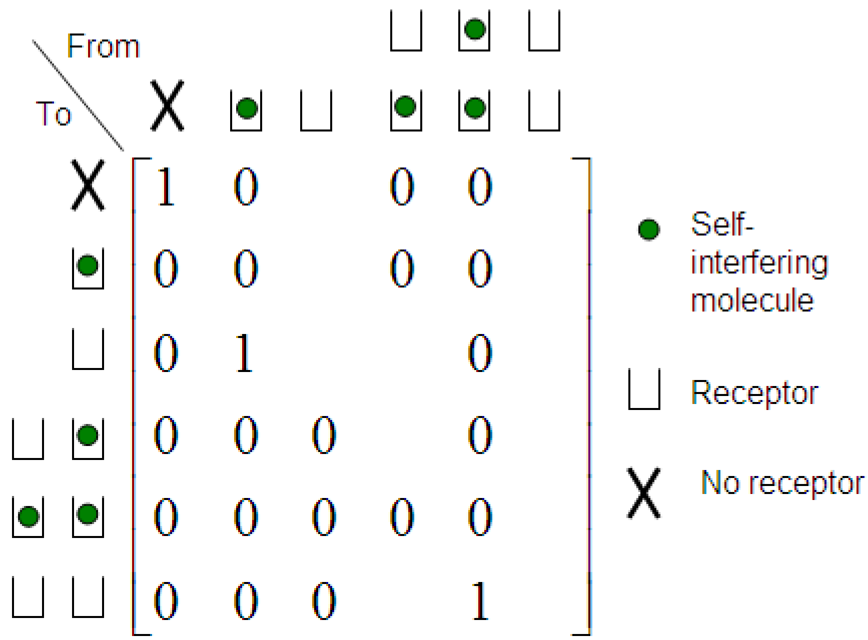

Fig. 9.8. The augmented transition matrix with state interpretation. This example accounts for 1-tap delay and $N = 2$. 0 means that there is no chance specific state transition is possible.

tional state represents the case with different combination of self-interfering molecules. An example is shown in Figure 9.8.

The way to find the expected number of time the receptors are depleted remains the same. For error probability, the result is shown in Equation (9.17).

$$P_e\left(\frac{Q1}{Q2};\tau\right) = \sum_{m=1}^{D} \mathbf{x}_k(m) * \left(\sum_{i=0}^{i=\tau-1} \sum_{j\in\Theta} B_m(i,j)\right) \tag{9.17}$$

where D is the total number of states and Θ is the set of the states that has received user molecules less then τ.

9.8 Simulation Result

In this section, we provide our simulation results for various cases. We use $N = 6$ for the every simulation. We assume that the self-interference only lasts one time

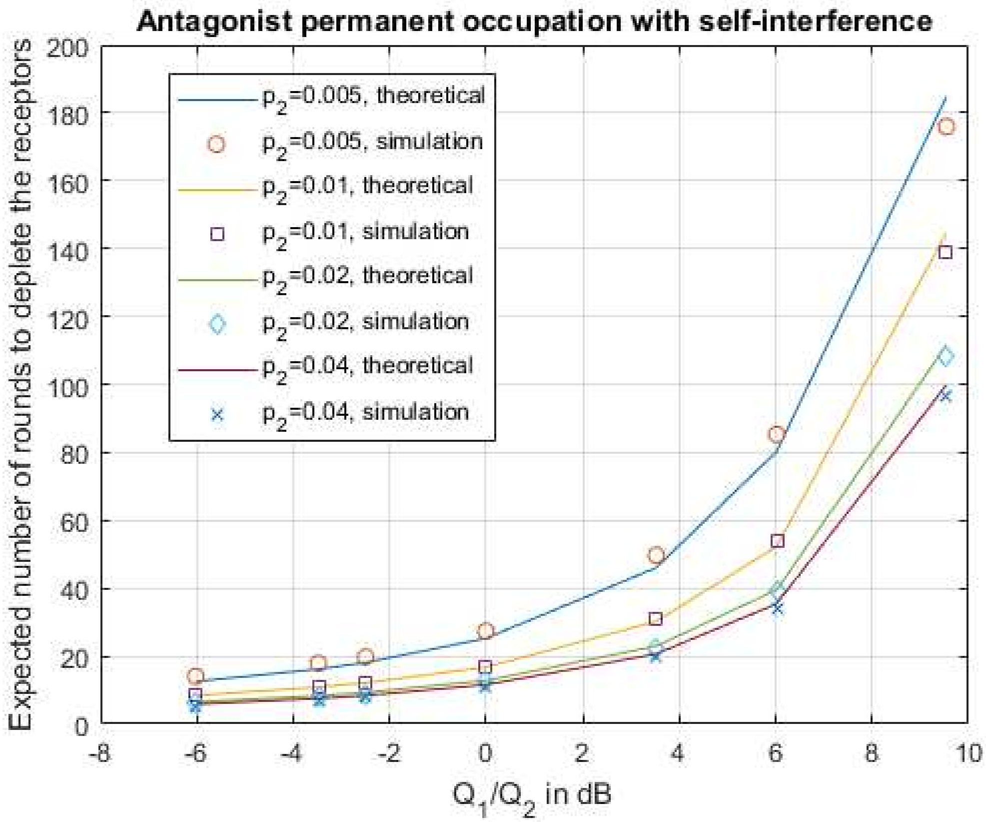

Fig. 9.9. Expected number of time the receptors are depleted versus SIR with $p_1 = 0.01$, $p_2 = 0.02$, and $N = 6$.

slot. Following the idea in [115], the signal-to-interference ratio (SIR) is defined in Equation (9.18).

$$SIR \equiv \frac{Q_1^2}{Q_2^2} \tag{9.18}$$

A. Expected number of time the receptors are depleted

The result is shown in Figure 9.9. The result shows that for fixed binding probabilities, the communication links stays longer for higher SIR. For fixed SIR, lower binding probability for the antagonist favors the communication link.

B. Error probability

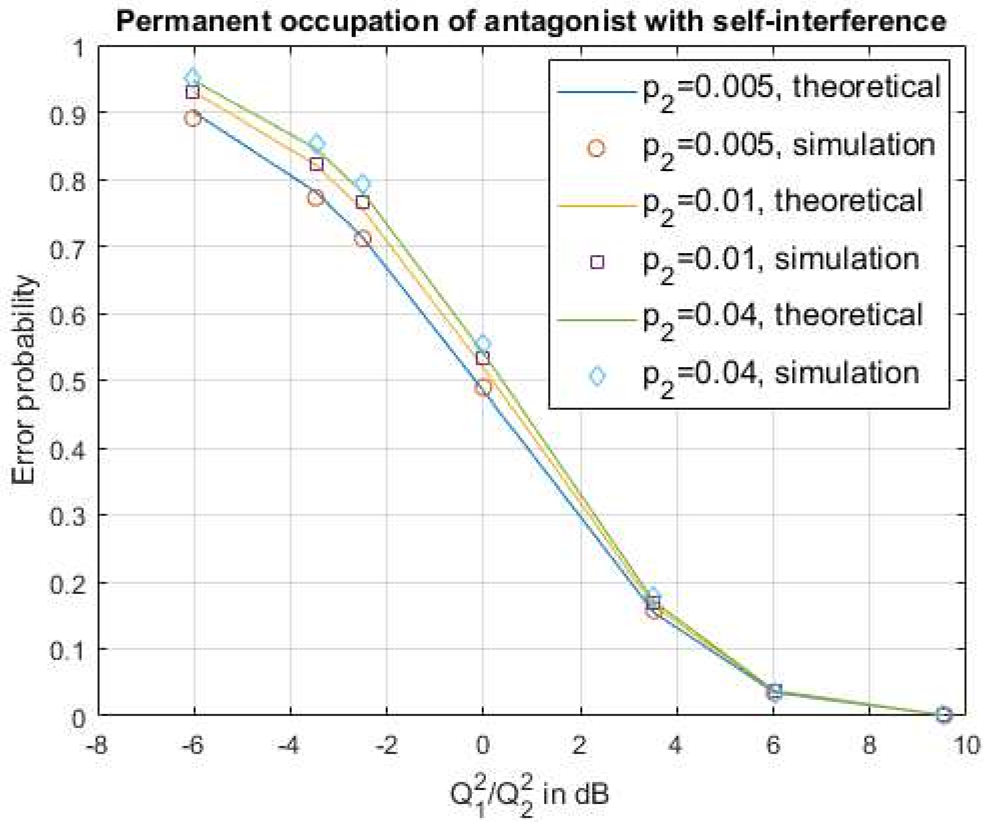

Fig. 9.10. The error probability versus SIR with $p_1 = 0.01$, $p_2 = 0.02$, $N = 6$, and $\tau = 3$.

The results are shown in Figure 9.10, 9.11, 9.12, 9.13, and 9.14. In Figure 9.10, higher SIR and lower binding probability for antagonist lower the error probability. In Figure 9.11, the error probability is lowered when the threshold is lower.

In Figure 9.12, there is a switching behavior for the error probability. This phenomenon is caused by the fact the self-interference of the user molecule. For higher SIR, the transition is more apparent. In Figure 9.13, lower binding probability for the antagonist achieves lower error probability in the transition time slots. In Figure 9.14, there is clearer lower error probability when the threshold is lower. All these results show that our analysis results and simulation results match.

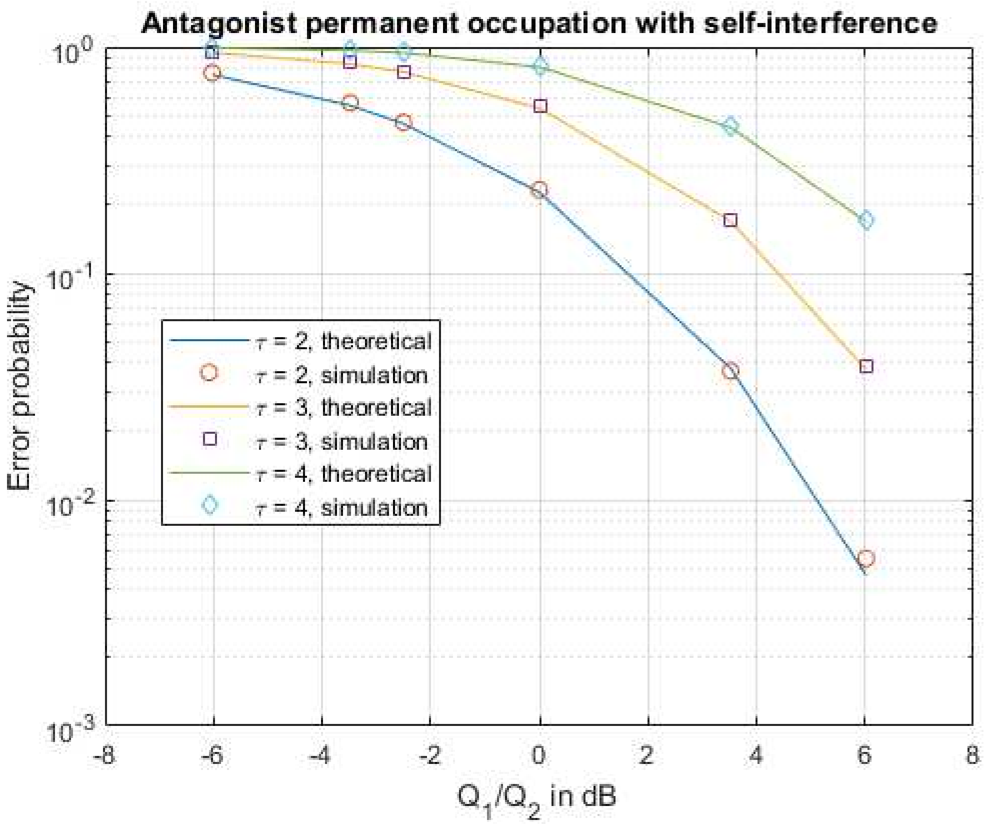

Fig. 9.11. The error probability versus SIR for different values of τ with $p_1 = 0.01$, $p_2 = 0.02$, and $N = 6$.

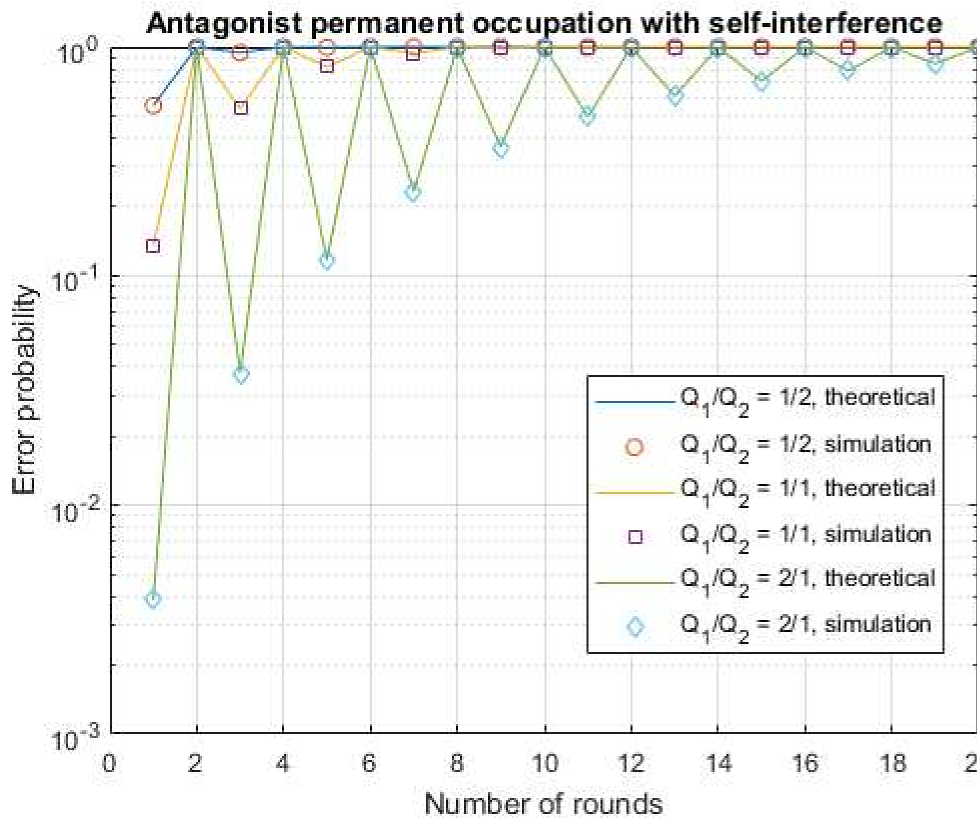

Fig. 9.12. The error probability versus time for different SIR with $p_1 = 0.01$, $p_2 = 0.02$, $N = 6$, and $\tau = 3$.

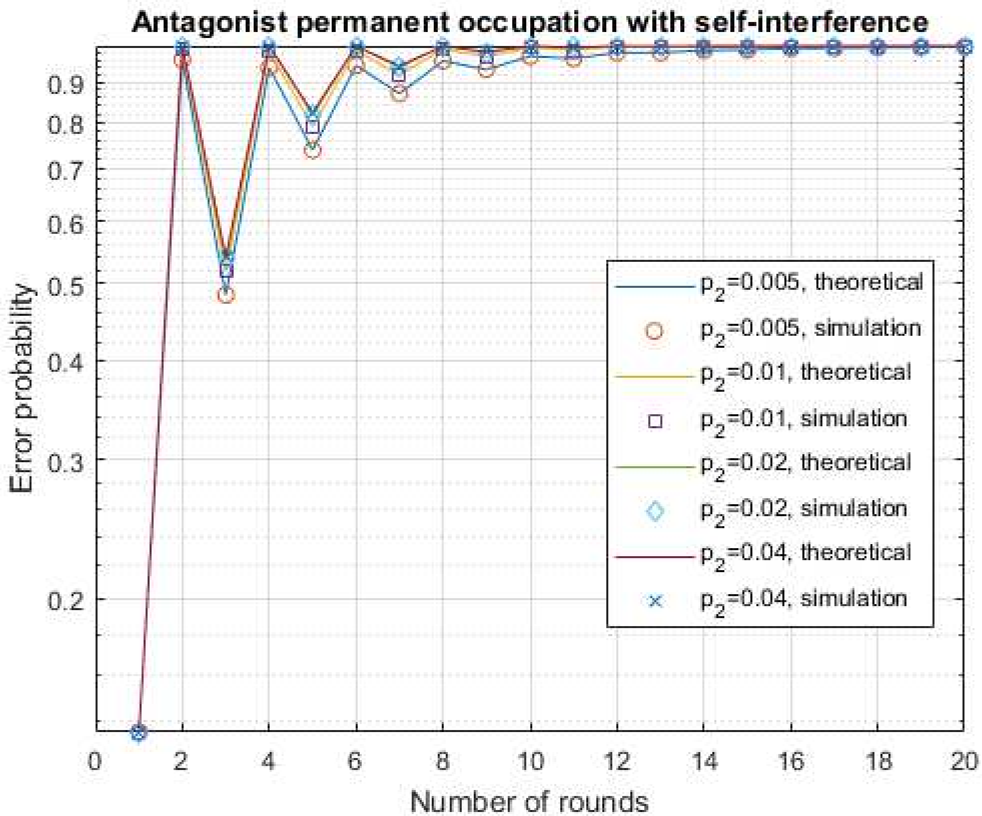

Fig. 9.13. The error probability versus time for different p_2 with $p_1 = 0.01$, $SIR = 1/1$, $N = 6$, and $\tau = 3$.

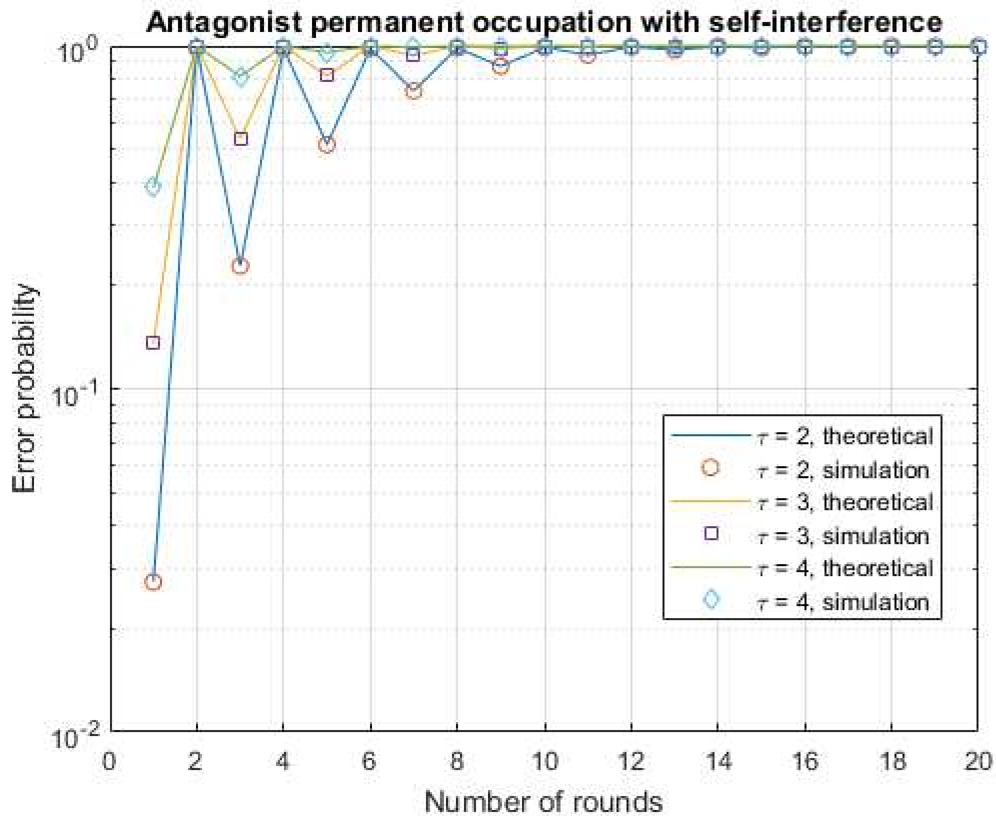

Fig. 9.14. The error probability versus time for different τ with $p_1 = 0.01$, $p_2 = 0.02$, $N = 6$, and $SIR = 1/1$.

9.9 Conclusion

In this work, we have investigated the nature of receptor antagonist and discussed its impact to diffusion based molecular communication. We first discussed the mean concentration of user and antagonist molecule at the receiver due to diffusion and showed that their ratio not only varies with time, but also depends on different transmission schemes. We used the particle counting method to model the molecular noise. The theoretical results are derived based on Markov chain and are accurate as shown in the simulation result. The presence of receptor antagonist deteriorates the molecular communication link in many ways such as disabling the available receptors and lowers the received user molecules.

10. PERFORMANCE ANALYSIS FOR NANOWIRE MOLECULE DETECTION WITH NONEXTENSIVE STATISTICAL MECHANICS

Silicon nanowire has been used to detect molecules for medical diagnostics. It also has the potential for being the core of the receiver circuitry in molecular communication. The operating frequency in this application is lower compared to regular wireless communication systems. The dominating noise comes from 1/f noise. The long-term memory and nonequilibrium mechanism gives rise to marginal probability density function being Kappa. We construct a channel model based on this idea an provide an optimal detection solution based on noise decorrelation. We also provide an approximation result for this algorithm. Simulation results show that even though increasing sample size lowers the detection error, there is not much gain for sample size greater than 50.

10.1 Introduction

Molecule detection helps our lives in many aspects. In medical diagnostics, the presence of certain types of molecule could mean the possibility of a certain disease [122]. For example, 2-propenenitrile, 2-butoxy-ethanol, furfural, 6-methyl-5-hepten-2-one and isoprene are associated with gastric cancer and/or ulcer [123]. For lung cancer, 2-methylpentane, acetone, and propanal are found to increase in concentration [124]. If we can identify these molecules and compare the result with the blueprint from literatures, then we have better knowledge in determining the type of disease the patient is suffering from.

One promising future technology is molecular communication. Transmission of information at nanoscale with wireless method requires very high operating frequency due to the extreme short length of antennas. To circumvent this difficulty, an alternative approach is to use diffusion-based molecular transmission. This is achieved to sending a group of molecules which will be received by the receiver due to concentration gradient. Many researches have been developed to enhance the performance of this system [125] [126]. One main concern is the receiver circuitry. Analytical result can be better understood if the distribution of noise and interference can be obtained.

In recent years, advance in silicon nanowire technology shows that it is possible to detect the target molecule via adsorption [127] [128]. Such process changes the resistivity of the nanowire. Hence, detection is possible, and provides a solution to the molecular communication receiver circuitry [129]. However, semiconductor devices have a well known additive low frequency noise in which we call 1/f noise. At the output of the nanowires, the measured noise is dominated by 1/f noise [127] [128]. Understanding the distribution of the sampled 1/f noise process becomes critical.

1/f noise process in devices is typically regarded as stationary [130]. It is caused by random resistivity fluctuations over time. Due to its long-term effect, this process can be regarded as a result of some non-linear mechanism with nonequilibrium environment [131] [132]. On the other hand, studies show [133] [134] that Kappa distribution is the steady-state tail distribution for describing a system with nonequilibrium and long-term memory. So one may wonder whether a connection exists between these two ideas or not.

To address this issue, [135] proposed a microscopic model with stochastic differential equation (SDE) to obtain 1/f noise power spectrum with Kappa marginal probability density function (pdf). Kappa distribution has been widely observed and analyzed in many places. For example, in high frequency (HF) communication, the tail distribution for the noise at sunrise is Kappa [49]. The nonequilibrium part comes from the interactions between the sun and the ionosphere at sunrise. The distribution of the sum of Kappa random variables can still be approximated to have Kappa tail when the weighting coefficients differ by a considerable amount [136]. [57] and [137] analyzed the bit error rate and the MIMO packet error rate of a communication system with dominant Kappa noise. In replace of the Q function for the Gaussian case, L function is used for the Kappa case.

The purpose of this work is to establish and analyze a channel model on silicon nanowires operating on lower frequencies for biomedical purpose. Lower frequency data needs to be carefully preserved because they could contain information due to biological events [138]. [139] provided an RC circuit model for silicon nanowires. [129] proposed a Gaussian noise model to account for the 1/f noise with Markov chain solution. In our work, we propose a Kappa 1/f noise model with optimal error performance based on noise decorrelation technique. We also provide an approximate analytical solution based on Kappa pdf. The number of the samples is taken into consideration. While taking more samples will provide better performance, it also increases computation complexity. A suitable value of sample size needs to be explored. Nanowire has already been tested for examining certain molecules exhaled from patients [122]. Our work could contribute to lower detection error.

This paper is organized as follows. In Section 10.2, we describe the silicon nanowire operating principle with corresponding noise process, and in Section 10.3, we summarize the SDE model that produces 1/f noise power spectrum with Kappa distribution. In Section 10.4, we establish the system model. In Section 10.5, we develop a optimal signal processing algorithm to detect molecule concentration and then analyze the error rate. In Section 10.6, we discuss a method for limiting detection range and derive the corresponding detection error probability. In Section 10.7, we show simulation results in various scenarios, and draw conclusions in Section 10.8.

10.2 Nanowire Sensor Principle

Past research in nanotechnology indicated that metals at nanoscale exhibit a change in conductivity as they adsorb or desorb molecules. This phenomenon can be thought of as a change of electron mean free path due to the change of wire geometry from alien molecules at mesoscopic level. Figure 10.1 and Figure 10.2 illustrates this idea. Such characteristic becomes more important in the nano regime because surface effects grows with decreasing dimension. Assume the molecule selectivity is high in this system. This technique enables a more precise estimation of the molecule concentration.

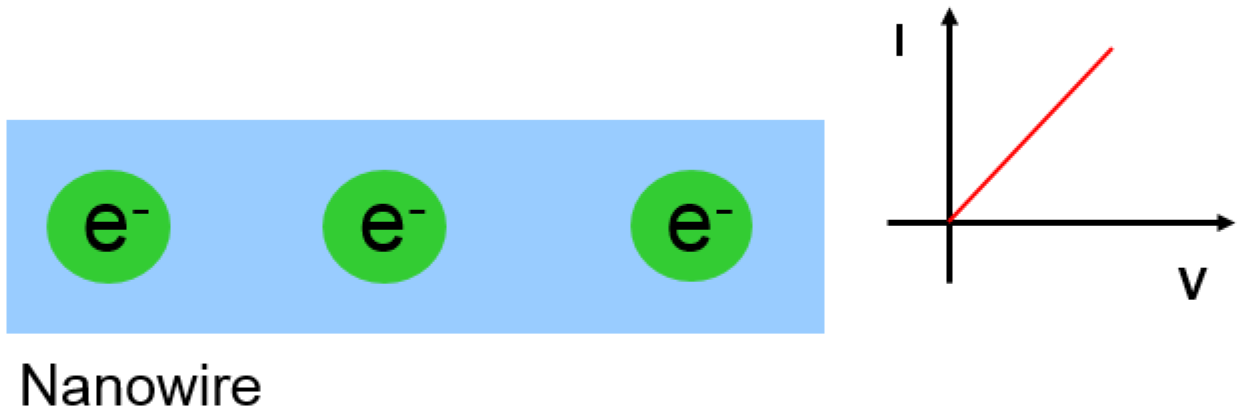

Fig. 10.1. The change of electron mean free path due to molecular adsorption. This figure shows a regular nanowire with the corresponding current-voltage plot.

The noise associated with nanowire is dominated by different sources at different frequencies. A typical plot of the noise power spectral density is shown in Figure 10.3. At lower frequencies, the 1/f noise dominates while at higher frequencies, the Lorentzian noise ($1/f^2$) dominates.

The Lorentzian noise is composed of two parts, thermal noise and chemical noise. Thermal noise is frequency flat prior to passing through the circuit system. The nanowire sensor can be regarded as an equivalent RC lowpass circuit. Hence, at the output of the sensor, the noise power spectrum has $1/f^2$ shape at higher frequencies and flat shape at lower frequencies. The cutoff frequency depends the circuit system.

Chemical noise in nanowire sensor is caused by the fluctuation of adsorption and desorption process. It has been shown that a perturbation imposed on the system causes the number of molecules of a state to change. It contributes a Lorentzian noise

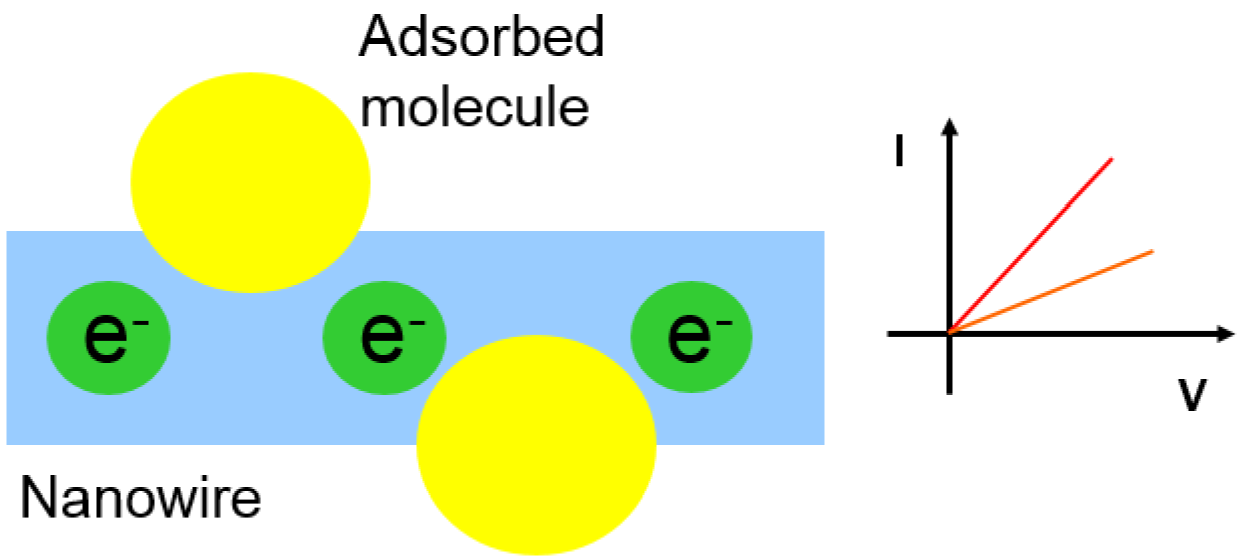

Fig. 10.2. This figure shows a nanowire with adsorbed molecules. The current-voltage plot also shows a corresponding change of conductivity.

power spectrum as it decays with $1/f^2$. The cutoff frequency depends on the chemical process.

Depending on the actual device and measuring environment, the cutoff frequencies for the two types of noise may change. But the sum of them still produces a Lorentzian spectrum.

10.3 Nonextensive Statistical Mechanics and 1/f Noise

1/f noise of a circuit is generated by resistance fluctuations even at nanoscale. It dominates the lower frequency regime and shows long term memory property. Nonextensive statistical mechanics, in which the entropy loses additivity, is used to describe correlated subsystems. This can be used to explain the 1/f noise of a circuit by considering a model based on stochastic differential equation. The following explanation is summarized from .

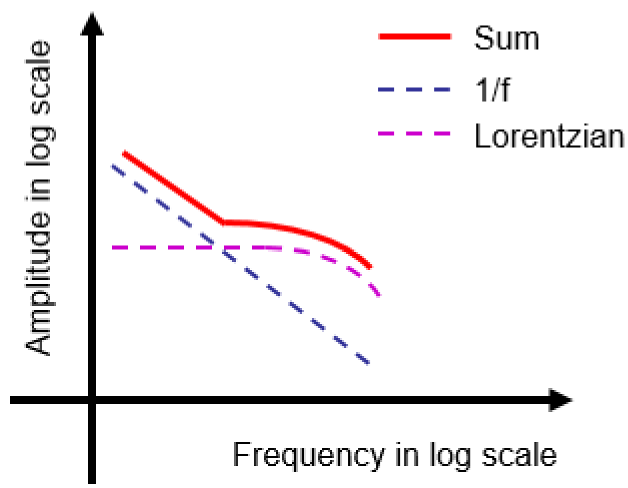

Fig. 10.3. A typical plot for noise power spectral density plot in nanowire.

Noise signal $x(t)$ at microscopic level is composed of random impulses that arrives at time t_k. We assume each impulse has the same coefficient A. That is,

$$x(t) = \sum_k A\delta(t - t_k). \tag{10.1}$$

The characterization of the noise power spectral density and marginal pdf is determined by the statistics of transit time. The model is given by

$$\begin{aligned} t_{k+1} &= t_k + \tau_k, \\ \tau_{k+1} &= \tau_k + \gamma\tau_k^{2\mu-1} + \sigma\tau_k^{\mu}\epsilon_k. \end{aligned} \tag{10.2}$$

Here, τ_k is the interarrival time between t_k and t_{k+1}. ϵ_k are i.i.d. Gaussian random variables with N(0,1) and σ manages the variance. γ is a coefficient of the nonlinear damping. μ models the degree of freedom in this noise process. The corresponding Itô SDE in k-space is given by

$$\frac{d\tau_k}{dk} = \gamma\tau_k^{2\mu-1} + \sigma\tau_k^{\mu}W(k), \tag{10.3}$$

where W is the Wiener process. The time domain representation of (10.3) is obtained by letting $dt_z = \tau_k dk$. Thus, we get

$$\frac{d\tau}{dt_z} = \gamma\tau^{2\mu-2}dt_z + \sigma\tau^{\mu-\frac{1}{2}}dW(t_z). \tag{10.4}$$

We focus on the behavior of x by transforming (10.4) with change of variable $x = A/\tau$. We obtain

$$dx = \sigma^2(\eta - \frac{1}{2}\lambda)x^{2\eta-1}dt + \sigma x^{\eta}dW(t). \tag{10.5}$$

where $t = \frac{1}{A^{3-2\mu}}t_z$, $\eta = \frac{5}{2} - \mu$, and $\lambda = 2\gamma + 2\sigma^2(\eta - 1)$. To discuss the marginal pdf, we consider the system with nonequilibrium. When the time the system takes to reach stationarity is much smaller than the scale at which the fluctuating parameter changes, the system should be described by the superposition of different local dynamics at different time intervals. This method is called superstatistics in statistical mechanics. We identify a fluctuating parameter $\bar{x}$ as a quantity related to the first arrival time of Wiener process. For practical purpose, we restrict during time T, the maximum value $\bar{x}$ can change is $\bar{x}_{max}$. Within T, the noise signal x has local stationary conditional pdf $g(x|\bar{t})$. The long-term stationary pdf of noise signal x is given by

$$f(x) = \int_0^\infty g(x|\bar{x})p(\bar{x})d\bar{x}. \tag{10.6}$$

We assume $g(x|\bar{x})$ is Gaussian. That is,

$$g(x|\bar{x}) = \frac{1}{\bar{x}\sqrt{\pi}} \exp\left(-\frac{x^2}{\bar{x}^2}\right). \tag{10.7}$$

The distribution of $\bar{x}$ is given by

$$p(\bar{x}) = \frac{1}{x_0\Gamma(\frac{\lambda-1}{2})} \left(\frac{x_0}{\bar{x}}\right)^\lambda \exp\left(\frac{x_0^2}{\bar{x}^2}\right). \tag{10.8}$$

Here, x_0 describes the exponential cutoff of the pdf of $\bar{x}$ for small values of $\bar{x}$. If we use change of variable $t = \bar{x}^2$ in (10.8), the new pdf is exactly the first arrival time distribution of Wiener process.

We modify (10.5) for $\bar{x}$ by considering parameter fluctuation and neglecting $\bar{x}_{max}$ for practical purpose. We obtain

$$d\bar{x} = \sigma^2(\eta - \frac{\lambda}{2} + \frac{x_0}{\bar{x}^2})\bar{x}^{2\eta-1}dt + \sigma\bar{x}^\eta dW. \tag{10.9}$$

By combining (10.6), (10.7), (10.8), and (10.9). We obtain the power spectrum of x to have 1/f slope while having marginal pdf to be Kappa.

10.4 System Model

Under the assumption that the sampling frequency is smaller than the cutoff frequency of the noise power spectrum contributed from Gaussian components, the system model is given by

$$\mathbf{y} = \mathbf{x} + \mathbf{n}. \tag{10.10}$$

where $\mathbf{y}$ is the received signal vector, $\mathbf{x}$ is the transmitted signal vector that represents the concentration of target molecule, and $\mathbf{n}$ is the noise vector with 1/f power spectrum and Kappa marginal pdf given by

$$f_n\left(t; K, \sigma\right) = \frac{1}{\sqrt{K}\sigma\beta\left(\frac{1}{2}, K+\frac{1}{2}\right)}\left(1+\frac{t^2}{K\sigma^2}\right)^{-K-1}, \qquad -\infty < t < \infty, K > \frac{1}{2}. \tag{10.11}$$

where the function $\beta\left(x, y\right)$, with positive real arguments here, is the beta function. K represents the degree of thermal equilibrium, and σ is a quantity that is related to the variance. The reason Gaussian noise is neglected is that the power contribution from Gaussian components is significantly smaller than that from the 1/f noise component in this range of frequencies.

The simplest detection case for this model is to distinguish whether a molecule of interest is present or not. This can achieved by setting up a lower (x_1) and a higher (x_0) value of concentration and decide which one was the case according to $\mathbf{y}$ and signal processing result. We derive an algorithm with error analysis in the next section.

10.5 Detection Error Analysis

Suppose x_0 is sent, that is, $\mathbf{x} = x_0[1{,}1{,}...{,}1]^T$. We denote this value as $\mathbf{x_0}$ Similarly, $\mathbf{x_1} = x_1[1{,}1{,}...{,}1]^T$. For 1/f noise, a practical assumption is to dictate that for frequencies below the measurement limit (f_0), the power spectral density is flat. That is,

$$S_n(f) = \begin{cases} \frac{\gamma}{2f_0} & , f < f_0 \\ \frac{\gamma}{1+\frac{f}{f_0}} & , f \geq f_0. \end{cases} \tag{10.12}$$

The autocorrelation function is the inverse Fourier transform of the power spectral density. For simulation purpose, we use a computer software to directly find the result. For analytical interest, we neglect the portion $f < f_0$ due to its minor effect on the inverse Fourier transform integral. Hence we obtain

$$\begin{aligned} R_n(\tau) &\approx \int_{-\infty}^{-f_0} \frac{\gamma f_0}{|f|} e^{j2\pi f\tau} df + \int_{f_0}^{\infty} \frac{\gamma f_0}{f} e^{j2\pi f\tau} df \\ &= \int_{f_0}^{\infty} 2\frac{\gamma f_0}{f} \cos(2\pi f\tau) df \\ &= -2\gamma f_0 \mathrm{Ci}(2\pi f_0 \tau). \end{aligned} \tag{10.13}$$

where Ci(x) is the cosine integral defined as

$$\mathrm{Ci}(x) = \int_{x}^{\infty} \frac{\cos t}{t} dt. \tag{10.14}$$

We can find the autocorrelation matrix $\mathbf{R_n}$ according to R_n. That is, $\mathbf{R_n}(i, j) = R_n(|i - j|)$. A plot of the $\mathbf{R_n}$ is shown in Figure 10.4. Let matrix $\mathbf{D}$ satisfy

$$\mathbf{R_n}^{-1} = \mathbf{D}^T\mathbf{D}, \tag{10.15}$$

then decorrelation of $\mathbf{n}$ can be achieved by multiplying $\mathbf{y}$ by $\mathbf{D}$. That is,

$$\mathbf{Dy} = \mathbf{Dx} + \mathbf{Dn} \tag{10.16}$$

Notice that $E[(\mathbf{Dn})(\mathbf{Dn})^T] = \mathbf{DRD}^T = \mathbf{D}(\mathbf{D^TD})^{-\mathbf{1}}\mathbf{D} = \mathbf{I}$. Let $\tilde{\mathbf{n}} = \mathbf{Dn}$ and $\tilde{n}_k$ to be the k-th element of $\tilde{\mathbf{n}}$, then $\tilde{\mathbf{n}}$ are uncorrelated. If the size of $\mathbf{y}$ is 1, then $\tilde{\mathbf{n}}$ has Kappa distribution with unit variance. For other sizes of $\mathbf{y}$, the result moves away from Kappa. For approximation purpose, we choose independently and identically distributed (i.i.d.) Kappa distribution.

We use the maximum likelihood criterion to decide whether x_0 is sent or not. That is,

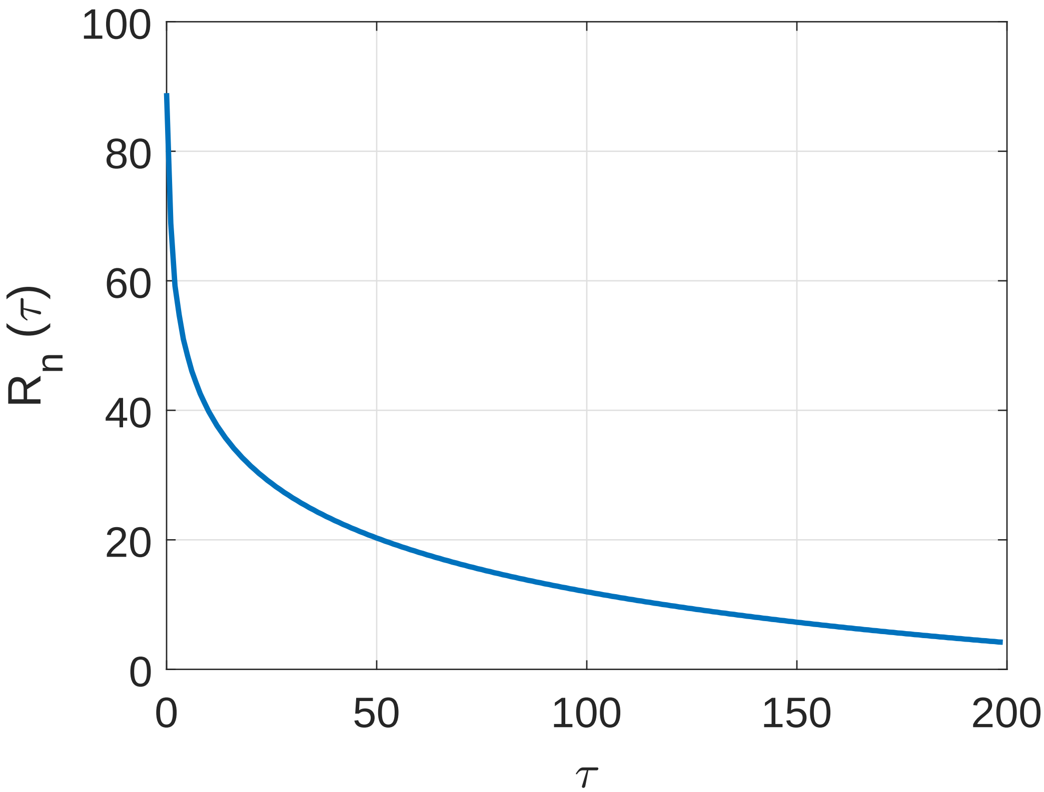

Fig. 10.4. The autocorrelation function of the noise process. We notice that this function has a thick tail.

$$T_i = ||\mathbf{Dx_0} + \tilde{\mathbf{n}} - \mathbf{Dx_i}||_2^2, \text{ for } i = 0, 1 \tag{10.17}$$

$$\text{If } T_0 \leq T_1, \text{ decide } x_0 \text{ is sent.} \tag{10.18}$$

To find the error probability associated with (10.18), notice that the error event is $\{T_0 > T_1\}$. Let the size of $\mathbf{y}$ be S. Denote the sum of row vectors of $\mathbf{D}$ as d_1, d_2, ... , d_S. That is,

$$d_k = \sum_{j=1}^{S} D_{k,j} \tag{10.19}$$

where $D_{i,j}$ is the (i,j) entry of $\mathbf{D}$. Then the error event can be simplified according to (10.17). That is,

$$2(\mathbf{x_0} - \mathbf{x_1})^T \mathbf{D}^T \tilde{\mathbf{n}} < -(\mathbf{x_0} - \mathbf{x_1})^T \mathbf{D}^T \mathbf{D} (\mathbf{x_0} - \mathbf{x_1}) \tag{10.20}$$

$$\Rightarrow \sum_{k=1}^{S} d_k \tilde{n}_k < -\frac{x_0 - x_1}{2} \sum_{k=1}^{S} d_k^2. \tag{10.21}$$

The detailed derivation is shown below.

Observe that

$$
\begin{aligned}
&2\left(\mathbf{x_0}-\mathbf{x_1}\right)^T\mathbf{D}^T\tilde{\mathbf{n}}\\
&=2\left(x_0-x_1\right)\begin{bmatrix}1 & 1 & \cdots & 1\end{bmatrix}\\
&\begin{bmatrix}D_{1,1} & D_{2,1} & \cdots & D_{S,1}\\ D_{1,2} & D_{2,2} & \cdots & D_{S,2}\\ \vdots & \vdots & \ddots & \vdots\\ D_{1,S} & D_{2,S} & \cdots & D_{S,S}\end{bmatrix}\begin{bmatrix}\tilde{n}_1\\ \tilde{n}_2\\ \vdots\\ \tilde{n}_S\end{bmatrix}\\
&=2\left(x_0-x_1\right)\begin{bmatrix}d_1 & d_2 & \cdots & d_S\end{bmatrix}\begin{bmatrix}\tilde{n}_1\\ \tilde{n}_2\\ \vdots\\ \tilde{n}_S\end{bmatrix}\\
&=2\left(x_0-x_1\right)\sum_{k=1}^{S}d_k\tilde{n}_k. \qquad (10.22)
\end{aligned}
$$

Also notice that

$$
\begin{aligned}
&\mathbf{D}\left(\mathbf{x_0}-\mathbf{x_1}\right)\\
&=\left(x_0-x_1\right)\begin{bmatrix}D_{1,1} & D_{1,2} & \cdots & D_{1,S}\\ D_{2,1} & D_{2,2} & \cdots & D_{2,S}\\ \vdots & \vdots & \ddots & \vdots\\ D_{S,1} & D_{S,2} & \cdots & D_{S,S}\end{bmatrix}\begin{bmatrix}1\\ 1\\ \vdots\\ 1\end{bmatrix}\\
&=\left(x_0-x_1\right)\begin{bmatrix}d_1 & d_2 & \cdots & d_S\end{bmatrix}^T. \qquad (10.23)
\end{aligned}
$$

By (10.22) and (10.24), (10.20) can be simplified as

$$
\begin{aligned}
&2\left(x_0 - x_1\right)\sum_{k=1}^{S} d_k \tilde{n}_k < \\
&-\left\|\left(x_0 - x_1\right)\begin{bmatrix} d_1 & d_2 & \cdots & d_S \end{bmatrix}^T\right\|_2^2 \\
&\Rightarrow 2\left(x_0 - x_1\right)\sum_{k=1}^{S} d_k \tilde{n}_k < -\left(x_0 - x_1\right)^2 \sum_{k=1}^{S} d_k^2.
\end{aligned}
\tag{10.24}
$$

Further simplification yields (10.21).

Let $\alpha = \sum_{k=1}^{S} d_k^2$, which is also the variance on the left hand side of (10.21). The approximated error probability is given by

$$
P_e = L\left(\left(\frac{x_0 - x_1}{2}\right)\sqrt{\alpha}; K\right). \tag{10.25}
$$

Here, the L function is defined as

$$
\begin{aligned}
&L\left(x; K\right) = \\
&\int_x^{\infty} \frac{1}{\sqrt{2K-1}\beta\left(\frac{1}{2}, K + \frac{1}{2}\right)}\left(1 + \frac{t^2}{2K-1}\right)^{-K-1} dt, \\
&-\infty < x < \infty, K > \frac{1}{2}
\end{aligned}
\tag{10.26}
$$

The derivation to (10.25) is provided as follows.

Since in (10.21), $\tilde{n}_k$ are i.i.d. Kappa with zero mean with unit variance, $X = \sum_{k=1}^{S} d_k \tilde{n}_k$ has mean zero and variance α. The distribution of X is approximated to have Kappa tail [136]. Here, we further approximate the overall distribution to be Kappa (the error caused by this approximation decreases as K increases). The variance of Kappa distribution given by (10.11) is $\frac{K\sigma^2}{2K-1}$ [136]. For X, α satisfies

$$
\alpha = \frac{K\sigma^2}{2K-1}. \tag{10.27}
$$

The error probability can be found as

$$
\begin{aligned}
P_e &= P\left(\left\{X < -\frac{x_0 - x_1}{2}\alpha\right\}\right) \\
&= \int_{-\infty}^{-\frac{x_0-x_1}{2}\alpha} \frac{1}{\sqrt{K}\sigma\beta\left(\frac{1}{2}, K+\frac{1}{2}\right)}\left(1+\frac{x^2}{K\sigma^2}\right)^{-K-1} dx \\
&= \int_{\frac{x_0-x_1}{2}\alpha}^{\infty} \frac{1}{\sqrt{K}\sigma\beta\left(\frac{1}{2}, K+\frac{1}{2}\right)}\left(1+\frac{x^2}{K\sigma^2}\right)^{-K-1} dx \qquad (10.28) \\
&= \int_{\frac{x_0-x_1}{2}\sqrt{\alpha}}^{\infty} \frac{\sqrt{\alpha}}{\sqrt{K}\sigma\beta\left(\frac{1}{2}, K+\frac{1}{2}\right)}\left(1+\frac{\alpha t^2}{K\sigma^2}\right)^{-K-1} dx \qquad (10.29) \\
&= \int_{\frac{x_0-x_1}{2}\sqrt{\alpha}}^{\infty} \frac{1}{\sqrt{2K-1}\beta\left(\frac{1}{2}, K+\frac{1}{2}\right)}\left(1+\frac{t^2}{2K-1}\right)^{-K-1} dx, \qquad (10.30)
\end{aligned}
$$

where (10.28) is obtained by the symmetric property of the Kappa function. (10.29) is obtained by substitution $t = \frac{x}{\sqrt{\alpha}}$. (10.30) is obtained by using (10.27). (10.25) follows from (10.30) and (10.26).

10.6 Accuracy Analysis

We have just demonstrated the capability of detecting whether the molecule of interest is present by selecting a proper threshold. The more practical question is find out whether the concentration of a molecule is within a certain range d or not. To build up the channel model, we introduce 3 concentration points: x_0, x_1, and x_2. x_0 represents the center of the range. x_1 and x_2 are spaced d units apart from x_0. Without loss of generality, we assume $x_2 > x_0 > x_1$. The mathematical model is given by (10.10). However, this time, there are 3 hypothesis. The maximum likelihood decision criterion that is similar to (10.18) is given by

$$
\hat{\mathbf{x}} = \arg\min_{\mathbf{x}\in\{\mathbf{x_i}\}} \|\mathbf{y} - \mathbf{D}\mathbf{x}\|_2, i = 0, 1, 2. \qquad (10.31)
$$

Figure 10.5 illustrate the system model. Following the similar technique that leads to (10.25), the detection error, P_e, given accuracy range d, is given by

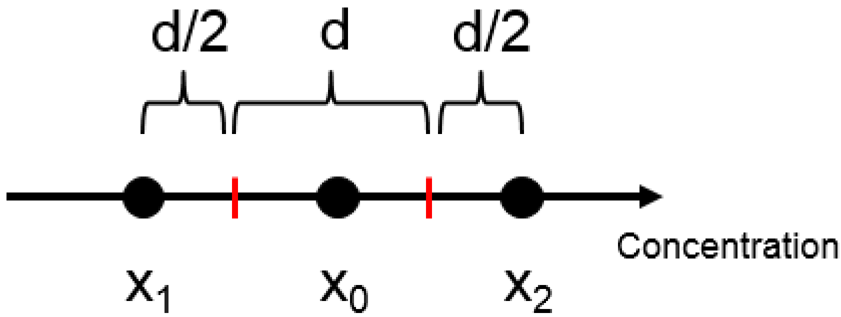

Fig. 10.5. A system model for measuring molecule concentration range. Here, the detection range lies in between the two red bars that extend from $x_0 - \frac{d}{2}$ to $x_0 - \frac{d}{2}$.

$$P_e = 2L\left(d\sqrt{\alpha}; K\right). \tag{10.32}$$

The derivation is shown below.

Following the decision criterion as described in (10.31), a detection error event occurs when $\mathbf{x_0}$ is transmitted but decided to be either $\mathbf{x_1}$ or $\mathbf{x_2}$. Since $x_2 > x_0 > x_1$, if $\mathbf{x_1}$ is decided, $\mathbf{x_2}$ will not be decided, and vice versa. Hence, $\{\hat{\mathbf{x}} = \mathbf{x_1} | \mathbf{x_0} \text{ sent}\}$ and $\{\hat{\mathbf{x}} = \mathbf{x_2} | \mathbf{x_0} \text{ sent}\}$ are disjoint. Hence the detection error probability can be found as

$$\begin{aligned} P_e &= P\left(\{\hat{\mathbf{x}} = \mathbf{x_1} | \mathbf{x_0} \text{ sent}\}\right) + P\left(\{\hat{\mathbf{x}} = \mathbf{x_2} | \mathbf{x_0} \text{ sent}\}\right) \\ &= L\left(\left(\frac{x_0 - x_1}{2}\right)\sqrt{\alpha}; K\right) + L\left(\left(\frac{x_2 - x_0}{2}\right)\sqrt{\alpha}; K\right) \qquad (10.33) \\ &= L\left(d\sqrt{\alpha}; K\right) + L\left(d\sqrt{\alpha}; K\right) \\ &= 2L\left(d\sqrt{\alpha}; K\right) \qquad (10.34) \end{aligned}$$

where 10.33 follow from Equation 10.25.

10.7 Simulation Results

In this section, we first obtain the simulated 1/f noise from Kay's method. The noise random process synthesis equation is given by

$$n[k] = \frac{1}{M/2}\sum_{i=1}^{M} \mathbf{A}_i \cos(2\pi \mathbf{F}_i k + \mathbf{\Phi}_i). \tag{10.35}$$

Here, $\mathbf{\Phi}_i$ are i.i.d. uniform random variables from $[0, 2\pi)$. M is a tuning parameter and we choose 10. $\mathbf{A}_i$ are i.i.d. random variables given by

$$p_A(a) = a\int_0^\infty \left[\psi_X\left(\sqrt{M/2}\right)\right]^{1/M} J_0(av)\, vdv. \tag{10.36}$$

where $J_0(.)$ is the Bessel function of the first kind, and ψ_X is the characteristic function of (10.11) given by

$$\psi_X(x) = \frac{2}{\Gamma\left(K+\frac{1}{2}\right)}\left(\frac{|\omega|\sqrt{K}\sigma}{2}\right)^{K+\frac{1}{2}} K_{K+\frac{1}{2}}\left(|\omega|\sqrt{K}\sigma\right). \tag{10.37}$$

where $K(.)$ is the modified Bessel function of the second kind. $\mathbf{F}_i$ are i.i.d. random variables given by

$$p_F(f) = \begin{cases} \gamma & , f < f_0 \\ \frac{\gamma f_0}{f} & , f \geq f_0. \end{cases} \tag{10.38}$$

The simulated 1/f noise with marginal Kappa pdf is shown in Figure 10.6 and 10.7.

With this random noise generator, given x_0 is sent, the simulated error probability with maximum likelihood criterion is shown in Figure 10.8, 10.9, and 10.10 for K = 1.6, 2.8, ad 5, respectively. These values are chosen to represent the degree of thermal non-equilibrium. 1.6 represents the case when the system is shifting very much towards thermal non-equilibrium, 5 represents a milder case and 2.8 lies in between. Here, the SNR in dB is defined as

$$\text{SNR } = 10\log_{10}\left(x_0^2 R(1,1)\right). \tag{10.39}$$

where $R(1,1)$ is the (1,1) entry of $\mathbf{R}$. All simulation results are based on $x_1 = \sqrt{20}$.

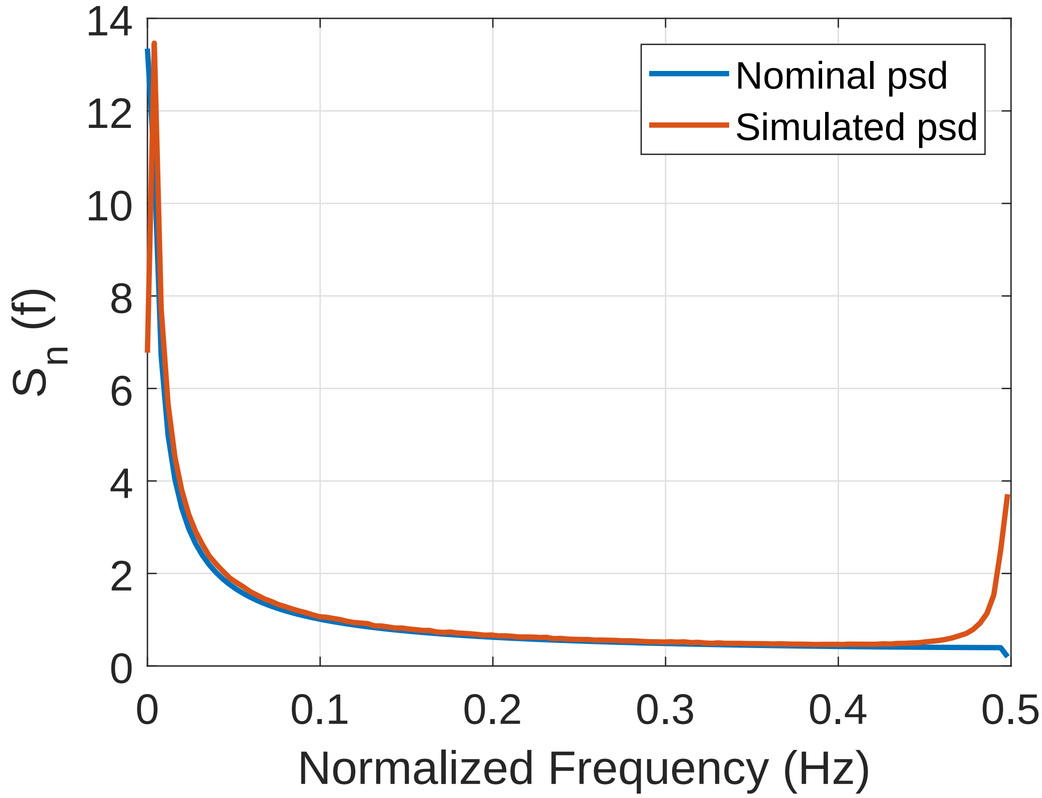

Fig. 10.6. A plot for the simulated and given 1/f noise power spectral density by using Kay's method. γ is chosen to make the area under curve is 1 to comply with Kay's method.

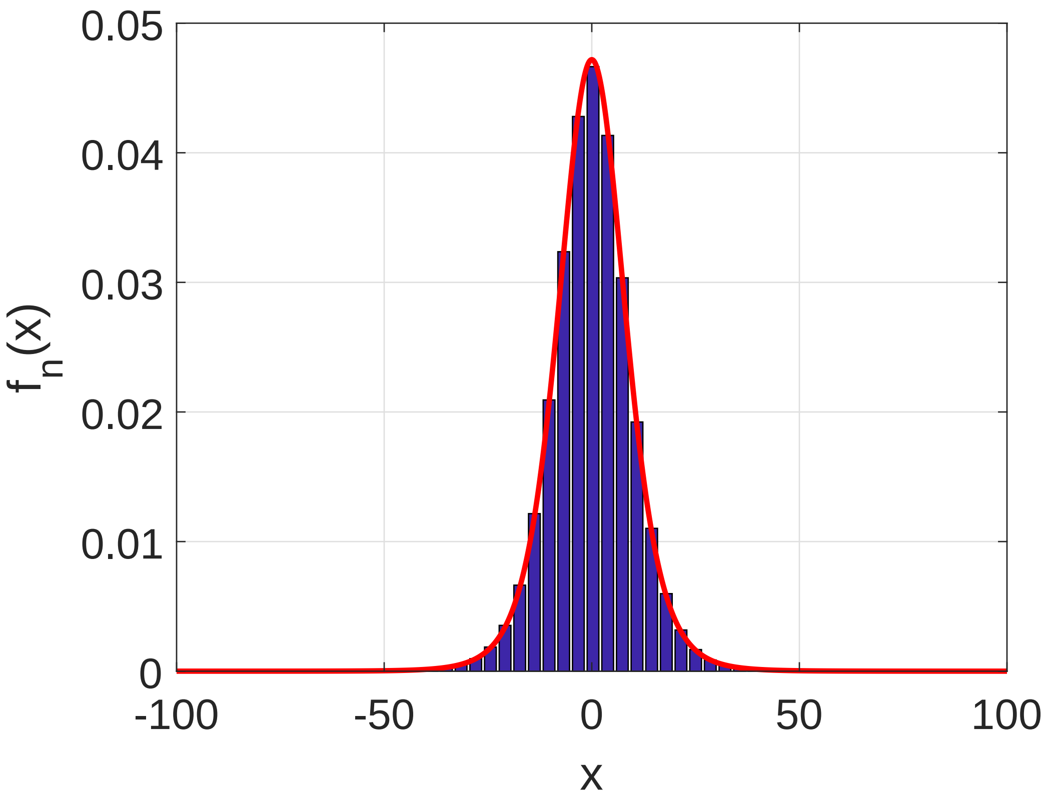

Fig. 10.7. A plot for the simulated and given 1/f noise with Kappa marginal pdf by using Kay's method. K = 2.8, σ = 12.5.

From these results, we can see that while increasing sample size does lower error rate, the complexity also increases. Furthermore, for sample size greater than 50, the error rate improvement is less significant. We believe that using sample size to be 50 is sufficient. Also, the figures shows some discrepancies between the approximated values and simulated values for larger sample size. This is because the 1/f noise autocorrelation matrix $\mathbf{R_n}$ has many similar values which is shown in Figure 10.4. Similar phenomenon can be observed on $\mathbf{D}$ as well. The noise statistics in the left hand side of (10.21) is affected by adding up a large number of similar weighted values of uncorrelated Kappa random variables. If we approximate the uncorrelated random variables to be independent, then the rate the tail decreases lies in between the Gaussian regime and polynomial regime. We could use the Generalized Gaussian distribution to characterize the pdf, but the relationship with (10.21) is much more complex to find. Our analytical result can be regarded as first-order approximation.

Figure 10.11, 10.12, and 10.13 show the simulation and approximation result for the detection error probability versus range accuracy with different sample size. These three sets of simulation represent the different degrees of thermal non-equilibrium on the nanowires. From the figure, we can see that as detection range decreases, the detection error probability increases. There is a tradeoff between range accuracy and detection error rate.

10.8 Conclusion

In this work, we examined the noise process involved in silicon nanowire with lower operating frequencies for biomedical purpose. In this regime, 1/f noise dominates. We explained why the marginal pdf is Kappa by using SDE with thermal nonequilibrium. Following these results, we build a channel model and used noise decorrelation to decide the molecule concentration hypothesis. The corresponding error rate is analyzed with approximation. Simulation results show that while increasing sample size does

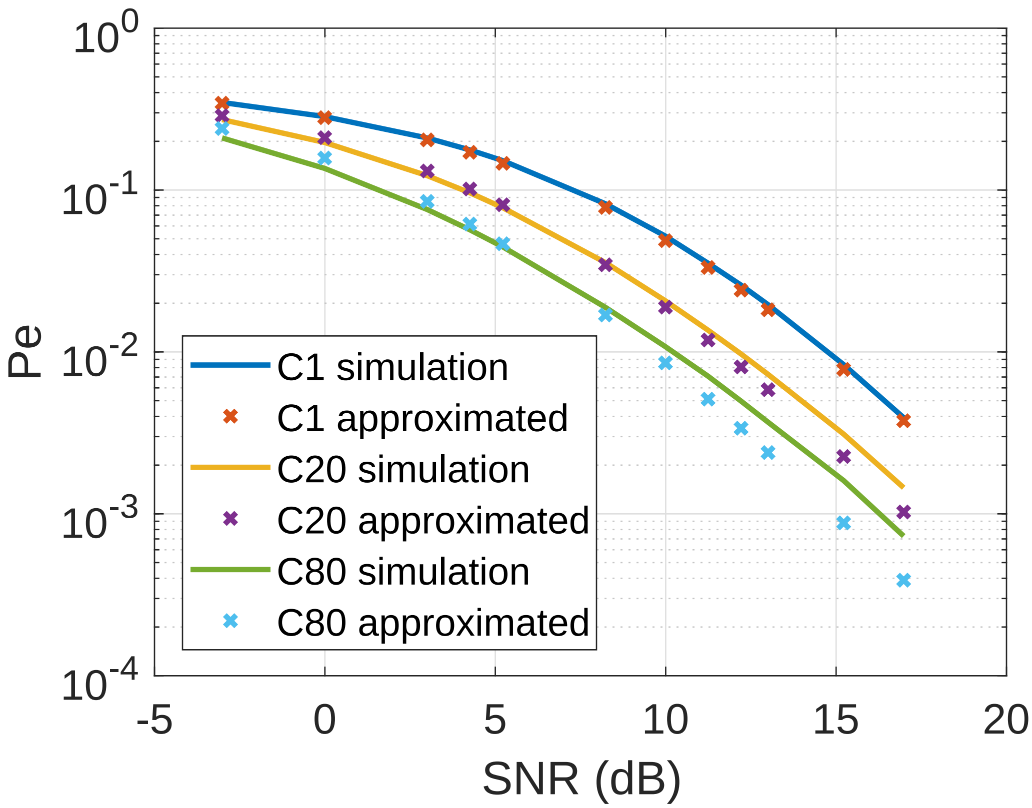

Fig. 10.8. The detection error probability given the molecule of interest is present. K = 1.6, $\sigma = 66$.

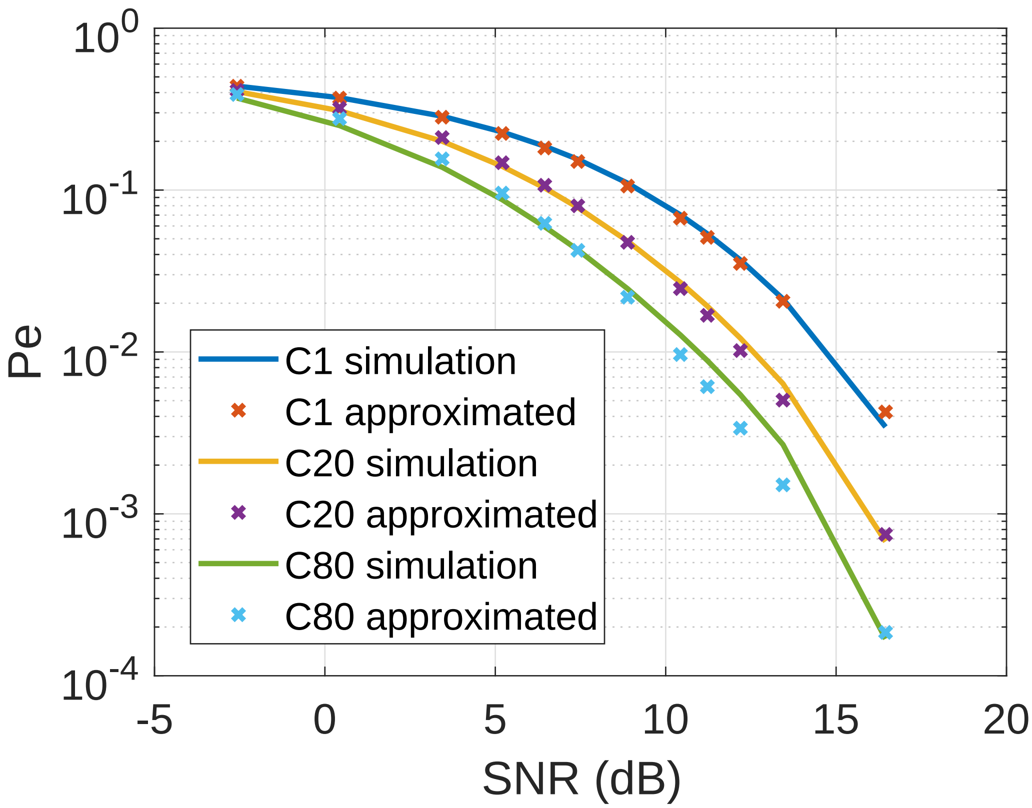

Fig. 10.9. The detection error probability given the molecule of interest is present. K = 2.8, σ = 12.5.

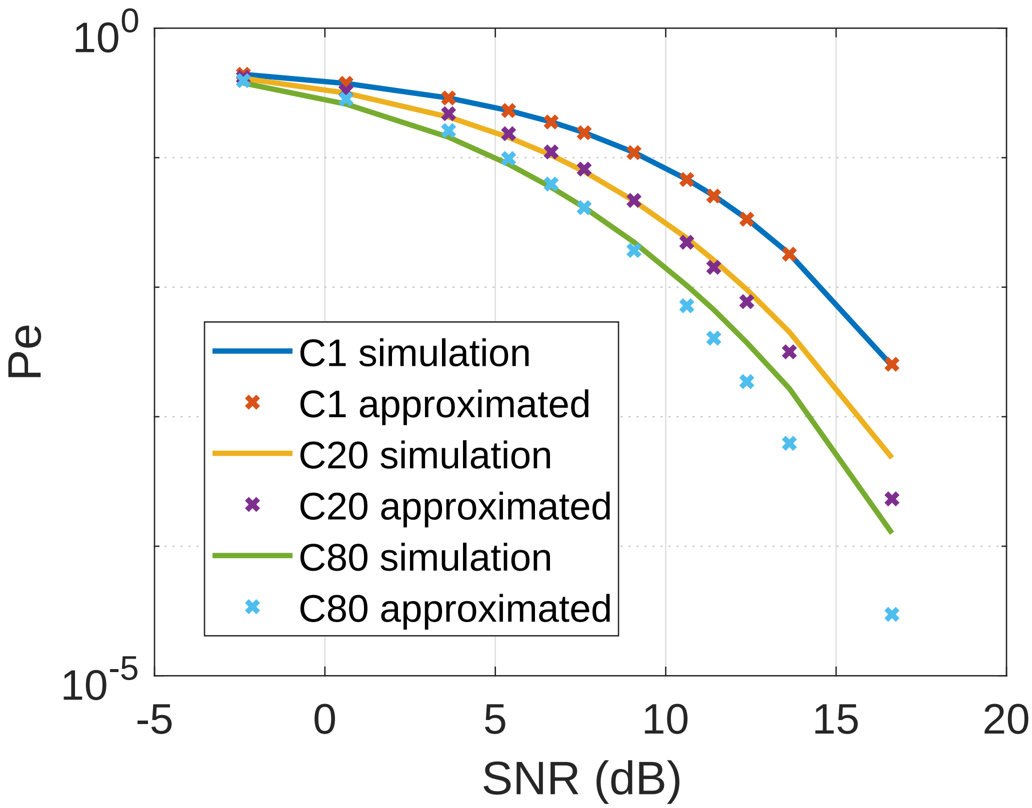

Fig. 10.10. The detection error probability given the molecule of interest is present. K = 5, $\sigma = 12.5$.

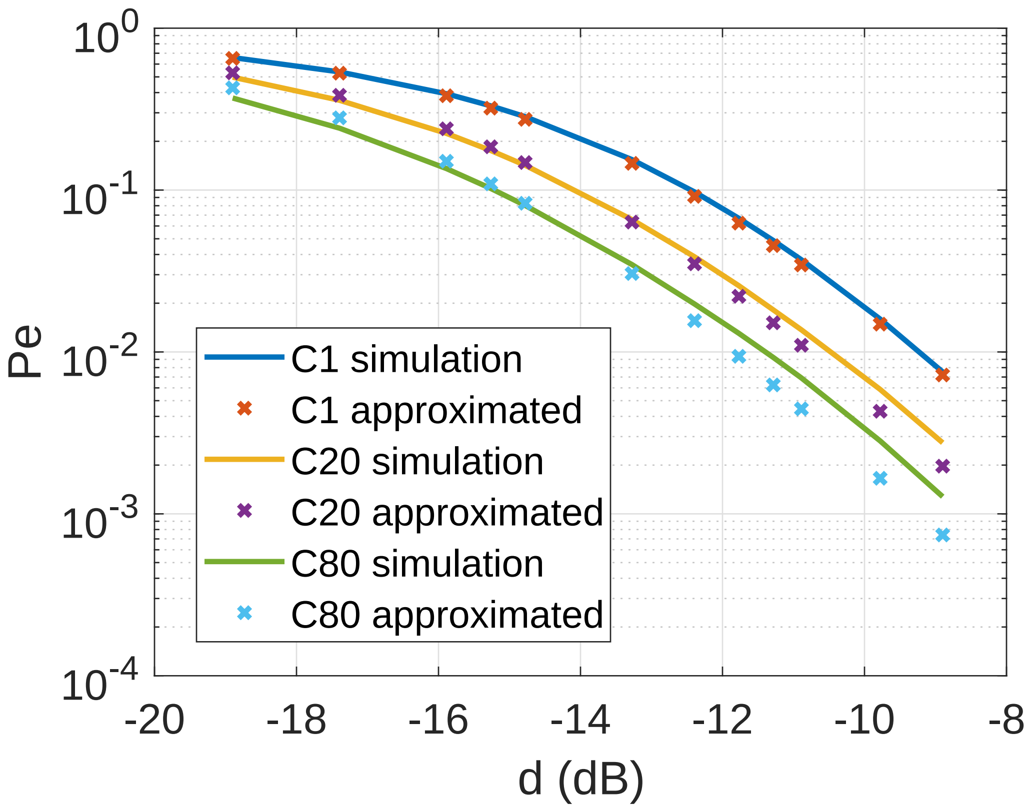

Fig. 10.11. The relationship between the detection error probability versus the detection precision. K = 1.6, $\sigma = 66$.

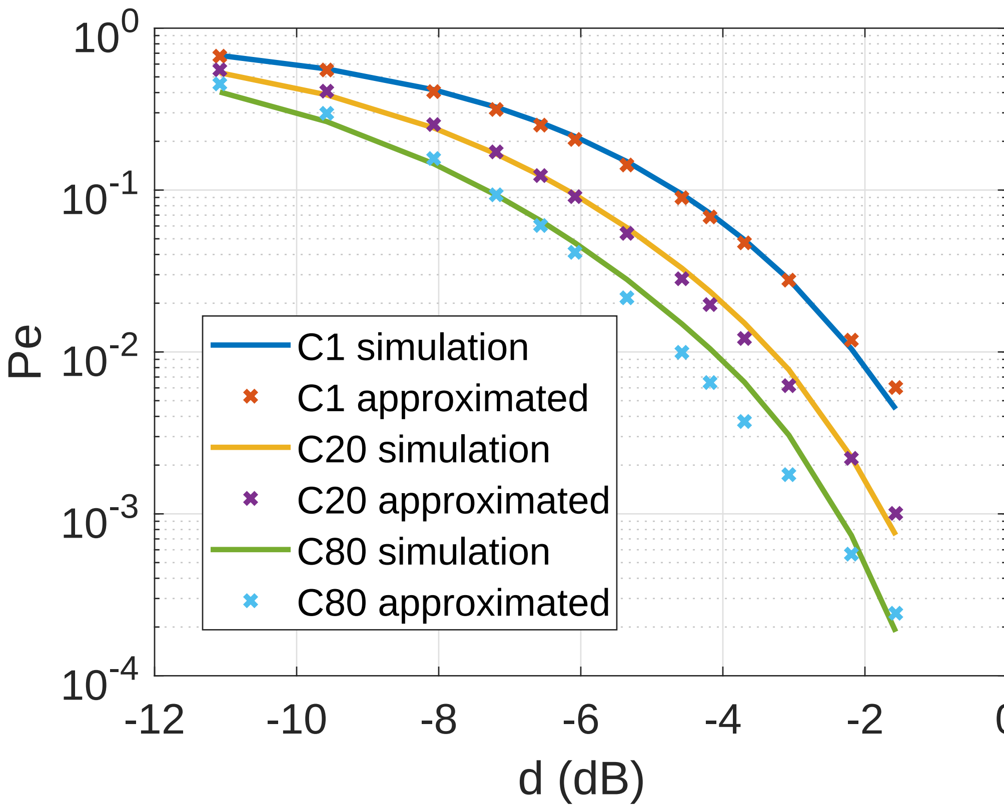

Fig. 10.12. The relationship between the detection error probability versus the detection precision. K = 2.8, σ = 12.5.

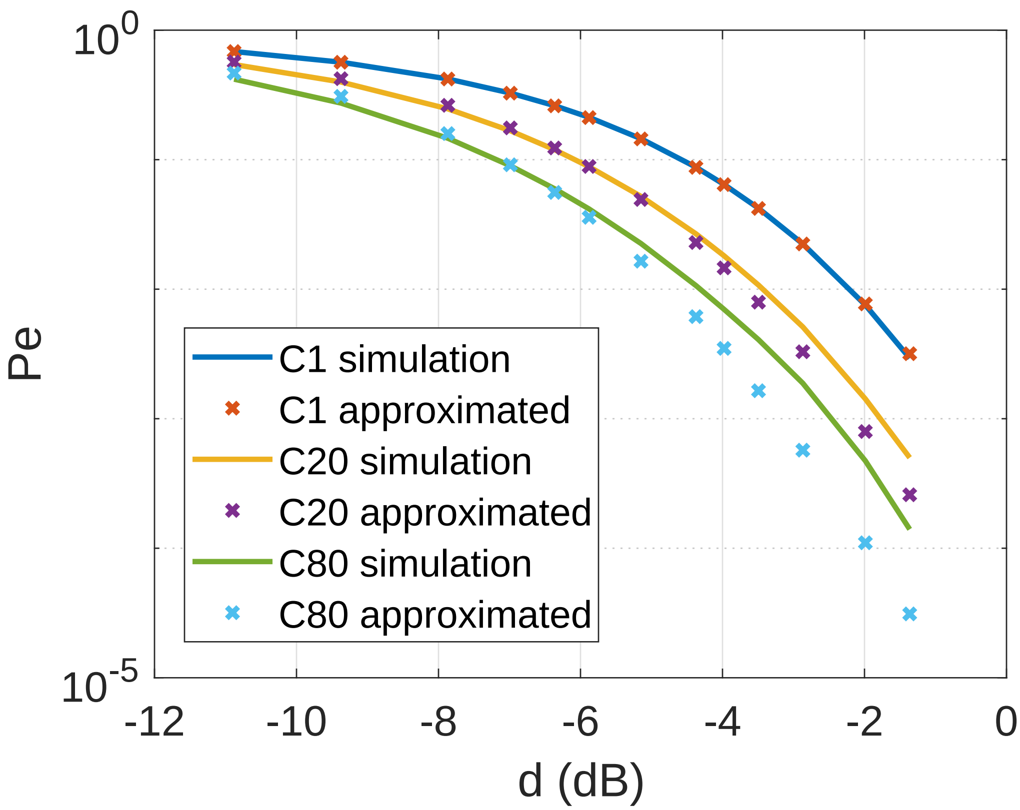

Fig. 10.13. The relationship between the detection error probability versus the detection precision. K = 5, σ = 12.5.

lower error rate, we do not see much gain over 50. For practical purpose, 50 is good enough.

11. FUTURE WORK

Many more works can be achieved based on my research. The applications based on nonequilibrium dynamics is huge. Here, I outline some of them.

11.1 Interference Analysis for Communication Networks

The distribution of interference is typically non-Gaussian. This is because the conditions leading to central limit theorem are not met. Users' activities could be correlated. A scenario similar to [133, 134] could exist in communication networks.

Several studies indicated that the bit error rate in some communication systems follow an asymptotic straight line on log-log plot. These indicate a power law tail for the interference distribution. For these cases, Kappa pdf is a good candidate for approximating the interference because there is no limitation to the argument of the pdf. Such an approximation allows easier computation and a more straightforward understanding of the tradeoff between SNR and bit error rate. An article could be written to validate this concept with examples from past literature. Concept from [133, 134] could be used to explain the nonequilibrium part of the system that leads to a power law tail.

11.2 Robust Noise Parameter Estimation

The core part of Kappa distribution is obtaining an accurate parameter for the pdf. Finding a fast and robust method is needed. It can be shown that Mallat's algorithm can be used to determine the noise parameters [140]. The robustness of this algorithm for Kappa pdf is unsolved. We need to prove that the accuracy improves as the sample size increases as well as showing the rate of convergence.

It is inevitable to have estimation error of the noise pdf parameters. How significant do the errors affect the performance. How sensitive is this issue. It needs to be solved.

11.3 Application to Other Areas

The analytical tools developed in my work can be applied to other problems involving power law tail distributions. They could arise from biology, finance, language, and so on [141]. More works can be followed after my work to support research in other areas encountering similar issues.

11.4 Molecular Communication

Every other work in molecular communication is vulnerable to interference from receptor antagonist. Analytical result is required to assess the robustness of every proposed molecular communication systems. Adjustments are required to improve existing molecular communication systems.

REFERENCES

REFERENCES

[1] S. B. Sahay, K. C. Bhagwat, and P. J. Mohan, "Exploitation of MIMO techniques for reliable hf communication," in *International Conference on Signal Processing and Communications (SPCOM)*, 2012, pp. 1–4.

[2] Wikipedia, "Ionosphere," *http://en.wikipedia.org/wiki/Ionosphere*, 2013.

[3] A. Malaga, "A characterization and prediction of wideband HF skywave propagation," in *IEEE Military Communications Conference (MILCOM)*, 1985, pp. 281–288.

[4] U. Navy, *National Training and Skills Development Web Site*. USA: Navy-Marine Corps Military Auxiliary Radio System (MARS) www.navymars.org/national/training/, 1998.

[5] S. M. Hunt, S. Close, A. J. Coster, E. Stevens, L. M. Schuett, and A. Vardaro, "Equatorial atmospheric and ionospheric modeling at kwajalein missile range equatorial atmospheric and ionospheric modeling at kwajalein missile," *MIT Lincoln Laboratory Journal*, vol. 12, pp. 45–64, 2000.

[6] Wikipedia, "Solar cycle," *http://en.wikipedia.org/wiki/Solar_cycle*, 2013.

[7] J. A. Richards, *Radio Wave Propagation An Introduction for the Non-Specialist*. Springer, 2008.

[8] *Introduction to HF Radio Propagation*. http://www.ips.gov.au/Category/Educational/Other%20Topics/ Radio%20Communication/Intro%20to%20HF%20Radio.pdf: Australian Government Bureau of Meteorology Radio and Space Weather Services, 2013.

[9] *The Ionosphere*. http://www.swpc.noaa.gov/Education/index.html: National Weather Service Space Weather Prediction Center, 2013.

[10] K. Lohmann and C. Lohmann, "The earth's magnetic field," *http://www.unc.edu/depts/oceanweb/turtles/juvenilemap/EarthMF.html*, 2004.

[11] E. Yizengaw, H. Wei, M. B. Moldwin, D. Galvan, L. Mandrake, A. Mannucci, and X. Pi, "The correlation between mid-latitude trough and the plasmapause," *Geophysical Research Letters*, vol. 32, 2005.

[12] J. Papon, M. Cohen, B. Cotts, and N. Haque, "Ionospheric morphology (slides)," in *IHY Workshop on Advancing VLF through the Global AWESOME Network*. http://nova.stanford.edu/∼vlf/IHY_Test/Tutorials/TheIonosphere/IonosphericMorphology.pdf, 2009.

[13] S.-G. Xiao, Z. Xiao, J.-K. Shi, D.-H. Zhang, Y.-Q. Hao, and W.-Q. Huang, "Application of the HF doppler observations to the study of spread-f," *Chinese Journal of Geophysics*, vol. 55, pp. 375–379, 2012.

[14] A. Gibson and M. Chryssomallis, "Amplitude statistics of HF signal and noise on a 2300 km path over europe," in *Eighth International Conference on Antennas and Propagation, 1993*, 1993, pp. 473–476.

[15] M. Chryssomallis and A. Gibson, "Amplitude statistics of HF signal and noise on a 2300 km path over europe," in *Electronics Letters*, 1992, pp. 1827–1828.

[16] J. Mastrangelo, J. Lemmon, L. Vogler, J. Hoffmeyer, L. E. Pratt, and C. Behm, "A new wideband high frequency channel simulation system," *IEEE Transactions on Communications*, vol. 45, pp. 26–34, 1997.

[17] J. Giesbrecht, "An empirical study of the probability density function of HF noise (part II)," *Fluctuation and Noise Letters*, vol. 8, pp. L305–L314, 2008.

[18] P. M. Fishman, C.-R. Liu, and P. A. Bello, "A statiscal model for burst duration and time betweeen bursts for WBHF atmospheric noise," in *IEEE Military Communcications Conference 1991*, 1991, pp. 948–954.

[19] J. Lemmon, "Model for the simulation of wideband hf and interference," in *5th International Conference on HF Radio Systems and Techniques*, 1991, pp. 349–353.

[20] H. Hall, *A New Model for Impulsive Phenomena: Application to Atmospheric-noise Communication Channels Interpretation of Impedance Probe Measurements in the Ionosphere*. USA: Ph.D. dissertation, Dept. Electrical Engeering, Stanford University, 1966.

[21] J. E. Giesbrecht, R. Clarke, and D. Abbott, "Modulation recognition for real HF signals," in *SPIE Proceedings, Microelectronics: Design, Technology, and Packaging II*, 2006, pp. 4–12.

[22] B. Barabashov, M. Anishin, and O. Pelevin, "Simulation model of ionospheric communication channel," in *The Second Conference on Antennas and Propagation*, 2007, pp. 1–3.

[23] S. Kay, "Representation and generation of non-gaussian wide-sense stationary random processes with arbitrary PSDs and a class of pdfs," *IEEE Transactions on Signal Processing*, vol. 58, pp. 3448–3458, 2010.

[24] Z. Yan, L. Zhang, T. Rahman, and D. Su, "Prediction of the hf ionospheric channel stability based on the modified ITS model," *IEEE Transactions on Antennas and Propagation*, vol. 61, pp. 3321–3333, 2013.

[25] W. C.C, J. J.R, and B. W.D, "Experimental confirmation of an hf channel model," *IEEE Transactions on Communication*, vol. 18, pp. 792–803, 1970.

[26] M. Iwama, "Estimation of background noise in hf-band," in *Asia-Pacific Symposium on Electromagnetic Compatibility and 19th International Zurich Symposium on Electromagnetic Compatibility*, 2008, pp. 470–473.

[27] J. G. Gonzalez, J. L. Paredes, and G. R. Arce, “Zero-order statistics: A mathematical framework for the processing and characterization of very impulsive signals,” *IEEE Transactions on Signal Processing*, vol. 54, pp. 3839–3851, 2006.

[28] J. G. Gonzalez, *Robust techniques for wireless communications in non-Gaussian environments*. USA: Ph.D. dissertation, Dept. Electr. Eng., Univ. of Delaware, Newark, DE, 1997.

[29] S. Edwards, *Sunrise Sunset Calendar*, http://www.sunrisesunset.com, 2016.

[30] V. Pierrard and M. Lazar, “Kappa distributions: Theory and applications in space plasmas,” *Solar Physics*, vol. 267, pp. 153–174, 2010.

[31] G. Livadiotis and D. McComas, “Understanding Kappa distributions: A toolbox for space science and astrophysics,” *Space Science Reviews*, vol. 175, pp. 183–214, 2013.

[32] M. Lazar, V. Pierrard, S. M. Shaaban, H. Fichtner, and S. Poedts, “Dual Maxwellian-Kappa modeling of the solar wind electrons: new clues on the temperature of Kappa populations,” *Astronomy and Astrophysics*, vol. 602, p. A44, 2017.

[33] N. N. Rao, *Elements of Engineering Electromagnetics 6th edition*. Pearson, 2004.

[34] J. Giesbrecht, *Aspects of HF Communications: HF Noise and Signal Features*. Australia: Ph.D. dissertation, Dept. Electr. Engeering, University of Adelaide, South Australia, 2008.

[35] M. Shen, F. H. Y. Chan, and P. J. Beadle, “A method for generating non-gaussian noise series with specified probability distribution and power spectrum,” in *International Symposium on Circuits and Systems 2003 (ISCAS ’03)*, 2003, pp. II–1–II–4.

[36] K. Valery Y and V. Z. Lyandres, “Stochastic differential eqations: An approach to the generation of continuous non-gaussian process,” *IEEE Transactions on Signal Processing*, vol. 43, pp. 2372–2385, 1995.

[37] L. H. Brace and A. J. Kliore, “The structure of the venus ionosphere,” *Space Science Reviews*, vol. 55, pp. 81–163, 1991.

[38] M. F. Vogt, P. Withers, K. Fallows, C. L. Flynn, D. J. Andrews, F. Duru, and D. D. Morgan, “Electron densities in the ionosphere of mars: A comparison of MARSIS and radio occultation measurements,” *Space Physics*, vol. 121, pp. 10 241–10 257, 2016.

[39] S. Atreya and T. Donahue, “The atmosphere and ionosphere of jupiter,” *Vistas in Astronomy*, vol. 25, pp. 315–335, 1981.

[40] A. J. Kliore, A. Nagy, S. Asmar, A. Anabtawi, E. Barbinis, D. Fleischman, D. Kahan, and J. Klose, “The ionosphere of saturn as observed by the cassini radio science system,” *Geophysical Research Letters*, vol. 41, pp. 5778–5782, 2014.

[41] M. O. Chandler and J. H. Waite, "The ionosphere of uranus: A myriad of possibilities," *Geophysical Research Letters*, vol. 13, pp. 6–9, 1986.

[42] ——, "The ionosphere of neptune," *Geophysical Research Letters*, vol. 16, pp. 945–947, 1989.

[43] J. Y. Liu, Y.-M. Chen, Y.-J. Chuo, and H. F. Tsai, "Variations of ionospheric total electron content during the Chi-Chi earthquake," *Geophysical Research Letters*, vol. 28, pp. 1383–1386, 2001.

[44] D. Ouzounov, S. Pulinets, A. Romanov, A. Romanov, K. Tsybulya, D. Davidenko, M. Kafatos, and P. Taylor, "Atmosphere-ionosphere response to the M9 tohoku earthquake revealed by multi-instrument space-borne and ground observations: Preliminary results," *Earthquake Science*, vol. 24, pp. 557–564, 2011.

[45] W. Jiang, Y. Ma, X. Zhou, Z. Li, X. An, and K. Wang, "Analysis of ionospheric vertical total electron content before the 2014 Mw8.2 chile earthquake," *Seismology*, vol. 21, pp. 1599–1612, 2017.

[46] F. T. Freund, "Pre-earthquake signals — part I: Deviatoric stresses turn rocks into a source of electric currents," *Natural Hazards and Earth System Sciences*, vol. 7, pp. 535–541, 2007.

[47] ——, "Pre-earthquake signals — part II: Flow of battery currents in the crust," *Natural Hazards and Earth System Sciences*, vol. 7, pp. 543–548, 2007.

[48] S. Pulinets and K. Boyarchuk, *Ionospheric Precursors of Earthquakes.* Springer-Verlag Berlin Heidelberg, 2005.

[49] H.-Y. Lo and J. S. Lehnert, "HF channel model at sunrise with dominant galactic noise," in *IEEE Antenna and Propagation Symposium*, 2018, pp. 1–2.

[50] R. B. Decker, S. M. Krimigis, E. C. Roelof, M. E. Hill, T. P. Armstrong, G. Gloeckler, D. C. Hamilton, and L. J. Lanzerotti, "Voyager 1 in the foreshock, termination shock, and heliosheath," *American Association for the Advancement of Science*, vol. 309, pp. 2020–2024, 2005.

[51] L. A. Fisk and G. Gloeckler, "The common spectrum for accelerated ions in the quiet-time solar wind," *The Astrophysical Journal Letters*, vol. 640, pp. 79–82, 2006.

[52] N. L. S. Jeffrey, L. Fletcher, and N. Labrosse, "Non-gaussian velocity distributions in solar flares from extreme ultraviolet lines: A possible diagnostic of ion acceleration," *The Astrophysical Journal*, vol. 836, pp. 79–82, 2016.

[53] G. Livadiotis, *Kappa Distributions Theory and Applications in Plasmas.* Elsevier, 2017.

[54] A. Papoulis and S. U. Pillai, *Probability, Random Variables, and Stochastic Processes.* McGraw Hill, 2002.

[55] Y. Feng, M. Wen, J. Zhang, F. Ji, and G. X. Ning, "Sum of arbitrarily correlated Gamma random variables with unequal parameters and its application in wireless communications," in *2016 International Conference on Computing, Networking and Communications (ICNC)*, 2016, pp. 1–5.

[56] K. Zhang, Z. Song, and Y. L. Guan, "Simulation of Nakagami fading channels with arbitrary cross-correlation and fading parameters," *IEEE Transactions on Wireless Communications*, vol. 3, pp. 1463–1468, 2004.

[57] H.-Y. Lo, J. S. Lehnert, and P. Tran, "Performance analysis for HF communication with dominant noise source," in *39th IEEE Sarnoff Symposium*, 2018, pp. 1–6.

[58] M. Leubner and Z. Voros, "A nonextensive entropy path to probability distributions in solar wind turbulence," *Nonlinear Processes in Geophysics*, vol. 12, pp. 171–180, 2005.

[59] M. Shinde and S. Gupta, "A model of HF impulsive atmospheric noise," *IEEE Transactions on Communications*, vol. EMC-16, pp. 71–75, 1974.

[60] A. Hazza, M. Shoaib, A. Salehl, and A. Fahd, "Classification of digitally modulated signals in presence of non-gaussian hf noise," in *International Symposium on Wireless Communication Systems*, 2010, pp. 815–819.

[61] N. Alyaoui, A. Kachouri, and M. Samet, "The fourth generation 3GPP LTE identification for cognitive radio," in *International Conference on Microelectronics (ICM)*, 2011, pp. 1–5.

[62] K. Yao, "A represenattion theorem and its applications to spherically-invariant random processes," *IEEE Transactions on Information Theory*, vol. 19, pp. 600–608, 1973.

[63] E. Conte and M. Longo, "Characterization of radar clutter as a spherically invariant random process," *IEE Proceeding of Communications, Radar and Signal Processing*, vol. 134, pp. 191–197, 1987.

[64] E. Conte, M. D. Bisceglie, M. Longo, and M. Lops, "Canonical detection in spherically invariant noise," *IEEE Transactions on Communication*, vol. 43, pp. 347–353, 1995.

[65] V. K. Bhargava, V. H. Poor, V. Tarokh, and S. Yoon, *Communications, Information and Network Security*. Springer, 2002.

[66] I. F. Blake and J. B. Thomas, "On a class of processes arising in linear estimation theory," *IEEE Transactions on Information Theory*, vol. 14, pp. 12–16, 1968.

[67] M. Rangaswamy, D. Weiner, and A. Ozturk, "Computer generation of correlated non-gaussian radar clutter," *IEEE Transactions on Aerospace and Electronic Systems*, vol. 31, pp. 106–116, 1995.

[68] ——, "Non-gaussian random vector identification using spherically invariant random processes," *IEEE Transactions on Aerospace and Electronic Systems*, vol. 29, pp. 111–124, 1993.

[69] A. Jeffrey and D. Zwillinger, *Table of Integreals, Series, and products, Seventh Edition*. Springer, 2007.

[70] D. Gesbert, M. Shafi, D.-S. Shiu, P. J. Smith, and A. Naguib, "From theory to practice: an overview of MIMO space-time coded wireless systems," *IEEE Journal on Selected Areas in Communications*, vol. 21, pp. 281–302, 2003.

[71] P. M. Ndao, Y. Erhel, D. Lemur, M. Oger, and J. L. Masson, "Implementation of a MIMO solution for ionosphereic HF (3-30 MHz) radio link," in *7th European Conference on Antennas and Propagation 2013 (EuCAP 2013)*, 2013, pp. 510–514.

[72] R. C. Daniels and S. W. Peters, "A new MIMO HF data link: Designing for high data rates and backwards compatibility," in *IEEE Military Communications Conference 2013 (MILCOM 2013)*, 2013, pp. 1256–1261.

[73] S. Gunashekar, E. Warrington, S. Salous, S. Feeney, H. Zhang, N. Abbasi, L. Bertel, D. Lemur, and M. Oger, "Early results of experiments to investigate the feasibility of employing MIMO techniques in the HF band," in *Loughborough Antennas and Propagation Conference 2008*, 2008, pp. 161–164.

[74] P. Ndao, Y. Erhel, D. Lemur, M. Oger, and J. Le Masson, "Design and test of a HF MIMO system of transmission set up with compact antenna arrays," in *IEEE International Conference on Microwaves, Communications, Antennas and Electronics Systems 2011*, 2011, pp. 1–4.

[75] S. Gunashekar, E. Warrington, W. Salousf, L. Bertel, D. Lemur, H. Zhang, and N. Abbasi, "An experimental investigation into the feasibility of MIMO techniques within the hf band," in *The Second European Conference on Antennas and Propagation 2007*, 2007, pp. 1–5.

[76] H. Liu, G. Li, X. Cheng, and D. Li, "Performance analysis framework of ML MIMO receiver over correlated Rayleigh fading channel," in *IEEE International Conference on Communications*, 2006, pp. 4137–4142.

[77] T. Duong, H. Trang, E. Hong, and S. Lee, "Performance evaluation of the V-BLAST system under correlated fading channels," in *AICT/SAPIR/ELETE'05*, 2005, pp. 220–225.

[78] Y. Ma, Z. Zheng, and Y. long Zhou, "Characteristics of MIMO channel in consideration of polarization," in *5th International Conference on Wireless Communications, Networking and Mobile Computing*, 2009, pp. 1–3.

[79] M. Coldrey, "Modeling and capacity of polarized MIMO channels," in *IEEE Vehicular Technology Conference VTC Spring 2008*, 2008, pp. 440–444.

[80] C. Guo, F. Liu, S. Chen, C. Feng, and Z. Zeng, "Advances on exploiting polarization in wireless communications: Channels, technologies, and applications," *IEEE Communications Surveys and Tutorials*, vol. 19, pp. 125–166, 2017.

[81] J.-A. Tsai, R. M. Buehrer, J. K. Shaw, and B. D. Woerner, "BER analysis of orthogonal transmit waveform with space-time diversity for MIMO CDMA systems," in *IEEE Vehicular Technology Conference*, 2002, pp. 1051–1055.

[82] E. Arikan, "Channel polarization: A method for constructing capacity-achieving codes for symmetric binary-input memoryless channels," *IEEE Transactions on Information Theory*, vol. 55, pp. 3051–3073, 2009.

[83] H. Vangala, Y. Hong, and E. Viterbo, "Efficient algorithms for systematic polar encoding," *IEEE Communications Letters*, vol. 20, pp. 17–20, 2016.

[84] H. Vangala, E. Viterbo, and Y. Hong, "Permuted successive cancellation decoder for polar codes," in *International Symposium on Information Theory and its Applications*, 2014, pp. 438–442.

[85] S. Zhao, P. Shi, and B. Wang, "Designs of bhattacharyya parameter in the construction of polar codes," in *International Conference on Wireless Communications, Networking and Mobile Computing*, 2011, pp. 1–4.

[86] Y. Lu and S. Goto, "A study on channel polarization and polar coding," in *9th IEEE International Conference on ASIC*, 2011, pp. 804–807.

[87] B. Tahir, S. Schwarz, and M. Rupp, "BER comparison between convolutional, turbo, LDPC, and polar codes," in *24th International Conference on Telecommunications (ICT)*, 2017, pp. 1–7.

[88] E. Arikan, "A performance comparison of polar codes and reed-muller codes," *IEEE Communications Letters*, vol. 12, pp. 447–449, 2008.

[89] Y. Zhang, A. Liu, K. Pan, C. Gong, and S. Yang, "A practical construction method for polar codes," *IEEE Communications Letters*, vol. 18, pp. 1871–1874, 2014.

[90] H. Vangala, E. Viterbo, and Y. Hong, "A comparitive study of polar code constructions for the AWGN channel," *arXiv:1501.02473v1*, pp. 1–9, 2015.

[91] E. Arikan, "Systematic polar coding," *IEEE Communications Letters*, vol. 15, pp. 860–862, 2011.

[92] Z. Liu, K. Chen, K. Niu, and Z. He, "Distance spectrum analysis of polar codes," in *IEEE Wireless Communications and Networking Conference (WCNC)*, 2014, pp. 490–495.

[93] T. Ruuben, M. A. Meister, E. Lossmann, J. Berdnikova, and U. Madar, "SNR estimation in HF communications channel," in *European Conference on Antennas and Propagation (EUCAP)*, 2012, pp. 2013–2015.

[94] E. Lossmann, M. A. Meister, and U. Madar, "On HF communication link parameter estimation in the Baltic region," in *IEEE-APS Topical Conference on Antennas and Propagation in Wireless Communications*, 2011, pp. 813–814.

[95] A. J. Gibson, U. M. Yilmaz, Y. Tulunay, C. B. Erol, A. ozguc, and T. Atac, "Characteristics of fading of HF signal and noise intensities on three paths between the United Kingdom and Turkey," *Radio Science*, vol. 30, pp. 649–658, 1995.

[96] S. Banerjee and M. Agrawal, "Underwater acoustic noise with generalized Gaussian statistics: Effects on error performance," in *MTS/IEEE OCEANS - Bergen*, Jun. 2013, pp. 1–8.

[97] M. A. Kishk and A. M. Alaa, "On the capacity of the underwater acoustic channel with dominant noise sources," in *International Symposium on Telecommunication Technologies*, Nov. 2014, pp. 183–187.

[98] S. Sparrer and R. F. H. Fischer, "Mixed generalized Gaussian noise channels: Capacity, decoding, and performance," in *International ITG Conference on Systems, Communications and Coding*, 2015, pp. 1–6.

[99] T. M. Cover and J. A. Thomas, *Elements of Information Theory.* Wiley, 1991.

[100] M. Simon and M.-S. Alouini, *Digital Communication over Fading Channels, 2nd edition.* Wiley-Interscience, 2005.

[101] X. Liu, "Probability of strictly positive secrecy capacity of the weibull fading channel," *IEEE Wireless Communication Letters*, vol. 2, pp. 50–53, 2013.

[102] M. Geller and E. W. Ng, "A table of integrals of the exponential integral," *Journal of Research of the National Bureau af Standards - B. Mathematics and Mathematical Science*, vol. 73B, pp. 191–210, Jul.–Sep. 1969.

[103] M. Stojanovic and J. Preisig, "Underwater acoustic communication channels: Propagation models and statistical characterization," *IEEE Communications Magazine*, vol. 47, pp. 84–89, 2009.

[104] P. Qarabaqi and M. Stojanovic, "Statistical characterization and computationally efficient modeling of a class of underwater acoustic communication channels," *IEEE Journal of Oceanic Engineering*, vol. 38, pp. 701–717, 2013.

[105] P. A. van Walree, "Propagation and scattering effects in underwater acoustic communication channels," *IEEE Journal of Oceanic Engineering*, vol. 38, pp. 614–631, 2013.

[106] M. Siderius, M. B. Porter, P. Hursky, and V. McDonald, "Effects of ocean thermocline variability on noncoherent underwater acoustic communications," *Journal of Acoustic Society of America*, vol. 121, pp. 1895–1908, 2007.

[107] M. Chitre, "A high-frequency warm shallow water acoustic communications channel model and measurements," *Journal of Acoustic Society of America*, vol. 122, pp. 2580–2586, 2007.

[108] P. A. van Walree and R. Otnes, "Ultrawideband underwater acoustic communication channels," *IEEE Journal of Oceanic Engineering*, vol. 38, pp. 678–688, 2013.

[109] F. Traverso, G. Vernazza, and A. Trucco, "Simulation of non-white and non-Gaussian underwater ambient noise," in *2012 Oceans - Yeosu*, May 2012, pp. 1–10.

[110] W. Diffie and M. Hellman, "New directions in cryptography," *IEEE Transactions on Information Theory*, vol. 22, pp. 644–654, 1976.

[111] M. Bloch, J. Barros, M. R. D. Rodrigues, and S. W. McLaughlin, "Wireless information-theoretic security," *IEEE Transactions on Information Theory*, vol. 54, pp. 2515–2534, Jun. 2008.

[112] B.-H. Koo, C. Lee, H. B. Yilmaz, N. Farsad, A. Eckford, and C.-B. Chae, "Molecular MIMO: From theory to prototype," *IEEE Journal on Selected Areas in Communications*, vol. 34, pp. 600–614, Mar. 2016.

[113] N. Yang, H. A. Suraweera, I. B. Collings, and C. Yuen, "Physical layer security of TAS/MRC with antenna correlation," *IEEE Transactions on Information Forensics and Security*, vol. 8, pp. 254–259, Jan. 2013.

[114] E. Hof and S. Shamai, "Secrecy-achieving polar-coding," in *IEEE Information Theory Workshop*, 2010, pp. 1–5.

[115] H. ShahMohammadian, G. G. Messier, and S. Magierowski, "Optimum receiver for molecule shift keying modulation in diffusion-based molecular communication channels," *Nano Communication Networks*, vol. 3, pp. 183–195, 2012.

[116] L. S. Meng, P. C. Yeh, K. C. Chen, and I. F. Akyildiz, "On receiver design for diffusion-based molecular communication," *IEEE Transactions on Signal Processing*, vol. 62, pp. 6032–6044, 2014.

[117] D. Purves, G. J. Augustine, D. Fitzpatrick, W. C. Hall, A.-S. LaMantia, J. O. McNamara, and L. E. White, *Neuroscience Fourth Edition*. Sinauer, 2008.

[118] A. O. Samson and M. Levitt, "Inhibition mechanism of the acetylcholine receptor by -neurotoxins as revealed by normal-mode dynamics," *Biochemistry*, vol. 47, pp. 4065–4070, 2009.

[119] H. P. Rang, J. M. Ritter, R. J. Flower, and G. Henderson, *Rang and Dale's Pharmacology*. Elsevier, 2016.

[120] L. P. Gine and I. F. Akyildiz, "Molecular communication options for long range nanonetworks," *Computer Networks*, vol. 53, pp. 2753–2766, 2009.

[121] E. L. Cussler, *Diffusion Thrid Edition*. Cambridge, 2009.

[122] N. Shehada, J. C. Cancilla, J. S. Torrecilla, E. S. Pariente, G. Brnstrup, S. Christiansen, D. W.Johnson, M. Leja, M. P. A.Davies, O. Liran, N. Peled, and H. Haick, "Silicon nanowire sensors enable diagnosis of patients via exhaled breath," *ACS Nano*, vol. 10, pp. 7047–7057, 2016.

[123] Z. q Xu, Y. Y. Broza, R. I. adn U Tisch, L. Ding, H. Liu, Q. Song, Y. y Pan, F. x Xiong, K. s Gu, G. p Sun, Z. d Chen, M. Leja, and H. Haick, "A nanomaterial-based breath test for distinguishing gastric cancer from benign gastric conditions," *British Journal of Cancer*, vol. 108, pp. 941–950, 2013.

[124] M. Hakim, Y. Y.Broza, O. Barash, N. Peled, M. Phillips, A. Amann, and H. Haick, "Volatile organic compounds of lung cancer and possible biochemical pathways," *Chemical Reviews*, vol. 112, pp. 5949–5966, 2012.

[125] N. Farsad, H. B. Yilmaz, A. Eckford, C. Chae, and W. Guo, "A comprehensive survey of recent advancements in molecular communication," *IEEE Communications Surveys Tutorials*, vol. 18, pp. 1887–1919, 2016.

[126] H.-Y. Lo, J. S. Lehnert, S. J. Lehnert, and P. Tran, "Interference modeling for molecular communication with receptor antagonist," in *IEEE International Conference on Nanotechnology*, 2018, pp. 1–4.

[127] G. Zheng, X. P. A. Gao, and C. M. Lieber, "Frequency domain detection of biomolecules using silicon nanowire biosensors," *Nano Letters*, vol. 10, pp. 3179–3183, 2010.

[128] T.-W. Hwang, S. P. Branagan, and P. W. Bohn, "Chemical noise produced by equilibrium adsorption desorption of surface pyridine at auagau bimetallic atom-scale junctions studied by fluctuation spectroscopy," *Journal of American Chemical Society*, vol. 135, pp. 4522–4528, 2013.

[129] M. Kuscu and O. B. Akan, “Modeling and analysis of sinw fet-based molecular communication receiver,” *IEEE Transactions on Communications*, vol. 64, pp. 3708–3721, 2016.

[130] P. Dutta and P. M. Horn, “Low-frequency fluctuations in solids: 1/f noise,” *Reviews of Modern Physics*, vol. 53, pp. 497–516, 1981.

[131] C. Barone, F. Romeo, S. Pagano, C. Attanasio, G. Carapella, C. Cirillo, A. Galdi, G. Grimaldi, A. Guarino, A. Leo, A. Nigro, and P. Sabatino, “Nonequilibrium fluctuations as a distinctive feature of weak localization,” *Scientific Reports*, vol. 5, p. 10175, 2015.

[132] M. Mihaila, D. Ursutiu, C. Grigoriu, M. Danila, D. Steriu, and F. Craciunoiu, “Nonequilibrium 1/f noise in platinum nanoparticle films,” in *IEEE International Semiconductor Conference*, 2003, pp. 43–46.

[133] G. Ruiz and C. Tsallis, “Emergence of q-statistical functions in a generalized binomial distribution with strong correlations,” *Journal of Mathematical Physics*, vol. 56, p. 053301, 2015.

[134] A.Kononovicius and J. Ruseckas, “Stochastic dynamics of N correlated binary variables and non-extensive statistical mechanics,” *Physical Letters A*, vol. 380, pp. 1582–1588, 2016.

[135] J. Ruseckas and B. Kaulakys, “Tsallis distributions and 1/f noise from nonlinear stochastic differential equations,” *Physical Review E*, vol. 84, p. 051125, 2011.

[136] H.-Y. Lo, J. S. Lehnert, and P. Tran, “The tail distribution of the sum of Kappa random variables with unequal weight and correlation,” in *39th IEEE Sarnoff Symposium*, 2018, pp. 1–5.

[137] ——, “Performance analysis for MIMO HF communications with dominant galactic noise,” in *IEEE Military Communications Conference*, 2018, pp. 1–6.

[138] P. R. F. Rocha, P. Schlett, U. Kintzel, V. Mailnder, L. K. J. Vandamme, G. Zeck, H. L. Gomes, F. Biscarini, and D. M. de Leeuw, “Electrochemical noise and impedance of Au electrode electrolyte interfaces enabling extracellular detection of glioma cell populations,” *Scientific Reports*, vol. 6, p. 34843, 2016.

[139] K. Georgakopouloua, A. Birbas, and C. Spathis, “Modeling of fluctuation processes on the biochemically sensorial surface of silicon nanowire field-effect transistors,” *Journal of Applied Physics*, vol. 177, p. 104505, 2015.

[140] S. G. Mallat, “A theory for multiresolution signal decomposition: the wavelet representation,” *IEEE Transactions on Pattern Analysis and Machine Intelligence*, vol. 11, pp. 674–693, 1989.

[141] P. Andriani and B. McKelvey, “Beyond Gaussian averages: redirecting international business and management research toward extreme events and power laws,” *Journal of International Business Studies*, vol. 38, pp. 1212–1230, 2007.

APPENDICES

A. MAJOR MATLAB CODE FOR THIS THESIS

In this appendix, major MATLAB code is presented for running simulations and making comparisons with theoretical results. Before showing the code, a description of the architecture of the code is presented. In this way, the code is more easily understood.

A.1 Math Part

The critical issue for simulation is the noise generator. That is, to produce a random variable such that it has Kappa distribution. We don't have this built-in function in MATLAB, so we need to devise a way to generate it.

In Chapter 5 of [54], there is a theorem that shows how to construct a probability density function from a uniform distribution. Because MATLAB and C have built-in uniform random number generators for the uniform distribution, it means that we can build our simulation based on this theorem. The theorem is given as follows (for proof, please read [54]):

Theorem A.1.1 (Uniform pdf to any pdf) *Given a random variable* $\boldsymbol{u}$ *with uniform distribution in the interval (0,1), we wish to find a function g(u) such that the distribution of the random variable y = g(u) is a specified function* $F_y(y)$*. Then g(u) is the inverse of the function* $u = F_y(y)$*:*

If $y = F_y^{-1}(\boldsymbol{u})$ *then* $P\{\boldsymbol{y} \leq y\} = F_y(y)$

With Theorem A.1.1 in mind, the way to generate a random variable $\mathbf{X}$ with a probability density function that is the Kappa distribution can be divided into 4 stages:

1. Find the cumulative distribution function of $\mathbf{X}$.

2. Find the inverse cumulative distribution function of **X**.

3. Generate a sample u from the uniform distribution.

4. Put u into the inverse cumulative distribution function. The output is a sample from the Kappa distribution.

Here is an example of MATLAB code for finding the cumulative distribution function of **X**.

A.2 CDF of X

```
%% find cdf ==================================

% Parameters for Kappa distribution
% In this example, we use the the data from [17]
K = 1.6;
sig = 66;

% step size for cdf integration
h = 0.001;

% range of integration for cdf
% theoretically we need to integrate from −∞ to ∞, but practically we take
% the range such that the integral out of the range is negligible
y = [-5*10^3:h:5*10^3];

z = size(y);
% The output of cdf
F = zeros(1,z(2));
counter = 1;
```

```
% The pdf
f = zeros(1,z(2));
f = 1/(sqrt(K)*sig*beta(1/2,K+1/2))*((1+(y.^2)/(K*(sig^2))).^(-K-1));
end

% Each point of cdf is found through numerical integration. However, calling the
% built-in integral function fails for some numbers. The trapezoid integration never
% fails for probability density funcitons.
for(counter=2:1:z(2))
F(counter) = F(counter-1) + (f(counter-1)+f(counter))*h/2;
end
```

Figure A.1 and Figure A.2 show the output function. That is, the cumulative distribution function.

In this section, a MATLAB example of finding the inverse cumulative distribution function is shown. It is assumed that the code from previous section has been fully run.

A.3 Inverse CDF of X

```
%% find inverse cdf ==========================

% input ranges from 0 to 1
% for accuracy, u is divided into around 10^6 subintervals
u = [0:0.000001:1];

sz = size(u);
% output of the inverse cdf F_inv(1:sz(2)) = 0;
```

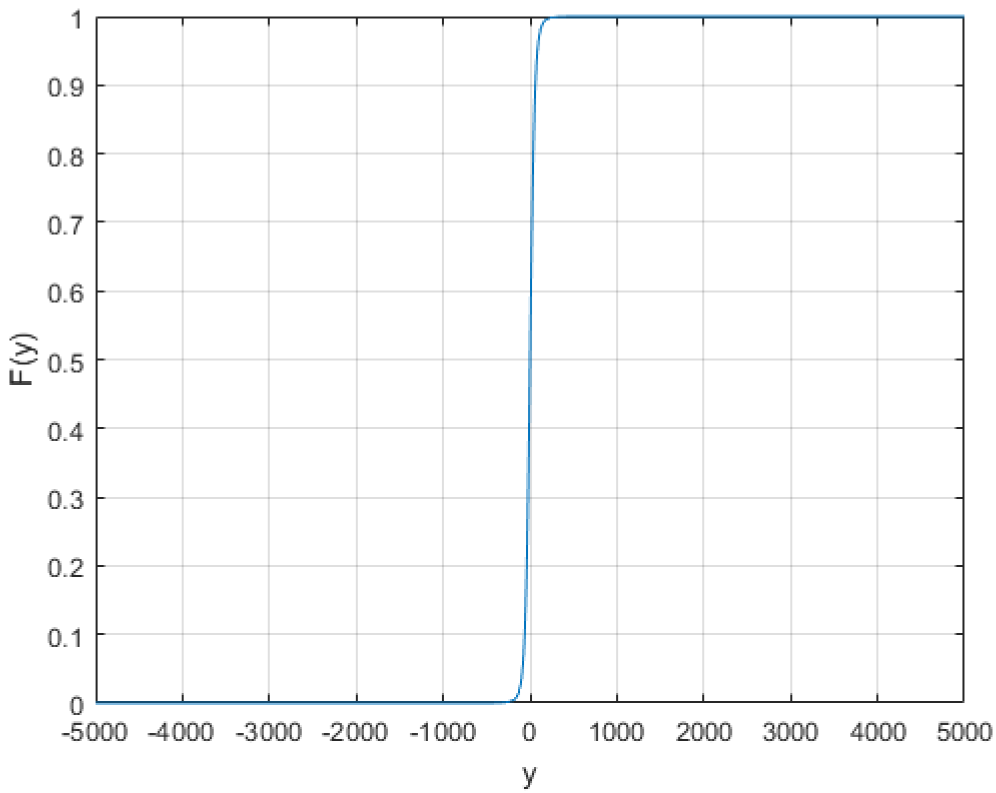

Fig. A.1. An example cdf plot. K = 1.6, σ = 66.

counter = 1;
counter2 = 1;
flag = 0;

% The smalles input, 0, should have $-\infty$ as output. However, in practice,
% this cannot be achieved, so set this value to the lower bound for generating
% cdf.
F_inv(1) = y(1);

% When we want to compute the output of inverse cdf for a particular input
% point, we can compare the input with all points of cdf and find the least

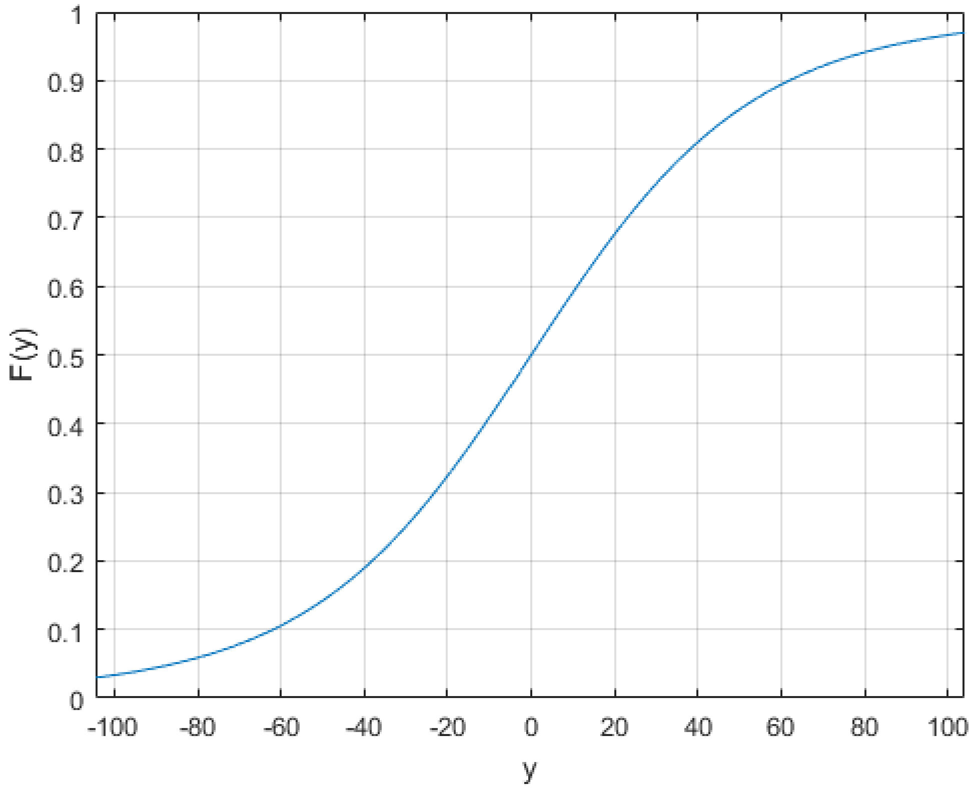

Fig. A.2. An example cdf plot. K = 1.6, σ = 66. This is the zoomed in version of Figure A.1.

% point that is greater than the input and assign that value. However, for a

% large number of inputs, this approach is very time-consuming. Due to the fact

% that the input and cdf are ordered, there exists a faster way for such

% computing. Figure A.3 illustrate the idea.

% Suppose the least number that is greater than u(i-1) is F_inv(j). Then to

% find the least number that is greater than u(i), we simply start the search

% range from F_inv(j), and search in the direction that increases F_inv. All

% values that are less than F_inv(j) are neglected due to the monoticity of

% F_inv.

% Such a process takes max(N1,N2) rounds, where N1 is the length of the first

% vector and N2 is the length of the second vector.

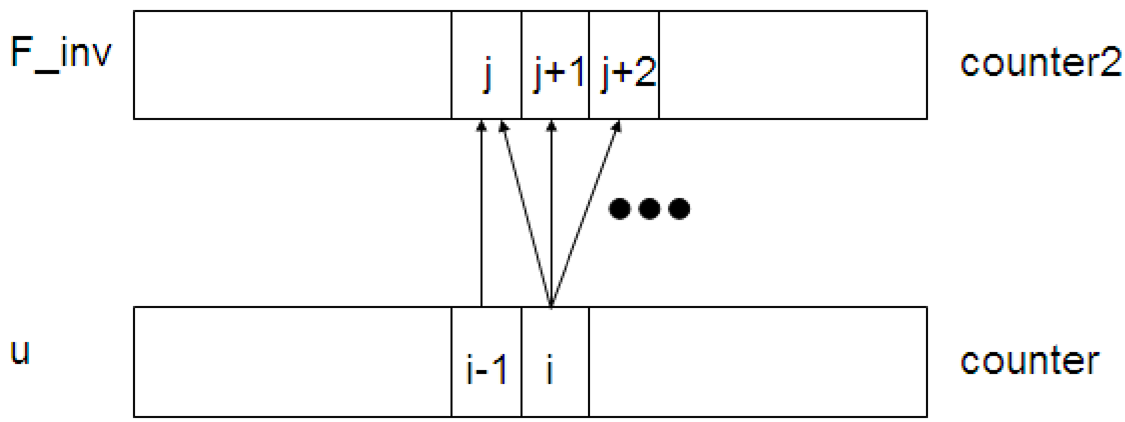

Fig. A.3. Fast algorithm for computing inverse cumulative density function.

for(counter=2:1:sz(2)-1)

while(flag==0)

if(counter2 >= z(2))

F_inv(counter) = y(z(2));

flag = 1;

else

if(F(counter2)>u(counter))

F_inv(counter) = y(counter2);

flag = 1;

else

counter2 = counter2 + 1;

end

```
end

end

flag = 0;

end

% The largest input, 1, should have ∞ as output. However, in practice,
% this cannot be achieved, so set this value to the upper bound for generating
% cdf.
F_inv(sz(2)) = y(z(2));
```

Figure A.4 and Figure A.5 show the output function. That is, the inverse cumulative distribution function.

With these results, we can generate the desired random variable **X** by calling those functions. The next section shows an example of using the random variable for BPSK simulation.

A.4 BPSK Simulation

```
%% BPSK ============================

% input
Eb = [10^2,2*10^2,3*10^2,4*10^2,5*10^2,6*10^2,8*10^2,10^3,2*10^3,6*10^3,10^4,
2*10^4,6*10^4,10^5,2*10^5,6*10^5];

counter = 1;
```

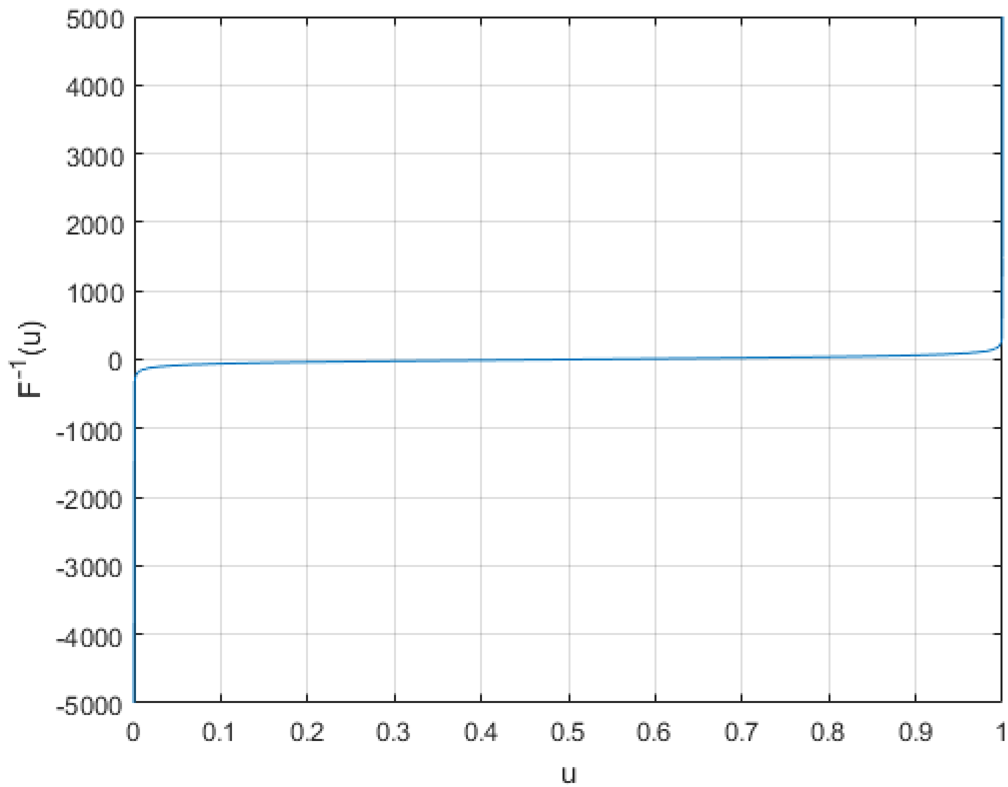

Fig. A.4. An example inverse cdf plot. K = 1.6, σ = 66.

% the number of error events to accumulate to conclude a simulation point Error_MAX = 500;

ipt = 0; %% x
opt = 0; %% y
n = 0; %% n

% flag variable used to control the while loop
flag = 0;

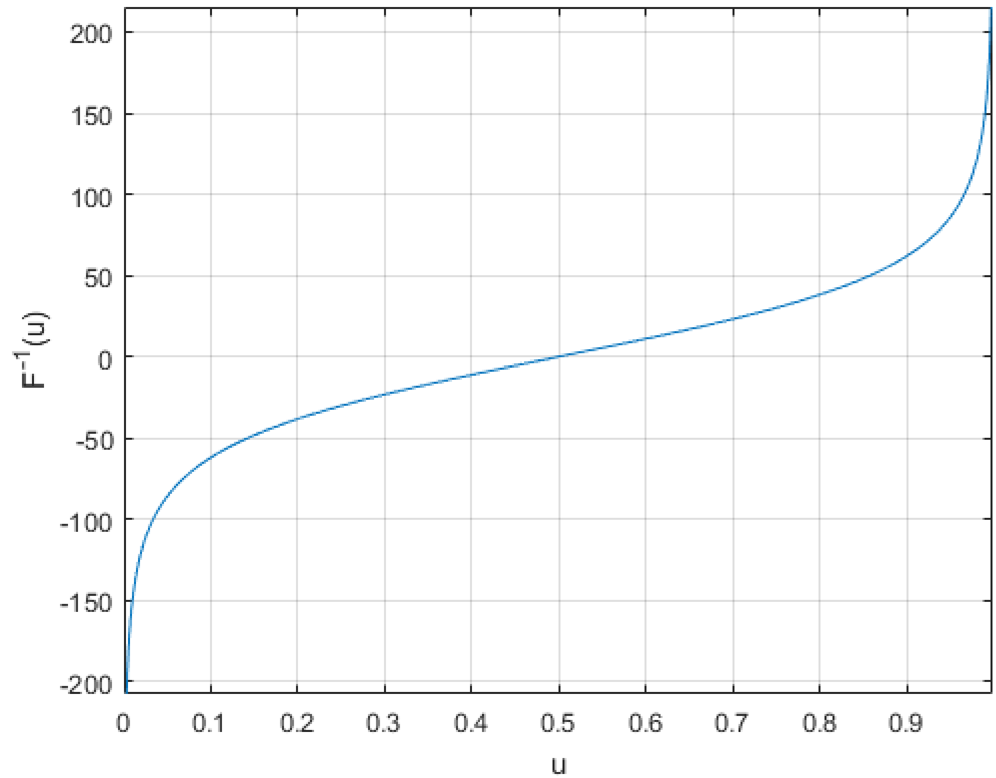

Fig. A.5. An example inverse cdf plot. K = 1.6, σ = 66. This is the zoomed in version of Figure A.4.

```
    zEb = size(Eb);
error_counter = 0;
trials = 0;
% the BER result vector
pe_BPSK_k = zeros(1,zEb(2));

    for(counter=1:1:zEb(2))
error_counter = 0;
trials = 0;
ipt = sqrt(Eb(counter));
while(error_counter < Error_MAX)
```

% rand generates a sample from uniform distribution

temp = rand;

% this generates the desired sample

n = F_inv(floor(temp*10^6)+1);

opt = ipt + n;

if(opt < 0)

error_counter = error_counter + 1;

end

trials = trials + 1;

end

pe_BPSK_k(counter) = error_counter/trials;

end

% compute the variance of the noise from simulation EA_2 = EA2(f,y);

% SNR in dB Eb_Var = 10*log10(Eb/EA_2);

% we can use the following command to view the BER curve
semilogy(Eb_Var_bpsk-10*log10(2),pe_BPSK_k)

This finishes BPSK simulation. The following MATLAB computes the theoretical result for BPSK.

A.5 BPSK Theoretical

%% theoretical
%% BPSK

```
%% 1x1

%% should be the same as the one used in simulation
Eb = [10^2,2*10^2,3*10^2,4*10^2,5*10^2,6*10^2,8*10^2,10^3,2*10^3,6*10^3,10^4,
2*10^4,6*10^4,10^5,2*10^5,6*10^5];

Eb_Var_thr = 10*log10(Eb/(K*sig^2/(2*K-1)));

thr_bpsk_uncorr = zeros(1,length(Eb));
for(counter=1:1:length(Eb))
thr_bpsk_uncorr(counter) = L_func(sqrt(Eb(counter)/(K*sig^2/(2*K-1))),K);
end

%% SNR in dB
Eb_Var_thr_bpsk = Eb_Var_thr;

% we can now view the theoretical curve with the following command
semilogy(Eb_Var_thr-10*log10(2),thr_bpsk_uncorr)
```

Utilization of the above code relies on the computation of L fucntion. In the following section, an example of MATLAB for L function is shown.

A.6 L function

```
function y = L_func(x,K)
%% compute L function
```

```
%% time interval for integration
dt = 0.001;

%% time vector for integration
%% assume the input is limited to +/- 100
t = [0:dt:1000];

%% find the index of t that is closest to x
%% temp_vector = abs(x-t);
%% [idx idx2] = min(temp_vector);
idx2 = floor((x-t(1))/(dt))+1;

%% Kappa distribution
f = 1/(sqrt(2*K-1)*beta(1/2,K+1/2))*((1+(t.^2)/(2*K-1)).^(-K-1));

%% output
y = 0;

%% integration starts from x to inf
for(counter=idx2:1:length(t))
y = y + f(counter)*dt;
end
```

A.7 EA2.m

```
function y=EA2(A,x)
%% compute the E[A^2] of random variable with pdf A and given
%% x-label x
```

```
%% assume mean is 0
%% length of x must be at least 2
%% assume uniform spacing on x-axis

    z = size(x);
h = x(2) - x(1); %% spacing on x-axis between 2 consecutive points
counter = 1;
y = 0;

    for(counter=1:1:z(2))
y = y + ((x(counter))^2)*A(counter)*h;
end
```

VITA

VITA

Hung-Yi Lo was born in Taipei, Taiwan, 1984. He received the Bachelor of Science (Electrical Engineering) in National Taiwan University in July, 2007. He joined Professor Lehnert's lab at Purdue University in August 2009. His research interests are wireless communication, signal processing, wireless networks, and biomedical engineering. He received the *IEEE 9th Annual Computing and Communication Workshop and Conference* Best Paper and Best Presenter awards for his work on underwater acoustic communication in 2019 at Las Vegas, Nevada.